

Constitutive Modelling for Sedimentary Evolution at Basin Scale



Swansea University
Prifysgol Abertawe

Foo Piew Tan

Zienkiewicz Centre for Computational Engineering
Swansea University

This dissertation is submitted for the degree of
Doctor of Philosophy


College of Engineering

April 2020

*Was du ererbt von deinen Vätern hast,
Erwirb es, um es zu besitzen. - Goethe*

Declaration

1. This work has not previously been accepted in substance for any degree and is not being concurrently submitted in candidature for any degree.

Signed..........(candidate)

Date.....

2. This thesis is the result of my own investigations, except where otherwise stated. Other sources are acknowledged by footnotes giving explicit references. A bibliography is appended.

Signed.....(candidate)

Date.....

3. I hereby give consent for my thesis, if accepted, to be available for photocopying and for inter-library loan, and for the title and summary to be made available to outside organisations.

Signed.....(candidate)

Date.....

Acknowledgements

Firstly, I would like to express my deepest appreciation to my supervisor, Professor Djordje Perić, who has convincingly provided invaluable guidance, constant support, and helped improving my general knowledge in the field of computational mechanics. In addition, without his immense support and persistent help in securing the funding, the goal of this PhD would not have been realised.

I would like to pay my special regards to Dr Tony Crook, whose assistance was a milestone in the completion of this thesis. It is whole-heartedly appreciated that his great advice and insights proved monumental towards the success of this study. It should be mentioned that it has been an absolute honour and privilege to work with Dr Tony Crook, who has had great and permanent influence on my attitude towards research.

I would like to recognise the invaluable assistance and support given by Swansea University staffs, especially of College of Engineering, Singleton Campus library, MyUniHub, and International@CampusLife. It is acknowledged that this project was funded by National Research Network (NRN) of Welsh Government.

I wish to thank Dr. Deniz D. Somer and Joshua Obradors-Prats for the numerous and productive technical discussions we had during this time. My PhD journey would not have been complete with my close friends, Dr. Emilio García Blanco and Sanjay Komala Sheshachala, for all wonderful moments we had over our regular dinner at Chinese Flavour Restaurant on Brynymor Road. I cannot thank enough Dr. Rui Liang for his friendship and great deal of help for providing a 3-month temporary home when I had enough with alcoholically intoxicated housemate. Also, I am indebted to Aunty Molly, Uncle Charles and all volunteers for turning English Corner into a special place in Swansea, especially for international students.

I owe a very important debt to Professor Vijay R. Raghavan (IIT Madras), whose commitment and enthusiasm towards research has inspired me to go beyond my comfort zone. Prof. Vijay has changed my life forever when he decided to provide financial support for me to study MSc. in Computer Modelling and Finite Elements in Engineering Mechanics at Swansea University. I would also like to thank Dr. William Pao who encouraged us to go outside Malaysia and explore the world.

This work is dedicated to my parents to whom I am indebted for their endless support, trust and unconditional love. Despite some challenges encountered in Malaysia, they have never failed to shower me with encouragement in my pursuit of something great. It is impossible to thank my parents adequately for every sacrifice they have made.

Throughout this chapter of my life, my loving girlfriend Yinan Liu has never failed to support me with great patience in our 4-year (and still counting) long distance relationship. Thank you for your trust in me.

Summary

This work is focused on the development of constitutive models for elastoplastic-fracture behaviour in scenarios characterised by large deformation ranging from laboratory to geological length scale. Both seepage and geomechanical fields are considered, with the assumption of isothermal field.

The standard Drucker-Prager model is enhanced by applying π -plane correction factor, and the use of hardening properties which depends on the evolution of effective plastic strain. Non-associative potential plastic flow function is used to derive the plastic flow vector. To ensure finite energy dissipation during softening, regularisation technique based on fracture energy approach is adopted. The resulting modified Drucker-Prager model is combined with rotating crack model (which relies on Rankine failure criterion) to develop an elastoplastic-fracture framework by considering multi-step stress update procedures. The advantage of multi-step stress update is that the framework allows the use of any elastoplastic model without any major change in the code. Performance of this set of constitutive models is assessed by studying several simulation examples, including bearing capacity of strip footing, crack propagation in a specimen with pre-existing inclined fault, influence of size effect on borehole instability, influence of pore pressure on thrust fault formation, and hydraulic fracture due to fluid injection. Overall, the numerical results show good agreement with available analytical solutions or experimental findings.

For basin-scale problem, SR4 model is used due to its capability to capture the evolution of pre-consolidation pressure p_c , that is not considered in Drucker-Prager model. In this case, the goal is to simulate basin-scale gravitational deformation in a prograding delta due to fluid overpressure in shale layer with synkinematic sedimentation. With the aid of adaptive remeshing algorithm, the result successfully produces distinct fault patterns across the prograding delta in terms of plastic strain distribution. In particular, three different zones are observed: extensional, transition, and compressional zone. The extensional zone is characterised by basinward-dipping normal faults, whereas the compressional zone is characterised by basinward-verging fore-thrust faults.

Overall, the simulation results illustrate the potential that the developed constitutive models under the integrated flow-geomechanical modelling framework could offer to future analysis of more complex geological evolution.

Table of contents

List of figures	xv
List of tables	xxiii
1 Introduction	1
1.1 The Aim of the Thesis	5
1.2 Outline of the thesis	5
2 Review of Flow-Geomechanical Governing Equations	9
2.1 Introduction	9
2.2 Linear Momentum Equation	9
2.3 Mass Balance Equation	10
2.3.1 Fluid Phase Mass Balance Equation	11
2.3.2 Solid Phase Mass Balance Equation	13
2.3.3 Combined Mass Balance Equation	16
2.4 Hydraulic Permeability	18
2.5 Fluid Diffusion Time Scale	20
3 Computational Strategies for Coupling Geomechanics with Fluid Flow	23
3.1 Kinematics and Geometry Descriptions	23
3.1.1 Motion as Configuration Mapping	23
3.1.2 Deformation Gradient	24
3.1.3 Velocity Gradient and Rate of Deformation Gradient	24
3.2 Weighted Residual Formulation	25
3.2.1 Strong Formulation	25
3.2.2 Weak Formulation	27
3.3 Finite Element Discretisation	28
3.3.1 Shape Function and Matrix Notation	28
3.3.2 Global Discretisation of Rate of Virtual Work	30

3.3.3	Element-Level Representation	33
3.4	Numerical Simplification and Strategies	34
3.4.1	Lumped Mass Matrix	34
3.4.2	Critical Time Step	34
3.4.3	Damping	35
3.4.4	Averaged Volumetric Strain	37
3.5	Time Discretisation and Solution Update	38
3.5.1	Geomechanical Field	38
3.5.2	Seepage Field	45
3.6	Split Schemes for Flow-Geomechanical Fields	45
3.6.1	Undrained Split Scheme	46
3.6.2	Fixed-Stress Split Scheme	49
4	Elastoplastic-fracture Constitutive Models for Pressure-Sensitive Geomaterials	53
4.1	Elastoplastic Constitutive Equations	53
4.2	Mohr-Coulomb Model	54
4.3	Drucker-Prager Model	55
4.4	Modified Drucker-Prager Model	57
4.4.1	Yield Function	57
4.4.2	Non-Associative Potential Plastic Flow Function	63
4.4.3	Hardening Law	65
4.4.4	Regularisation of State Variables	66
4.5	SR4 Model	68
4.5.1	Yield Functions	68
4.5.2	Non-Associative Potential Plastic Flow Functions	74
4.5.3	Hardening Law	77
4.6	Return Mapping Algorithm	78
4.6.1	Initial Value Problem	78
4.6.2	Incremental Constitutive Problem	78
4.6.3	Decomposition of Stress Tensor into Deviatoric and Hydrostatic Components	79
4.6.4	Modified Drucker-Prager Model	81
4.6.5	SR4 Model	85
4.7	Elastoplastic-Fracture Model	91
4.7.1	Rotating Crack Model	91
4.7.2	Implementation with Elastoplastic Models	102
4.8	Single Element Test	106

4.8.1	Elastoplastic Models	106
4.8.2	Elastoplastic-Fracture Model	116
5	Numerical Examples: Lab-scale Test Simulations	119
5.1	Introduction	119
5.2	Bearing Capacity of Strip Footing	119
5.2.1	Introduction	119
5.2.2	Model Setup and Material Parameters	121
5.2.3	Results	122
5.3	Crack Propagation and Coalescence in a Specimen with Pre-existing Inclined Fault	127
5.3.1	Introduction	127
5.3.2	Rock Specimen Types	128
5.3.3	Test 1: Formation of Tensile Wing Crack	129
5.3.4	Test 2: Effect of Inclination Angle	132
5.3.5	Test 3: Effect of Cohesive Strength on Secondary Crack	137
5.3.6	Test 4: Effect of Bridge Angle on Crack Coalescence	146
5.3.7	Concluding Remarks	156
5.4	Influence of Size Effect on Borehole Instability	156
5.4.1	Introduction	156
5.4.2	Modelling Setup	156
5.4.3	Results	158
5.5	Uniaxial Consolidation and Sedimentation of Soil Column	162
5.5.1	Uniaxial Consolidation of Soil Column	162
5.5.2	Sedimentation of Soil Column	167
5.6	Influence of Pore Pressure on Thrust Fault Formation	171
5.6.1	Introduction	171
5.6.2	Modelling Setup and Material Properties	172
5.6.3	Solution Control and Loading Stages	174
5.6.4	Results	175
5.6.5	Concluding Remarks	180
5.7	Hydraulic Fracture due to Fluid Injection	181
5.7.1	Modelling Setup	181
5.7.2	Simulation Groups	181
5.7.3	Results: 1 st Simulation Group	183
5.7.4	Results: 2 nd Simulation Group	183
5.7.5	Concluding Remarks	186

6 Basin Scale Simulation: Gravity Spreading in Prograding Delta due to Over-	
pressure	191
6.1 Introduction	191
6.1.1 Background	191
6.1.2 Decollement Layer	191
6.1.3 Overpressure Generation	192
6.1.4 Feedback Mechanism	193
6.1.5 Nigeria Delta Field	193
6.2 Some Previous Modelling Studies	196
6.2.1 Sedimentary Progradation using Sandbox Models	196
6.2.2 Influence of Fluid Overpressure on Deformation	198
6.2.3 Sedimentary Progradation via Mechanical and Viscous Compaction Mechanisms	199
6.2.4 Key Aspects of Literature Findings	203
6.3 Modelling Setup	204
6.3.1 Geometry and Boundary Conditions	204
6.3.2 Material Properties	206
6.4 Results	209
6.5 Concluding Remarks	216
7 Conclusions	219
7.1 Dry Case: Elastoplastic-Fracture Model	219
7.2 Elastoplastic-Fracture Model Coupled with Flow Field	220
7.3 Prograding Delta due to Gravitational Instability Triggered by Overpressured Shale Layer with Synkinematic Sedimentation	220
7.4 Recommendations for Further Research	221
References	223
Appendix A Modified Drucker-Prager Return-Mapping Algorithms	237
Appendix B SR4 Return-Mapping Algorithms	243
Appendix C Material Properties for Section 5.6 Simulation Tests	251

List of figures

1.1	Schematic of rock cycle. Figure obtained from [63]	1
1.2	Global distribution of sediment thickness. Figure obtained from [99]	3
1.3	Niger delta tectonic structure. Figure obtained from [45]	4
1.4	Figures obtained from [124], showing the fault patterns obtained from sand-box model	4
2.1	Biot's coefficient as function of porosity, whose curve is controlled by parameter a	10
3.1	Illustration of coarse time step in seepage field followed by multiple fine time steps in geomechanical field in simulating flow-geomechanical fields in split form	47
3.2	Illustration of pore pressure increment Δp_f^N in mechanical step before the start of the current seepage flow step. The term Δp_f^N is used to provide smooth transition of total pore pressure over the current seepage flow time step Δt_p	48
3.3	Illustration of total mean stress increment $\Delta \bar{p}^N$ and volumetric strain increment $\Delta \epsilon_v^N$ over Δt^N for the computation of pore fluid pressure \bar{p}_f^{K+1} at the current mechanical step (t^{N+1})	51
4.1	Mohr-Coulomb yield surface $\tau - \sigma$ space	55
4.2	Drucker-Prager yield surface in principal stress space	55
4.3	Approximation of Drucker-Prager model to Mohr-Coulomb yield surface	56
4.4	Shape of yield locus for frictional materials on deviatoric plane [3]	57
4.5	Experimental findings that yield surface associated with CTC test ($q > 0$) is larger than that with RTE test ($q < 0$)	58
4.6	Representation of multiaxial yield criterion in terms of principal stresses	61
4.7	Effect of cohesion d and friction angle β on the geometry of modified Drucker-Prager yield surface in deviatoric plane	62

4.8	Effect of β_0 on the yield surface geometry. Care should be taken when calibrating β_0 to avoid non-convexity of the yield locus.	63
4.9	Regularisation of cohesion-effective plastic strain (left) and preconsolidation pressure-volumetric plastic strain (right) softening slopes under the influence of element sizes	66
4.10	Two fracture modes. Mode I is characterised by fracture opening mode via tensile failure. Mode II is characterised by shearing mode over fracture surface. Mode III is characterised by tearing mode.	67
4.11	Illustration of SR4 model in $p - q$ plane	68
4.12	The shape of SR4 yield locus in deviatoric plane is sensitive to the effective mean stress p . As p approaches p_t , the shape tends to be more triangular. Vice versa, as p approaches p_c , the shape tends to be more rounded. The size of yield locus is maximum when $p = p_{\Phi_{crit}}$	73
4.13	Illustration of hardening/softening law, describing the evolution of specific volume as function of the natural logarithm of effective mean pressure p	77
4.14	Illustration of linear softening in $f_t - \varepsilon_f$ plot, showing tensile strength is reduced to zero when reaching the critical fracture strain $\varepsilon_{f,c}$	93
4.15	Total strain as sum of fracture strain and elastically unloaded strain during fracture stress update	96
4.16	Failure criterion based on Mohr-Coulomb model	103
4.17	Rankine state boundary line becomes steeper as Lode angle θ changes from $\theta = -\frac{\pi}{6}$ to $\theta = \frac{\pi}{6}$	103
4.18	Increasing size of Rankine state boundary locus with tensile strength f_t	104
4.19	Increasing size of Rankine state boundary locus with tensile strength f_t	104
4.20	Influence of coupling constant η on the slope of $d-f_t$ plot. $\eta < 0$ for sublinear behaviour and $\eta > 0$ for supralinear behaviour.	106
4.21	Illustration of boundary conditions applied on a single element. The top boundary is prescribed with vertically downward displacement for compressional loading, and vertically upward displacement for extensional loading. Confining pressure p_{conf} is fixed throughout the loading process.	107
4.22	Stress paths of each element initially loaded with different confining pressures p_{conf} . Lower π -plane correction factor g results in larger elastic domain under compressional loading condition, and vice versa for extensional loading condition.	108

4.23	The effect of π -plane correction factor can also be visualised in terms of stress-strain response of the test specimen. The key highlight is that the magnitude of yield stress of extensional loading is different from that of compressional loading.	108
4.24	Axisymmetric illustration of conventional triaxial compression (CTC) and triaxial extension (TXE) tests for SR4 model	109
4.25	Hardening properties for SR4 elastoplastic model	111
4.26	Effect of confining pressure p_{conf} on the final yield surface under CTC condition at fixed initial pre-consolidation pressure (-3MPa). For low confining pressure (0.1-1.0MPa), the stress path approaches the shear side of initial yield surface, resulting in the shrinkage of yield surface towards critical state condition. For high confining pressure (1.5MPa), the stress path approaches the compression side of initial yield surface, resulting in the expansion of yield surface towards critical state condition.	112
4.27	Effect of confining pressure p_{conf} on the evolution of volumetric, axial, and radial strains under CTC condition. Positive radial strain, negative volumetric and axial strains recovered. Strain hardening is observed for $p_{conf} = 1.5\text{MPa}$, which corresponds to expansion of yield surface.	113
4.28	Effect of confining pressure p_{conf} on the final yield surface under TXE condition at fixed initial pre-consolidation pressure (-3MPa). For low confining pressure (0.1-0.3MPa), the stress path approaches the shear side of initial yield surface, resulting in the shrinkage of yield surface towards critical state condition. For high confining pressure (1.0-1.5MPa), the stress path approaches the compression side of initial yield surface, resulting in the expansion of yield surface towards critical state condition. Note that, because the stress path slope in TXE condition is lower than the CTC counterpart, plastic compression takes place at relatively lower confining pressure (i.e. $p_{conf} = 1.0\text{MPa}$), compared to CTC case.	114
4.29	Effect of confining pressure p_{conf} on the evolution of volumetric, axial, and radial strains under TXE condition. Positive axial strain, negative volumetric and radial strains recovered. Strain hardening is observed for $p_{conf} = 1.0\text{MPa}$ and $p_{conf} = 1.5\text{MPa}$, which corresponds to expansion of respective yield surface.	115
4.30	A block of size 1m by 1m is subjected to prescribed displacement on the right side under the boundary conditions as illustrated in the figure	116

4.31	Effect of coupled tensile strength-cohesion on the stress-strain constitutive behaviour under monotonic loading condition	117
4.32	Stress-strain behaviour due to cyclic loading at different level of η_1	118
5.1	Problem definition of strip footing using Drucker-Prager model [54]	120
5.2	Geometry and boundary conditions of strip footing simulation domain	121
5.3	Different mesh sizes to be simulated in the strip footing problem	121
5.4	Comparison of outer edge assumption and plane strain assumption	123
5.5	Numerical solution approaching Prandtl's solution asymptotically as mesh size decreases	123
5.6	Mesh convergence plot for plane strain assumption	124
5.7	Plastic strain contour when $u = 5mm$	124
5.8	Evolution of plastic strain rate as settlement increases	125
5.9	Vertical stress σ_{yy} as failure progresses during limit load	126
5.10	Displacement and velocity vectors during failure of strip footing	126
5.11	Illustration of crack type in the vicinity of pre-existing fracture under compressive stress condition. Figure obtained from [19].	127
5.12	Types of rock specimen used in the current study	128
5.13	Formation of tensile wing crack. Direction of crack propagation becoming increasingly parallel to the loading direction.	130
5.14	Highly compressive stress field at the tip of pre-existing fracture	131
5.15	Displacement and velocity field at time 0.018s	131
5.16	Tensile wing crack created in experiment by [176].	132
5.17	$\beta_{inc} = 60^\circ$. (a) Damage factor (b) Figure obtained from [176]	133
5.18	$\beta_{inc} = 45^\circ$. (a) Damage factor (b) Figure obtained from [176]	133
5.19	$\beta_{inc} = 30^\circ$. (a) Damage factor (b) Figure obtained from [176]	134
5.20	$\beta_{inc} = 15^\circ$. (a) Damage factor (b) Figure obtained from [176]	134
5.21	$\beta_{inc} = 0^\circ$. (a) Damage factor (b) Figure obtained from [176]	134
5.22	$\beta_{inc} = 45^\circ$ corresponds to the lowest strength of rock specimen. Such finding agrees with the laboratory result conducted by [176].	135
5.23	The migration of principal stress 1 as the inclination angle decreases	136
5.24	Secondary crack observed in experimental test by [19]	137
5.25	Crack propagation angle as defined in [167]	137
5.26	Load displacement curve for specimen with varying initial cohesive strength	138
5.27	Tensile wing crack and secondary crack propagation of specimen with $\beta_{inc} = 45^\circ$ and initial cohesion as 10MPa	139

5.28	Evolution of plastic strain in specimen with $\beta_{inc} = 45^\circ$ and initial cohesion as 10MPa	140
5.29	Evolution of cohesive strength in specimen with $\beta_{inc} = 45^\circ$ and initial cohesion as 10MPa	141
5.30	Horizontal displacement of specimen with $\beta_{inc} = 45^\circ$ and initial cohesion as 10MPa	142
5.31	Crack propagation pattern for specimen with different initial cohesive strength	143
5.32	Plastic strain distribution for specimen with different initial cohesive strength	144
5.33	(Tested on specimen having 45° of inclination angle) Crack propagation angle decreases as water content is increased. Experimental data obtained from [167].	145
5.34	Crack propagation angle β_{inc2} decreases with initial cohesive strength . . .	145
5.35	Evolution of damage factor for Type 2 rock specimen with $\beta_{brg} = 45^\circ$. . .	146
5.36	Evolution of cohesive strength for Type 2 rock specimen with $\beta_{brg} = 45^\circ$. .	147
5.37	Evolution of tensile strength f_{t1} for Type 2 rock specimen with $\beta_{brg} = 45^\circ$.	148
5.38	Crack pattern for specimen with $\beta_{brg} = 45^\circ$	149
5.39	Evolution of damage factor for Type 2 rock specimen with $\beta_{brg} = 90^\circ$. . .	150
5.40	Evolution of cohesive strength for Type 2 rock specimen with $\beta_{brg} = 90^\circ$. .	150
5.41	Evolution of tensile strength for Type 2 rock specimen with $\beta_{brg} = 90^\circ$. . .	151
5.42	Crack pattern for specimen with $\beta_{brg} = 90^\circ$	152
5.43	Evolution of damage factor for Type 2 rock specimen with $\beta_{brg} = 120^\circ$. . .	153
5.44	Evolution of cohesive strength for Type 2 rock specimen with $\beta_{brg} = 120^\circ$.	153
5.45	Evolution of tensile strength f_{t1} for Type 2 rock specimen with $\beta_{brg} = 120^\circ$	154
5.46	Crack pattern for specimen with $\beta_{brg} = 120^\circ$	155
5.47	Geometry and boundary conditions of borehole cross section	157
5.48	Mean stress-displacement curve for specimen of different sizes	158
5.49	Dependence of collapse pressure on the specimen size	159
5.50	Plastic strain contour of specimen with different size during final rupture . .	160
5.51	Displacement contour and vector plot for each specimen during borehole breakout stage	161
5.52	Axial splitting of brittle Berea sandstone. Figure obtained from [68].	161
5.53	Initial and boundary conditions of soil column for solving Terzaghi's solution	163
5.54	Comparison of analytical (line plot) and numerical (dotted plot) prediction of pore pressure evolution during consolidation of fully saturated soil column. Time step size = $0.2(10^{-6})$	164

5.55	Evolution of pore pressure and effective mean stress near the column top surface	165
5.56	Properties of fluid conductivity and permeability	166
5.57	Comparison of pore pressure evolution	166
5.58	Geometry of the initial model. The top surface is subjected to sedimentation with (a) high sedimentation rate (1000m/Ma) and (b) low sedimentation rate (500m/Ma)	167
5.59	Comparison of pore pressure evolution at the column base during sedimentation for different hydraulic permeabilities	169
5.60	Comparison of pore pressure variation with depth at 1.1Ma for different hydraulic permeabilities	169
5.61	Comparison of pore pressure evolution at the column base during sedimentation for different sedimentation rates	170
5.62	Comparison of pore pressure variation with depth at 2.1Ma for different sedimentation rates	170
5.63	Experimental setup by Cobbold et al. [38]	171
5.64	Dimension of model geometry	172
5.65	Prescribed boundary conditions	172
5.66	Geometry sets of simulation model	173
5.67	Pore pressure contour before the displacement of sliding wall	175
5.68	Comparison between simulation and Cobbold's [38] results	176
5.69	Pore pressure contour in final configurations (Group 1)	176
5.70	Plastic strain development (Group 1)	177
5.71	Cloud plotting of yielding points in Layer 1 (Group 1)	177
5.72	Cloud plotting of stress points (elastic state) in Layer 1 (Group 1)	178
5.73	Topological evolution of top surface due to pore pressure (Group 1)	178
5.74	Deformation style of sand layers (Group 2)	178
5.75	Plastic strain development (Group 2)	179
5.76	Cloud plotting of yielding points in Layer 1 (Group 2)	179
5.77	Cloud plotting of stress points (elastic state) in Layer 1 (Group 2)	180
5.78	Topological evolution of top surface due to pore pressure (Group 2)	180
5.79	Comparison of top surface slope between Group 1 and Group 2 simulations	180
5.80	Geometry and spatial discretisation	182
5.81	Pore pressure distribution for different permeabilities at fixed $k_y = 10^{-14}m^2$ at $t = 0.5s$	184

5.82	Tensile strength distribution for different permeabilities at fixed $k_y = 10^{-14}m^2$ at $t = 0.5s$	184
5.83	Principal stress 1 distribution for different permeabilities at fixed $k_y = 10^{-14}m^2$ at $t = 0.5s$	185
5.84	Vertical (y) displacement for different permeabilities at fixed $k_y = 10^{-14}m^2$ at $t = 0.5s$	185
5.85	Volumetric strain evolution of a sample element near initial fracture tip for $k_x = 10^{-14}m^2$	186
5.86	Volumetric strain evolution of a sample element near initial fracture tip for $k_x = 10^{-12}m^2$	186
5.87	Volumetric strain evolution of a sample element near initial fracture tip for $k_x = 10^{-10}m^2$	187
5.88	Volumetric strain evolution of a sample element near initial fracture tip for different k_x at final simulation time $t = 0.5s$	187
5.89	Pore pressure evolution at the initial fracture tip for different k_x and fixed k_y	188
5.90	Effect of cohesion-tensile strength coupling on the initiation of stress softening. The coupling factor η_1 is set as 0.01.	188
5.91	The reduction of tensile strength contributes to the reduction of cohesion via the cohesion-tensile strength coupling factor η_1	189
6.1	Figure obtained from [37], showing extensional, transitional and compressional province along a generic cross section of Niger Delta.	194
6.2	Figure obtained from [37], showing the seismic profiles and interpretation of Southern lobe (left) and Western lobe (right) in Niger Delta.	195
6.3	Figures obtained from [37], showing the seismic profile of vents identified in Niger Delta.	196
6.4	Figures obtained from [124], showing the fault patterns obtained from three different sandbox models	197
6.5	Figure obtained from [129]. The structure at the top was generated under drained conditions, whereas the structure at the bottom was generated under coupled hydro-mechanical conditions. This comparison highlights the importance of accounting for overpressure generation in simulating fold and thrust faults.	199
6.6	Figures obtained from [120], showing the distribution of Hubbert-Rubey pore pressure parameter along with solid-matrix velocity vector in a purely disequilibrium compaction model (top), and in a model with disequilibrium and viscous compaction mechanisms (bottom).	200

6.7	Figures obtained from [89], showing a lithospheric model to account for isostatic equilibrium.	200
6.8	Permeability-porosity trend based on (6.2), with $k_0 = 10^{-18} \text{ m}^2$ and $n_0 = 0.1$	201
6.9	Figures obtained from [89], showing the evolution of basal deformation during initialisation stage.	202
6.10	Figures obtained from [89], showing the evolution of sedimentary deformation deposited at different times during stress relaxation stage.	202
6.11	Figures obtained from [89], showing the horizontal strate rate as well as Hubbert-Rubey pore pressure distribution in the delta towards the end of stress relaxation stage	203
6.12	Description of geometry and boundary conditions for 160km model of prograding delta	204
6.13	Porosity-depth relationship for overburden and shale according to Scalter-Christie correlation	208
6.14	Incipient deltaic progradation as Hubbert-Rubey pore pressure ratio λ_{HR} is close to 1.	209
6.15	Prograding delta due to basal fluid overpressure with synkinematic sedimentation	210
6.16	Plastic strain development during progradation	212
6.17	Plastic strain as representation of faults. Fore-thrust faults in compressional domain, and concave-upward normal faults in extensional domain	213
6.18	Pore pressure distribution during at final simulation time $t = 8.7\text{Ma}$	214
6.19	Figure obtained from [37], showing the large deviation from hydrostatic distribution towards higher value of pore pressure as depth approaches shale layer	214
6.20	Magnified velocity vectors in both compressional and extensional region . .	215
6.21	Displacement components at final simulation time $t = 8.7\text{Ma}$	216
7.1	Increasing trend of landslide happening in Malaysia in recent years. Data obtained from [95, 96].	222

List of tables

2.1	Material constants for modified form of Kozeny-Carmen model (2.46)	18
2.2	Piecewise-linear porosity-permeability (log mD) data for sandstone, siltstone, and shale [83]	19
4.1	Material properties for modified Drucker-Prager model range test	107
4.2	Material properties of SR4 model used for CTC and TXE tests	110
4.3	Material properties for elastoplastic-fracture 1D element demonstration	116
4.4	Prescribed cyclic displacement	118
5.1	Properties of quasi-brittle material	129
5.2	Initial properties of elastoplastic material	129
5.3	Initial properties of elastoplastic material	157
5.4	Hardening properties for borehole breakout simulation	157
5.5	Material properties for Terzaghi's benchmark test	163
5.6	Material properties for Terzaghi's benchmark test	165
5.7	Material properties for uniaxial consolidation test	168
5.8	Adaptive remeshing as function of effective plastic strain	172
5.9	Cases with different prescribed basal pore pressure	173
5.10	Surface interaction for contact boundary condition	174
5.11	Compressional/Tangential penalty and friction coefficient	174
5.12	Simulation groups	174
5.13	Properties of quasi-brittle material	182
6.1	Geometry values for 160km model with reference to Figure 6.12	205
6.2	Coordinates for new deposition layer at different simulation time. Each new layer is defined by 4 points (i.e. P_1 - P_4) with reference to Figure 6.12.	205
6.3	Prescription of pore fluid pressure (MPa) at different segments of shale base layer at different simulation times	206
6.4	Adaptive remeshing criteria for shale layer	206

6.5	Adaptive remeshing criteria based on plastic strain for overburden layer . . .	206
6.6	Adaptive remeshing criteria based on plastic strain rate for overburden layer	206
6.7	SR4 material paramaters and properties for overburden	207
6.8	SR4 material paramaters and properties for shale	208
C.1	Poroelastic properties for Sand 1, 2, 3	251
C.2	Poroelastic properties for Wall	251
C.3	Hydraulic permeabilities	251
C.4	Sand 1 hardening properties	252
C.5	Sand 2 hardening properties	252
C.6	Sand 3 hardening properties	252
C.7	Air properties	252

Chapter 1

Introduction

Rocks are mainly categorised into three types: sedimentary, metamorphic, and igneous. These rocks do not remain the same forever because of rock cycle. Rock cycle is driven by the Earth internal heat engine, which is responsible for mantle convection as well as hydrological cycle driven by the Sun. In other words, rock cycle is impossible without sufficient heat from the planet core and liquid water (e.g. Moon).

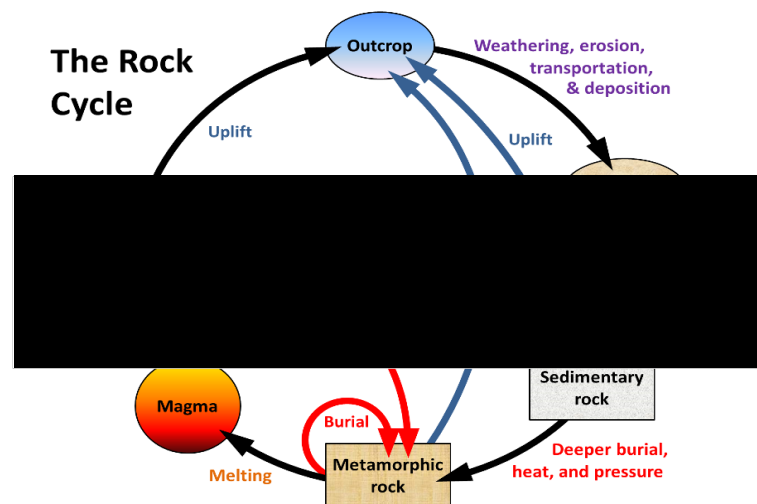


Fig. 1.1 Schematic of rock cycle. Figure obtained from [63]

Rock cycle is summarised in Figure 1.1. At depth below the Earth surface where the temperature is in the range of 800°C - 1300°C , magma is completely in molten form. If the magma is trapped within the crust and undergoes cooling process, it will be crystallised as intrusive igneous rock. On other hand, if the magma is erupted onto the Earth surface, it will be cooled relatively faster and crystallised as extrusive igneous rock. Any rock that is exposed (e.g. via tectonic-related uplifting process) to the Earth surface are subjected to weathering

process, which may come in the form of biological (e.g. rock disintegration by plants), chemical (e.g. acidic rain), and physical (e.g. thermal stress caused by change in temperature) processes. Weathered rocks are fragmented rocks that are typically transported by fluid movement to surfaces at lower height, where they are eventually deposited. When more new sediments are deposited in the same place, the buried sediments undergo compaction and cementation, becoming sedimentary rocks. If these rocks are continuously buried to a greater depth and subjected to intense heat and pressure, they will be transformed back to metamorphic rock.

Despite the straightforward explanation provided by rock cycle concept, the computational modelling of each physical phenomenon is far from being straightforward. This requires an integrated modelling framework that properly accounts for the coupling between the reaction, transport and mechanical dynamic evolution of the geophysical rock formation. Such a modelling framework relies on the computation of simultaneous evolution of a number of different fields including: the state variables that describe the internal state of the rock formation (i.e. the material state boundary surface), rock permeability, fluid properties, the evolving rock texture and mineralogy, thermal conductivity, fault and fracture characteristics, etc., to name a few.

In view of this, thermo-hydro-mechanical (THM) models have been applied in various fields for different needs. In hydrocarbon industry, THM analysis is required to simulate changes induced by reservoir production [33, 79, 78, 100, 35, 139, 154, 55, 113, 164, 107, 163]. Depleted reservoirs are re-utilised for CO₂ sequestration [145, 146]. THM models are also frequently applied to simulations related to the storage of nuclear waste products [32, 23, 127, 147].

THM analysis has also been extended to the modelling of sedimentary basin. Sedimentary basin is defined as region that is subjected to prolonged crustal subsidence that provides space for infilling by sediments. Over geological time, the sediments accumulate to considerable thickness that varies across the globe (Figure 1.2). Some examples of sedimentary rocks include sandstone, shale, siltstone, limestone and rock salt. In terms of geomechanical modelling, the applications of THM analysis include

- General description of basin development [4]
- Porosity evolution in North Sea fields [161, 21, 22]
- Influence of compaction and diagenesis on overpressure development [150, 130, 178, 149, 74]
- Pore pressure generation via disequilibrium compaction [22, 174], via hydrocarbon maturation [179, 82] and via aquathermal pressuring [104]

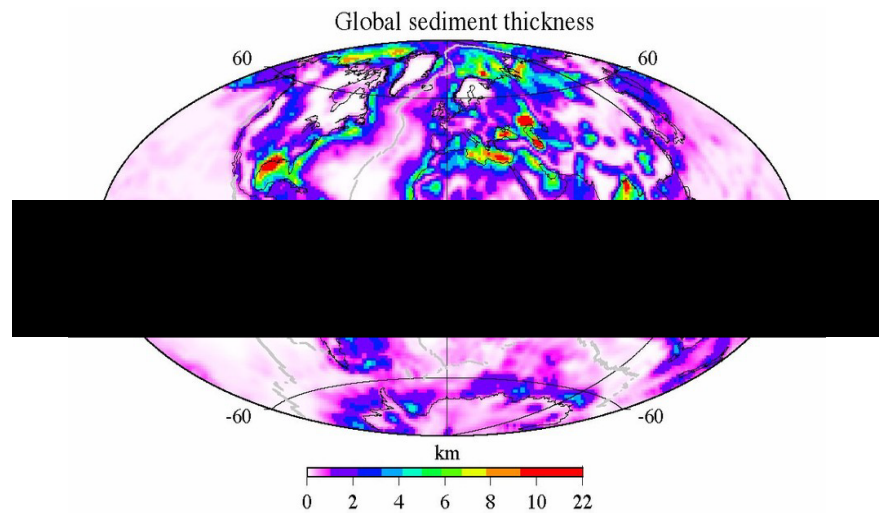


Fig. 1.2 Global distribution of sediment thickness. Figure obtained from [99]

- Simulations of sedimentation and large-strain consolidation in sedimentary basins using constitutive relations for mechanical compaction and permeability change based on experimental data for several clays compacted to high effective stress [80]
- Simulation of compaction in sedimentary basins [105]
- Basin modelling studies [5]
- Detailed description of the assumptions adopted in basin and petroleum systems modelling [83]
- Overview of fluid flow including the influence of temperature [17]
- Basin scale heat flow analysis without deformation [4, 83]
- Crustal-like thermo-mechanical models [6, 25, 134, 137, 180]
- Probabilistic calibration of 1D heat flow [182]

In crustal-scale modelling, porous flow field is generally neglected so that a thermo-mechanical (TM) analysis is performed. The sediments, in these simulations, are commonly treated as being viscous non-Newtonian. However, in some cases, more complex models are used, including multi-mechanism creep model for the lithosphere [137], combined viscous and brittle deformation model for near surface sediment [136], and viscous models with pressure-dependent stress potentials [29, 75].

However, there are limited publications related to the numerical simulation of fault initiation and propagation within sedimentary rocks in a prograding delta due to gravity instability triggered by overpressured shale layer and synkinematic sedimentation. The best example related to this geologic activity is Niger delta. Referring to Figure 1.3, Niger delta can be divided into three main zones: extensional, transition, and compressional zones. Extensional zone is characterised by basinward-dipping normal faults, whereas compressional zone is characterised by basinward-verging fore-thrust faults.

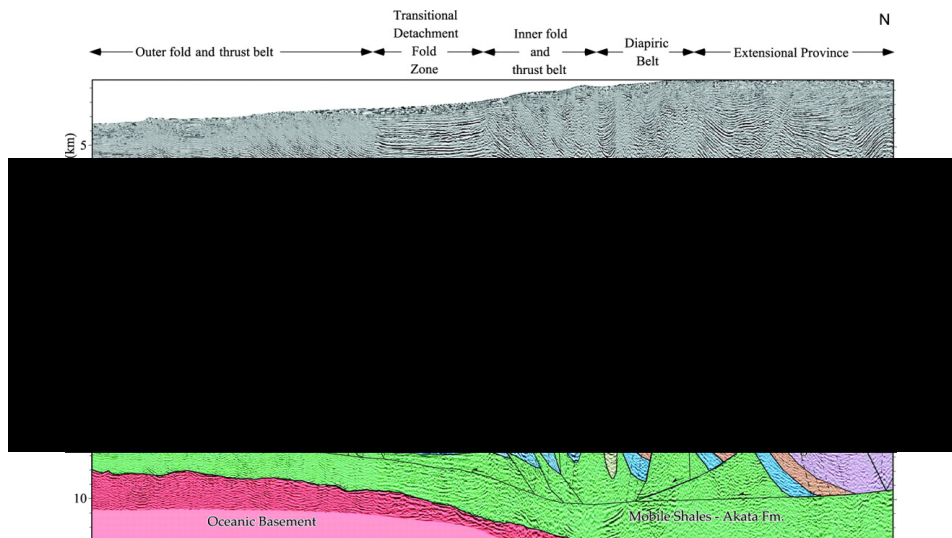


Fig. 1.3 Niger delta tectonic structure. Figure obtained from [45]

In view of this geologic structure, sandbox modelling technique has been used by [124] to produce excellent results, in which fault patterns as observed in the field are successfully replicated. As shown in Figure 1.4, two distinct regions are evident in the final deformation configuration. Extensional zone is characterised by normal faults, while compressional zone is characterised by fore-thrust faults. However, for this specific case, analog model is usually limited by the cohesive strength of sand material, which is insufficient to contain high fluid pressure in the base layer. Therefore, the representation of overpressured shale layer in the sandbox model may not be accurate.

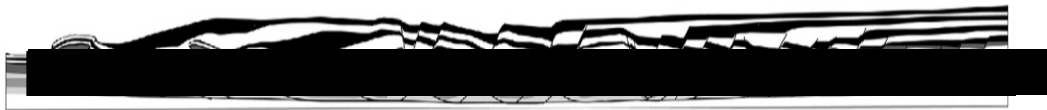


Fig. 1.4 Figures obtained from [124], showing the fault patterns obtained from sandbox model

As for numerical modelling, large-scale delta instability under shale tectonics in continental margin has been simulated by [89]. The authors take isostatic compensation into account in the simulation of the delta progradation. The shale material is assumed to be Bingham visco-plastic fluid once the yield stress is exceeded. That is, when the pore fluid pressure is elevated close to the lithostatic pressure, shale starts to flow viscously. Although no synkinematic sedimentation is taken into account¹, normal and fore-thrust faults are able to be visualised in terms of horizontal strain rate. In addition, the distribution of Hubbert-Rubey pore pressure ratio reflects very well the distribution of fore-thrust faults in the compressional zone.

1.1 The Aim of the Thesis

The aim of the thesis is to develop a coupled geomechanical/flow-modelling framework for the simulation of basin-scale evolution over geological time frames, with focus on the elastoplastic-fracture constitutive modelling. The models are evaluated via a series of numerical examples. Later in the penultimate chapter, the simulation result of large-scale delta instability due to overpressured shale layer is presented. The author maintains that faults should be visualised in terms of plastic strain, as opposed to strain rate. Using the constitutive models in the developed computational framework, it will be shown that synthetic basinward-dipping normal faults as well as basinward-verging fore-thrust faults are successfully reproduced in terms of plastic strain in the extensional and compressional regions, respectively. The final deformation configuration is the result of gravitational instability triggered by overpressured shale layer, and of progradation due to synkinematic sedimentation on the top surface, for which the slope angle gradually reduces. The latter is an indication of weak basal strength.

1.2 Outline of the thesis

This thesis is organised as follows,

- **Chapter 2.** A brief overview of governing equation related to seepage and geomechanical fields is presented. For the seepage field, the governing equation (2.45) is formulated by combining the mass balance equation of both fields. For geomechanical fields, the governing equation (2.1) is simply derived from linear momentum balance equation with the application of effective stress principle.

¹, which essentially contributes to the increase of overpressure via disequilibrium compaction mechanism

- **Chapter 3.** In this chapter, fundamental topics of nonlinear continuum mechanics are briefly discussed as precursor of the formulation of weak-form governing equations based on the principle of virtual power. Next, the equations are spatially discretised using finite element method, and temporally discretised using explicit central difference time integration scheme. Several numerical strategies are discussed, including lumped mass matrix, artificial bulk viscosity damping, and averaged volumetric strain method. Stress update procedure based on Green-Naghdi stress rate is derived by exploiting pull back and push forward operations. Finally, undrained and fixed stress split schemes, which allow seepage and geomechanical fields to be solved separately, are presented. In the adopted split schemes, a single flow time step in the seepage field encapsulates multiple fine time steps in the geomechanical field.
- **Chapter 4.** This chapter presents the elastoplastic-fracture constitutive models for pressure-sensitive geomaterials. The yield functions for modified Drucker-Prager and SR4 model are introduced, along with the corresponding non-associative potential plastic flow functions, the hardening laws, and the return-mapping algorithm. Both models are incorporated with π -plane correction factor. The techniques of regularisation of plastic state variables are also discussed. Next, rotating crack model based on Rankine failure criterion and its implementation with elastoplastic models are introduced. Using Drucker-Prager model as an example, possible coupling between cohesion and tensile strength is explored via power law formulation. Finally, various single-element tests are performed. Using modified Drucker-Prager model, the first test is to validate that the stress path does not cross the yield surface into the realm of inadmissible stress state. The second test is to validate the material response under conventional triaxial compression (CTC) and triaxial extension (TXE) conditions using SR4 model. The third test is to obtain correct stress-strain response for a elastoplastic-fracture model with the consideration of coupled cohesion-tensile strength.
- **Chapter 5.** Numerical examples of laboratory-scale test simulation are presented using the developed elastoplastic-fracture framework. In this chapter, only the modified Drucker-Prager model is used. (1) Bearing capacity of strip footing is predicted and compared against analytical solution to verify the accuracy of numerical solutions. (2) Crack propagation and coalescence are simulated using specimen with pre-existing inclined fault. Both quasi-brittle and relatively soft materials are simulated. Secondary crack, that is of shear origin, is successfully reproduced in specimen with two inclined fault. Good agreement is observed between numerical and experimental findings. (3) Next, the influence of size effect on borehole instability is simulated to validate

that regularisation algorithm is successfully implemented. In particular, the collapse pressure of larger specimen is predicted to be lower than that of smaller specimen. (4) Uniaxial consolidation and sedimentation of soil column are analysed in separate simulation tests and compared against available analytical solutions. (5) The complexity of hydromechanical simulation test is elevated by analysing the influence of pore pressure on thrust fault formation. This test involves frequent adaptive remeshing due to the formation of strain localisation that depends on the level of pore pressure in the base layer. (6) Finally, the entire elastoplastic-fracture framework coupled with pore pressure field is put into test by simulating hydraulic fracture induced by fluid injection.

- **Chapter 6.** This goal of this chapter is to simulate basin-scale gravitational deformation in a prograding delta due to fluid overpressure in shale layer with synkinematic sedimentation. SR4 elastoplastic model is used in this chapter to take into account the important influence of preconsolidation pressure p_c . With the aid of adaptive remeshing algorithm, the result successfully produces distinct fault patterns across the prograding delta in terms of plastic strain distribution. In particular, three different zones are observed: extensional, transition, and compressional zone. The extensional zone is characterised by basinward-dipping normal faults, whereas the compressional zone is characterised by basinward-verging fore-thrust faults.
- **Chapter 7.** This chapter concludes the thesis with a summary of contributions and important results obtained during the course of this work. Some suggestions for further research work is also included.

Chapter 2

Review of Flow-Geomechanical Governing Equations

2.1 Introduction

In this chapter, a brief overview of governing equations that cover both porous flow and geomechanical fields is presented. The condition of pore fluid within porous media is assumed to be incompressible, fully saturated, single-phased flow under isothermal equilibrium condition. It is noted hereby that the derivation of mass balance equations is based on the summary provided by [111].

2.2 Linear Momentum Equation

In geomechanical field, the linear momentum balance equation for solid phase within porous media is given by

$$\nabla \cdot \underbrace{(\boldsymbol{\sigma}' - \alpha p_f \mathbf{I})}_{\text{Total stress tensor, } \boldsymbol{\sigma}} + \underbrace{((1-n)\rho_s + n\rho_f)}_{\text{Bulk density, } \rho} \mathbf{b} = \rho \mathbf{a}, \quad (2.1)$$

where $\boldsymbol{\sigma}'$ is effective stress tensor, α is Biot's coefficient, p_f is pore fluid pressure, n is porosity, ρ_s is density of solid phase, ρ_f is density of fluid phase, \mathbf{b} is body force per unit deformed volume, $\mathbf{a} = \ddot{\mathbf{u}}$ is acceleration field of solid phase, and \mathbf{u} is displacement field.

Biot's coefficient α , which controls the proportion of fluid pressure to resist confining pressure, is given by

$$\alpha = 1 - \frac{K'}{K_s}, \quad (2.2)$$

where K' is the drained bulk modulus and K_s is the solid phase bulk modulus.

The lower bound of α is obtained by having $K' = K_s$. This is when the porosity $n = 0$, resulting in $\alpha = 0$. The upper bound of α is obtained when the porosity n reaches a critical value, beyond which the material particles start to fluidize. In this case, $K' = 0$, resulting in $\alpha = 1$. In view of this, an empirical porosity-dependent model of Biot's coefficient is given by [150]

$$\alpha(n) = \frac{n}{n + a(n_0 - n)}, \quad (2.3)$$

where n_0 is the porosity during deposition, and parameter a is an empirically determined material constant.

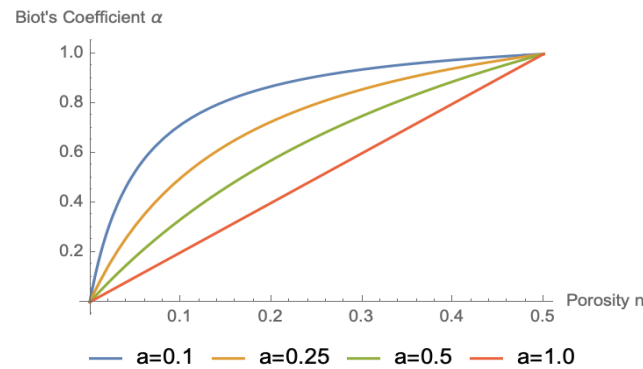


Fig. 2.1 Biot's coefficient as function of porosity, whose curve is controlled by parameter a

2.3 Mass Balance Equation

Mass balance equations for fluid field and solid field are derived and combined to capture the contribution of volumetric strain from geomechanical field to the evolution of pore fluid pressure in fluid field as well as to update the stress states in geomechanical field using the converged solution of pore fluid pressure in fluid field.

Before proceeding to the derivation of mass balance equation, it is stated hereby that throughout the simulations in the current study, it is assumed that fluid flow within porous

medium obeys Darcy's law, which is defined by

$$\mathbf{q} = -\frac{\mathbf{K}}{\mu_f} (\nabla p_f - \rho_f \mathbf{g}), \quad (2.4)$$

where \mathbf{q} is Darcy flow velocity vector, \mathbf{K} is hydraulic permeability tensor, and μ_f is fluid viscosity.

In general, the deformation of porous medium and the evolution of pore fluid pressure are concurrent, and therefore the calculation of Darcy flow velocity should be proportional to the difference between fluid velocity vector \mathbf{v}_f and solid particle velocity vector \mathbf{v}_s , such that

$$\mathbf{q} = n (\mathbf{v}_f - \mathbf{v}_s). \quad (2.5)$$

2.3.1 Fluid Phase Mass Balance Equation

Based on the principle of mass conservation, the fluid continuity equation is given by

$$\frac{\partial (n\rho_f)}{\partial t} + \nabla \cdot (n\rho_f \mathbf{v}_f) = 0. \quad (2.6)$$

In the following derivations, it is intended to introduce the $p_f - \rho_f$ constitutive relation into the fluid continuity equation via fluid compressibility coefficient β_f , which is given by

$$\beta_f = -\frac{1}{V_f} \left. \frac{\partial V_f}{\partial p_f} \right|_{\text{isothermal}}. \quad (2.7)$$

Now, consider the mass conservation of fluid expressed in difference form

$$\begin{aligned} \rho_{f0} V_{f0} &= \rho_f V_f = (\rho_{f0} + \Delta\rho_f) (V_{f0} + \Delta V_f) \\ &\approx \rho_{f0} V_{f0} + \rho_{f0} \Delta V_f + V_{f0} \Delta\rho_f, \end{aligned} \quad (2.8)$$

where V_f is the fluid volume.

Via rearrangement, we obtain

$$\frac{\Delta V_f}{V_{f0}} = -\frac{\Delta\rho_f}{\rho_{f0}}. \quad (2.9)$$

In the limit of small perturbation¹, we may express the above relation as

$$\frac{\partial V_f}{V_f} = -\frac{\partial \rho_f}{\rho_f}, \quad (2.10)$$

or in time rate form,

$$\frac{1}{V_f} \frac{\partial V_f}{\partial t} = -\frac{1}{\rho_f} \frac{\partial \rho_f}{\partial t}. \quad (2.11)$$

On the other hand, the fluid compressibility equation (2.7) can be rearranged into time rate form as

$$\frac{1}{V_f} \frac{\partial V_f}{\partial t} = -\beta_f \frac{\partial p_f}{\partial t}, \quad (2.12)$$

which leads us to forming the following $p_f - \rho_f$ constitutive relation

$$\frac{\partial \rho_f}{\partial t} = \rho_f \beta_f \frac{\partial p_f}{\partial t}. \quad (2.13)$$

Now, the fluid continuity equation is further expanded²

$$n \frac{\partial \rho_f}{\partial t} + \rho_f \frac{\partial n}{\partial t} + \rho_f \nabla \cdot (n \mathbf{v}_f) = 0. \quad (2.14)$$

By using (2.13), the continuity equation is now expressed as

$$n \beta_f \frac{\partial p_f}{\partial t} + \frac{\partial n}{\partial t} + \nabla \cdot (n \mathbf{v}_f) = 0. \quad (2.15)$$

¹The transformation is achieved by expressing $\ln(x)$ using Taylor's expansion series in the vicinity of $x = x_0$:

$$\begin{aligned} \ln(x_0 + \Delta x) &= \ln(x_0) + \Delta x \left. \frac{\partial \ln(x)}{\partial x} \right|_{x=x_0} + \text{higher order terms} \\ \Rightarrow \ln(x_0 + \Delta x) - \ln(x_0) &\approx \frac{\Delta x}{x_0} \\ \Rightarrow \int_{x_0}^{x_0 + \Delta x} \frac{dx}{x} &\approx \frac{\Delta x}{x_0} \end{aligned}$$

²The fluid density is assumed to be independent of spatial variation.

The term $\nabla \cdot (n\mathbf{v}_f)$ may be alternatively re-expressed by including the solid particle velocity vector

$$\begin{aligned}\nabla \cdot (n\mathbf{v}_f) &= \nabla \cdot (n(\mathbf{v}_f - \mathbf{v}_s)) + \nabla \cdot (n\mathbf{v}_s) \\ &= \nabla \cdot \mathbf{q} + \nabla \cdot (n\mathbf{v}_s),\end{aligned}\quad (2.16)$$

so that we can now include, in the following fluid continuity equation, the contribution of solid deformation on the evolution of pore fluid pressure p_f via the term $\nabla \cdot (n\mathbf{v}_s)$, which will be derived later

$$n\beta_f \frac{\partial p_f}{\partial t} + \frac{\partial n}{\partial t} + \nabla \cdot \mathbf{q} + \nabla \cdot (n\mathbf{v}_s) = 0. \quad (2.17)$$

2.3.2 Solid Phase Mass Balance Equation

Similar to the fluid continuity equation, the mass balance equation of solid phase of a porous medium is expressed by

$$\frac{\partial ((1-n)\rho_s)}{\partial t} + \nabla \cdot ((1-n)\rho_s\mathbf{v}_s) = 0. \quad (2.18)$$

In a similar fashion to the fluid field, in the following derivations, it is intended to introduce the constitutive relation between solid density ρ_s and pore fluid pressure p_f as well as the mean stress p via solid compressibility coefficient C_s . Now, consider a solid specimen undergoing two stages of compressive loading:

- Stage 1: Increase of confining pressure = increase in pore fluid pressure ($\Delta p_{conf} = \Delta p_f$)
- Stage 2: Increase of confining pressure = increase in effective stress ($\Delta p_{conf} = -\Delta p'$, since the convention of compression-negative is applied to p')

Recall the definition of unjacketed compressibility C_s

$$C_s = - \frac{1}{V} \frac{\Delta V}{\Delta p_{conf}} \Big|_{p_d = \text{constant}}, \quad (2.19)$$

where V is bulk volume and p_d is differential pressure. The current goal is formulate the volume change of solid phase ΔV_s in response to differential pore fluid pressure Δp_f and mean stress Δp .

In Stage 1, as the confining pressure increases, the bulk volume decreases. Since the relation $\Delta p_{conf} = \Delta p_f$ holds in this stage, the corresponding bulk compressibility is simply

expressed by

$$C_s = - \left. \frac{1}{V} \frac{\Delta V}{\Delta p_f} \right|_{\Delta p' = 0}, \quad (2.20)$$

which yields the bulk volume change for Stage 1 as

$$\frac{\Delta V}{V} = -C_s \Delta p_f. \quad (2.21)$$

In addition, as p_{conf} increases, the pore volume V_p should decrease with the bulk volume V , despite $\Delta p_f > 0$ since $\Delta p' = 0$. It follows that a pore compressibility can be defined

$$C_\phi = - \left. \frac{1}{V_p} \frac{\Delta V_p}{\Delta p_f} \right|_{\Delta p' = 0}, \quad (2.22)$$

which yields the pore volume change for Stage 1 as

$$\frac{\Delta V_p}{V_p} = -C_\phi \Delta p_f. \quad (2.23)$$

The total volume change of solid phase ΔV_s in Stage 1 may now be expressed as

$$\begin{aligned} \frac{\Delta V_s}{V_s} &= \frac{\Delta V}{V_s} - \frac{\Delta V_p}{V_s} \\ &= \frac{\Delta V}{(1-n)V} - \frac{\Delta V_p}{V - V_p} \\ &= \frac{1}{1-n} \left(\frac{\Delta V}{V} \right) - \frac{\Delta V_p}{V_p/n - V_p} \\ &= \frac{1}{1-n} \left(\frac{\Delta V}{V} \right) - \frac{n}{1-n} \left(\frac{\Delta V_p}{V_p} \right). \end{aligned} \quad (2.24)$$

By substitution of (2.21) and (2.23), the volume change of solid phase due to the loading as prescribed in Stage 1 is given by

$$\left. \frac{\Delta V_s}{V_s} \right|_{\text{Stage 1}} = \frac{-C_s \Delta p_f + n C_\phi \Delta p_f}{1-n}. \quad (2.25)$$

In Stage 2, as the confining pressure increases, the bulk volume also decreases. Since the relation $\Delta p_{conf} = -\Delta p'$ holds in this stage, the corresponding solid phase compressibility is

simply expressed by

$$C_s = -\frac{1}{V_s} \frac{\Delta V_s}{\Delta p_{conf}} = \frac{1}{V_s} \frac{\Delta V_s}{\Delta p'}, \quad (2.26)$$

which yields

$$\frac{\Delta V_s}{V_s} = C_s \Delta p'. \quad (2.27)$$

The effective mean stress is expressed in a volume-averaged fashion [120], such that

$$(1 - n)p' = p + p_f, \quad (2.28)$$

where the total mean stress p is simply linked to the confining pressure via $p = -p_{conf}$ that is transferred to the solid phase in the presence of pore fluid pressure p_f at a volume fraction $1 - n$. The difference form of (2.28) is then

$$\Delta p' = \frac{\Delta p + \Delta p_f}{1 - n}. \quad (2.29)$$

By substitution of the above equation into (2.27), the volume change of solid phase due to the loading as prescribed in Stage 2 is then given by

$$\left. \frac{\Delta V_s}{V_s} \right|_{\text{Stage 2}} = \frac{C_s \Delta p + C_s \Delta p_f}{1 - n}. \quad (2.30)$$

Finally, the net volume change of solid phase is computed simply by

$$\frac{\Delta V_s}{V_s} = \left. \frac{\Delta V_s}{V_s} \right|_{\text{Stage 1}} + \left. \frac{\Delta V_s}{V_s} \right|_{\text{Stage 2}} = \frac{C_s \Delta p + n C_\phi \Delta p_f}{1 - n}. \quad (2.31)$$

In the limit of small perturbation and in time rate form, (2.31) is expressed in differential form as

$$\frac{1}{V_s} \frac{\partial V_s}{\partial t} = \frac{1}{1 - n} \left(C_s \frac{\partial p}{\partial t} + n C_\phi \frac{\partial p_f}{\partial t} \right). \quad (2.32)$$

Now, consider the mass conservation of solid phase expressed in difference form as done for pore fluid field

$$\begin{aligned}\rho_{s0}V_{s0} &= \rho_s V_s = (\rho_{s0} + \Delta\rho_s)(V_{s0} + \Delta V_s) \\ &\approx \rho_{s0}V_{s0} + \rho_{s0}\Delta V_s + V_{s0}\Delta\rho_s.\end{aligned}\quad (2.33)$$

Via rearrangement and in the limit of small perturbation, we obtain

$$\frac{\partial V_s}{V_s} = -\frac{\partial \rho_s}{\rho_s}, \quad (2.34)$$

or in time rate form,

$$\frac{1}{V_s} \frac{\partial V_s}{\partial t} = -\frac{1}{\rho_s} \frac{\partial \rho_s}{\partial t}. \quad (2.35)$$

By comparing equation above and (2.32) we can immediately form the following equation

$$\frac{\partial \rho_s}{\partial t} = \frac{\rho_s}{1-n} \left(-C_s \frac{\partial p}{\partial t} - nC_\phi \frac{\partial p_f}{\partial t} \right). \quad (2.36)$$

Now, the continuity equation for solid field is further expanded³

$$\begin{aligned}-\rho_s \frac{\partial n}{\partial t} + (1-n) \frac{\partial \rho_s}{\partial t} + \rho_s \nabla \cdot ((1-n) \mathbf{v}_s) &= 0 \\ -\rho_s \frac{\partial n}{\partial t} + (1-n) \frac{\partial \rho_s}{\partial t} + \rho_s \nabla \cdot \mathbf{v}_s &= \rho_s \nabla \cdot (n\mathbf{v}_s).\end{aligned}\quad (2.37)$$

By substitution of (2.36) into the above equation, we arrive at

$$-\frac{\partial n}{\partial t} + \left(-C_s \frac{\partial p}{\partial t} - nC_\phi \frac{\partial p_f}{\partial t} \right) + \nabla \cdot \mathbf{v}_s = \nabla \cdot (n\mathbf{v}_s). \quad (2.38)$$

2.3.3 Combined Mass Balance Equation

By comparing the term $\nabla \cdot (n\mathbf{v}_s)$ in equation above (solid phase mass balance equation) with that of (2.17) (fluid mass balance equation)

$$n\beta_f \frac{\partial p_f}{\partial t} + \frac{\partial n}{\partial t} + \nabla \cdot \mathbf{q} + \nabla \cdot (n\mathbf{v}_s) = 0,$$

³The term $\nabla \rho_s$ is not accounted for. More descriptions are given in the rigorous derivation by [100], p/g 22 beginning from Equation 2.56.

we may now re-express the solid-fluid continuity equations further as

$$\begin{aligned} n\beta_f \frac{\partial p_f}{\partial t} + \frac{\partial n}{\partial t} + \nabla \cdot \mathbf{q} - \frac{\partial n}{\partial t} + \left(-C_s \frac{\partial p}{\partial t} - nC_\phi \frac{\partial p_f}{\partial t} \right) + \nabla \cdot \mathbf{v}_s &= 0 \\ \nabla \cdot \mathbf{v}_s + n(\beta_f - C_\phi) \frac{\partial p_f}{\partial t} - C_s \frac{\partial p}{\partial t} &= -\nabla \cdot \mathbf{q}. \end{aligned} \quad (2.39)$$

The total mean stress p can be expressed in terms of unjacketed compressibility coefficient C_s and Biot's constant α

$$\begin{aligned} p &= p' - \alpha p_f \\ &= \frac{\varepsilon_v}{C} - \alpha p_f \\ &= \frac{1 - \alpha}{C_s} \varepsilon_v - \alpha p_f, \end{aligned} \quad (2.40)$$

since $\alpha = 1 - \frac{C_s}{C}$ with C as the drained compressibility (solid skeleton compressibility). It then follows that

$$C_s \frac{\partial p}{\partial t} = (1 - \alpha) \frac{\partial \varepsilon_v}{\partial t} - \alpha C_s \frac{\partial p_f}{\partial t}. \quad (2.41)$$

By substitution of the term $C_s \frac{\partial p}{\partial t}$ into (2.39),

$$\nabla \cdot \mathbf{v}_s + n(\beta_f - C_\phi) \frac{\partial p_f}{\partial t} - (1 - \alpha) \frac{\partial \varepsilon_v}{\partial t} + \alpha C_s \frac{\partial p_f}{\partial t} = -\nabla \cdot \mathbf{q}, \quad (2.42)$$

from which we can simplify to obtain the governing equation for pore fluid and solid fields:

$$\alpha \nabla \cdot \mathbf{v}_s + \underbrace{(n(\beta_f - C_\phi) + \alpha C_s)}_{\text{Storativity term, } S} \frac{\partial p_f}{\partial t} = -\nabla \cdot \mathbf{q}. \quad (2.43)$$

For homogeneous porous media, we have $C_\phi = C_s$. The storativity term S is then simplified as

$$S = n\beta_f + (\alpha - n)C_s = \frac{n}{K_f} + \frac{\alpha - n}{K_s}, \quad (2.44)$$

where K_f and K_s are the stiffness of fluid and solid grain, respectively. By assuming Darcy's law for pore fluid flow (2.4) and recognising $\nabla \cdot \mathbf{v}_s = \frac{\partial \varepsilon_v}{\partial t}$, the form of (2.43) is then further

Rock Type	$S_0(10^4)$	p	q
Sandstone	1	5	2
Pure Chalk	250	3	2
Kaolinite	4800	3	2
Mud	69000	3	2

Table 2.1 Material constants for modified form of Kozeny-Carmen model (2.46)

simplified as

$$\alpha \frac{\partial \varepsilon_v}{\partial t} + \left(\frac{n}{K_f} + \frac{\alpha - n}{K_s} \right) \frac{\partial p_f}{\partial t} = \nabla \cdot \left(\frac{\mathbf{K}}{\mu_f} (\nabla p_f - \rho_f \mathbf{g}) \right), \quad (2.45)$$

which is similar to [100]'s version by assuming incompressible, single-phased flow fully saturated in porous medium under isothermal equilibrium condition.

2.4 Hydraulic Permeability

The discharge of pore fluid is largely driven by the change of porosity, which has direct influence on the hydraulic permeability. A empirical model based on Kozeny-Carmen relationship [150], which relates permeability with porosity using the analogy of an array of regular spheres, is expressed by

$$k = k_0 \frac{n^p}{(1-n)^q}, \quad \text{where } k_0 = \frac{A}{S_0^2}. \quad (2.46)$$

where k is hydraulic permeability (m^2) and k_0 is the reference permeability. This model includes the effect of specific surface of rock matrix S_0 [m^2/m^3], and some material constants A, p, q :

Typical value of A is 0.2, and the material constants are provided in Table 2.1. Another variant of empirical Kozeny-Carmen model is given by [165], who defined a multi-stage relationship between permeability and porosity

$$k = \begin{cases} \frac{20n^5}{S_0^2(1-n)^2} & , n < 0.1 \\ \frac{0.2n^3}{S_0^2(1-n)^2} & , n \geq 0.1 \end{cases}. \quad (2.47)$$

Sandstone		Siltstone		Shale	
Porosity	log mD	Porosity	log mD	Porosity	log mD
0.01	-1.8	0.01	-8.52	0.01	-6.28
0.25	3.00	0.25	-3.00	0.25	-1.00
0.41	4.33	0.70	-1.00	0.55	0.71

Table 2.2 Piecewise-linear porosity-permeability (log mD) data for sandstone, siltstone, and shale [83]

In the case of low porosity, the rapid decrease in permeability is attributable to the finding [165] that some pore throats are effectively closed, leading to reduced connectivity of pore network. On the other hand, [83] suggested plotting the log permeability⁴ ($\log mD$) versus porosity in a piecewise linear manner. A sample properties for typical sandstone and shale as well as organic-lean siltstone are shown in Table 2.2.

For the case of hydraulic fracturing, it is found that [70] the enhancement of permeability as a result of micro-cracking is generally significant. A model related to such permeability augmentation was proposed by a review paper [110]

$$k = k_0(n - n_c)^p, \quad (2.48)$$

where k_0 refers to the characteristic permeability as $n - n_c = 0.01$, $p \approx 3.8 \pm 0.4$ is an empirical parameter, and n_c is the fluid flow percolation threshold, below which no connected fracture network should exist. The review shows that, using the relation above, the permeability increase could reach six orders of magnitude higher in response to a 4% porosity increase.

Another permeability augmentation model for hydraulic fracturing is given by [83], where the permeability is function of pore fluid pressure p_f and fracturing pressure $p_{f,cr}$. Similar to the concept of tensile strength, fracturing pressure represents the level of excess pressure at which hydraulic fracture occurs. The value of $p_{f,cr}$ varies according to burial depth and lithology of the geomaterials. Expressed in terms of logarithm, the fracture permeability is given by

$$\log k_f = \log k + \lambda_f \frac{p_f - p_{f,cr}}{p_{f,cr}}, \quad (2.49)$$

where k and k_f are, respectively, intact and fracture permeabilities, and λ_f is a material constant. It is given [83] that the value of λ_f for clastic rocks is typically $3 \log mD = 10^3 mD$.

⁴The use of log permeability is demonstrated in [83]. In general, $a \log mD = 10^a mD$

2.5 Fluid Diffusion Time Scale

In compaction-dominant evolution (e.g. deltaic progradation), fluid overpressure may arise locally depending on the hydraulic permeability of the surrounding geomaterials. In the context of hydrocarbon industry, for instance, this phenomenon may be important as high overpressure normally triggers hydraulic fracturing, which in turn defines new migration paths for the fluid as a means to relieve the overpressure. Therefore, in the context of geomechanical modelling, the time scale associated with fluid diffusion t_d is often compared with the time scale related to solid deformation⁵ t_e . If $t_d \gg t_e$, the condition tends to be undrained, whereas if $t_e \gg t_d$, the condition tends to be drained.

The time scale for fluid diffusion can be derived by normalising the mass balance equation. In the followings, the choice of reference parameters are similar to that of [120]. To recap, the mass balance equation is given by

$$\alpha \frac{\partial \varepsilon_v}{\partial t} + S \frac{\partial p_f}{\partial t} = \nabla \cdot \left(\frac{\mathbf{K}}{\mu_f} (\nabla p_f - \rho_f \mathbf{g}) \right),$$

where $S = \frac{n}{K_f} + \frac{\alpha - n}{K_s}$.

Now, by letting the following dimensionless parameters be defined as

$$t^* = \frac{t}{t_e} \quad (2.50)$$

$$\mathbf{x}^* = \frac{1}{L} \mathbf{x} \quad (2.51)$$

$$S^* = SLg\Delta\rho \quad (2.52)$$

$$p_f^* = \frac{p_f}{Lg\Delta\rho} \quad (2.53)$$

$$\mathbf{K}^* = \frac{1}{k_0} \mathbf{K} \quad (2.54)$$

$$\mathbf{g}^* = \frac{1}{g} \mathbf{g} \quad (2.55)$$

$$\mu_f^* = \frac{\mu_f}{\mu_{f0}} \quad (2.56)$$

$$\rho_f^* = \frac{\rho_f}{\Delta\rho}, \quad (2.57)$$

where t_e is solid deformation time scale, L is characteristic length, $\Delta\rho$ is the difference between solid density ρ_s and fluid density ρ_f , k_0 is reference hydraulic permeability, μ_{f0} is

⁵This subscript e here means 'event'. In the current context, it means any geological event (such as lateral compression) that generates overpressure so that fluid diffusion can occur.

the reference fluid viscosity, and g is simply gravity constant, we may obtain the following dimensionless form of mass balance equation

$$\frac{\alpha}{S^*} \frac{\partial \varepsilon_v}{\partial t^*} + \frac{\partial p_f^*}{\partial t^*} = \frac{t_e}{t_d} \nabla \cdot \left(\frac{\mathbf{K}^*}{\mu_f^*} (\nabla p_f^* - \rho_f^* \mathbf{g}^*) \right), \quad (2.58)$$

where

$$t_d = \frac{S^* \mu_{f0} L}{k_0 \Delta \rho g_0} = \frac{SL^2 \mu_{f0}}{k_0}. \quad (2.59)$$

It is clear from the above equation that, the diffusion time scale t_d increases with $1/k_0$, which is expected; low hydraulic permeability increases the fluid diffusion time. Furthermore, if $t_d \gg t_e$ such that $\frac{t_e}{t_d} \approx 0$, the right side of (2.58) will be rendered zero, signifying undrained condition as the fluid diffusion rate is virtually zero.

Chapter 3

Computational Strategies for Coupling Geomechanics with Fluid Flow

3.1 Kinematics and Geometry Descriptions

This section briefly discusses some of the fundamental ingredients originating from the literature of nonlinear continuum mechanics (e.g. [54]) that are important for the development of finite element formulations in the later sections.

3.1.1 Motion as Configuration Mapping

Consider a three-dimensional Euclidean \mathcal{E} space containing an open region Ω with a regular boundary $\partial\Omega$ occupied by a body \mathcal{B} that undergoes deformation over a time interval $[t_n, t_{n+1}]$, causing each material particle of the body to be re-positioned from a reference configuration to a deformed configuration. The motion of the material particles is assumed to be captured by a smooth, injective and orientation-preserving configuration mapping function, defined by

$$\boldsymbol{\varphi} : \Omega \rightarrow \mathcal{E}. \quad (3.1)$$

Using the configuration mapping function, the position vectors of each material particle \mathbf{X} in reference configuration are mapped uniquely into a deformed configuration of \mathcal{B} via

$$\mathbf{x} = \boldsymbol{\varphi}(\mathbf{X}, t). \quad (3.2)$$

3.1.2 Deformation Gradient

The stretching process of a deformable body causes the change in the relative distance between any given points; that is the distance $|\Delta\mathbf{X}|$ in a reference configuration has changed into $|\Delta\mathbf{x}|$ in a deformed configuration. In another word, rigid body motion can take place when $|\Delta\mathbf{x}| = |\Delta\mathbf{X}|$, indicating the body is either stationary, or has rotated about any axis without being stretched.

In relation to the description above, a deformation gradient \mathbf{F} is introduced and defined as a two-point push-forward second order tensor that transforms infinitesimal material fibres $d\mathbf{X}$ into a deformed configuration $d\mathbf{x}$, such that

$$d\mathbf{x} = \mathbf{F}d\mathbf{X}. \quad (3.3)$$

In terms of displacement vector \mathbf{u} , deformation gradient can be alternatively expressed by

$$\mathbf{F} = \frac{\partial \boldsymbol{\varphi}(\mathbf{X}, t)}{\partial \mathbf{X}} = \mathbf{I} + \nabla_{\mathbf{X}} \mathbf{u}, \quad (3.4)$$

where $\nabla_{\mathbf{X}}$ is the material gradient operator.

3.1.3 Velocity Gradient and Rate of Deformation Gradient

The rate of deformation gradient is given by

$$\dot{\mathbf{F}} = \frac{d}{dt} \left(\frac{\partial \boldsymbol{\varphi}}{\partial \mathbf{X}} \right) = \frac{d}{d\mathbf{X}} \left(\frac{\partial \boldsymbol{\varphi}}{\partial t} \right) = \frac{\partial \mathbf{v}}{\partial \mathbf{X}} = \frac{\partial \mathbf{v}}{\partial \mathbf{x}} \frac{\partial \boldsymbol{\varphi}}{\partial \mathbf{X}} = \mathbf{l}\mathbf{F}, \quad (3.5)$$

which leads us to define the following spatial velocity gradient

$$\mathbf{l} = \nabla_{\mathbf{x}} \mathbf{v} = \dot{\mathbf{F}}\mathbf{F}^{-1}, \quad (3.6)$$

where $\nabla_{\mathbf{x}}$ is the spatial gradient operator. The spatial velocity gradient can also be decomposed into its symmetric and skew-symmetric component tensors

$$\begin{aligned} \mathbf{l} &= \frac{1}{2} (\mathbf{l} + \mathbf{l}^T) + \frac{1}{2} (\mathbf{l} - \mathbf{l}^T) \\ &= \mathbf{d} + \mathbf{w}, \end{aligned} \quad (3.7)$$

where \mathbf{d} is the symmetric rate of deformation tensor and \mathbf{w} is the skew-symmetric spin tensor.

The objectivity of \mathbf{d} can be demonstrated in the following. Consider an element vector $d\mathbf{X}$ in a reference configuration that is stretched to $d\mathbf{x}$ and rotated to $d\tilde{\mathbf{x}}$ via an orthogonal

tensor \mathbf{Q} , so that we can express

$$\begin{aligned} d\tilde{\mathbf{x}} &= \mathbf{Q}d\mathbf{x} \\ &= \mathbf{Q}\mathbf{F}d\mathbf{X} \\ &= \tilde{\mathbf{F}}d\mathbf{X}, \end{aligned} \quad (3.8)$$

where $\tilde{\mathbf{F}}$ is an effective deformation gradient. Then, using (3.6),

$$\begin{aligned} \tilde{\mathbf{l}} &= \dot{\tilde{\mathbf{F}}}\tilde{\mathbf{F}}^{-1} = \frac{d}{dt}(\mathbf{Q}\mathbf{F})(\mathbf{Q}\mathbf{F})^{-1} \\ &= \frac{d}{dt}(\mathbf{Q}\mathbf{F})(\mathbf{F}^{-1}\mathbf{Q}^T) \\ &= \dot{\mathbf{Q}}\mathbf{F}\mathbf{F}^{-1}\mathbf{Q}^T + \mathbf{Q}\dot{\mathbf{F}}\mathbf{F}^{-1}\mathbf{Q}^T \\ &= \dot{\mathbf{Q}}\mathbf{Q}^T + \mathbf{Q}\mathbf{l}\mathbf{Q}^T. \end{aligned} \quad (3.9)$$

Accordingly, the transpose of $\tilde{\mathbf{l}}$ is simply given by

$$\tilde{\mathbf{l}}^T = \mathbf{Q}\dot{\mathbf{Q}}^T + \mathbf{Q}\mathbf{l}^T\mathbf{Q}^T. \quad (3.10)$$

Finally, the objectivity of \mathbf{d} can be demonstrated as follows

$$\tilde{\mathbf{d}} = \frac{1}{2}(\tilde{\mathbf{l}} + \tilde{\mathbf{l}}^T) \quad (3.11)$$

$$= \mathbf{Q}\left(\frac{1}{2}(\mathbf{l} + \mathbf{l}^T)\right)\mathbf{Q}^T + \frac{1}{2}(\dot{\mathbf{Q}}\mathbf{Q}^T + \mathbf{Q}\dot{\mathbf{Q}}^T) \quad (3.12)$$

$$= \mathbf{Q}d\mathbf{Q}^T + \frac{1}{2}\frac{d}{dt}(\mathbf{Q}\mathbf{Q}^T). \quad (3.13)$$

Due to the orthogonality of \mathbf{Q} , the term $\frac{d}{dt}(\mathbf{Q}\mathbf{Q}^T) = \frac{d}{dt}\mathbf{I} = \mathbf{0}$ vanishes, leaving only

$$\tilde{\mathbf{d}} = \mathbf{Q}d\mathbf{Q}^T. \quad (3.14)$$

3.2 Weighted Residual Formulation

3.2.1 Strong Formulation

The behaviour of solid and fluid phases within a given continuum body \mathcal{B} with boundary $\partial\mathcal{B}$ inside a three-dimensional Euclidean space \mathbb{R}^3 is described by the set of the governing

equations (2.1,2.45).

$$\begin{aligned}\nabla \cdot \boldsymbol{\sigma} + \rho \mathbf{b} - \rho \mathbf{a} &= \mathbf{0}; \\ \alpha \nabla \cdot \mathbf{v}_s + S \frac{\partial p_f}{\partial t} + \nabla \cdot \mathbf{q} &= 0,\end{aligned}$$

where $\boldsymbol{\sigma} = \boldsymbol{\sigma}' - \alpha p_f \mathbf{I}$, $\rho = (1 - n)\rho_s + n\rho_f$, $S = \left(\frac{n}{K_f} + \frac{\alpha - n}{K_s}\right)$, and $\mathbf{q} = \frac{\mathbf{K}}{\mu_f} (-\nabla p_f + \rho_f \mathbf{g})$.

The absence of fluid acceleration term in the Darcy flow equation is justified by the assumption [100] where the geomechanical problems in the current study are of transient quasi-static type; dynamic problems associated with high frequency is beyond the scope of the current study.

On the boundary $\partial \mathcal{B}$ of the same continuum body \mathcal{B} , the parts $\Gamma_{D,s}$ and $\Gamma_{D,f}$ are subjected to Dirichlet boundary conditions, respectively, in solid and fluid fields, whereas the parts $\Gamma_{N,s}$ and $\Gamma_{N,f}$ are subjected to Neumann boundary conditions, respectively, in solid and fluid fields. The conditions to be satisfied are that

$$\Gamma_{D,s} \cap \Gamma_{N,s} = \emptyset; \quad \Gamma_{D,s} \cup \Gamma_{N,s} = \partial \mathcal{B} \quad (\text{Solid field}); \quad (3.15)$$

$$\Gamma_{D,f} \cap \Gamma_{N,f} = \emptyset; \quad \Gamma_{D,f} \cup \Gamma_{N,f} = \partial \mathcal{B} \quad (\text{Fluid field}). \quad (3.16)$$

Then, the boundary and initial conditions for the governing equations are

$$\mathbf{u} = \tilde{\mathbf{u}} \text{ on } \Gamma_{D,s} \times \mathbb{t}; \quad (3.17)$$

$$\boldsymbol{\sigma} \cdot \mathbf{n} = \tilde{\mathbf{t}} \text{ on } \Gamma_{N,s} \times \mathbb{t}; \quad (3.18)$$

$$p_f = \tilde{p}_f \text{ on } \Gamma_{D,f} \times \mathbb{t}; \quad (3.19)$$

$$\rho_f \bar{\mathbf{q}} \cdot \mathbf{n} = \tilde{Q}_f \text{ on } \Gamma_{N,f} \times \mathbb{t}; \quad (3.20)$$

$$\left. \begin{aligned} \mathbf{u} &= \mathbf{u}_0 \\ p_f &= p_{f0} \end{aligned} \right\} \text{ within } \mathcal{B} \text{ and/or on } \partial \mathcal{B}, \quad (3.21)$$

where $\tilde{\mathbf{u}}$, $\tilde{\mathbf{t}}$, \tilde{p}_f and \tilde{Q}_f are, respectively, the prescribed displacement, traction, pore fluid pressure, and fluid mass flux (SI unit = $[\text{kg m}^{-2} \text{s}^{-1}]$) on the boundary $\partial \mathcal{B}$ over an interval of time $\mathbb{t} = [0, T] \subset \mathbb{R}^+$, whereas \mathbf{u}_0 and p_{f0} are the initial values of displacement and pore fluid pressure applied within the body \mathcal{B} and/or the boundary $\partial \mathcal{B}$ at time $t = 0$. The prescribed fluid mass flux \tilde{Q}_f is defined as the Darcy flow velocity projected in parallel with the unit normal vector \mathbf{n} multiplied by the fluid density ρ_f .

3.2.2 Weak Formulation

In the following, the weak formulation of the set of governing equations is constructed based on the principle of virtual power. We define, as two separate arbitrary differentiable vector fields, the kinematically admissible virtual displacement variation ($\delta \mathbf{u}$) and virtual pressure variation (δp_f) that independently allow arbitrarily tiny changes in the displacement and pore fluid pressure within a deformable body, while satisfying displacement and pore fluid pressure boundary conditions, such that $\delta \mathbf{u} = \mathbf{0}$ on $\Gamma_{D,s}$ and $\delta p_f = 0$ on $\Gamma_{D,f}$. It then follows that the time rate of virtual displacement variation is termed as virtual velocity variation $\delta \mathbf{v}$.

In the following, virtual velocity variation $\delta \mathbf{v}$ and virtual pressure variation δp_f are applied, respectively, to the linear momentum and mass balance equations to form virtual work rate δW_1 and δW_2 . For linear momentum equations,

$$\begin{aligned} \delta W_1 &= \int_{\Omega} (\nabla \cdot \boldsymbol{\sigma} + \rho \mathbf{b} - \rho \ddot{\mathbf{u}}) \cdot \delta \mathbf{v} dv \\ &= \int_{\Omega} (\nabla \cdot \boldsymbol{\sigma}) \cdot \delta \mathbf{v} dv + \int_{\Omega} \rho \mathbf{b} \cdot \delta \mathbf{v} dv - \int_{\Omega} \rho \ddot{\mathbf{u}} \cdot \delta \mathbf{v} dv = 0. \end{aligned} \quad (3.22)$$

By using chain rule and Divergence theorem, the term $\int_{\Omega} (\nabla \cdot \boldsymbol{\sigma}) \cdot \delta \mathbf{v} dv$ is further expanded as

$$\begin{aligned} \int_{\Omega} (\nabla \cdot \boldsymbol{\sigma}) \cdot \delta \mathbf{v} dv &= \int_{\Omega} \nabla \cdot (\boldsymbol{\sigma} \delta \mathbf{v}) dv - \int_{\Omega} \boldsymbol{\sigma} : \nabla_x \delta \mathbf{v} dv \\ &= \int_{\partial \Omega} \tilde{\mathbf{i}} \cdot \delta \mathbf{v} da - \int_{\Omega} \boldsymbol{\sigma} : \delta \mathbf{l} dv, \end{aligned} \quad (3.23)$$

and so we may express δW_1 as

$$\delta W_1 = \int_{\partial \Omega} \tilde{\mathbf{i}} \cdot \delta \mathbf{v} da - \int_{\Omega} \boldsymbol{\sigma} : \delta \mathbf{l} dv + \int_{\Omega} \rho \mathbf{b} \cdot \delta \mathbf{v} dv - \int_{\Omega} \rho \ddot{\mathbf{u}} \cdot \delta \mathbf{v} dv = 0. \quad (3.24)$$

As for the mass balance equation,

$$\begin{aligned} \delta W_2 &= \int_{\Omega} \left(\alpha \nabla \cdot \mathbf{v}_s + S \frac{\partial p_f}{\partial t} + \nabla \cdot \mathbf{q} \right) \delta p_f dv \\ &= \int_{\Omega} \alpha (\nabla \cdot \mathbf{v}_s) \delta p_f dv + \int_{\Omega} S \frac{\partial p_f}{\partial t} \delta p_f dv + \int_{\Omega} (\nabla \cdot \mathbf{q}) \delta p_f dv = 0. \end{aligned} \quad (3.25)$$

Similarly, by using chain rule and Divergence theorem, the term $\int_{\Omega} (\nabla \cdot \mathbf{q}) \delta p_f dv$ can be further expanded into

$$\begin{aligned} \int_{\Omega} (\nabla \cdot \mathbf{q}) \delta p_f dv &= \int_{\Omega} \nabla \cdot (\delta p_f \mathbf{q}) dv - \int_{\Omega} \mathbf{q} \cdot \nabla \delta p_f dv \\ &= \int_{\partial\Omega} \delta p_f \bar{\mathbf{q}} \cdot \mathbf{n} da - \int_{\Omega} \mathbf{q} \cdot \nabla \delta p_f dv \\ &= \int_{\partial\Omega} \delta p_f \frac{\tilde{Q}_f}{\rho_f} da - \int_{\Omega} \mathbf{q} \cdot \nabla \delta p_f dv, \end{aligned} \quad (3.26)$$

so that we may express

$$\delta W_2 = \int_{\Omega} \alpha (\nabla \cdot \mathbf{v}_s) \delta p_f dv + \int_{\Omega} S \frac{\partial p_f}{\partial t} \delta p_f dv + \int_{\partial\Omega} \delta p_f \frac{\tilde{Q}_f}{\rho_f} da - \int_{\Omega} \mathbf{q} \cdot \nabla \delta p_f dv = 0. \quad (3.27)$$

3.3 Finite Element Discretisation

3.3.1 Shape Function and Matrix Notation

Let $N_i^{(e)}(\mathbf{x})$ be a shape function of a generic finite element e located at node i , whose coordinate is \mathbf{x}^i . Then, the piecewise interpolation function of a generic field f defined over a finite element domain Ω^e is expressed by

$$f(\mathbf{x}) \equiv \sum_{i=1}^{n_{node}} \bar{f}^i N_i^{(e)}(\mathbf{x}), \quad (3.28)$$

where n_{node} is the number of nodes per element, and \bar{f}^i is the approximate value of f at \mathbf{x}^i .

Now, if the generic field f is defined over a whole domain $\Omega = \{\Omega^{e1}, \dots, \Omega^{en}\}$, where e_n is the total number of discrete non-overlapping elements in the domain Ω , its piecewise interpolation function is expressed by

$$f(\mathbf{x}) \equiv \sum_{i=1}^{n_{point}} \bar{f}^i N_i^g(\mathbf{x}), \quad (3.29)$$

where n_{point} is the sum of nodes within the discretised domain, and $N_i^g(\mathbf{x})$ is the global shape function, which in matrix form, is expressed as global interpolation matrix [54]

$$\mathbf{N}^g(\mathbf{x}) = [\text{diag}[N_1^g(\mathbf{x})] \quad \text{diag}[N_1^g(\mathbf{x})] \quad \dots \quad \text{diag}[N_{n_{point}}^g(\mathbf{x})]], \quad (3.30)$$

where $\text{diag}[N_i^g(\mathbf{x})]$ is given as a diagonal matrix whose size is the number of spatial dimensions

$$\text{diag}[N_i^g] = \begin{bmatrix} N_i^g & 0 & \cdots & 0 \\ 0 & N_i^g & \cdots & 0 \\ & & \ddots & \\ 0 & 0 & \cdots & N_i^g \end{bmatrix}. \quad (3.31)$$

On the other hand, the discretisation of strain, for instance, will involve the derivative of shape function. In conjunction with this need, a global gradient operator \mathbf{B}^g in matrix form is given as follows.

For three dimensional problems,

$$\mathbf{B}^g = \begin{bmatrix} N_{1,1}^g & 0 & 0 & N_{2,1}^g & 0 & 0 & \cdots & N_{n_{\text{point}},1}^g & 0 & 0 \\ 0 & N_{1,2}^g & 0 & 0 & N_{2,2}^g & 0 & \cdots & 0 & N_{n_{\text{point}},2}^g & 0 \\ 0 & 0 & N_{1,3}^g & 0 & 0 & N_{2,3}^g & \cdots & 0 & 0 & N_{n_{\text{point}},3}^g \\ N_{1,2}^g & N_{1,1}^g & 0 & N_{2,2}^g & N_{2,1}^g & 0 & \cdots & N_{n_{\text{point}},2}^g & N_{n_{\text{point}},1}^g & 0 \\ 0 & N_{1,3}^g & N_{1,2}^g & 0 & N_{2,3}^g & N_{2,2}^g & \cdots & 0 & N_{n_{\text{point}},3}^g & N_{n_{\text{point}},2}^g \\ N_{1,3}^g & 0 & N_{1,1}^g & N_{2,3}^g & 0 & N_{2,1}^g & \cdots & N_{n_{\text{point}},3}^g & 0 & N_{n_{\text{point}},1}^g \end{bmatrix}. \quad (3.32)$$

For plane strain and plane stress problems,

$$\mathbf{B}^g = \begin{bmatrix} N_{1,1}^g & 0 & N_{2,1}^g & 0 & \cdots & N_{n_{\text{point}},1}^g & 0 \\ 0 & N_{1,2}^g & 0 & N_{2,2}^g & \cdots & 0 & N_{n_{\text{point}},2}^g \\ N_{1,2}^g & N_{1,1}^g & N_{2,2}^g & N_{2,1}^g & \cdots & N_{n_{\text{point}},2}^g & N_{n_{\text{point}},1}^g \end{bmatrix}. \quad (3.33)$$

For operation involving the trace of a tensor, a trace operator vector is introduced. For three dimensional problems,

$$\mathbf{m} = \{1, 1, 1, 0, 0, 0\}^T, \quad (3.34)$$

whereas for plane strain and plane stress problems,

$$\mathbf{m} = \{1, 1, 0\}^T. \quad (3.35)$$

As for the stress and strain tensors, its equivalent vector form is arranged using Voigt's notation. For three dimensional problems,

$$\boldsymbol{\sigma} = \{\sigma_{11}, \sigma_{22}, \sigma_{33}, \sigma_{12}, \sigma_{23}, \sigma_{31}\}^T; \quad (3.36)$$

$$\boldsymbol{\varepsilon} = \{\varepsilon_{11}, \varepsilon_{22}, \varepsilon_{33}, 2\varepsilon_{12}, 2\varepsilon_{23}, 2\varepsilon_{31}\}^T. \quad (3.37)$$

For plane strain and plane stress problems¹,

$$\boldsymbol{\sigma} = \{\sigma_{11}, \sigma_{22}, \sigma_{12}\}^T; \quad (3.38)$$

$$\boldsymbol{\varepsilon} = \{\varepsilon_{11}, \varepsilon_{22}, 2\varepsilon_{12}\}^T. \quad (3.39)$$

3.3.2 Global Discretisation of Rate of Virtual Work

Using the global shape function \mathbf{N}^g and global gradient operator \mathbf{B}^g , the rates of virtual work δW_1 and δW_2 are discretised as follows. In particular, \mathbf{N}_u^g and \mathbf{N}_p^g are applied, respectively, for solid and fluid fields. For δW_1 ,

$$\begin{aligned} \delta W_1 &= \int_{\partial\Omega} \tilde{\mathbf{i}} \cdot \delta \mathbf{v} da - \int_{\Omega} \boldsymbol{\sigma} : \delta \mathbf{l} dv + \int_{\Omega} \rho \mathbf{b} \cdot \delta \mathbf{v} dv - \int_{\Omega} \rho \ddot{\mathbf{u}} \cdot \delta \mathbf{v} dv \\ &= \int_{\partial\Omega} \tilde{\mathbf{i}} \cdot \mathbf{N}_u^g \delta \bar{\mathbf{v}} da - \int_{\Omega} \boldsymbol{\sigma}^T \mathbf{B}^g \delta \bar{\mathbf{v}} dv + \int_{\Omega} \rho \mathbf{b} \cdot \mathbf{N}_u^g \delta \bar{\mathbf{v}} dv - \int_{\Omega} \rho (\mathbf{N}_u^g \ddot{\mathbf{u}})^T \cdot \mathbf{N}_u^g \delta \bar{\mathbf{v}} dv \\ &= \left(\int_{\partial\Omega} (\mathbf{N}_u^g)^T \tilde{\mathbf{i}} da - \int_{\Omega} (\mathbf{B}^g)^T \boldsymbol{\sigma} dv + \int_{\Omega} (\mathbf{N}_u^g)^T \rho \mathbf{b} dv - \int_{\Omega} (\mathbf{N}_u^g)^T \mathbf{N}_u^g \rho \ddot{\mathbf{u}} dv \right)^T \delta \bar{\mathbf{v}} = 0. \end{aligned} \quad (3.40)$$

The total stress representation is further expanded as

$$\begin{aligned} \int_{\Omega} (\mathbf{B}^g)^T \boldsymbol{\sigma} dv &= \int_{\Omega} (\mathbf{B}^g)^T (\boldsymbol{\sigma}' - \alpha \mathbf{m} \mathbf{N}_p^g \bar{\mathbf{p}}_f) dv \\ &= \int_{\Omega} (\mathbf{B}^g)^T \boldsymbol{\sigma}' dv - \int_{\Omega} (\mathbf{B}^g)^T \alpha \mathbf{m} \mathbf{N}_p^g \bar{\mathbf{p}}_f dv. \end{aligned} \quad (3.41)$$

By substitution and utilising the arbitrariness of the value of $\delta \bar{\mathbf{v}}$, we formulate the following from $\delta W_1 = 0$

$$\mathbf{M}^g \ddot{\mathbf{u}} + \int_{\Omega} (\mathbf{B}^g)^T \boldsymbol{\sigma}' dv - \mathbf{Q}^g \bar{\mathbf{p}}_f = \mathbf{f}_u^g, \quad (3.42)$$

¹ σ_{33} is solved separately in plane strain as function of σ_{11} and σ_{22} , whereas ε_{33} is solved separately in plane stress as function of ε_{11} and ε_{22} .

where

$$\mathbf{M}^g = \int_{\Omega} (\mathbf{N}_u^g)^T \mathbf{N}_u^g ((1-n)\rho_s + n\rho_f) dv; \quad (3.43)$$

$$\mathbf{Q}^g = \int_{\Omega} (\mathbf{B}^g)^T \alpha m \mathbf{N}_p^g dv; \quad (3.44)$$

$$\mathbf{f}_u^g = \int_{\partial\Omega} (\mathbf{N}_u^g)^T \tilde{\mathbf{t}} da + \int_{\Omega} (\mathbf{N}_u^g)^T ((1-n)\rho_s + n\rho_f) \mathbf{b} dv. \quad (3.45)$$

For δW_2 , because the expressions are much longer, the derivation is done separately as follows

$$\delta W_2 = \underbrace{\int_{\Omega} \alpha (\nabla \cdot \mathbf{v}_s) \delta p_f dv}_A + \underbrace{\int_{\Omega} S \frac{\partial p_f}{\partial t} \delta p_f dv}_B + \underbrace{\int_{\partial\Omega} \delta p_f \frac{\tilde{Q}_f}{\rho_f} da}_C - \underbrace{\int_{\Omega} \mathbf{q} \cdot \nabla \delta p_f dv}_D = 0. \quad (3.46)$$

Part A:

Logarithmic form of the solid volumetric strain is implicitly assumed

$$\nabla \cdot \mathbf{v}_s = \frac{\partial \bar{\epsilon}_v}{\partial t}, \quad \text{where } d\epsilon_v = \frac{dV_s}{V_s}, \quad (3.47)$$

and so in matrix form,

$$\int_{\Omega} \alpha (\nabla \cdot \mathbf{v}_s) \delta \mathbf{p}_f dv = \left(\int_{\Omega} \alpha \frac{\partial \bar{\epsilon}_v}{\partial t} \mathbf{N}_p^g dv \right) \delta \bar{\mathbf{p}}_f = \left(\int_{\Omega} (\mathbf{N}_p^g)^T \alpha \frac{\partial \bar{\epsilon}_v}{\partial t} dv \right)^T \delta \bar{\mathbf{p}}_f. \quad (3.48)$$

Part B:

In matrix form,

$$\begin{aligned} \int_{\Omega} S \left(\frac{\partial \mathbf{p}_f}{\partial t} \right)^T \delta \mathbf{p}_f dv &= \left(\int_{\Omega} S \left(\frac{\partial \bar{\mathbf{p}}_f}{\partial t} \right)^T (\mathbf{N}_p^g)^T \mathbf{N}_p^g dv \right) \delta \bar{\mathbf{p}}_f \\ &= \left(\int_{\Omega} (\mathbf{N}_p^g)^T S \mathbf{N}_p^g \frac{\partial \bar{\mathbf{p}}_f}{\partial t} dv \right)^T \delta \bar{\mathbf{p}}_f. \end{aligned} \quad (3.49)$$

Part C:

In matrix form,

$$\begin{aligned} \int_{\partial\Omega} \frac{\tilde{Q}_f}{\rho_f} \delta \mathbf{p}_f da &= \left(\int_{\partial\Omega} \frac{\tilde{Q}_f}{\rho_f} \mathbf{N}_p^g da \right) \delta \bar{\mathbf{p}}_f \\ &= \left(\int_{\partial\Omega} (\mathbf{N}_p^g)^T \frac{\tilde{Q}_f}{\rho_f} da \right)^T \delta \bar{\mathbf{p}}_f. \end{aligned} \quad (3.50)$$

Part D:

Darcy's law is assumed for \mathbf{q} , and so the matrix form is expanded as

$$\begin{aligned} \int_{\Omega} \mathbf{q} \cdot \nabla \delta \mathbf{p}_f dv &= \int_{\Omega} \frac{\mathbf{K}}{\mu_f} (-\nabla p_f + \rho_f \mathbf{g}) \cdot \nabla \delta \mathbf{p}_f dv \\ &= - \int_{\Omega} \frac{\mathbf{K}}{\mu_f} \nabla p_f \cdot \nabla \delta \mathbf{p}_f dv + \int_{\Omega} \frac{\mathbf{K}}{\mu_f} \rho_f \mathbf{g} \cdot \nabla \delta \mathbf{p}_f dv \\ &= \left(- \int_{\Omega} \frac{\mathbf{K}}{\mu_f} (\nabla \mathbf{N}_p^g)^T \bar{\mathbf{p}}_f \nabla \mathbf{N}_p^g dv + \int_{\Omega} \frac{\mathbf{K}}{\mu_f} \rho_f \mathbf{g} \nabla \mathbf{N}_p^g dv \right) \delta \bar{\mathbf{p}}_f \\ &= \left(- \int_{\Omega} (\nabla \mathbf{N}_p^g)^T \frac{\mathbf{K}}{\mu_f} (\nabla \mathbf{N}_p^g) \bar{\mathbf{p}}_f dv + \int_{\Omega} (\nabla \mathbf{N}_p^g)^T \frac{\mathbf{K}}{\mu_f} \rho_f \mathbf{g} dv \right)^T \delta \bar{\mathbf{p}}_f. \end{aligned} \quad (3.51)$$

Combining all the contributions, we obtain

$$\begin{aligned} \delta W_2 &= \left(\int_{\Omega} (\mathbf{N}_p^g)^T \boldsymbol{\alpha} \frac{\partial \bar{\boldsymbol{\varepsilon}}_v}{\partial t} dv + \int_{\Omega} (\mathbf{N}_p^g)^T \mathbf{S} \mathbf{N}_p^g \frac{\partial \bar{\mathbf{p}}_f}{\partial t} dv + \int_{\partial\Omega} (\mathbf{N}_p^g)^T \frac{\tilde{Q}_f}{\rho_f} da \right. \\ &\quad \left. + \int_{\Omega} (\nabla \mathbf{N}_p^g)^T \frac{\mathbf{K}}{\mu_f} (\nabla \mathbf{N}_p^g) \bar{\mathbf{p}}_f dv - \int_{\Omega} (\nabla \mathbf{N}_p^g)^T \frac{\mathbf{K}}{\mu_f} \rho_f \mathbf{g} dv \right)^T \delta \bar{\mathbf{p}}_f. \end{aligned} \quad (3.52)$$

Then, by utilising the arbitrariness of the value of $\delta \bar{\mathbf{p}}_f$, we formulate the following from $\delta W_2 = 0$

$$\mathbf{H}^g \bar{\mathbf{p}}_f + \mathbf{S}^g \frac{\partial \bar{\mathbf{p}}_f}{\partial t} + \mathbf{A}^g \frac{\partial \bar{\boldsymbol{\varepsilon}}_v}{\partial t} = \mathbf{f}_p, \quad (3.53)$$

where

$$\begin{aligned}
\mathbf{H}^g &= \int_{\Omega} (\nabla \mathbf{N}_p^g)^T \frac{\mathbf{K}}{\mu_f} (\nabla \mathbf{N}_p^g) dv; \\
\mathbf{S}^g &= \int_{\Omega} (\mathbf{N}_p^g)^T \mathbf{S} \mathbf{N}_p^g dv; \\
\mathbf{A}^g &= \int_{\Omega} (\mathbf{N}_p^g)^T \alpha dv; \\
\mathbf{f}_p &= \int_{\Omega} (\nabla \mathbf{N}_p^g)^T \frac{\mathbf{K}}{\mu_f} \rho_f \mathbf{g} dv - \int_{\partial\Omega} (\mathbf{N}_p^g)^T \frac{\tilde{\mathbf{Q}}_f}{\rho_f} da.
\end{aligned} \tag{3.54}$$

3.3.3 Element-Level Representation

In finite element algorithms, computation of global solution as function of global internal and external forces are based on the assembly of the corresponding forces from element level. In the following, linear momentum and mass balance equations in terms of shape functions at element level are shown.

Linear Momentum Equation

$$\mathbf{M}\ddot{\mathbf{u}} + \int_{\Omega} \mathbf{B}^T \boldsymbol{\sigma}' dv - \mathbf{Q}\bar{\mathbf{p}}_f = \mathbf{f}_u, \tag{3.55}$$

where

$$\mathbf{M} = \int_{\Omega} \mathbf{N}_u^T \mathbf{N}_u ((1-n)\rho_s + n\rho_f) dv; \tag{3.56}$$

$$\mathbf{Q} = \int_{\Omega} \mathbf{B}^T \alpha m \mathbf{N}_p dv; \tag{3.57}$$

$$\mathbf{f}_u = \int_{\partial\Omega} \mathbf{N}_u^T \tilde{\mathbf{i}} da + \int_{\Omega} \mathbf{N}_u^T ((1-n)\rho_s + n\rho_f) \mathbf{b} dv. \tag{3.58}$$

Mass Balance Equation

$$\mathbf{H}\bar{\mathbf{p}}_f + \mathbf{S} \frac{\partial \bar{\mathbf{p}}_f}{\partial t} + \mathbf{A} \frac{\partial \bar{\epsilon}_v}{\partial t} = \mathbf{f}_p, \tag{3.59}$$

where

$$\begin{aligned}
\mathbf{H} &= \int_{\Omega} (\nabla \mathbf{N}_p)^T \frac{\mathbf{K}}{\mu_f} (\nabla \mathbf{N}_p) dv; \\
\mathbf{S} &= \int_{\Omega} (\mathbf{N}_p)^T S \mathbf{N}_p dv; \\
\mathbf{A} &= \int_{\Omega} (\mathbf{N}_p)^T \alpha dv; \\
\mathbf{f}_p &= \int_{\Omega} (\nabla \mathbf{N}_p)^T \frac{\mathbf{K}}{\mu_f} \rho_f \mathbf{g} dv - \int_{\partial\Omega} (\mathbf{N}_p)^T \frac{\tilde{Q}_f}{\rho_f} da.
\end{aligned} \tag{3.60}$$

3.4 Numerical Simplification and Strategies

3.4.1 Lumped Mass Matrix

The linear momentum equation is solved explicitly in time to obtain the solution of displacement field $\bar{\mathbf{u}}$. As will be shown later, an explicit time integration will require the inverse of consistent mass matrix \mathbf{M} for each update. In view of this, nodal lumping method² is used to reduce the incurred computational cost by replacing the consistent mass matrix with a diagonal lumped mass matrix. At element level, the lumped mass matrix is given by

$$\mathbf{M} = \int_{\Omega} \frac{1}{n_{node}} \text{diag}[1] ((1-n)\rho_s + n\rho_f) dv, \tag{3.61}$$

where $\text{diag}[1]$ is a $n_{node} \times n_{node}$ diagonal matrix defined as

$$\text{diag}[1] = \begin{bmatrix} 1 & 0 & \cdots & 0 \\ 0 & 1 & \cdots & 0 \\ & & \ddots & \\ 0 & 0 & \cdots & 1 \end{bmatrix}. \tag{3.62}$$

3.4.2 Critical Time Step

The geomechanical problems to be solved in the current study is of quasi-static type. Therefore, if the inertia effect is negligible, the acoustic stress wave of speed c is less likely to travel beyond the domain bounded by the element characteristic length l^e in a single time step, as compared with highly dynamic cases. This then gives us the opportunity to reduce the computational cost by artificially increasing the critical time step Δt_{cr} via mass scaling

²suitable for linear elements [97]

constant f_{mass} , such that

$$\Delta t_{cr} = \text{Min} \left| \frac{l^e}{c} \right| = \text{Min} \left| \frac{l^e}{\sqrt{\frac{E}{f_{mass}\rho}}} \right| = \sqrt{f_{mass}} \left(\text{Min} \left| \frac{l^e}{\sqrt{\frac{E}{\rho}}} \right| \right), \quad (3.63)$$

where E is the Young's modulus. The expression of c is estimated using one dimensional approach. This idealization is compensated by introducing a critical time step factor f_{crit} , so that the effective critical time step size is given by $f_{crit}\Delta t_{cr}$. In the default settings of ParaGeo, $f_{crit} = 0.9$ is used for two dimensional problems, and $f_{crit} = 0.7$ is used for three dimensional problems.

However, in order to simulate quasi-static condition, the effect of applied traction, for instance, should propagate quickly throughout the domain. This can be achieved by increasing the natural frequency of the system, which is equivalent to increasing the acoustic stress wave speed c . As a result, in order to simulate quasi-static condition, the critical time step Δt_{cr} needs to be reduced.

In the implementation, a target time step Δt_{targ} is specified by the user, along with an initial mass scaling constant such that $f_{mass} < 1$. The solution mass of all elements will be reduced accordingly. This will create variable element critical time steps as the characteristic element length generally varies across the domain.

For elements whose effective critical time step $f_{crit}\Delta t_{crit} > \Delta t_{targ}$, higher acoustic stress wave c is allowed due to higher l^e . These elements are responsible for simulating quasi-static condition in the domain. On the other hand, for elements whose effective critical time step $f_{crit}\Delta t_{crit} < \Delta t_{targ}$, the mass scaling constant f_{mass} will then be automatically scaled to achieve $f_{crit}\Delta t_{crit} = \Delta t_{targ}$. These elements are responsible for reducing the computational cost by allowing higher critical time step when solving the system.

3.4.3 Damping

Mass Proportional Damping

The phenomenon of damping in geological basin scale is, in general, difficult to be quantified. One of the techniques to capture the effect of damping is via proportional Rayleigh damping method via damping matrix \mathbf{C} , such that

$$\mathbf{C} = \alpha_{\xi} \mathbf{M} + \beta \mathbf{K}, \quad (3.64)$$

, where α_ξ and β are parameters dependent on given damping ratio ξ and the corresponding natural frequencies ω .

The stiffness matrix \mathbf{K} is however not assembled during stress update in the explicit time scheme, and therefore, the damping matrix is further simplified [97] to mass proportional damping matrix $\mathbf{C} = \alpha_\xi \mathbf{M}$. It is clear that \mathbf{C} inherits diagonality from the lumped mass matrix. In index form, it is given by

$$C_{ii} = \alpha_{\xi_i} M_{ii} = 2\omega_i \xi_i M_{ii}, \quad \text{for } i = 1, \dots, n \quad , \quad (3.65)$$

where ω_i is the target frequency, ξ_i is the damping factor with 1 being the critical damping of the lowest frequency, and n is the degrees of freedom.

The proportional coefficient α_ξ is determined by [97]

$$\alpha_\xi = \text{Min} \begin{cases} 2\xi \sqrt{\frac{\bar{\mathbf{u}}^T \tilde{\mathbf{K}} \bar{\mathbf{u}}}{\bar{\mathbf{u}}^T \mathbf{M} \bar{\mathbf{u}}}} \\ \frac{4\xi}{\Delta t_{cr}} \end{cases} \quad (3.66)$$

where Δt_{cr} is the critical time step, which will be discussed in the next section.

The local diagonal stiffness matrix $\tilde{\mathbf{K}}$ is estimated [97] as

$$\tilde{K}_{ij}^N = \delta_{ij} \frac{f_{int,i}^N - f_{int,i}^{N-1}}{\dot{u}_i^{N-1/2} \Delta t} \quad , \quad (3.67)$$

where N is the current mechanical time step and $\mathbf{f}_{int} = \int_{\Omega} \mathbf{B}^T \boldsymbol{\sigma}' dv$ is the internal force.

With the mass proportional damping matrix, the linear momentum equation is recast as

$$\mathbf{M}\ddot{\mathbf{u}} + \mathbf{C}\dot{\mathbf{u}} + \mathbf{f}_{int} - \mathbf{Q}\bar{\mathbf{p}}_f = \mathbf{f}_u \quad (3.68)$$

where $\dot{\mathbf{u}}$ is the solid velocity vector.

Artificial Bulk Viscosity Damping

By default, in quasi-static simulation, artificial bulk viscosity damping term is applied in ParaGeo to attenuate high-frequency oscillations in the effective mean stress during compression. This method was introduced by [177] for the purpose of mitigating oscillation

in the simulation of shock wave propagation. The damping term is given by

$$q_{vis} = \begin{cases} \rho l_e^2 Q_{quad} \dot{\epsilon}_v^2 & \text{for } \dot{\epsilon}_v < 0 \\ 0 & \text{for } \dot{\epsilon}_v > 0 \end{cases}, \quad (3.69)$$

where l_e is the element characteristic length and Q_{quad} is a dimensionless constant.

Bulk viscosity damping can also be specified to treat post-shock small oscillations via a linear term of the standard bulk viscosity model. Combined with artificial bulk viscosity damping term above, we obtain

$$q_{vis} = \begin{cases} -\rho (Q_{lin}c - Q_{quad}l_e\dot{\epsilon}_v) l_e\dot{\epsilon}_v & \text{for } \dot{\epsilon}_v < 0 \\ 0 & \text{for } \dot{\epsilon}_v > 0 \end{cases}, \quad (3.70)$$

where c is the element elastic wave speed, and Q_{lin} is another dimensionless constant.

It follows that, during stress update, the computation of incremental effective mean stress is dependent on the loading mode

$$\Delta p^* = \begin{cases} \Delta p - q_{vis} & = \left(K + \rho \left(Q_{lin}c - Q_{quad}l_e \frac{\Delta \epsilon_v}{\Delta t} \right) \frac{l_e}{\Delta t} \right) \Delta \epsilon_v & \text{for } \Delta \epsilon_v < 0 \\ \Delta p & = K \Delta \epsilon_v & \text{for } \Delta \epsilon_v > 0 \end{cases}, \quad (3.71)$$

where Δp^* is the damped increment in effective mean stress. In ParaGeo, the recommended value for each dimensionless constant are $Q_{lin} = 1.5$ and $Q_{quad} = 0.06$.

3.4.4 Averaged Volumetric Strain

While the use of linear element is preferred in ParaGeo especially when dealing with contact problems, the lack of degree of freedom in linear element will readily cause the system to suffer from volumetric locking. In this case, small perturbation of strain in a linear element will induce very high resistance against deformation, and thus renders incompressibility in the linear element.

To curb with this problem, averaged volumetric strain method [57] is employed in ParaGeo. The main idea is to effectively increase the degree of freedom of a linear element by allowing each node to absorb the effect from its surrounding elements via averaged volumetric strain.

Using the averaged volumetric strain method, the rate of small³ strain tensor of an element is given by

$$\dot{\boldsymbol{\epsilon}} = \dot{\boldsymbol{\epsilon}}_{dev} + \left(\frac{2}{3} \dot{\epsilon}_v + \frac{1}{3} \dot{\tilde{\epsilon}}_v \right) \mathbf{I}, \quad (3.72)$$

where the averaged volumetric strain rate $\dot{\tilde{\epsilon}}_v$ is given by

$$\dot{\tilde{\epsilon}}_v = \frac{1}{n_{node}} \sum_{i=1}^{n_{node}} \left(\frac{\sum_{e=1}^{n_{oe,i}} \dot{\epsilon}_{v,e} \Omega_e}{\sum_{e=1}^{n_{oe,i}} \Omega_e} \right), \quad (3.73)$$

where n_{node} is the number of node per linear element, and n_{oe} is the number of element e surrounding the current node i , while $\dot{\epsilon}_{v,e}$ and Ω_e are, respectively, the volumetric strain rate and the volume of element e surrounding the current node i .

3.5 Time Discretisation and Solution Update

The use of monolithic Newton-Raphson method to solve coupled flow-geomechanical system is explained in detail by [100]. However, it is reported [24] that a more advanced monolithic solver is required to solve saddle point problem that is inherent in the coupled fields involving nonlinear Biot equations, and to account for constitutive models that are not Lipschitz continuous [171].

While the coupled approach offers the benefit of unconditional stability, the advantage of using sequential approach [101, 153, 154, 106, 55, 162, 164, 90] is that existing solver of different fields can be utilised as long as the corresponding numerical parameters are well calibrated to ensure solution stability. Furthermore, sequential approach may appeal to the industrial demands because large opportunity cost will, otherwise, be incurred for the construction of multi-field robust monolithic solvers. In ParaGeo, sequential approach is adopted, whereby both seepage and geomechanical fields are solved separately using different time step sizes.

3.5.1 Geomechanical Field

To recap, the linear momentum equation is given by

$$\mathbf{M}\ddot{\mathbf{u}}(t) - \mathbf{Q}\bar{\mathbf{p}}_f(t) = \mathbf{f}_u(t) - \mathbf{f}_{int}(t), \quad (3.74)$$

³The use of small strain is justified by the application of Green-Nagdhi stress rate (which will be presented in later section) that assumes small strain increment for each time step.

where

$$\begin{aligned}\mathbf{M} &= \int_{\Omega} \mathbf{N}_u^T \mathbf{N}_u ((1-n)\rho_s + n\rho_f) dv \approx \int_{\Omega} \frac{1}{n_{node}} \text{diag}[1] ((1-n)\rho_s + n\rho_f) dv; \\ \mathbf{Q} &= \int_{\Omega} \mathbf{B}^T \alpha m \mathbf{N}_p dv; \\ \mathbf{f}_u &= \int_{\partial\Omega} \mathbf{N}_u^T \tilde{\mathbf{t}} da + \int_{\Omega} \mathbf{N}_u^T ((1-n)\rho_s + n\rho_f) \mathbf{b} dv; \\ \mathbf{f}_{int} &= \int_{\Omega} \mathbf{B}^T \boldsymbol{\sigma}' dv.\end{aligned}$$

The linear momentum equation is solved explicitly by using central difference time discretisation method. Before discretising the linear momentum in time, it is necessary to define some of the following parameters.

Central Difference Time Discretisation

Time Increment

$$\Delta t^{N+1} = t^{N+1} - t^N; \quad \Delta t^N = t^N - t^{N-1}; \quad \Delta t^{N+1/2} = \frac{\Delta t^{N+1} + \Delta t^N}{2} \quad (3.75)$$

Displacement Field

$$\bar{\mathbf{u}}^{N+1} = \bar{\mathbf{u}}(t^{N+1}); \quad \bar{\mathbf{u}}^N = \bar{\mathbf{u}}(t^N); \quad \bar{\mathbf{u}}^{N-1} = \bar{\mathbf{u}}(t^{N-1}) \quad (3.76)$$

Velocity Field

$$\dot{\bar{\mathbf{u}}}^{N+1/2} = \frac{\bar{\mathbf{u}}^{N+1} - \bar{\mathbf{u}}^N}{\Delta t^{N+1/2}}; \quad \dot{\bar{\mathbf{u}}}^N = \frac{\bar{\mathbf{u}}^{N+1/2} - \bar{\mathbf{u}}^{N-1/2}}{\Delta t^{N+1/2}}; \quad \dot{\bar{\mathbf{u}}}^{N-1/2} = \frac{\bar{\mathbf{u}}^N - \bar{\mathbf{u}}^{N-1}}{\Delta t^N} \quad (3.77)$$

Acceleration Field

$$\ddot{\bar{\mathbf{u}}}^N = \frac{\dot{\bar{\mathbf{u}}}^{N+1/2} - \dot{\bar{\mathbf{u}}}^{N-1/2}}{\Delta t^{N+1/2}} \quad (3.78)$$

The velocity term $\dot{\bar{\mathbf{u}}}^N$ can be alternatively expressed in terms of velocity terms

$$\begin{aligned}\dot{\bar{\mathbf{u}}}^N &= \frac{\bar{\mathbf{u}}^{N+1/2} - \bar{\mathbf{u}}^{N-1/2}}{\Delta t^{N+1/2}} \\ &= \frac{\frac{1}{2}(\bar{\mathbf{u}}^{N+1} + \bar{\mathbf{u}}^N) - \frac{1}{2}(\bar{\mathbf{u}}^N + \bar{\mathbf{u}}^{N-1})}{\Delta t^{N+1/2}} \\ &= \frac{\bar{\mathbf{u}}^{N+1} - \bar{\mathbf{u}}^{N-1}}{2\Delta t^{N+1/2}}.\end{aligned}\quad (3.79)$$

By recognising that

$$\begin{aligned}\bar{\mathbf{u}}^{N+1} &= \Delta t^{N+1} \dot{\bar{\mathbf{u}}}^{N+1/2} + \bar{\mathbf{u}}^N \\ \bar{\mathbf{u}}^N &= \Delta t^N \dot{\bar{\mathbf{u}}}^{N-1/2} + \bar{\mathbf{u}}^{N-1},\end{aligned}\quad (3.80)$$

we may now express

$$\begin{aligned}\dot{\bar{\mathbf{u}}}^N &= \frac{\bar{\mathbf{u}}^{N+1} - \bar{\mathbf{u}}^{N-1}}{2\Delta t^{N+1/2}} \\ &= \frac{1}{2\Delta t^{N+1/2}} \left(\Delta t^{N+1} \dot{\bar{\mathbf{u}}}^{N+1/2} + \Delta t^N \dot{\bar{\mathbf{u}}}^{N-1/2} \right).\end{aligned}\quad (3.81)$$

With the explicit expressions of $\ddot{\bar{\mathbf{u}}}^N$ and $\dot{\bar{\mathbf{u}}}^N$, the linear momentum equation at time N can be expanded into

$$\begin{aligned}\mathbf{M}^N \bar{\mathbf{u}}^N - \mathbf{Q}^N \bar{\mathbf{p}}_f^* &= \mathbf{f}_u^N - \mathbf{f}_{int}^N \\ \mathbf{M}^N \left(\frac{\dot{\bar{\mathbf{u}}}^{N+1/2} - \dot{\bar{\mathbf{u}}}^{N-1/2}}{\Delta t^{N+1/2}} \right) - \mathbf{Q}^N \bar{\mathbf{p}}_f^* &= \mathbf{f}_u^N - \mathbf{f}_{int}^N,\end{aligned}\quad (3.82)$$

where the subscript $*$ represents the corresponding current value of pore pressure that is solved separately from the mechanical field.

After rearrangement of the above equation, we obtain⁴

$$\dot{\bar{\mathbf{u}}}^{N+1/2} = (\mathbf{M}^N)^{-1} \left(\mathbf{M}^N \dot{\bar{\mathbf{u}}}^{N-1/2} + \Delta t^{N+1/2} (\mathbf{f}_u^N - \mathbf{f}_{int}^N + \mathbf{Q}^N \bar{\mathbf{p}}_f^*) \right). \quad (3.83)$$

⁴In staggered scheme, porosity (and therefore the porosity-dependent quantities, e.g. \mathbf{M} , \mathbf{Q} , \mathbf{f}_u) assumes the value from the last mechanical time step N . Accuracy is improved by applying iterative scheme, whereby the subsequent converged pore pressure value yields a better estimate of effective yield stress and thus, resulting in more accurate evolution of porosity throughout the deformation history.

After solving for velocity field $\dot{\mathbf{u}}^{N+1/2}$, we proceed with updating procedure of the displacement field through

$$\bar{\mathbf{u}}^{N+1} = \bar{\mathbf{u}}^N + \dot{\mathbf{u}}^{N+1/2} \Delta t^{N+1}, \quad (3.84)$$

from which the current volume of deformed configuration can be computed.

Using the logarithmic definition of the volumetric strain (3.47), porosity is updated following [120]

$$\frac{dn}{1-n} = d\varepsilon_v, \quad (3.85)$$

which yields by integration

$$n^{N+1} = 1 - \frac{1-n^N}{e^{\Delta\varepsilon_v^{N+1}}}. \quad (3.86)$$

The updated porosity, along with other contributing variables, is used to update the storativity term S and diagonal global permeability matrix \mathbf{K}^g . This matrix is initialised by the user input values, which represent the permeability in directions that are mutually orthogonal. Using the angle between the local reference system of interest and the reference system defined by the eigenvectors of \mathbf{K}^g , an orthogonal transformation matrix \mathbf{P} can be formulated in order to calculate the anisotropic permeability \mathbf{K} at local reference system

$$\mathbf{K} = \mathbf{P}^T \mathbf{K}^g \mathbf{P}. \quad (3.87)$$

For two dimensional problems, we construct \mathbf{K}^g as

$$\mathbf{K}^g = \begin{bmatrix} K_X(n) & 0 \\ 0 & K_Y(n) \end{bmatrix}, \quad (3.88)$$

where $K_X(n)$ and $K_Y(n)$, defined by user, are the eigenvalues of \mathbf{K}^g that could vary with porosity n .

The rotation matrix is given by

$$\mathbf{P} = \begin{bmatrix} \cos \theta & \sin \theta \\ -\sin \theta & \cos \theta \end{bmatrix}. \quad (3.89)$$

Then, the directional permeability tensor \mathbf{K} can be obtained as

$$\mathbf{K} = \begin{bmatrix} K_X(n) \cos^2 \theta + K_Y(n) \sin^2 \theta & (K_X(n) - K_Y(n)) \cos \theta \sin \theta \\ (K_X(n) - K_Y(n)) \cos \theta \sin \theta & K_Y(n) \cos^2 \theta + K_X(n) \sin^2 \theta \end{bmatrix}. \quad (3.90)$$

If $K_X = K_Y = K$, we can then recover isotropic permeability matrix, in which case,

$$\mathbf{K} = \mathbf{K}^g = K(n) \begin{bmatrix} 1 & 0 \\ 0 & 1 \end{bmatrix}. \quad (3.91)$$

As for the forcing terms, whereas the external forcing term \mathbf{f}_u can be updated for the next mechanical time step via $\mathbf{f}_u^{N+1} = \mathbf{f}_u(t^{N+1})$, the update of internal forcing term \mathbf{f}_{int}^{N+1} is described in the next section.

Green-Naghdi Stress Rate

In ParaGeo, stress update is performed using objective stress rate. This method is based on hypoelastic theory. It is reported that this theory poses some limitations on the accuracy of the behaviour of elastic deformation, where dissipation of energy is reported to take place within a closed (elastic) cycle. However, such inaccuracy is insignificant [54] to materials with small elastic domain, which also applies to the type of geomaterials used in the current study.

Green-Naghdi stress rate is adopted and used in ParaGeo for plane strain problems

$$\begin{aligned} \boldsymbol{\sigma}^\Delta &= \mathbf{R} \left(\frac{d}{dt} (\mathbf{R}^T \boldsymbol{\sigma}' \mathbf{R}) \right) \mathbf{R}^T, \\ &= \mathbf{R} (\mathbf{R}^T \boldsymbol{\sigma}' \mathbf{R}) \mathbf{R}^T \end{aligned} \quad (3.92)$$

where \mathbf{R} is an orthogonal tensor. Note that $\boldsymbol{\sigma}^\Delta$ is a simplified version of Truesdell stress rate, given by

$$\boldsymbol{\sigma}^\circ = J^{-1} \mathbf{F} \left(\frac{d}{dt} (J \mathbf{F}^{-1} \boldsymbol{\sigma}' \mathbf{F}^{-T}) \right) \mathbf{F}^T. \quad (3.93)$$

It is clear from the expression of $\boldsymbol{\sigma}^\circ$ that Green-Naghdi stress rate assumes

$$\mathbf{F} = \mathbf{R}\mathbf{U} \approx \mathbf{R}; \quad J = \det \mathbf{F} \approx 1, \quad (3.94)$$

which admits small increment via $\mathbf{U} \approx \mathbf{I}$.

In terms of strain increment, it means that the rate of Green-Lagrange strain tensor becomes

$$\dot{\mathbf{E}} = \frac{1}{2}\dot{\mathbf{C}} = \dot{\boldsymbol{\varepsilon}} + \frac{1}{2}\frac{\partial}{\partial t}((\nabla_{\mathbf{X}}\mathbf{u})^T(\nabla_{\mathbf{X}}\mathbf{u})) \approx \dot{\boldsymbol{\varepsilon}}, \quad (3.95)$$

where $\dot{\boldsymbol{\varepsilon}}$ is the time rate of small tensor defined by

$$\dot{\boldsymbol{\varepsilon}} = \frac{1}{2}((\nabla_{\mathbf{X}}\mathbf{u})^T + (\nabla_{\mathbf{X}}\mathbf{u})). \quad (3.96)$$

Stress Update Procedure

In the computation of Green-Naghdi stress rate

$$\boldsymbol{\sigma}^\Delta = \underbrace{\mathbf{R} \left(\overbrace{\mathbf{R}^T \dot{\boldsymbol{\sigma}}' \mathbf{R}}^{\text{Pull Back}} \right) \mathbf{R}^T}_{\text{Push Forward}}, \quad (3.97)$$

the time rate of Cauchy stress tensor is firstly transformed into total Lagrangian configuration via pull-back operation. In this configuration, the Cauchy stress $\boldsymbol{\sigma}'_{\mathbf{X}}{}^{N+1}$ is updated via the standard elastoplastic predictor-corrector algorithm [54]. Then, the updated Cauchy stress tensor is push-forward into updated Lagrangian configuration as $\boldsymbol{\sigma}'_{\mathbf{x}}{}^{N+1}$.

To calculate Cauchy stress increment, the rate of deformation \mathbf{d} is integrated over time increment to obtain the spatial strain increment tensor $\Delta\boldsymbol{\varepsilon}_{\mathbf{x}}{}^{N+1}$ with second order accuracy

$$\int_t^{t+\Delta t} \mathbf{d} dt \approx \left(\frac{\mathbf{d}^{N+1} + \mathbf{d}^N}{2} \right) \Delta t = \mathbf{d}^{N+1/2} \Delta t = \Delta\boldsymbol{\varepsilon}_{\mathbf{x}}{}^{N+1/2}. \quad (3.98)$$

Pull Back Operation

The Cauchy stress tensor at time t^N and the strain increment tensor are transformed from updated Lagrangian configuration into total Lagrangian configuration, as follows

$$\Delta\boldsymbol{\varepsilon}_{\mathbf{X}}{}^{N+1/2} = \mathbf{R}^{T,N+1/2} \Delta\boldsymbol{\varepsilon}_{\mathbf{x}}{}^{N+1/2} \mathbf{R}^{N+1/2}, \quad (3.99)$$

$$\boldsymbol{\sigma}'_{\mathbf{X}}{}^N = \mathbf{R}^{T,N} \boldsymbol{\sigma}'_{\mathbf{x}}{}^N \mathbf{R}^N. \quad (3.100)$$

Then, the standard elastoplastic predictor-corrector algorithm can proceed by beginning with the computation of trial stress

$$\boldsymbol{\sigma}'_{\mathbf{X}}{}^{\text{trial},N+1} = \boldsymbol{\sigma}'_{\mathbf{X}}{}^N + \mathbb{C} : \Delta\boldsymbol{\varepsilon}_{\mathbf{X}}{}^{N+1/2}, \quad (3.101)$$

where \mathbb{C} is the fourth-order elasticity tensor.

If $\boldsymbol{\alpha}^N$ is the hardening internal variable at time t^N , and $\Phi(\boldsymbol{\sigma}_{\mathbf{X}}^{\text{trial},N+1}, \boldsymbol{\alpha}^N)$ is the yield criterion, then if $\Phi(\boldsymbol{\sigma}_{\mathbf{X}}^{\text{trial},N+1}, \boldsymbol{\alpha}^N) > 0$, plastic strain increment $\Delta\boldsymbol{\varepsilon}_{\mathbf{X}}^{\text{in}}$ is computed from (generally non-associative) plastic flow potential Ψ , such that

$$\Delta\boldsymbol{\varepsilon}_{\mathbf{X}}^{\text{in},N+1/2} = \Delta\lambda \frac{\partial\Psi}{\partial\boldsymbol{\sigma}}, \quad (3.102)$$

where $\Delta\lambda$ is the plastic multiplier.

The corrected stress is then updated by

$$\boldsymbol{\sigma}_{\mathbf{X}}^{\prime N+1} = \boldsymbol{\sigma}_{\mathbf{X}}^{\prime N} + \mathbb{C} : \left(\Delta\boldsymbol{\varepsilon}_{\mathbf{X}}^{N+1/2} - \Delta\boldsymbol{\varepsilon}_{\mathbf{X}}^{\text{in},N+1/2} \right). \quad (3.103)$$

Push Forward Operation

The stress update is completed by transforming the Cauchy stress tensor from total Lagrangian configuration back to updated Lagrangian configuration

$$\boldsymbol{\sigma}_{\mathbf{x}}^{\prime N+1} = \mathbf{R}^{N+1} \boldsymbol{\sigma}_{\mathbf{X}}^{\prime N+1} \mathbf{R}^{T,N+1}. \quad (3.104)$$

With the updated Cauchy stress tensor, the internal force \mathbf{f}_{int} is updated for the next mechanical time step via $\int_{\Omega} \mathbf{B}^T \boldsymbol{\sigma}^{\prime N+1} dv$.

A direct way of computing \mathbf{R} for planar deformation is proposed by [140]. If the deformation gradient tensor at time t is given in the following matrix form

$$\mathbf{F}^t = \begin{bmatrix} F_{11}^t & F_{12}^t & 0 \\ F_{21}^t & F_{22}^t & 0 \\ 0 & 0 & F_{33}^t \end{bmatrix}, \quad (3.105)$$

then the orthogonal rotation tensor \mathbf{R} at time t can be obtained as

$$\mathbf{R}^t = \begin{bmatrix} A & -B & 0 \\ B & A & 0 \\ 0 & 0 & 1 \end{bmatrix}. \quad (3.106)$$

where

$$A = \frac{F_{11}^t + F_{22}^t}{\sqrt{(F_{11}^t + F_{22}^t)^2 + (F_{21}^t - F_{12}^t)^2}}; \quad (3.107)$$

$$B = \frac{F_{21}^t - F_{12}^t}{\sqrt{(F_{11}^t + F_{22}^t)^2 + (F_{21}^t - F_{12}^t)^2}}. \quad (3.108)$$

3.5.2 Seepage Field

To recap, the mass balance equation is given by

$$\mathbf{H}\bar{p}_f + \mathbf{S}\frac{\partial\bar{p}_f}{\partial t} + \mathbf{A}\frac{\partial\bar{\epsilon}_v}{\partial t} = \mathbf{f}_p, \quad (3.109)$$

where

$$\begin{aligned} \mathbf{H} &= \int_{\Omega} (\nabla\mathbf{N}_p)^T \frac{\mathbf{K}}{\mu_f} (\nabla\mathbf{N}_p) dv; \\ \mathbf{S} &= \int_{\Omega} (\mathbf{N}_p)^T \mathbf{S} \mathbf{N}_p dv = \int_{\Omega} \mathbf{N}_p^T \left(\frac{n}{K_f} + \frac{\alpha - n}{K_s} \right) \mathbf{N}_p dv; \\ \mathbf{A} &= \int_{\Omega} (\mathbf{N}_p)^T \alpha dv; \\ \mathbf{f}_p &= \int_{\Omega} (\nabla\mathbf{N}_p)^T \frac{\mathbf{K}}{\mu_f} \rho_f \mathbf{g} dv - \int_{\partial\Omega} (\mathbf{N}_p)^T \frac{\tilde{Q}_f}{\rho_f} da. \end{aligned} \quad (3.110)$$

In the adopted coupling strategy (discussed in the next section), the mass balance equation is firstly solved before the linear momentum equation. In the implementation, a single, coarse time step in the seepage field encapsulates multiple fine time steps in the geomechanical field. The mass balance equation is solved implicitly using backward Euler method⁵ for pore pressure, which is then superimposed with mechanically generated pore pressure⁶.

$$\mathbf{S} \left(\frac{\bar{p}_f^{K+1} - \bar{p}_f^K}{\Delta t_p} \right) + \mathbf{H}\bar{p}_f^{K+1} + \mathbf{A}\frac{\Delta\bar{\epsilon}_v^N}{\Delta t_p} = \mathbf{f}_p^{K+1}; \quad (3.111)$$

where subscript K denotes the current time in seepage field, Δt_p is the time step size for flow field, and $\Delta\bar{\epsilon}_v^N$ represents the the change of volumetric strain over the last mechanical time step.

3.6 Split Schemes for Flow-Geomechanical Fields

In this section, it is demonstrated how the solvers from both fields communicate with each other using intermediate solution via split scheme. In particular, it is about the strategy of how pore pressure is transferred from the seepage field to geomechanical field, as well as how

⁵by involving Newton Raphson method

⁶Via linear interpolation, pore pressure contributed by seepage field for a given mechanical intermediate step are added to the pore pressure generated in the previous mechanical step to yield total pore pressure.

volumetric strain, porosity and updated coordinates are transferred from the geomechanical field to the seepage field.

In general, geomechanical and seepage fields may exhibit different level of coupling strengths, depending on the sediment properties and the rate of loading. The mechanism that influences the coupling strength is the rate of pore pressure generation induced by volumetric strain. For low permeability sediment, the characteristic time scale for diffusion process is large; the dissipation of excess pore pressure generated by mechanical compaction will take longer time before reaching new mechanical equilibrium. In this case, the coupling strength of geomechanical-porous field is higher than that of high permeability sediment because of the longer drainage period. Furthermore, cases where loading rate is high or sediment with high compressibility are also associated with high coupling strength due to increased rate of volumetric strain and pore pressure generation, respectively.

The application of split scheme method requires some assumptions regarding the state of one field when another field is being solved. This is related to the treatment towards pore pressure term $Q\bar{p}_f$ in (3.55) and volumetric strain term $A \frac{\partial \bar{\epsilon}_v}{\partial t}$ in (3.59), as will be shown in the next section.

Different possible type of split schemes are investigated by [93, 91, 92, 94], including drained split, undrained split, fixed strain split, and fixed stress split schemes. It is found that drained and fixed strain split schemes exhibit poor solution stability, whereas undrained and fixed-stress split schemes share the same stability behaviour but differ in convergence and accuracy. Compared with undrained split scheme, fixed-stress scheme yields less stiff system and is convergent for an incompressible system with first order accuracy in nonlinear problem. Therefore, fixed-stress split scheme is preferred by the authors. However, problem related to pore pressure diffusion driven by volumetric strain is not considered in their investigations. In addition, non-continuous loading direction as commonly introduced by transient dynamic algorithm is also not accounted for. Such changes in loading direction could mis-guide the predictor in undrained and fixed-stress algorithms in terms of loading direction.

In ParaGeo solver, two split schemes are adopted, i.e. undrained and fixed stress schemes, which are discussed in the followings.

3.6.1 Undrained Split Scheme

Solution Update

In both split schemes, seepage field is solved firstly using coarse time step size, followed by geomechanical field using fine time step sizes (Figure 3.1). Equation (3.111) is solved for updated pore pressure from seepage field \bar{p}_f^{K+1} .

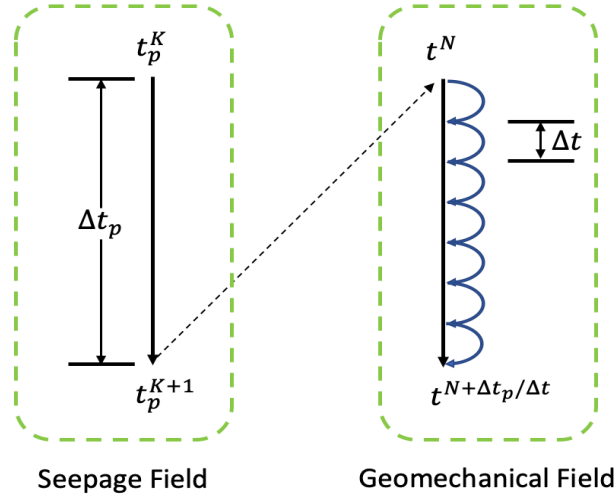


Fig. 3.1 Illustration of coarse time step in seepage field followed by multiple fine time steps in geomechanical field in simulating flow-geomechanical fields in split form

In geomechanical field, a linear interpolation based on $\bar{\mathbf{p}}_f^{K+1}$ and $\bar{\mathbf{p}}_f^K$ is constructed to account for the pore pressure contribution from the seepage field

$$\bar{\mathbf{p}}_{f,seepage}^{N+1} = (1-f)\bar{\mathbf{p}}_f^K + f\bar{\mathbf{p}}_f^{K+1}. \quad (3.112)$$

The time ratio f , which corresponds to the time increment in both fields, is given by

$$f = i \frac{\Delta t}{\Delta t_p}, \quad i = [0, I] \in \mathbb{Z}. \quad (3.113)$$

where \mathbb{Z} is the integer space and $I = \frac{\Delta t_p}{\Delta t}$.

In undrained split scheme, it is assumed that a locally undrained⁷ response is generated due to the deformation of solid matrix for every mechanical time step Δt . For a single element, this corresponds to zero outflow, whereby

$$\alpha \frac{\partial \bar{\epsilon}_v}{\partial t} + S \frac{\partial p_f}{\partial t} = \nabla \cdot \left(\frac{\mathbf{K}}{\mu_f} (\nabla p_f - \rho_f \mathbf{g}) \right) = 0,$$

⁷, which is a good characteristic of low permeability formation

from which the equation can be discretised to formulate an estimate of pore pressure increment generated by geomechanical field⁸

$$\Delta p_{f,mech}^N = -\frac{\alpha}{S} \Delta \bar{\epsilon}_v^N = -\frac{\alpha}{S} \ln \left(\frac{V^N}{V^{N-1}} \right). \quad (3.114)$$

It can be demonstrated that the computation of total pore pressure contributed by both fields using the relation

$$\bar{\mathbf{p}}_f^{N+1} = \bar{\mathbf{p}}_{f,seepage}^{N+1} + \Delta \mathbf{p}_{f,mech}^N \quad (3.115)$$

tends not to produce smooth pore pressure, as demonstrated by [91].

To improve the total pore pressure trend, a pore pressure increment $\Delta \mathbf{p}_{f0,mech}$ in mechanical field before the start of the current seepage flow step is used to provide smooth transition of total pore pressure over the current seepage flow time step Δt_p (Figure 3.2). The improved total pore pressure is given by

$$\bar{\mathbf{p}}_f^{N+1} = \bar{\mathbf{p}}_{f,seepage}^{N+1} + f \Delta \mathbf{p}_{f,mech}^N + (1-f) \Delta \mathbf{p}_{f0,mech}, \quad (3.116)$$

which is then used in the current mechanical time step t^{N+1} to compute the current effective Cauchy stress tensor $\boldsymbol{\sigma}^{N+1}$.

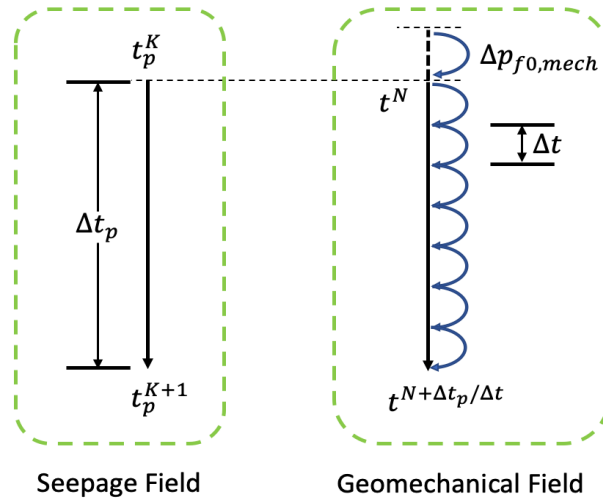


Fig. 3.2 Illustration of pore pressure increment $\Delta p_{f,mech}^N$ in mechanical step before the start of the current seepage flow step. The term $\Delta p_{f0,mech}^N$ is used to provide smooth transition of total pore pressure over the current seepage flow time step Δt_p

⁸It is not possible to compute $\Delta p_{f,mech}^{N+1}$ because the current deformed volume V^{N+1} is not available at the current mechanical time step.

Because of the presence of $\Delta \mathbf{p}_{f,mech}^N$ in (3.116) instead of $\Delta \mathbf{p}_{f,mech}^{N+1}$, there is always a difference of pore pressure in seepage and mechanical fields. Therefore, iterative method is not adopted for undrained split scheme. Instead, incremental update method is preferred by enforcing sufficiently small mechanical time step size. A general convention adopted in the current study is that

$$\Delta t = \frac{\Delta t_p}{100}. \quad (3.117)$$

3.6.2 Fixed-Stress Split Scheme

Modified Mass Balance Equation

To recap, the mass balance equation (2.45) is given by

$$\alpha \frac{\partial \bar{\varepsilon}_v}{\partial t} + \left(\frac{n}{K_f} + \frac{\alpha - n}{K_s} \right) \frac{\partial p_f}{\partial t} = \nabla \cdot \left(\frac{\mathbf{K}}{\mu_f} (\nabla p_f - \rho_f \mathbf{g}) \right).$$

Using the principle of effective stress, the effective mean stress p' is introduced

$$p' = p + \alpha p_f, \quad (3.118)$$

so that

$$\begin{aligned} \varepsilon_v &= \frac{p'}{K'} = \frac{p}{K'} + \frac{\alpha p_f}{K'}; \\ \Rightarrow \alpha \frac{\partial \varepsilon_v}{\partial t} &= \frac{\alpha}{K'} \frac{\partial p}{\partial t} + \frac{\alpha^2}{K'} \frac{\partial p_f}{\partial t}, \end{aligned} \quad (3.119)$$

where p is the total mean stress and K' is the drained bulk modulus. By substitution, we then obtain the modified mass balance equation

$$\frac{\alpha}{K'} \frac{\partial p}{\partial t} + \left(\frac{n}{K_f} + \frac{\alpha - n}{K_s} + \frac{\alpha^2}{K'} \right) \frac{\partial p_f}{\partial t} = \nabla \cdot \left(\frac{\mathbf{K}}{\mu_f} (\nabla p_f - \rho_f \mathbf{g}) \right). \quad (3.120)$$

The equivalent element-wise spatially discretised version is given by

$$\mathbf{S} \frac{\partial \bar{\mathbf{p}}_f}{\partial t} + \mathbf{H} \bar{\mathbf{p}}_f + \mathbf{G} \frac{\partial \bar{p}}{\partial t} = \mathbf{f}_p, \quad (3.121)$$

where

$$\begin{aligned}
\mathbf{H} &= \int_{\Omega} (\nabla \mathbf{N}_p)^T \frac{\mathbf{K}}{\mu_f} (\nabla \mathbf{N}_p) dv; \\
\mathbf{S} &= \int_{\Omega} (\mathbf{N}_p)^T \mathbf{S} \mathbf{N}_p dv = \int_{\Omega} \mathbf{N}_p^T \left(\frac{n}{K_f} + \frac{\alpha - n}{K_s} + \frac{\alpha^2}{K'} \right) \mathbf{N}_p dv; \\
\mathbf{G} &= \frac{1}{K'} \mathbf{A} = \int_{\Omega} (\mathbf{N}_p)^T \frac{\alpha}{K'} dv; \\
\mathbf{f}_p &= \int_{\Omega} (\nabla \mathbf{N}_p)^T \frac{\mathbf{K}}{\mu_f} \rho_f \mathbf{g} dv - \int_{\partial\Omega} (\mathbf{N}_p)^T \frac{\tilde{\mathbf{Q}}_f}{\rho_f} da.
\end{aligned} \tag{3.122}$$

Using the same strategy of time discretisation, we obtain

$$\mathbf{S} \left(\frac{\bar{\mathbf{p}}_f^{K+1} - \bar{\mathbf{p}}_f^K}{\Delta t_p} \right) + \mathbf{H} \bar{\mathbf{p}}_f^{K+1} + \mathbf{G} \frac{\Delta \bar{p}^N}{\Delta t_p} = \mathbf{f}_p^{K+1}; \tag{3.123}$$

where subscript K denotes the current time in seepage field, and $\Delta \bar{p}^N$ represents the change of total mean stress over the previous mechanical time step.

Solution Update

In fixed stress split scheme, seepage field is also solved firstly using (3.123) over coarse time step size, followed by geomechanical field using fine time step sizes. In this split scheme, the assumption is that the computation of $\bar{\mathbf{p}}_f^{K+1}$ is based on the increment of total mean stress $\Delta \bar{p}^N$ of the last mechanical time step.

The drained bulk modulus K' , which appears in the storativity term S as $\frac{\alpha^2}{K'}$ and the \mathbf{G} matrix, is estimated by

$$K' = \frac{\Delta \bar{p}^N}{\Delta \varepsilon_v^N}. \tag{3.124}$$

With the seepage field pore pressure solution, a linear interpolation based on $\bar{\mathbf{p}}_f^{K+1}$ and $\bar{\mathbf{p}}_f^K$ is constructed for geomechanical field

$$\bar{\mathbf{p}}_{f,seepage}^{N+1} = (1 - f) \bar{\mathbf{p}}_f^K + f \bar{\mathbf{p}}_f^{K+1}. \tag{3.125}$$

Because no pore pressure is assumed to be generated by solid deformation in geomechanical field, we may have

$$\bar{\mathbf{p}}_f^{N+1} = \bar{\mathbf{p}}_{f,seepage}^{N+1}, \tag{3.126}$$

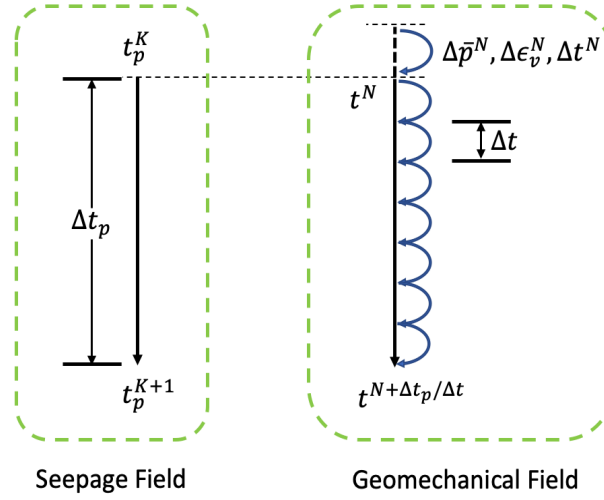


Fig. 3.3 Illustration of total mean stress increment $\Delta\bar{p}^N$ and volumetric strain increment $\Delta\epsilon_v^N$ over Δt^N for the computation of pore fluid pressure \bar{p}_f^{K+1} at the current mechanical step (t^{N+1})

which is then used in the current mechanical time step t^{N+1} to compute the current effective Cauchy stress tensor $\boldsymbol{\sigma}^{N+1}$.

When using fixed-stress algorithm, a performance issue may arise due to stress reversal. For example, the predictor algorithm of \bar{p}_f^{K+1} still assumes $\Delta\bar{p}^N$, while it should be $-\Delta\bar{p}^N$ in the current mechanical time step. To resolve this issue, fixed-stress split scheme should be implemented with iteration. Another issue is that, when the total mean stress p is predominantly dependent on pore pressure, significant change of effective stress will have small effect in the predictor algorithm of \bar{p}_f^{K+1} . In practice, however, hydraulic fracture will most likely to take place before the total mean stress becomes predominantly dependent on pore pressure. In this case, the enhanced hydraulic permeability along the fracture propagation path will help diffuse local excess pore pressure.

Chapter 4

Elastoplastic-fracture Constitutive Models for Pressure-Sensitive Geomaterials

4.1 Elastoplastic Constitutive Equations

Let¹ $\Phi(\boldsymbol{\sigma}, \mathbf{A})$ be a yield criteria function that maps any set of stress $\boldsymbol{\sigma}$ and thermodynamical hardening forces \mathbf{A} into a scalar value that defines elastic domain \mathcal{E} , plastically admissible domain $\bar{\mathcal{E}}$ and yield locus \mathcal{Y} as

$$\mathcal{E} = \{\boldsymbol{\sigma} | \Phi(\boldsymbol{\sigma}, \mathbf{A}) < 0\}; \quad (4.1)$$

$$\bar{\mathcal{E}} = \{\boldsymbol{\sigma} | \Phi(\boldsymbol{\sigma}, \mathbf{A}) \leq 0\}; \quad (4.2)$$

$$\mathcal{Y} = \{\boldsymbol{\sigma} | \Phi(\boldsymbol{\sigma}, \mathbf{A}) = 0\}, \quad (4.3)$$

where yield locus \mathcal{Y} is a set of stresses forming the boundary that lies exactly between admissible stress space (elastic domain) and inadmissible stress space.

Assuming initially elastic behaviour, if an incremental stress update results in $\Phi^{trial}(\boldsymbol{\sigma}, \mathbf{A}) > 0$, then it is required to bring the stress state back to the plastically admissible domain, such that²

$$\dot{\boldsymbol{\sigma}} = \mathbf{D}^e : (\dot{\boldsymbol{\epsilon}} - \dot{\boldsymbol{\epsilon}}^p), \quad (4.4)$$

¹For the convenience of notational brevity, effective stress tensor is hereby denoted by $\boldsymbol{\sigma}$ instead of $\boldsymbol{\sigma}'$.

²In the application, geomaterials are assumed to have small elastic domain. Therefore, the incremental strain tensor can be decomposed as $\dot{\boldsymbol{\epsilon}} = \dot{\boldsymbol{\epsilon}}^e + \dot{\boldsymbol{\epsilon}}^p$.

where $\dot{\boldsymbol{\epsilon}}$ is the incremental rate of total strain tensor and $\dot{\boldsymbol{\epsilon}}^p$ is the incremental rate of plastic strain tensor.

Using plastic flow rule, the plastic strain tensor is defined by

$$\dot{\boldsymbol{\epsilon}}^p = \dot{\gamma} \mathbf{N} = \dot{\gamma} \frac{\partial \Psi}{\partial \boldsymbol{\sigma}}, \quad (4.5)$$

where $\dot{\gamma}$ is the rate of plastic multiplier satisfying $\dot{\gamma} > 0$, and \mathbf{N} is the plastic flow vector derived from the derivative of a non-negative, convex plastic flow potential function $\Psi(\boldsymbol{\sigma}, \mathbf{A})$.

The dissipative mechanism associated with plastic deformation is characterised [54] by the evolution of internal variables $\boldsymbol{\alpha}$, such that

$$\dot{\boldsymbol{\alpha}} = \dot{\gamma} \mathbf{H} = -\dot{\gamma} \frac{\partial \Psi}{\partial \mathbf{A}}, \quad (4.6)$$

where \mathbf{H} is the generalised hardening modulus. Finally, the evolution of $\dot{\boldsymbol{\epsilon}}_p$ and $\dot{\boldsymbol{\alpha}}$ must be complemented by loading/unloading conditions

$$\Phi \leq 0, \quad \dot{\gamma} \geq 0, \quad \Phi \dot{\gamma} = 0. \quad (4.7)$$

4.2 Mohr-Coulomb Model

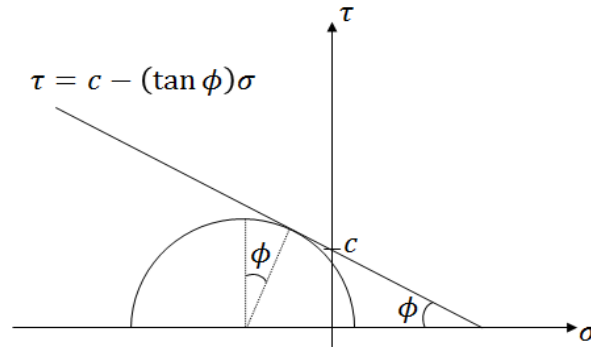
Mohr-Coulomb model is one of the classical, pressure-sensitive frictional model, which is mathematically represented by

$$\tau = c - \tan(\phi) \sigma, \quad (4.8)$$

where σ is the effective normal stress, c is the cohesion, and ϕ is the friction angle. The increase of shear strength due to the increase of compressive normal stress, as illustrated in Figure 4.1, is well explained by [160]. The density of porous material increases with compressive normal stress. The increase of density naturally increases the rolling and sliding friction between particle grains. As a result, the kinematic constraints become stricter due to particle interlocking condition. Therefore, the shear strength increases with normal stress. In general, the yield limit of Mohr-Coulomb model exhibits strong dependence on the hydrostatic pressure.

The yield function of Mohr-Coulomb can be alternatively expressed in principal stress space [54]

$$\Phi_{principal}^{MC} = (\sigma_1 - \sigma_3) + (\sigma_1 + \sigma_3) \sin \phi - 2c \cos \phi, \quad (4.9)$$

Fig. 4.1 Mohr-Coulomb yield surface $\tau - \sigma$ space

where $\sigma_1 > \sigma_2 > \sigma_3$, or in terms of stress invariants [131, 46]

$$\Phi_{invariant}^{MC} = \left(\cos \theta - \frac{1}{\sqrt{3}} \sin \theta \sin \phi \right) \sqrt{J_2(\mathbf{s})} + p(\boldsymbol{\sigma}) \sin \phi - c \cos \phi, \quad (4.10)$$

where \mathbf{s} is the deviatoric stress tensor defined by $\mathbf{s} = \boldsymbol{\sigma} - p\mathbf{I}$, J_2 is the second invariant of \mathbf{s} defined by $\frac{1}{2}\mathbf{s} : \mathbf{s}$, and $\theta \in [-\frac{\pi}{6}, \frac{\pi}{6}]$ is Lode angle. It will be shown (4.10) is useful in deriving tensile cut-off model in the later sections.

4.3 Drucker-Prager Model

Drucker-Prager model was proposed [61] as a smooth version of Mohr-Coulomb yield surface. Alternatively, it can also be interpreted as pressure-sensitive von Mises yield criteria since the yield surface radius as viewed on deviatoric plane changes with mean pressure p .

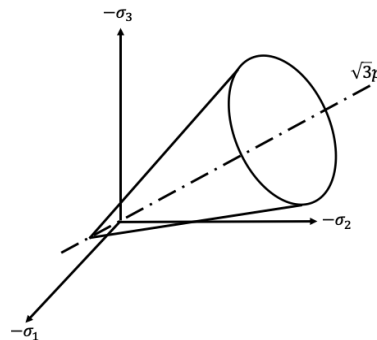


Fig. 4.2 Drucker-Prager yield surface in principal stress space

The mathematical expression is given by

$$\Phi_{std}^{DP}(\boldsymbol{\sigma}, \bar{c}) = \sqrt{J_2(\mathbf{s})} + \eta p - \bar{c}, \quad (4.11)$$

where η and \bar{c} are material parameters and the subscript std refers to “standard”. To fit the Mohr-Coulomb criterion, the Drucker-Prager model can be reformulated [54] as

$$\Phi_{std}^{DP}(\boldsymbol{\sigma}, c) = \sqrt{J_2(\mathbf{s})} + \eta p - \xi c. \quad (4.12)$$

If Drucker-Prager yield locus coincides with the outer edges of Mohr-Coulomb yield locus, then

$$\eta = \frac{6 \sin \phi}{\sqrt{3}(3 - \sin \phi)}; \quad \xi = \frac{6 \cos \phi}{\sqrt{3}(3 - \sin \phi)}. \quad (4.13)$$

Otherwise, if Drucker-Prager yield locus coincides with the inner edges of Mohr-Coulomb yield locus, then

$$\eta = \frac{6 \sin \phi}{\sqrt{3}(3 + \sin \phi)}; \quad \xi = \frac{6 \cos \phi}{\sqrt{3}(3 + \sin \phi)}. \quad (4.14)$$

It is also possible to predict Mohr-Coulomb yield criterion using Drucker-Prager model under plane strain conditions [34] via

$$\eta = \frac{3 \tan \phi}{\sqrt{9 + 12 \tan^2 \phi}}; \quad \xi = \frac{3}{\sqrt{9 + 12 \tan^2 \phi}}. \quad (4.15)$$

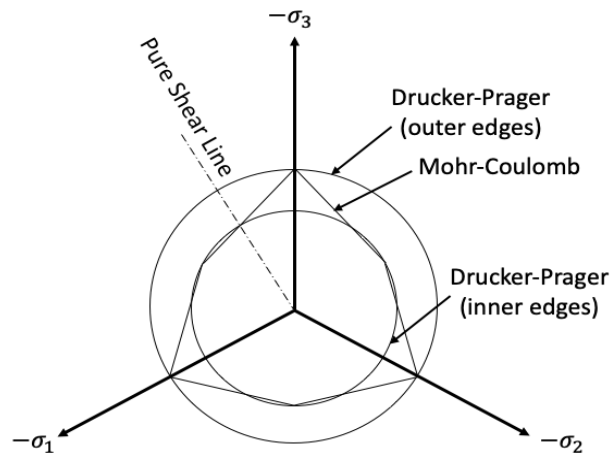


Fig. 4.3 Approximation of Drucker-Prager model to Mohr-Coulomb yield surface

4.4 Modified Drucker-Prager Model

4.4.1 Yield Function

As opposed to the circular geometry of yield surface on deviatoric plane (Figure 4.2), it has been observed that frictional material exhibits [3] non-circular geometry with rounded corners (Figure 4.4), which is also different from the standard Mohr-Coulomb model with sharp corners.

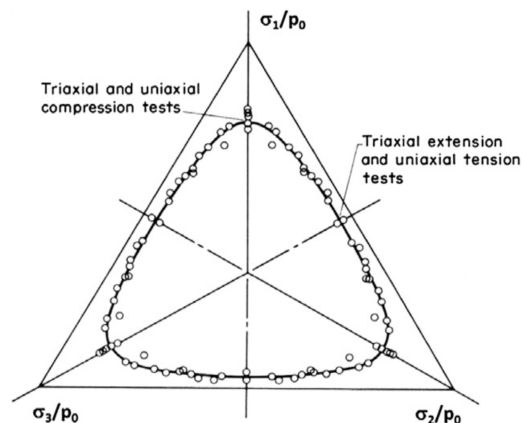


Fig. 4.4 Shape of yield locus for frictional materials on deviatoric plane [3]

In addition, other experimental evidence [187, 191] also show that yield surface corresponding to compressive triaxial test (CTC) is larger than the one corresponding to reduced triaxial test (RTE) (Figure 4.5).

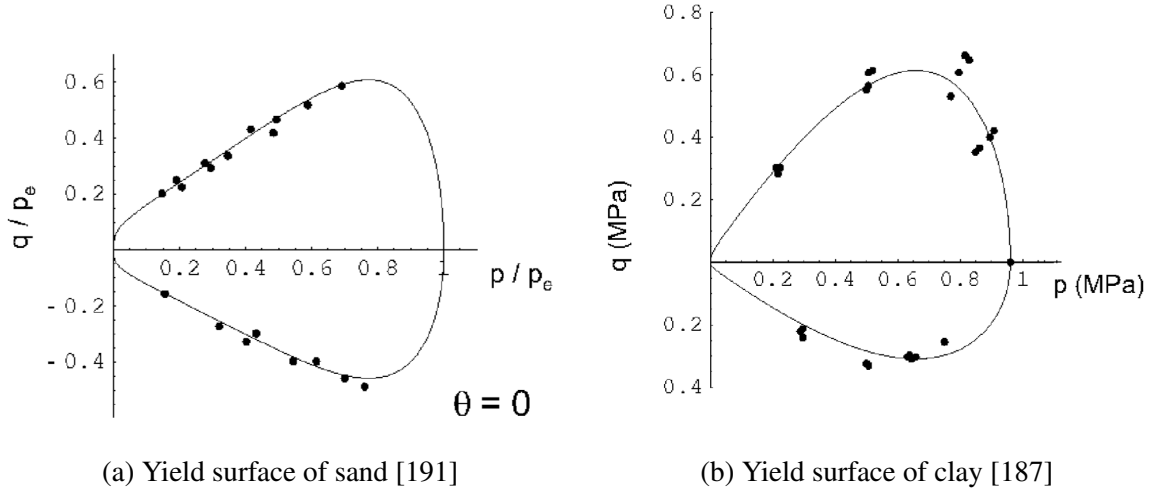


Fig. 4.5 Experimental findings that yield surface associated with CTC test ($q > 0$) is larger than that with RTE test ($q < 0$)

In view of the experimental findings, the standard Drucker-Prager yield function is modified, not only to take in account the changes of yield surface shape on deviatoric plane, but also the evolution of friction angle and cohesive strength as effective plastic strain accumulates. The modified Drucker-Prager yield function is given as follows

$$\Phi^{DP}(\boldsymbol{\sigma}, \bar{\epsilon}^p) = g(\theta, p)q + \tan \beta(\bar{\epsilon}^p)p - d(\bar{\epsilon}^p), \quad (4.16)$$

where β and d are, respectively, friction angle and cohesion in $p - q$ meridional plane, and $\bar{\epsilon}^p$ is the regularised accumulated effective plastic strain, defined [54] as

$$\dot{\bar{\epsilon}}^p = \sqrt{\frac{2}{3} \dot{\boldsymbol{\epsilon}}^p : \dot{\boldsymbol{\epsilon}}^p} = \sqrt{\frac{2}{3}} \|\dot{\boldsymbol{\epsilon}}^p\|. \quad (4.17)$$

Friction Angle and Cohesion in Meridional Plane

In terms of effective deviatoric stress q , the modified Drucker-Prager yield locus is obtained by setting $\Phi^{DP} = 0$

$$g(\theta, p)q = -(\tan \beta)p + d. \quad (4.18)$$

The friction angle β and cohesion d can then be determined using the assumption made with respect to the Mohr-Coulomb yield criterion.

If the Drucker-Prager yield locus coincides with the outer edges of the Mohr-Coulomb yield locus, then

$$\eta = \frac{6 \sin \phi}{\sqrt{3}(3 - \sin \phi)}; \quad \xi = \frac{6 \cos \phi}{\sqrt{3}(3 - \sin \phi)}. \quad (4.19)$$

By substituting into the standard Drucker-Prager model, we have

$$\begin{aligned} \Phi_{std}^{DP} &= \sqrt{J_2(\mathbf{s}(\boldsymbol{\sigma}))} + \eta p(\boldsymbol{\sigma}) - \xi c \\ &= \sqrt{J_2(\mathbf{s}(\boldsymbol{\sigma}))} + \left(\frac{6 \sin \phi}{\sqrt{3}(3 - \sin \phi)} \right) p(\boldsymbol{\sigma}) - \left(\frac{6 \cos \phi}{\sqrt{3}(3 - \sin \phi)} \right) c. \end{aligned} \quad (4.20)$$

Then, by setting $\Phi_{std}^{DP} = 0$ and multiplying the equation above with a factor $\sqrt{3}$, we utilize the relation $q = \sqrt{3}J_2$ to obtain

$$q = -\frac{6 \sin \phi}{3 - \sin \phi} p + \frac{6 \cos \phi}{3 - \sin \phi} c. \quad (4.21)$$

By setting³ $g = 1$ and comparing (4.18) and (4.21), we obtain

$$\boxed{\beta = \tan^{-1} \left[\frac{6 \sin \phi}{3 - \sin \phi} \right]; \quad d = \frac{6 \cos \phi}{3 - \sin \phi} c.} \quad (4.22)$$

An alternative way of deriving the above relation is to start from the invariant representation of the Mohr-Coulomb yield function [131, 47]

$$\Phi_{invariant}^{MC} = \left(\cos \theta - \frac{1}{\sqrt{3}} \sin \theta \sin \phi \right) \sqrt{J_2(\mathbf{s})} + p(\boldsymbol{\sigma}) \sin \phi - c \cos \phi. \quad (4.23)$$

Similarly, following the definition of $q = \sqrt{3}J_2$, the yield function above is pre-multiplied by $\sqrt{3}$ to produce

$$\Phi_{invariant}^{MC} = \left(\cos \theta - \frac{1}{\sqrt{3}} \sin \theta \sin \phi \right) q + \sqrt{3} p(\boldsymbol{\sigma}) \sin \phi - \sqrt{3} c \cos \phi, \quad (4.24)$$

from which we obtain

$$q = -\frac{\sqrt{3} \sin \phi}{\left(\cos \theta - \frac{1}{\sqrt{3}} \sin \theta \sin \phi \right)} p + \frac{\sqrt{3} \cos \phi}{\left(\cos \theta - \frac{1}{\sqrt{3}} \sin \theta \sin \phi \right)} c. \quad (4.25)$$

³When $g = 1$, the yield surface coincides with all outer edges of Mohr-Coulomb surface (i.e., pure compression stress state).

Lode angle $\theta = 30^\circ$ corresponds to the outer edges of Mohr-Coulomb yield surface (i.e., pure compression stress state). Therefore, by substituting this Lode angle value, we can recover the standard Drucker-Prager model which coincides with the outer edges of Mohr-Coulomb surface

$$q = -\frac{6 \sin \phi}{3 - \sin \phi} p + \frac{6 \cos \phi}{3 - \sin \phi} c.$$

Finally, similar procedure as demonstrated above can be repeated to unravel (4.22).

However, in some cases, the outer-edge assumption may perform poorly to obtain analytical result. For example, in a strip-footing example [54], it was found that this assumption predicts a limit load value that is 140% higher than Prandtl's solution, whereas the inner-edge assumption predicts 17% higher. The best candidate was the version of Drucker-Prager model that predicts identical limit load as Mohr-Coulomb criterion under plane strain conditions [34]. That is,

$$\eta = \frac{3 \tan \phi}{\sqrt{9 + 12 \tan^2 \phi}}; \xi = \frac{3}{\sqrt{9 + 12 \tan^2 \phi}}. \quad (4.26)$$

By substituting the material parameters using plane strain assumption, one obtains

$$\begin{aligned} \Phi(\boldsymbol{\sigma}, c) &= \sqrt{J_2(\mathbf{s}(\boldsymbol{\sigma}))} + \eta p(\boldsymbol{\sigma}) - \xi c \\ &= \sqrt{J_2(\mathbf{s}(\boldsymbol{\sigma}))} + \left(\frac{3 \tan \phi}{\sqrt{9 + 12 \tan^2 \phi}} \right) p(\boldsymbol{\sigma}) - \left(\frac{3}{\sqrt{9 + 12 \tan^2 \phi}} \right) c. \end{aligned} \quad (4.27)$$

Following the definition of $q = \sqrt{3J_2}$, the yield function above is pre-multiplied by $\sqrt{3}$ to produce

$$q = - \left(\frac{3\sqrt{3} \tan \phi}{\sqrt{9 + 12 \tan^2 \phi}} \right) p(\boldsymbol{\sigma}) + \left(\frac{3\sqrt{3}}{\sqrt{9 + 12 \tan^2 \phi}} \right) c. \quad (4.28)$$

In comparison⁴ with (4.18) when $g = 1$, we arrive at

$$\beta = \tan^{-1} \left[\frac{3\sqrt{3} \tan \phi}{\sqrt{9 + 12 \tan^2 \phi}} \right]; \quad d = \frac{3\sqrt{3}c}{\sqrt{9 + 12 \tan^2 \phi}}. \quad (4.29)$$

⁴In this strip footing benchmark problem, the variable g is specifically set as 1 throughout the simulation to approach the analytical solution.

π -plane Correction Factor

The $g(\theta, p)$ factor is a π -plane correction term, which controls the radius of yield surface ($\rho_s = \|\mathbf{s}\|$) as viewed on deviatoric plane. Eekelen [170] reviewed expressions that were

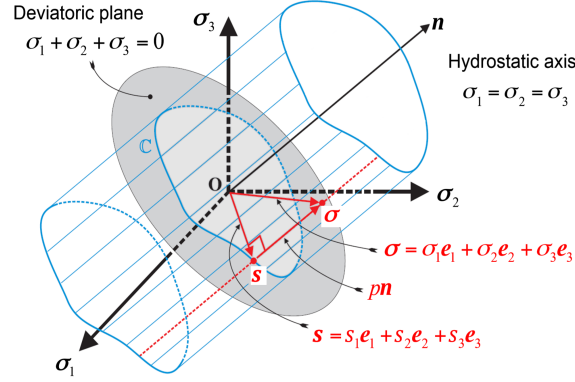


Fig. 4.6 Representation of multi-axial yield criterion in terms of principal stresses

proposed to correct the deviatoric term as function of Lode angle θ . A useful general expression is given by

$$g(\theta, p) = \left(\frac{1}{1 - \beta(p)} \left(1 + \beta(p) \frac{r^3}{q^3} \right) \right)^\alpha, \quad (4.30)$$

where α is material constant, $r^3 = \frac{27}{2} \det(\mathbf{s})$, $q = \sqrt{3J_2}$, and $\beta(p)$ is expressed in a similar way as [56]

$$\beta(p) = \beta_0 \exp\left(-\beta_1 \frac{p}{p_c}\right), \quad (4.31)$$

where β_0 and β_1 are material constants⁵, which define, respectively, the shape in deviatoric and meridional planes, and p_c is the pre-consolidation pressure. The parameters α , β_0 , and β_1 are obtained by fitting the experimental data.

It is clear that, since $p_c \rightarrow \infty$ for Drucker-Prager model, we obtain $\beta(p) = \beta_0$, indicating that the shape of Drucker-Prager yield surface in deviatoric plane is only dependent on the deviatoric part of stress tensor.

To demonstrate the effect of cohesion d and friction angle β , we first recognise that

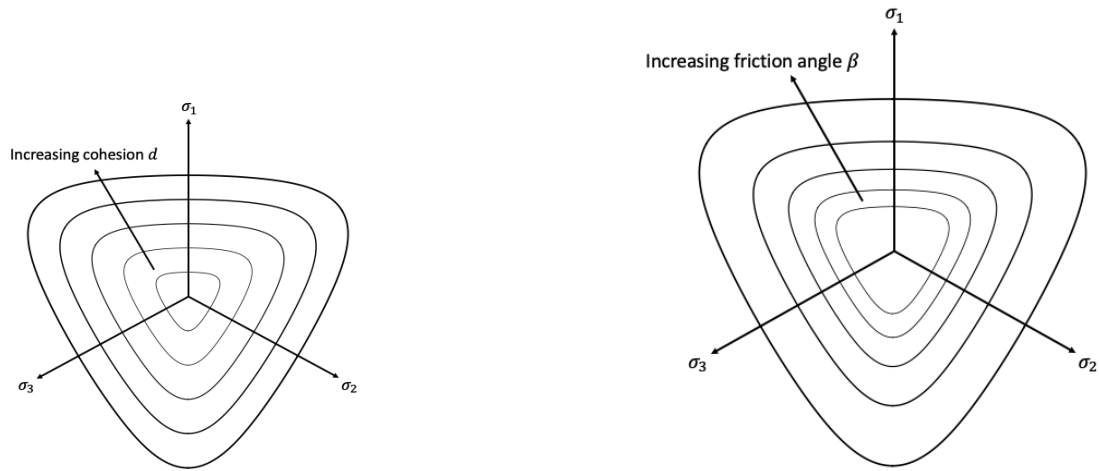
$$q = \sqrt{3J_2} = \sqrt{\frac{3}{2} \mathbf{s} : \mathbf{s}} = \sqrt{\frac{3}{2}} \|\mathbf{s}\| = \sqrt{\frac{3}{2}} \rho_s^{DP}. \quad (4.32)$$

⁵When $\beta_0 = 0$, $g = 1$. This value recovers the standard Drucker-Prager model, whereby the yield surface on deviatoric plane is circular with constant radius.

On the yield locus, we have $\Phi^{DP} = 0$. Then, an explicit expression of ρ_s^{DP} can be formulated as

$$\rho_s^{DP} = \sqrt{\frac{2}{3}}q = \sqrt{\frac{2}{3}} \left(\frac{d - \tan \beta (\bar{\epsilon}^p)p}{g(\theta, p)} \right). \quad (4.33)$$

Assuming $\alpha = 0.25$ and $\beta_0 = 0.60$, the effect of cohesion d and friction angle β on the geometry of the modified Drucker-Prager yield surface can be illustrated in Figure 4.7. It is clearly shown that, in deviatoric plane, the yield surface increases in size with cohesion and friction angle, while the shape does not change since $\beta(p) = \beta_0$ is always constant.



(a) Yield surface increases with cohesion.

(b) Yield surface increases with friction angle.

Fig. 4.7 Effect of cohesion d and friction angle β on the geometry of modified Drucker-Prager yield surface in deviatoric plane

It is noted that β_0 has to be carefully calibrated to avoid non-convexity, as illustrated in Figure 4.8

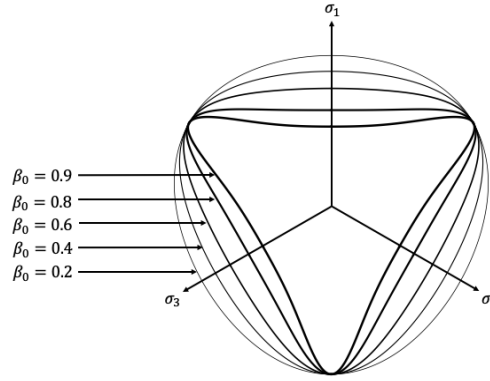


Fig. 4.8 Effect of β_0 on the yield surface geometry. Care should be taken when calibrating β_0 to avoid non-convexity of the yield locus.

4.4.2 Non-Associative Potential Plastic Flow Function

The plastic strain tensor is derived from a non-associative plastic flow potential

$$\dot{\boldsymbol{\epsilon}}^p = \dot{\gamma} \mathbf{N} = \dot{\gamma} \frac{\partial \Psi}{\partial \boldsymbol{\sigma}}, \quad (4.34)$$

where

$$\Psi(\boldsymbol{\sigma}, \bar{\boldsymbol{\epsilon}}^p) = q + \tan \psi (\bar{\boldsymbol{\epsilon}}^p) p - d(\bar{\boldsymbol{\epsilon}}^p). \quad (4.35)$$

It is clear that the potential function takes a similar form of the yield function, except that the friction angle is replaced by dilation angle ψ associated with plastic volumetric deformation, and that $g = 1$. Some experiments show that normality rule does not always apply. For example [189], in true triaxial tests of sand, it is demonstrated that the incremental direction of plastic flow tends more to be radial than normal to yield surface.

The plastic flow vector \mathbf{N} can be split into deviatoric and volumetric parts

$$\frac{\partial \Psi}{\partial \boldsymbol{\sigma}} = \frac{\partial \Psi}{\partial q} \frac{\partial q}{\partial \boldsymbol{\sigma}} + \frac{\partial \Psi}{\partial p} \frac{\partial p}{\partial \boldsymbol{\sigma}}. \quad (4.36)$$

From (4.35), we can directly determine

$$\frac{\partial \Psi}{\partial q} = 1; \quad \frac{\partial \Psi}{\partial p} = \tan \psi. \quad (4.37)$$

For $\frac{\partial p}{\partial \boldsymbol{\sigma}}$, it can be shown that⁶

$$\begin{aligned}\frac{\partial p}{\partial \boldsymbol{\sigma}} &= \frac{1}{3} \frac{\partial \text{Tr}(\boldsymbol{\sigma})}{\partial \boldsymbol{\sigma}} = \frac{1}{3} \frac{\partial \sigma_{kk}}{\partial \sigma_{mn}} (\mathbf{e}_m \otimes \mathbf{e}_n) \\ &= \frac{1}{3} \delta_{km} \delta_{kn} (\mathbf{e}_m \otimes \mathbf{e}_n) = \frac{1}{3} \delta_{mn} (\mathbf{e}_m \otimes \mathbf{e}_n) \\ &= \frac{1}{3} \mathbf{I}.\end{aligned}\quad (4.38)$$

The derivation of $\frac{\partial q}{\partial \boldsymbol{\sigma}}$ starts by expressing q in terms of $\boldsymbol{\sigma}$

$$\begin{aligned}q &= \sqrt{3J_2} = \sqrt{\frac{3}{2} (\mathbf{s} : \mathbf{s})} = \sqrt{\frac{3}{2} ((\boldsymbol{\sigma} - p\mathbf{I}) : (\boldsymbol{\sigma} - p\mathbf{I}))^{1/2}} \\ &= \sqrt{\frac{3}{2} (\boldsymbol{\sigma} : \boldsymbol{\sigma} - 2p \text{Tr}(\boldsymbol{\sigma}) + 3p^2)^{1/2}} \\ &= \sqrt{\frac{3}{2} \left(\boldsymbol{\sigma} : \boldsymbol{\sigma} - \frac{2}{3} (\text{Tr}(\boldsymbol{\sigma}))^2 + \frac{1}{3} (\text{Tr}(\boldsymbol{\sigma}))^2 \right)^{1/2}} \\ &= \sqrt{\frac{3}{2} \left(\boldsymbol{\sigma} : \boldsymbol{\sigma} - \frac{1}{3} (\text{Tr}(\boldsymbol{\sigma}))^2 \right)^{1/2}}.\end{aligned}\quad (4.39)$$

It then follows that

$$\begin{aligned}\frac{\partial q}{\partial \boldsymbol{\sigma}} &= \sqrt{\frac{3}{2}} \left(\frac{1}{2} \right) \left(\underbrace{\boldsymbol{\sigma} : \boldsymbol{\sigma} - \frac{1}{3} (\text{Tr}(\boldsymbol{\sigma}))^2}_{\mathbf{s}:\mathbf{s}} \right)^{-1/2} \left(\underbrace{\frac{\partial (\boldsymbol{\sigma} : \boldsymbol{\sigma})}{\partial \boldsymbol{\sigma}}}_{2\boldsymbol{\sigma}} - \underbrace{\frac{1}{3} \frac{\partial (\text{Tr}(\boldsymbol{\sigma}))^2}{\partial \text{Tr}(\boldsymbol{\sigma})}}_{\frac{2}{3}\text{Tr}(\boldsymbol{\sigma})} \underbrace{\frac{\partial \text{Tr}(\boldsymbol{\sigma})}{\partial \boldsymbol{\sigma}}}_{\mathbf{I}} \right) \\ &= \sqrt{\frac{3}{2}} \left(\frac{1}{2} \right) \frac{1}{(\mathbf{s} : \mathbf{s})^{1/2}} (2\mathbf{s}) = \sqrt{\frac{3}{2}} \frac{\mathbf{s}}{\|\mathbf{s}\|}.\end{aligned}\quad (4.40)$$

Since $J_2 = \frac{1}{2} (\mathbf{s} : \mathbf{s})$, we can express

$$\begin{aligned}\sqrt{J_2} &= \frac{1}{\sqrt{2}} (\mathbf{s} : \mathbf{s})^{1/2} = \frac{1}{\sqrt{2}} \|\mathbf{s}\|; \\ \Rightarrow \|\mathbf{s}\| &= \sqrt{2J_2},\end{aligned}\quad (4.41)$$

⁶ $\text{Tr}(\boldsymbol{\sigma})$ represents trace operator acting on tensor $\boldsymbol{\sigma}$

and so,

$$\frac{\partial q}{\partial \boldsymbol{\sigma}} = \sqrt{\frac{3}{2}} \frac{\mathbf{s}}{\|\mathbf{s}\|} = \frac{1}{2} \sqrt{\frac{3}{J_2}} \mathbf{s}. \quad (4.42)$$

By substitution, the plastic flow vector \mathbf{N} can be simplified to

$$\begin{aligned} \mathbf{N} &= \frac{\partial \Psi}{\partial \boldsymbol{\sigma}} = \frac{\partial \Psi}{\partial q} \frac{\partial q}{\partial \boldsymbol{\sigma}} + \frac{\partial \Psi}{\partial p} \frac{\partial p}{\partial \boldsymbol{\sigma}} \\ &= \frac{1}{2} \sqrt{\frac{3}{J_2}} \mathbf{s} + \frac{\tan \psi}{3} \mathbf{I} \\ &= \mathbf{N}_d + N_v \mathbf{I}. \end{aligned} \quad (4.43)$$

Finally, the plastic strain tensor for the modified Drucker-Prager model is obtained as

$$\begin{aligned} \dot{\boldsymbol{\epsilon}}^p &= \dot{\gamma} \mathbf{N} = \dot{\gamma} \mathbf{N}_d + \dot{\gamma} N_v \mathbf{I} \\ &= \frac{\dot{\gamma}}{2} \sqrt{\frac{3}{J_2}} \mathbf{s} + \frac{1}{3} \dot{\gamma} \tan \psi \mathbf{I} \\ &= \dot{\boldsymbol{\epsilon}}_d^p + \frac{1}{3} \dot{\boldsymbol{\epsilon}}_v^p \mathbf{I}. \end{aligned} \quad (4.44)$$

4.4.3 Hardening Law

Following [54] the derivation for the standard Drucker-Prager and Mohr-Coulomb models, cohesion $d \in \mathbf{A}$ is taken as the thermodynamical force, while the accumulated effective plastic strain $\bar{\boldsymbol{\epsilon}}^p \in \boldsymbol{\alpha}$ is taken as the hardening internal variable. Using the definition of hardening law, we express

$$\dot{\bar{\boldsymbol{\epsilon}}}^p = -\dot{\gamma} \frac{\partial \Psi}{\partial d} = -\dot{\gamma}(-1) = \dot{\gamma}. \quad (4.45)$$

For the modified Drucker-Prager model, the cohesion, friction angle and dilation angle are input by the user as function of $\bar{\boldsymbol{\epsilon}}^p$, such that

$$d \equiv d(\bar{\boldsymbol{\epsilon}}^p); \quad (4.46)$$

$$\beta \equiv \beta(\bar{\boldsymbol{\epsilon}}^p); \quad (4.47)$$

$$\psi \equiv \psi(\bar{\boldsymbol{\epsilon}}^p). \quad (4.48)$$

4.4.4 Regularisation of State Variables

Concomitant with the large scale evolution of geological structure is the development and propagation of strain localization in the form of shear bands or faults. However, when modelling post-localization evolution using the standard continuum method, the localization band width is found to be sensitive to the mesh size, rather than the material length scale. Furthermore, the fault propagation is also found to be aligned with element edges. Several methods have been proposed to solve the aforementioned issues, including gradient plasticity method and Cosserat continuum method.

In the current work, a regularisation method based on fracture energy approach [135, 11, 50] is adopted. The key is to ensure finite energy dissipation during softening, regardless of the element size. This is achieved by regularising the effective plastic strain

$$\bar{\epsilon}^{p,e} = \bar{\epsilon}^{p,m} \left(\frac{l_c^m}{l_c^e} \right)^n, \quad (4.49)$$

where $\bar{\epsilon}^{p,e}$ and $\bar{\epsilon}^{p,m}$ are, respectively, the regularised and unregularised effective plastic strain, l_c^e is the characteristic element length, l_c^m is the characteristic material length, and n is the material constant (generally $0.6 \leq n \leq 1.0$).

This expression, along with an illustrative examples in Figure 4.9, implies that the softening slope becomes steeper as the element size increases. Such change is consistent with the requirement that the dissipated energy is independent of the element size. For instance, in order to maintain the same energy dissipation in the failure zone, elements with larger volume undergoes smaller strain associated with the deformation while elements with smaller volume undergoes larger strain associated with the deformation.

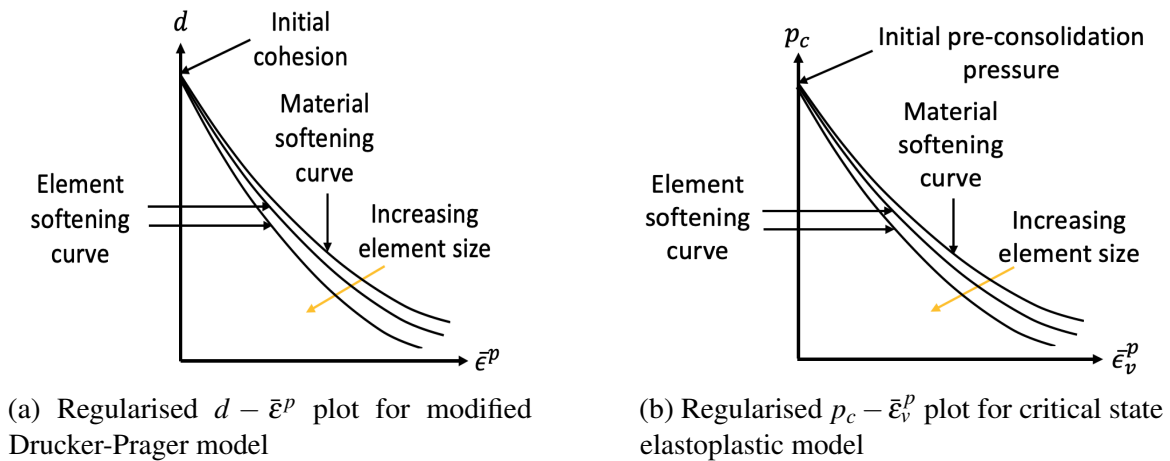


Fig. 4.9 Regularisation of cohesion-effective plastic strain (left) and preconsolidation pressure-volumetric plastic strain (right) softening slopes under the influence of element sizes

The value of characteristic material length l_c^m is dependent on the simulation scale. For cases where the characteristic deformation scale of the simulation is of the same order as the deformation scale of the experimental test (e.g. wellbore stability analysis), the characteristic length corresponds to the width of a single shear band (e.g. 2 – 3mm). On the other hand, in large scale simulation, where the deformation scale is many orders of magnitude greater than the experimental scale (e.g. the effect of up-scaling), the characteristic length for mesh regularisation is not the length associated with a single fracture, but associated with the fault zone. This provides a characteristic length that is the same order as the element discretization.

The advantages of using the fracture energy approach are that

- Mesh invariance of the global energy dissipation is approximately maintained within an acceptable range of element size.
- The approach may be implemented to regularize both mode I and mode II localization.
- It is straightforward to implement within any finite strain framework and for a range of constitutive models

The limitation of the method is that localization width should be equal or less than the characteristic length of the finite elements (i.e. strictly for sub- h and iso- h models). Nonetheless, it has been shown [50] that the aforementioned regularisation strategy correctly reproduces the size effects⁷ in mode II localization (Figure 4.10) in the simulation of thick-wall cylinder tests for Berea sandstone and Castlegate sandstone.

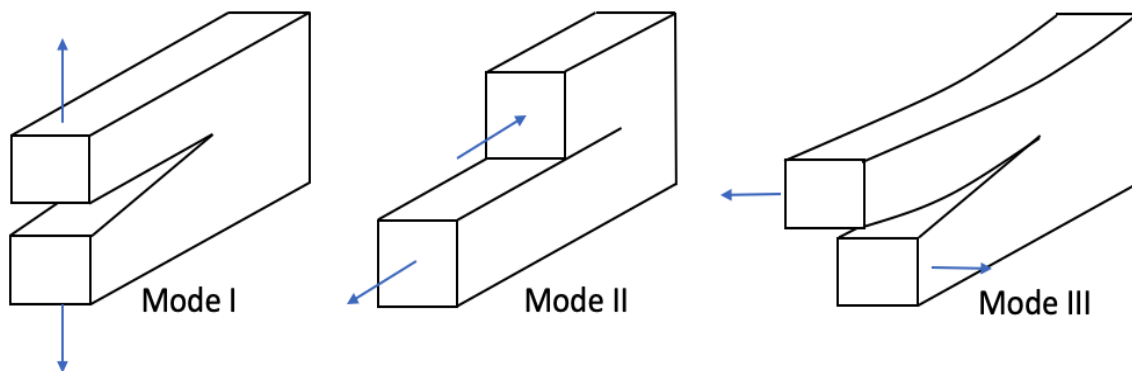


Fig. 4.10 Two fracture modes. Mode I is characterised by fracture opening mode via tensile failure. Mode II is characterised by shearing mode over fracture surface. Mode III is characterised by tearing mode.

⁷the sample internal radii ranges from 8mm to 200mm

4.5 SR4 Model

4.5.1 Yield Functions

SR4 model [49] is a critical state elastoplastic model (Figure 4.11) that is composed of two functions, which continuously intersect at the maximum deviatoric stress $q_{\Phi_{peak}}$. The shear (or dilation) side is defined by SR3 surface [50], while the compression side is defined by an ellipse in a similar manner with the standard Cam-Clay model [187].

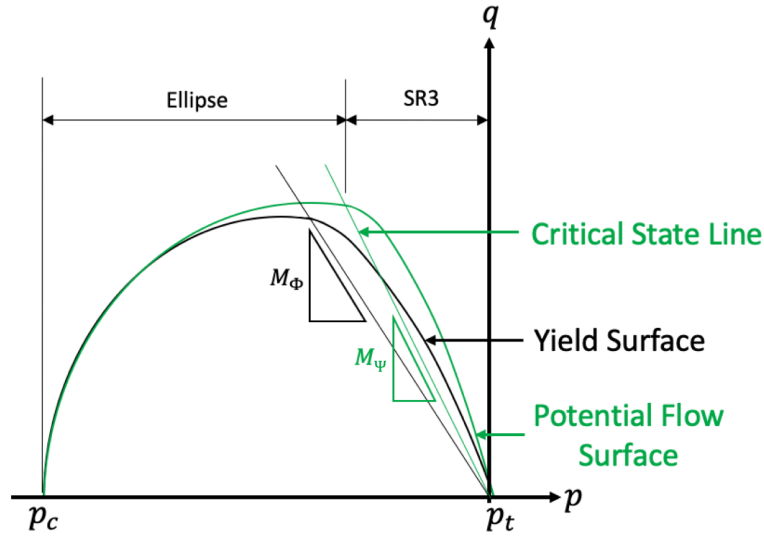


Fig. 4.11 Illustration of SR4 model in $p - q$ plane

The shear side of SR4 model is given by the SR3 surface

$$\Phi_{shear}^{SR4}(\boldsymbol{\sigma}, \boldsymbol{\varepsilon}_v^p) = g(\theta, p)q + (p - p_t) \tan \beta \left(\frac{p - p_c}{p_t - p_c} \right)^{1/n}, \quad (4.50)$$

where p_t is the tensile intercept, p_c is the pre-consolidation pressure, β is the friction angle defined in meridional $p - q$ plane, and n is a material constant.

The hydrostatic stress value corresponding to $q_{\Phi_{peak}}$ is denoted by $p_{\Phi_{peak}}$, which can be derived by enforcing $\left. \frac{\partial q}{\partial p} \right|_{p=p_{\Phi_{peak}}} = 0$. We start by setting $\Phi_{shear}^{SR4} = 0$ to yield

$$q = -\frac{p - p_t}{g} \tan \beta \left(\frac{p - p_c}{p_t - p_c} \right)^{1/n}, \quad (4.51)$$

from which

$$\frac{\partial q}{\partial p} = -\frac{\left(\frac{p_c - p}{p_c - p_t}\right)^{1/n} (p + \eta p - \eta p_c - p_t) \tan \beta}{g \eta (p - p_c)}, \quad (4.52)$$

so that, for $\left.\frac{\partial q}{\partial p}\right|_{p=p_{\Phi peak}} = 0$, we obtain

$$p_{\Phi peak} = \frac{\eta p_c + p_t}{1 + \eta}. \quad (4.53)$$

The corresponding $q_{\Phi peak}$ is then

$$gq = q_{\Phi peak} = -(p_{\Phi peak} - p_t) \tan \beta \left(\frac{p_{\Phi peak} - p_c}{p_t - p_c}\right)^{1/n}. \quad (4.54)$$

Then, using the expressions for $p_{\Phi peak}$ and $q_{\Phi peak}$ as well as the relation $p_{\Phi peak} = \frac{\eta p_c + p_t}{1 + \eta}$, we define

$$\begin{aligned} M_{\Phi} &= \frac{q_{\Phi peak}}{p_{\Phi peak}} = -\frac{p_{\Phi peak} - p_t}{p_{\Phi peak}} \tan \beta \left(\frac{p_{\Phi peak} - p_c}{p_t - p_c}\right)^{1/n} \\ &= -\frac{\eta(p_c - p_t)(\eta + 1)^{-\frac{1}{n}}}{\eta p_c + p_t} \tan \beta. \end{aligned} \quad (4.55)$$

Note that the denominator is simply $\eta p_c + p_t = (1 + \eta)p_{\Phi peak}$, and the term $\eta(p_c - p_t)$ in the numerator is alternatively expressed as follows

$$\begin{aligned} \eta p_c + p_t &= \eta p_c + p_t - \eta p_t + \eta p_t \\ &= \eta(p_c - p_t) + (1 + \eta)p_t \\ &= (1 + \eta)p_{\Phi peak} \\ \Rightarrow \eta(p_c - p_t) &= (1 + \eta)(p_{\Phi peak} - p_t). \end{aligned} \quad (4.56)$$

It follows that the expression for M_{Φ} can be further simplified to

$$\begin{aligned} M_{\Phi} &= -\frac{\eta(p_c - p_t)(\eta + 1)^{-\frac{1}{n}}}{\eta p_c + p_t} \tan \beta \\ &= -\frac{(1 + \eta)(p_{\Phi peak} - p_t)(\eta + 1)^{-\frac{1}{n}}}{(1 + \eta)p_{\Phi peak}} \tan \beta \\ &= -(\eta + 1)^{-\frac{1}{n}} \left(1 - \frac{p_t}{p_{\Phi peak}}\right) \tan \beta. \end{aligned} \quad (4.57)$$

On the compression side, the yield locus of the cap model is constructed from a general ellipse function

$$\frac{p^2}{a^2} + \frac{q^2}{b^2} = 1, \quad (4.58)$$

where a and b are the radii on p and q axes, respectively.

Since the center of the yield surface lies on the point $(p_{\Phi_{crit}}, 0)$, and in order to take into account of the π -plane correction term, the ellipse function then takes the form

$$\frac{(p - p_{\Phi_{peak}})^2}{a^2} + \frac{(gq)^2}{b^2} = 1. \quad (4.59)$$

Considering that the cap model is constructed for the compression side of the SR4 yield locus, the radius a can be conveniently formulated as

$$a = p_{\Phi_{peak}} - p_c, \quad (4.60)$$

whereas b is simply the maximum deviatoric stress of the yield surface, given by

$$b = q_{\Phi_{peak}} = M_{\Phi} p_{\Phi_{peak}}. \quad (4.61)$$

By rearranging the equations above, we obtain

$$\begin{aligned} (gq)^2 &= b^2 \left(1 - \frac{(p - p_{\Phi_{peak}})^2}{a^2} \right) \\ &= M_{\Phi}^2 p_{\Phi_{peak}}^2 \left(1 - \left(\frac{p - p_{\Phi_{peak}}}{p_{\Phi_{peak}} - p_c} \right)^2 \right), \end{aligned} \quad (4.62)$$

from which we can form the yield function of the SR4 cap model

$$\Phi_{cap}^{SR4}(\boldsymbol{\sigma}, \boldsymbol{\varepsilon}_v^p) = (gq)^2 - M_{\Phi}^2 p_{\Phi_{peak}}^2 \left(1 - \left(\frac{p - p_{\Phi_{peak}}}{p_{\Phi_{peak}} - p_c} \right)^2 \right) \quad (4.63)$$

It can be verified for the cap model yield locus that

$$\begin{aligned} \frac{\partial q}{\partial p} &= \frac{mp_{\Phi_{peak}}(p_{\Phi_{peak}} - p)}{(p_{\Phi_{peak}} - p_c)^2 g \sqrt{1 - \left(\frac{p_{\Phi_{peak}} - p}{p_{\Phi_{peak}} - p_c} \right)^2}} = 0 \\ \Rightarrow p &= p_{\Phi_{peak}}, \end{aligned} \quad (4.64)$$

which, substituted back into (4.62), recovers⁸

$$\begin{aligned} (gq)^2 &= q_{\Phi_{peak}}^2 = M_{\Phi}^2 p_{\Phi_{peak}}^2; \\ \Rightarrow M_{\Phi} &= \frac{q_{\Phi_{peak}}}{p_{\Phi_{peak}}} \end{aligned} \quad (4.65)$$

To recap, the shear side of SR4 yield locus is given by

$$\Phi_{shear}^{SR4}(\boldsymbol{\sigma}, \boldsymbol{\varepsilon}_v^p) = gq + (p - p_t) \tan \beta \left(\frac{p - p_c}{p_t - p_c} \right)^{1/n}, \quad (4.66)$$

while the compression side of SR4 yield locus is given by⁹

$$\Phi_{cap}^{SR4} = gq - M_{\Phi} p_{\Phi_{peak}} \sqrt{1 - \left(\frac{p - p_{\Phi_{peak}}}{p_{\Phi_{peak}} - p_c} \right)^2}, \quad (4.68)$$

where

$$p_{\Phi_{peak}} = \frac{n p_c + p_t}{1 + n}; \quad (4.69)$$

$$M_{\Phi} = \frac{q_{\Phi_{peak}}}{p_{\Phi_{peak}}} = -(n + 1)^{-\frac{1}{n}} \left(1 - \frac{p_t}{p_{\Phi_{peak}}} \right) \tan \beta. \quad (4.70)$$

Friction Angle β under CTC Condition

Recall from the standard Drucker-Prager model that

$$\Phi_{std}^{DP}(\boldsymbol{\sigma}, \bar{c}) = q + \bar{\eta} p - \bar{\xi} c,$$

and if the yield locus coincides with the outer edges of Mohr-Coulomb yield locus, then

$$\bar{\eta} = \frac{6 \sin \phi}{3 - \sin \phi}; \quad \bar{\xi} = \frac{6 \cos \phi}{3 - \sin \phi}.$$

The coincidence with the outer edges of Mohr-Coulomb is a representation of conventional triaxial compression (CTC) condition, whereby the stress condition is described by

⁸In this case, $gq = q_{\Phi_{peak}}$.

⁹Since the yield locus is given by $\Phi_{cap}^{SR4} = 0$, the following expression

$$\Phi_{cap}^{SR4}(\boldsymbol{\sigma}, \boldsymbol{\varepsilon}_v^p) = (gq)^2 - M_{\Phi}^2 p_{\Phi_{peak}}^2 \left(1 - \left(\frac{p - p_{\Phi_{peak}}}{p_{\Phi_{peak}} - p_c} \right)^2 \right) = 0 \quad (4.67)$$

has been rearranged as (4.68).

$\sigma_1 > \sigma_2 = \sigma_3$. In SR4 model, the friction angle is estimated from CTC tests. In view of this, we require the function $q_{\Phi peak} = M_{\Phi} p_{\Phi peak}$ to be parallel with $q = -\bar{\eta} p + \bar{\xi} c$ in $p - q$ plane. Effectively, this means $-\bar{\eta} = M_{\Phi}$, which can be expanded as

$$-\frac{6 \sin \phi}{3 - \sin \phi} = -(\eta + 1)^{-\frac{1}{n}} \left(1 - \frac{p_t}{p_{\Phi peak}} \right) \tan \beta \quad (4.71)$$

to yield

$$\beta = \arctan \left[\frac{6k \sin \phi}{3 - \sin \phi} \right] \quad \text{or} \quad \phi = \arcsin \left[\frac{3 \tan \beta}{6k + \tan \beta} \right], \quad (4.72)$$

where

$$k = \frac{(\eta + 1)^{\frac{1}{n}}}{1 - \frac{p_t}{p_{\Phi peak}}}. \quad (4.73)$$

Yield Surface in Deviatoric Plane

Recall the π -plane correction factor

$$g(\theta, p) = \left(\frac{1}{1 - \beta(p)} \left(1 + \beta(p) \frac{r^3}{q^3} \right) \right)^{\alpha},$$

where α is material constant, $r^3 = \frac{27}{2} \det(\mathbf{s})$, $q = \sqrt{3J_2}$, and $\beta(p)$ is given by

$$\beta(p) = \beta_0 \exp \left(-\beta_1 \frac{p}{p_c} \right).$$

In the modified Drucker-Prager model, since $p_c \rightarrow \infty$, we have $\beta(p) \rightarrow \beta_0$, which is constant. Therefore, it is expected that the shape of the Drucker-Prager yield surface in deviatoric plane is unchanged. However, for SR4 model, the value of p_c is finite. Hence, its shape in deviatoric plane should be sensitive to the effective mean stress p , as described by the equation of $\beta(p)$.

Recall that, in deviatoric plane, the Lode angle-dependent radius of yield locus is given by $\rho = \sqrt{\frac{2}{3}} q$. So, for the shear side ($p \geq p_{\Phi peak}$), the corresponding radius is given by

$$\rho_{shear}^{SR4} = \sqrt{\frac{2}{3}} \left(\frac{p_t - p}{g(\theta, p)} \tan \beta \left(\frac{p - p_c}{p_t - p_c} \right)^{1/n} \right), \quad (4.74)$$

and for the compression side ($p \leq p_{\Phi peak}$), we have

$$\rho_{cap}^{SR4} = \sqrt{\frac{2}{3}} \left(\frac{M_{\Phi} p_{\Phi peak}}{g(\theta, p)} \sqrt{1 - \left(\frac{p - p_{\Phi peak}}{p_{\Phi peak} - p_c} \right)^2} \right). \quad (4.75)$$

Figure 4.12 shows the response of the shape of SR4 yield locus in deviatoric plane to the changes of effective mean stress p . The left figure is described by ρ_{cap}^{SR4} , while the right figure is described by ρ_{shear}^{SR4} . As p approaches tensile intercept p_t , the shape increasingly resembles triangle, whereas when p approaches preconsolidation pressure p_c , the shape becomes increasingly rounded. Either way, the size of the yield locus becomes smaller. The yield locus is the largest when $p = p_{\Phi crit}$, which is also observed in Figure 4.11.

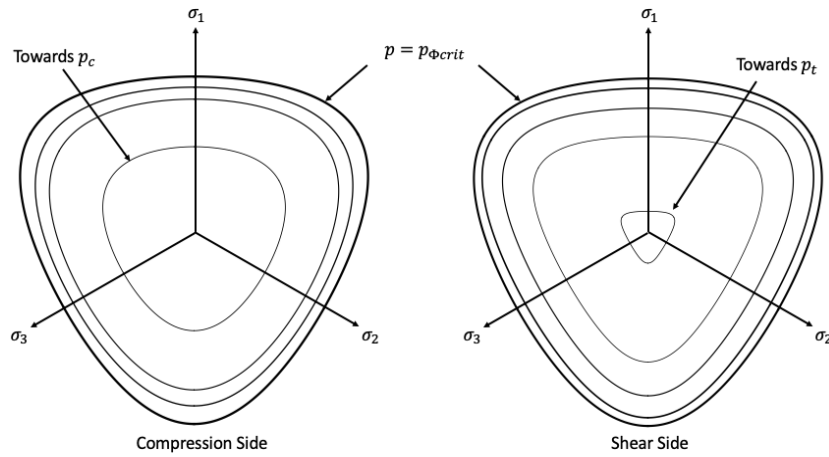


Fig. 4.12 The shape of SR4 yield locus in deviatoric plane is sensitive to the effective mean stress p . As p approaches p_t , the shape tends to be more triangular. Vice versa, as p approaches p_c , the shape tends to be more rounded. The size of yield locus is maximum when $p = p_{\Phi crit}$.

4.5.2 Non-Associative Potential Plastic Flow Functions

The potential flow function takes the similar form as yield function, except that the friction angle β is replaced by dilation angle ψ , and that the yield locus in deviatoric plane is circular (i.e. $g = 1$). Accordingly, for shear side, the SR4 potential function is given by

$$\Psi_{shear}^{SR4} = q + (p - p_t) \tan \psi \left(\frac{p - p_c}{p_t - p_c} \right)^{1/m}, \quad (4.76)$$

while the compression side of SR4 potential function is given by

$$\Psi_{cap}^{SR4} = q - M_{\Psi} p_{\Psi crit} \sqrt{1 - \left(\frac{p - p_{\Psi crit}}{p_{\Psi crit} - p_c} \right)^2}, \quad (4.77)$$

where

$$p_{\Psi crit} = \frac{m p_c + p_t}{1 + m} \quad (4.78)$$

$$M_{\Psi} = \frac{q_{\Psi crit}}{p_{\Psi crit}} = -(m + 1)^{-\frac{1}{m}} \left(1 - \frac{p_t}{p_{\Psi crit}} \right) \tan \psi, \quad (4.79)$$

with $M_{\Psi crit}$ as the slope of critical state line.

The plastic strain tensor is given by

$$\dot{\boldsymbol{\epsilon}}^p = \dot{\gamma} \mathbf{N} = \dot{\gamma} \frac{\partial \Psi}{\partial \boldsymbol{\sigma}},$$

where

$$\frac{\partial \Psi}{\partial \boldsymbol{\sigma}} = \frac{\partial \Psi}{\partial q} \frac{\partial q}{\partial \boldsymbol{\sigma}} + \frac{\partial \Psi}{\partial p} \frac{\partial p}{\partial \boldsymbol{\sigma}}.$$

It has already been shown in Section 4.4.2 that

$$\frac{\partial q}{\partial \boldsymbol{\sigma}} = \frac{1}{2} \sqrt{\frac{3}{J_2}} \mathbf{s}; \quad \frac{\partial p}{\partial \boldsymbol{\sigma}} = \frac{1}{3} \mathbf{I}.$$

The derivation of $\frac{\partial \Psi}{\partial q}$ and $\frac{\partial \Psi}{\partial p}$ depends on whether the potential function is on the shear side or the compression side. For the shear side,

$$\frac{\partial \Psi_{shear}^{SR4}}{\partial q} = 1; \quad (4.80)$$

$$\frac{\partial \Psi_{shear}^{SR4}}{\partial p} = \tan \psi \left(1 + \frac{1}{m} \left(\frac{p - p_t}{p - p_c} \right) \right) \left(\frac{p - p_c}{p_t - p_c} \right)^{1/m}. \quad (4.81)$$

The plastic strain tensor can then be expanded as

$$\begin{aligned} \dot{\boldsymbol{\epsilon}}^p &= \dot{\gamma} \left(\frac{\partial \Psi_{shear}^{SR4}}{\partial q} \frac{\partial q}{\partial \boldsymbol{\sigma}} + \frac{\partial \Psi_{shear}^{SR4}}{\partial p} \frac{\partial p}{\partial \boldsymbol{\sigma}} \right) \\ &= \frac{\dot{\gamma}}{2} \sqrt{\frac{3}{J_2}} \mathbf{s} + \frac{1}{3} \left(\dot{\gamma} \tan \psi \left(1 + \frac{1}{m} \left(\frac{p - p_t}{p - p_c} \right) \right) \left(\frac{p - p_c}{p_t - p_c} \right)^{1/m} \right) \mathbf{I} \\ &= \dot{\boldsymbol{\epsilon}}_d^p + \frac{1}{3} \dot{\epsilon}_v^p \mathbf{I}. \end{aligned} \quad (4.82)$$

For the compression side,

$$\frac{\partial \Psi_{cap}^{SR4}}{\partial q} = 1; \quad (4.83)$$

$$\frac{\partial \Psi_{cap}^{SR4}}{\partial p} = \frac{M_\Psi (p - p_{\Psi_{crit}}) p_{\Psi_{crit}}}{(p_c - p_{\Psi_{crit}})^2 \sqrt{1 - \left(\frac{p - p_{\Psi_{crit}}}{p_c - p_{\Psi_{crit}}} \right)^2}}. \quad (4.84)$$

The plastic strain tensor on the compression side is then given by

$$\begin{aligned} \dot{\boldsymbol{\epsilon}}^p &= \dot{\gamma} \left(\frac{\partial \Psi_{cap}^{SR4}}{\partial q} \frac{\partial q}{\partial \boldsymbol{\sigma}} + \frac{\partial \Psi_{cap}^{SR4}}{\partial p} \frac{\partial p}{\partial \boldsymbol{\sigma}} \right) \\ &= \frac{\dot{\gamma}}{2} \sqrt{\frac{3}{J_2}} \mathbf{s} + \frac{1}{3} \left(\dot{\gamma} \frac{M_\Psi (p - p_{\Psi_{crit}}) p_{\Psi_{crit}}}{(p_c - p_{\Psi_{crit}})^2 \sqrt{1 - \left(\frac{p - p_{\Psi_{crit}}}{p_c - p_{\Psi_{crit}}} \right)^2}} \right) \mathbf{I} \\ &= \dot{\boldsymbol{\epsilon}}_d^p + \frac{1}{3} \dot{\epsilon}_v^p \mathbf{I} \end{aligned} \quad (4.85)$$

To recap, on the shear side, the rate of deviatoric and volumetric plastic strains is expressed by

$$\dot{\boldsymbol{\epsilon}}_d^p = \frac{\dot{\gamma}}{2} \sqrt{\frac{3}{J_2}} \mathbf{s} = \dot{\gamma} \mathbf{N}_d; \quad (4.86)$$

$$\dot{\epsilon}_v^p = \dot{\gamma} \tan \psi \left(1 + \frac{1}{m} \left(\frac{p - p_t}{p - p_c} \right) \right) \left(\frac{p - p_c}{p_t - p_c} \right)^{1/m} = 3\dot{\gamma} N_v, \quad (4.87)$$

so that

$$\mathbf{N}_d = \frac{1}{2} \sqrt{\frac{3}{J_2}} \mathbf{s}; \quad (4.88)$$

$$N_v = \frac{\tan \psi}{3} \left(1 + \frac{1}{m} \left(\frac{p - p_t}{p - p_c} \right) \right) \left(\frac{p - p_c}{p_t - p_c} \right)^{1/m}. \quad (4.89)$$

On the compression side, we have

$$\dot{\boldsymbol{\epsilon}}_d^p = \frac{\dot{\gamma}}{2} \sqrt{\frac{3}{J_2}} \mathbf{s} = \dot{\gamma} \mathbf{N}_d; \quad (4.90)$$

$$\dot{\epsilon}_v^p = \dot{\gamma} \frac{M_\Psi (p - p_{\Psi \text{crit}}) p_{\Psi \text{crit}}}{(p_c - p_{\Psi \text{crit}})^2 \sqrt{1 - \left(\frac{p - p_{\Psi \text{crit}}}{p_c - p_{\Psi \text{crit}}} \right)^2}} = 3\dot{\gamma} N_v, \quad (4.91)$$

so that

$$\mathbf{N}_d = \frac{1}{2} \sqrt{\frac{3}{J_2}} \mathbf{s}; \quad (4.92)$$

$$N_v = \frac{M_\Psi (p - p_{\Psi \text{crit}}) p_{\Psi \text{crit}}}{3(p_c - p_{\Psi \text{crit}})^2 \sqrt{1 - \left(\frac{p - p_{\Psi \text{crit}}}{p_c - p_{\Psi \text{crit}}} \right)^2}},$$

where

$$p_{\Psi \text{crit}} = \frac{m p_c + p_t}{1 + m};$$

$$M_\Psi = \frac{q_{\Psi \text{crit}}}{p_{\Psi \text{crit}}} = -(m + 1)^{-\frac{1}{m}} \left(1 - \frac{p_t}{p_{\Psi \text{crit}}} \right) \tan \psi,$$

so that we can compute the rate of plastic strain tensor as

$$\dot{\boldsymbol{\epsilon}}^p = \dot{\gamma} (\mathbf{N}_d + N_v \mathbf{I}) = \dot{\boldsymbol{\epsilon}}_d^p + \frac{1}{3} \dot{\epsilon}_v^p \mathbf{I}. \quad (4.93)$$

4.5.3 Hardening Law

In ParaGeo, there are two methods to describe the evolution of preconsolidation pressure p_c and tensile intercept p_t as functions of internal hardening variable, i.e. volumetric plastic strain ε_v^p . The first method relies on the empirical input in the form of data points, such that the value of p_c and p_t can be obtained via interpolation

$$p_c = p_c(\varepsilon_v^p); \quad (4.94)$$

$$p_t = p_t(\varepsilon_v^p). \quad (4.95)$$

The second method describes p_c and p_t using exponential functions in the following forms

$$p_c = p_{c0} \exp\left(-\frac{v\varepsilon_v^p}{\lambda - \kappa}\right); \quad (4.96)$$

$$p_t = p_{t0} \exp\left(-\frac{v\varepsilon_{v,max}^p}{\lambda - \kappa}\right), \quad (4.97)$$

where p_{c0} and p_{t0} are, respectively, initial preconsolidation pressure and tensile intercept, v is the specific volume, λ is the slope of the normal compression line, κ is the slope of the unloading-reloading line, and $\varepsilon_{v,max}^p$ is the maximum dilational volumetric plastic strain.

The specific volume v is the ratio between bulk volume and solid volume, given by

$$v = \frac{V_{bulk}}{V_s} = 1 + e = \frac{1}{1 - n}, \quad (4.98)$$

where e is the void ratio and n is the porosity.

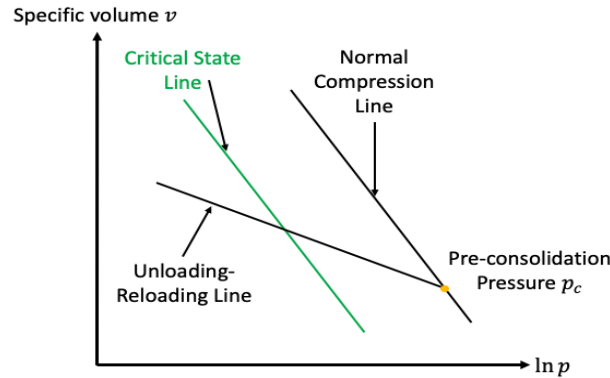


Fig. 4.13 Illustration of hardening/softening law, describing the evolution of specific volume as function of the natural logarithm of effective mean pressure p .

Unlike p_c , the tensile strength is treated as non-recoverable¹⁰ when the loading becomes compressive again. Therefore, $\varepsilon_{v,max}^p$ is used instead of ε_v^p in defining the hardening law of p_t . Preconsolidation pressure p_c and tensile intercept p_t are regularised accordingly as described in Section 4.4.4 to ensure local finite energy dissipation during the formation and propagation of shear bands.

In compaction-dominant field scale environment where sediments undergo large change in porosity, the volumetric strain associated with lower porosity material is expected to be smaller for a given effective mean pressure increment [84]. This phenomenon can be modelled using a p_c -dependent bulk modulus K equation [128]

$$K = K_0 + (1 + A_{un}) \frac{p_c}{\kappa} + A_{un} \frac{p'}{(1-n)\kappa}, \quad (4.99)$$

where K_0 is the bulk modulus at deposition, κ is the unloading-reloading slope, and A_{un} is the constant dependence factor.

4.6 Return Mapping Algorithm

4.6.1 Initial Value Problem

Let a motion be prescribed between a given time t_0 and the next instant of time T . Then, with respect to this motion, the small elastic strain tensor $\boldsymbol{\varepsilon}^e(t)$, hardening internal variables $\boldsymbol{\alpha}(t)$, and plastic multiplier rate $\dot{\gamma}$ are solved using the initial values of small elastic strain tensor $\boldsymbol{\varepsilon}^e(t_0)$, hardening internal variables $\boldsymbol{\alpha}(t_0)$, and the history of the total strain tensor $\boldsymbol{\varepsilon}(t)$ for $t \in [t_0, T]$ to satisfy the following elastoplastic constitutive equations:

$$\begin{aligned} \dot{\boldsymbol{\varepsilon}}^e(t) &= \dot{\boldsymbol{\varepsilon}}(t) - \dot{\gamma} \mathbf{N}(\boldsymbol{\sigma}(t), \mathbf{A}(t)); \\ \dot{\boldsymbol{\alpha}} &= \dot{\gamma} \mathbf{H}(\boldsymbol{\sigma}(t), \mathbf{A}(t)), \end{aligned} \quad (4.100)$$

subject to the constraints

$$\dot{\gamma} \geq 0, \quad \Phi(\boldsymbol{\sigma}(t), \mathbf{A}(t)) \leq 0, \quad \dot{\gamma} \Phi(\boldsymbol{\sigma}(t), \mathbf{A}(t)) = 0. \quad (4.101)$$

4.6.2 Incremental Constitutive Problem

In the current work, the initial value problem is solved using backward Euler method, which leads into incremental elastoplastic constitutive problem as stated in the following.

¹⁰unless a separate healing algorithm is called upon.

Let a motion be prescribed between a given time t^n and the next instant of time t^{n+1} , such that $\Delta t = t^{n+1} - t^n$ is defined as the time step of the time interval. Then, with respect to this motion, the current small elastic strain tensor $\boldsymbol{\varepsilon}^e(t^{n+1})$, hardening internal variables $\boldsymbol{\alpha}(t^{n+1})$, and plastic multiplier increment $\Delta\gamma$ are solved using the initial values of small elastic strain tensor $\boldsymbol{\varepsilon}^e(t^n)$, hardening internal variables $\boldsymbol{\alpha}(t^n)$, and the prescribed incremental total strain $\Delta\boldsymbol{\varepsilon}$ over Δt to satisfy the following system of algebraic equations

$$\begin{aligned}\boldsymbol{\varepsilon}^{e,n+1} &= \boldsymbol{\varepsilon}^{e,n} + \Delta\boldsymbol{\varepsilon} - \Delta\gamma\mathbf{N}(\boldsymbol{\sigma}^{n+1}, \mathbf{A}^{n+1}); \\ \boldsymbol{\alpha}^{n+1} &= \boldsymbol{\alpha}^n + \Delta\gamma\mathbf{H}(\boldsymbol{\sigma}^{n+1}, \mathbf{A}^{n+1}),\end{aligned}\quad (4.102)$$

subject to the constraints

$$\Delta\gamma \geq 0, \quad \Phi(\boldsymbol{\sigma}^{n+1}, \mathbf{A}^{n+1}) \leq 0, \quad \Delta\gamma\Phi(\boldsymbol{\sigma}^{n+1}, \mathbf{A}^{n+1}) = 0. \quad (4.103)$$

4.6.3 Decomposition of Stress Tensor into Deviatoric and Hydrostatic Components

Similar to plastic strain tensor, it is useful to deconstruct $\boldsymbol{\sigma}^{n+1}$ into its deviatoric and volumetric components. In the current work, geomaterials are assumed to have small elastic domain, and so they are treated to behave linearly elastic. By denoting \mathbb{C} as the fourth-order isotropic elasticity tensor, we expand the current stress tensor $\boldsymbol{\sigma}^{n+1}$ as¹¹

$$\begin{aligned}\boldsymbol{\sigma}^{n+1} &= \boldsymbol{\sigma}^n + \mathbb{C} : (\Delta\boldsymbol{\varepsilon}^{n+1/2} - \Delta\boldsymbol{\varepsilon}^{p,n+1/2}) \\ &= (\boldsymbol{\sigma}^n + \mathbb{C} : \Delta\boldsymbol{\varepsilon}^{n+1/2}) - \mathbb{C} : \Delta\boldsymbol{\varepsilon}^{p,n+1/2} \\ &= \boldsymbol{\sigma}^{trial,n+1} - \mathbb{C} : \Delta\boldsymbol{\varepsilon}^{p,n+1/2} \\ &= (\boldsymbol{s}^{trial,n+1} + p^{trial,n+1}\mathbf{I}) - 2G\Delta\gamma\mathbf{N}_d^{n+1} - 3K\Delta\gamma\mathbf{N}_v^{n+1}\mathbf{I} \\ &= (\boldsymbol{s}^{trial,n+1} - 2G\Delta\gamma\mathbf{N}_d^{n+1}) + (p^{trial,n+1} - 3K\Delta\gamma\mathbf{N}_v^{n+1})\mathbf{I} \\ &= \boldsymbol{s}^{n+1} + p^{n+1}\mathbf{I},\end{aligned}\quad (4.104)$$

from which we have formulated

$$\boldsymbol{s}^{n+1} = \boldsymbol{s}^{trial,n+1} - 2G\Delta\gamma\mathbf{N}_d^{n+1} \quad (4.105)$$

$$p^{n+1} = p^{trial,n+1} - 3K\Delta\gamma\mathbf{N}_v^{n+1} \quad (4.106)$$

¹¹The superscript $n+1/2$ implies time integration scheme using central difference method.

Since we use meridional $p - q$ plane to describe stress states and yield locus, it will be useful to derive an expression for q^{n+1} . We first note that

$$\begin{aligned} \mathbf{s}^{n+1} &= \mathbf{s}^{trial,n+1} - 2G\Delta\gamma\mathbf{N}_d^{n+1}; \\ &= \mathbf{s}^{trial,n+1} - G\Delta\gamma\sqrt{3} \left(\frac{1}{\sqrt{J_2^{n+1}}} \mathbf{s}^{n+1} \right). \end{aligned} \quad (4.107)$$

By utilising the relation $\sqrt{J_2^{n+1}} = \frac{1}{\sqrt{2}}\|\mathbf{s}^{n+1}\|$, we express

$$\frac{1}{\sqrt{J_2^{n+1}}} \mathbf{s}^{n+1} = \sqrt{2} \frac{\mathbf{s}^{n+1}}{\|\mathbf{s}^{n+1}\|}. \quad (4.108)$$

The term $\frac{\mathbf{s}^{n+1}}{\|\mathbf{s}^{n+1}\|}$ is the unit vector corresponding to the direction followed by the correction path of deviatoric stress tensor on deviatoric plane in the return-mapping algorithm. It is assumed that this direction is parallel to that of the trial stress state, i.e.

$$\frac{\mathbf{s}^{n+1}}{\|\mathbf{s}^{n+1}\|} = \frac{\mathbf{s}^{trial,n+1}}{\|\mathbf{s}^{trial,n+1}\|}. \quad (4.109)$$

Hence, we can express

$$\frac{1}{\sqrt{J_2^{n+1}}} \mathbf{s}^{n+1} = \sqrt{2} \frac{\mathbf{s}^{trial,n+1}}{\|\mathbf{s}^{trial,n+1}\|} = \frac{1}{\sqrt{J_2^{trial,n+1}}} \mathbf{s}^{trial,n+1}. \quad (4.110)$$

Substituting into (4.107), we obtain

$$\mathbf{s}^{n+1} = \mathbf{s}^{trial,n+1} \left(1 - \Delta\gamma G \sqrt{\frac{3}{J_2^{trial,n+1}}} \right). \quad (4.111)$$

Also, observe that the (4.107) can also be rearranged into

$$\mathbf{s}^{n+1} = \mathbf{s}^{trial,n+1} \left(\frac{1}{1 + \Delta\gamma G \sqrt{\frac{3}{J_2^{n+1}}}} \right). \quad (4.112)$$

Comparing (4.111) and (4.112), it is clear that

$$\left(1 - \Delta\gamma G \sqrt{\frac{3}{J_2^{trial,n+1}}}\right) \left(1 + \Delta\gamma G \sqrt{\frac{3}{J_2^{n+1}}}\right) = 1, \quad (4.113)$$

which can be expanded and simplified as

$$\begin{aligned} \Delta\gamma G \sqrt{\frac{3}{J_2^{n+1}}} - \Delta\gamma G \sqrt{\frac{3}{J_2^{trial,n+1}}} - (\Delta\gamma G)^2 \sqrt{\frac{3}{J_2^{n+1}}} \sqrt{\frac{3}{J_2^{trial,n+1}}} &= 0; \\ \frac{1}{\sqrt{J_2^{n+1}}} - \frac{1}{\sqrt{J_2^{trial,n+1}}} - \Delta\gamma G \frac{\sqrt{3}}{\sqrt{J_2^{n+1}} \sqrt{J_2^{trial,n+1}}} &= 0; \\ \sqrt{J_2^{n+1}} &= \sqrt{J_2^{trial,n+1}} - \Delta\gamma \sqrt{3} G. \end{aligned}$$

Since $q = \sqrt{3J_2}$, we now obtain

$$\begin{aligned} \sqrt{3J_2^{n+1}} &= \sqrt{3J_2^{trial,n+1}} - 3G\Delta\gamma; \\ \Rightarrow q^{n+1} &= q^{trial,n+1} - 3G\Delta\gamma. \end{aligned} \quad (4.114)$$

To recap,

$$\boxed{\begin{aligned} p^{n+1} &= p^{trial,n+1} - 3K\Delta\gamma N_v^{n+1} \\ q^{n+1} &= q^{trial,n+1} - 3G\Delta\gamma \end{aligned}}. \quad (4.115)$$

4.6.4 Modified Drucker-Prager Model

Smooth Return Algorithm

The consistency condition for the discrete form of modified Drucker-Prager yield function is given by

$$\Phi^{n+1} = gq^{n+1} + (\tan \beta^{n+1}) p^{n+1} - d^{n+1} = 0, \quad (4.116)$$

where the notation $^{n+1}$ denotes the updated incremental time step.

It is assumed that the π -plane correction factor g that is computed using trial stress state remains unchanged in return-mapping algorithm, i.e.

$$g^{trial} = g^{n+1}, \quad (4.117)$$

which is hereby denoted as g for notational brevity.

Then, by substituting the expressions for p^{n+1} and q^{n+1} into the consistency equations, we obtain

$$\Phi^{n+1} = g \left(q^{trial,n+1} - 3G\Delta\gamma \right) + (\tan \beta^{n+1}) \left(p^{trial,n+1} - \Delta\gamma K \tan \psi^{n+1} \right) - d^{n+1} = 0, \quad (4.118)$$

where the relation $N_v^{n+1} = \frac{\tan \psi^{n+1}}{3}$ has been applied.

To complete the equation, the hardening law is embedded to update the plastic state variables

$$\begin{aligned} d^{n+1} &= d(\bar{\epsilon}^{p,n+1}); \\ \beta^{n+1} &= \beta(\bar{\epsilon}^{p,n+1}); \\ \psi^{n+1} &= \psi(\bar{\epsilon}^{p,n+1}), \end{aligned} \quad (4.119)$$

where the hardening internal variable (i.e. effective plastic strain) is updated (4.45)

$$\bar{\epsilon}^{p,n+1} = \bar{\epsilon}^{p,n} + \Delta\gamma. \quad (4.120)$$

The full consistency equation for smooth return algorithm is then expressed by

$$\begin{aligned} \Phi^{n+1}(\Delta\gamma) &= g \left(q^{trial,n+1} - 3\Delta\gamma G \right) + \tan \beta(\bar{\epsilon}^{p,n} + \Delta\gamma) \left(p^{trial,n+1} - \Delta\gamma K \tan \psi(\bar{\epsilon}^{p,n} + \Delta\gamma) \right) \\ &\quad - d(\bar{\epsilon}^{p,n} + \Delta\gamma) = 0. \end{aligned} \quad (4.121)$$

The scalar function $\Phi^{n+1}(\Delta\gamma)$ is solved iteratively using standard Newton-Raphson method for the unknown incremental plastic multiplier $\Delta\gamma$, satisfying $\Delta\gamma > 0$. The derivative of $\Phi^{n+1}(\Delta\gamma)$ with respect to $\Delta\gamma$ is given by

$$\begin{aligned} \frac{\partial \Phi(\Delta\gamma)}{\partial \Delta\gamma} &= -3gG + \left(\frac{\partial \tan \beta}{\partial \beta} \frac{\partial \beta}{\partial \bar{\epsilon}^{p,n+1}} \frac{\partial \bar{\epsilon}^{p,n+1}}{\partial \Delta\gamma} \right) p^{n+1} + \tan \beta^{n+1} \\ &\quad \left(-K \tan \psi^{n+1} - \Delta\gamma K \frac{\partial \tan \psi}{\partial \psi} \frac{\partial \psi}{\partial \bar{\epsilon}^{p,n+1}} \frac{\partial \bar{\epsilon}^{p,n+1}}{\partial \Delta\gamma} \right) + \frac{\partial \Phi}{\partial d} \frac{\partial d}{\partial \bar{\epsilon}^{p,n+1}} \frac{\partial \bar{\epsilon}^{p,n+1}}{\partial \Delta\gamma} \quad (4.122) \\ &= -3gG + k_\beta p^{n+1} \sec^2 \beta - K \tan \beta^{n+1} (\tan \psi^{n+1} + k_\psi \Delta\gamma \sec^2 \psi) - k_d, \end{aligned}$$

where k_β , k_ψ and k_d are the slopes associated, respectively, with friction angle β , dilation angle ψ and cohesion d with respect to effective plastic strain $\bar{\epsilon}^p$.

Then, in the Newton-Raphson algorithm, the update during the i^{th} iteration is performed by

$$\begin{aligned}\Delta\gamma^{i+1} &= \Delta\gamma^i + \Delta(\Delta\gamma)|_{\Delta\gamma=\Delta\gamma^i} \\ &= \Delta\gamma^i - \left[\left(\frac{\partial\Phi(\Delta\gamma)}{\partial\Delta\gamma} \right)^{-1} \Phi(\Delta\gamma) \right]_{\Delta\gamma=\Delta\gamma^i}\end{aligned}\quad (4.123)$$

until $\text{Abs} [(\Phi(\Delta\gamma^{i+1}))] \leq \text{tolerance}$.

Apex Return Algorithm

If the smooth return algorithm yields $q^{n+1} < 0$, then the subroutine of apex return algorithm is required since, by definition, the effective deviatoric stress $q = \sqrt{3J_2}$ is always non-negative.

In apex return algorithm, the stress correction procedure is done solely on the axis of effective mean stress p , which corresponds only to the change of volumetric plastic strain $\Delta\varepsilon_v^p$. In view of this, we observe from plastic flow rule and hardening law that

$$\begin{aligned}\Delta\varepsilon_v^p &= \Delta\gamma \tan \psi; \\ \Delta\bar{\varepsilon}^p &= \Delta\gamma,\end{aligned}\quad (4.124)$$

from which we may form the relation

$$\Delta\varepsilon_v^p = \Delta\bar{\varepsilon}^p \tan \psi. \quad (4.125)$$

The resulting consistency equation for apex return algorithm is therefore given by

$$\Phi^{n+1}(\Delta\bar{\varepsilon}^p) = \tan \beta (\bar{\varepsilon}^{p,n} + \Delta\bar{\varepsilon}^p) \left(p^{trial,n+1} - K \Delta\bar{\varepsilon}^p \tan \psi (\bar{\varepsilon}^{p,n} + \Delta\bar{\varepsilon}^p) \right) - d (\bar{\varepsilon}^{p,n} + \Delta\bar{\varepsilon}^p) = 0. \quad (4.126)$$

This scalar function $\Phi^{n+1}(\Delta\bar{\varepsilon}^p)$ is solved iteratively using standard Newton-Raphson method for the unknown effective plastic strain $\Delta\bar{\varepsilon}^p$. The derivative of $\Phi^{n+1}(\Delta\bar{\varepsilon}^p)$ with

respect to $\Delta\bar{\epsilon}^p$ is given by

$$\begin{aligned} \frac{\partial\Phi(\Delta\bar{\epsilon}^p)}{\partial\Delta\bar{\epsilon}^p} &= \left(\frac{\partial \tan \beta}{\partial \beta} \frac{\partial \beta}{\partial \bar{\epsilon}^{p,n+1}} \frac{\partial \bar{\epsilon}^{p,n+1}}{\partial \Delta\bar{\epsilon}^p} \right) p^{n+1} + \tan \beta^{n+1} \\ &\quad \left(-K \tan \psi^{n+1} - K \Delta\bar{\epsilon}^p \frac{\partial \tan \psi}{\partial \psi} \frac{\partial \psi}{\partial \bar{\epsilon}^{p,n+1}} \frac{\partial \bar{\epsilon}^{p,n+1}}{\partial \Delta\bar{\epsilon}^p} \right) + \frac{\partial \Phi}{\partial d} \frac{\partial d}{\partial \bar{\epsilon}^{p,n+1}} \frac{\partial \bar{\epsilon}^{p,n+1}}{\partial \Delta\bar{\epsilon}^p} \\ &= k_\beta p^{n+1} \sec^2 \beta - K \tan \beta^{n+1} (\tan \psi^{n+1} + k_\psi \Delta\bar{\epsilon}^p \sec^2 \psi) - k_d. \end{aligned} \quad (4.127)$$

Then, in the Newton-Raphson algorithm, the update during the i^{th} iteration is performed by

$$\begin{aligned} \Delta\bar{\epsilon}^{p,i+1} &= \Delta\bar{\epsilon}^{p,i} + \Delta(\Delta\bar{\epsilon}^p)|_{\Delta\bar{\epsilon}^p=\Delta\bar{\epsilon}^{p,i}} \\ &= \Delta\bar{\epsilon}^{p,i} - \left[\left(\frac{\partial\Phi(\Delta\bar{\epsilon}^p)}{\partial\Delta\bar{\epsilon}^p} \right)^{-1} \Phi(\Delta\bar{\epsilon}^p) \right]_{\Delta\bar{\epsilon}^p=\Delta\bar{\epsilon}^{p,i}} \end{aligned} \quad (4.128)$$

until $\text{Abs}[(\Phi(\Delta\bar{\epsilon}^{p,i+1}))] \leq \text{tolerance}$.

In case of *critical state* condition, dilation angle $\psi = 0$. This state corresponds to a failure condition at which soil deformation takes place at zero volumetric plastic strain under continuous loading due to plastic failure. We may then assume that the cohesive strength is reduced to zero under this condition.

$$\psi = 0 \Leftrightarrow d = 0. \quad (4.129)$$

Note that, with the condition of $d^{n+1} = 0$, we only have one option left for the value of p^{n+1} in the consistency equation, and that is

$$p^{n+1} = p^{trial,n+1} - K \Delta\epsilon_v^p = 0; \quad (4.130)$$

$$\Rightarrow \Delta\epsilon_v^p = \frac{p^{trial,n+1}}{K}. \quad (4.131)$$

The effective plastic strain is then updated via

$$\bar{\epsilon}^{p,n+1} = \bar{\epsilon}^{p,n} + \Delta\gamma, \quad (4.132)$$

where

$$\Delta\gamma = \frac{q^{trial,n+1}}{3G}, \quad (4.133)$$

which is obtained from $q^{n+1} = 0$. The pseudocodes for the return-mapping algorithm are all listed in Appendix.

4.6.5 SR4 Model

Shear Side Return

The consistency condition for the discrete form of SR4 model yield function on the shear side requires that

$$\Phi_{shear}^{SR4,n+1} = gq^{n+1} + (p^{n+1} - p_t^{n+1}) \tan \beta \left(\frac{p^{n+1} - p_c^{n+1}}{p_t^{n+1} - p_c^{n+1}} \right)^{1/m} = 0, \quad (4.134)$$

which is solved along with

$$\begin{aligned} \Delta \varepsilon_v^p &= 3\Delta\gamma N_v^{n+1}; \\ N_v^{n+1} &= \frac{\tan \psi}{3} \left(1 + \frac{1}{m} \left(\frac{p^{n+1} - p_t^{n+1}}{p^{n+1} - p_c^{n+1}} \right) \right) \left(\frac{p^{n+1} - p_c^{n+1}}{p_t^{n+1} - p_c^{n+1}} \right)^{1/m}. \end{aligned}$$

By substituting the expressions for p^{n+1} and q^{n+1} into the equations above, we obtain

$$\begin{aligned} &\Phi_{shear}^{SR4,n+1}(\Delta\gamma, \Delta \varepsilon_v^p) \\ &= g \left(q^{trial,n+1} - 3G\Delta\gamma \right) + \left(p^{trial,n+1} - K\Delta \varepsilon_v^p - p_t^{n+1} \right) \tan \beta \left(\frac{p^{trial,n+1} - K\Delta \varepsilon_v^p - p_c^{n+1}}{p_t^{n+1} - p_c^{n+1}} \right)^{1/m} = 0, \end{aligned} \quad (4.135)$$

which is to be solved with function $f_{2,shear}(\Delta\gamma, \Delta \varepsilon_v^p, N_v^{n+1})$

$$f_{2,shear}(\Delta\gamma, \Delta \varepsilon_v^p, N_v^{n+1}) = \Delta \varepsilon_v^p - 3\Delta\gamma N_v^{n+1} = 0, \quad (4.136)$$

and function $f_{3,shear}(\Delta \varepsilon_v^p, N_v^{n+1})$

$$\begin{aligned} &f_{3,shear}(\Delta \varepsilon_v^p, N_v^{n+1}) \\ &= N_v^{n+1} - \frac{\tan \psi}{3} \left(1 + \frac{1}{m} \left(\frac{p^{trial,n+1} - K\Delta \varepsilon_v^p - p_t^{n+1}}{p^{trial,n+1} - K\Delta \varepsilon_v^p - p_c^{n+1}} \right) \right) \left(\frac{p^{trial,n+1} - K\Delta \varepsilon_v^p - p_c^{n+1}}{p_t^{n+1} - p_c^{n+1}} \right)^{1/m} = 0. \end{aligned} \quad (4.137)$$

The unknowns $\Delta\gamma, \Delta\epsilon_v^p, N_v^{n+1}$ are solved using Newton-Raphson method by iterating vector \mathbf{x} as follows

$$\mathbf{x}^{i+1} = \mathbf{x}^i - \left[\left(\frac{\partial \mathbf{f}}{\partial \mathbf{x}} \right)^{-1} \Delta \mathbf{x} \right]_{\mathbf{x}=\mathbf{x}^i}, \quad (4.138)$$

where

$$\mathbf{x} = \begin{Bmatrix} \Delta\gamma \\ \Delta\epsilon_v^p \\ N_v^{n+1} \end{Bmatrix}; \quad \mathbf{f} = \begin{Bmatrix} \Phi_{shear}^{SR4,n+1}(\Delta\gamma, \Delta\epsilon_v^p) \\ f_{2,shear}(\Delta\gamma, \Delta\epsilon_v^p, N_v^{n+1}) \\ f_{3,shear}(\Delta\epsilon_v^p, N_v^{n+1}) \end{Bmatrix}. \quad (4.139)$$

If the derivative of \mathbf{f} is given by

$$\frac{\partial \mathbf{f}}{\partial \mathbf{x}} = \begin{bmatrix} f_{1,1} & f_{1,2} & f_{1,3} \\ f_{2,1} & f_{2,2} & f_{2,3} \\ f_{3,1} & f_{3,2} & f_{3,3} \end{bmatrix}, \quad (4.140)$$

then its inverse is expressed by

$$\left(\frac{\partial \mathbf{f}}{\partial \mathbf{x}} \right)^{-1} = \mathbb{F} \begin{bmatrix} f_{2,2}f_{3,3} - f_{2,3}f_{3,2} & f_{1,3}f_{3,2} - f_{1,2}f_{3,3} & f_{1,2}f_{2,3} - f_{1,3}f_{2,2} \\ f_{3,1}f_{2,3} - f_{2,1}f_{3,3} & f_{1,1}f_{3,3} - f_{1,3}f_{3,1} & f_{1,3}f_{2,1} - f_{1,1}f_{2,3} \\ f_{2,1}f_{3,2} - f_{2,2}f_{3,1} & f_{1,2}f_{3,1} - f_{1,1}f_{3,2} & f_{1,1}f_{2,2} - f_{1,2}f_{2,1} \end{bmatrix}, \quad (4.141)$$

where

$$\mathbb{F} = \frac{1}{-f_{1,3}f_{2,2}f_{3,1} + f_{1,2}f_{2,3}f_{3,1} + f_{1,3}f_{2,1}f_{3,2} - f_{1,1}f_{2,3}f_{3,2} - f_{1,2}f_{2,1}f_{3,3} + f_{1,1}f_{2,2}f_{3,3}}. \quad (4.142)$$

The components of \mathbf{f} for the shear side of SR4 model are as follows¹²

$$\begin{aligned}
f_{1,1} &= \frac{\partial \Phi_{shear}^{SR4,n+1}}{\partial \Delta \gamma} = -3gG; \\
f_{1,2} &= \frac{\partial \Phi_{shear}^{SR4,n+1}}{\partial \Delta \varepsilon_v^p} \\
&= \frac{\tan \beta}{\mathfrak{n}(p_c^{n+1} - p_t^{n+1})^2} \left(\frac{K \Delta \varepsilon_v^p + p_c^{n+1} - p^{trial,n+1}}{p_c^{n+1} - p_t^{n+1}} \right)^{\frac{1-\mathfrak{n}}{\mathfrak{n}}} \\
&\left((K \Delta \varepsilon_v^p)^2 (k_{p_c} - k_{p_t}) + k_{p_c} (p_t^{n+1})^2 - k_{p_t} p_c^{n+1} (\mathfrak{n}(p_c^{n+1} - p_t^{n+1}) + p_t^{n+1}) \right. \\
&+ (-2k_{p_c} p_t^{n+1} + k_{p_t} (p_c^{n+1} + \mathfrak{n} p_c^{n+1} + p_t^{n+1} - \mathfrak{n} p_t^{n+1})) p^{trial,n+1} + (k_{p_c} - k_{p_t}) (p^{trial,n+1})^2 \\
&- K(p_c^{n+1} - p_t^{n+1}) (\mathfrak{n} p_c^{n+1} + p_t^{n+1} - (1 + \mathfrak{n}) p^{trial,n+1}) - K \Delta \varepsilon_v^p (K(1 + \mathfrak{n})(p_c^{n+1} - p_t^{n+1}) \\
&+ k_{p_t} (p_c^{n+1} + \mathfrak{n} p_c^{n+1} + p_t^{n+1} - \mathfrak{n} p_t^{n+1} - 2p^{trial,n+1}) + 2k_{p_c} (p^{trial,n+1} - p_t^{n+1})) \left. \right); \\
f_{1,3} &= \frac{\partial \Phi_{shear}^{SR4,n+1}}{\partial N_v^{n+1}} = 0; \\
f_{2,1} &= \frac{\partial f_{2,shear}}{\partial \Delta \gamma} = -3N_v^{n+1}; \\
f_{2,2} &= \frac{\partial f_{2,shear}}{\partial \Delta \varepsilon_v^p} = 1; \\
f_{2,3} &= \frac{\partial f_{2,shear}}{\partial N_v^{n+1}} = -3\Delta \gamma; \\
f_{3,1} &= \frac{\partial f_{3,shear}}{\partial \Delta \gamma} = 0; \\
f_{3,2} &= \frac{\partial f_{3,shear}}{\partial \Delta \varepsilon_v^p} \\
&= -\frac{\tan \psi (K \Delta \varepsilon_v^p (1 + \mathfrak{m}) + 2\mathfrak{m} p_c^{n+1} + p_t^{n+1} (1 - \mathfrak{m}) - (1 + \mathfrak{m}) p^{trial,n+1})}{3\mathfrak{m}^2 (K \Delta \varepsilon_v^p + p_c^{n+1} - p^{trial,n+1})^3} (K \Delta \varepsilon_v^p (k_{p_t} - k_{p_c}) \\
&+ k_{p_t} p_c^{n+1} + K(p_c^{n+1} - p_t^{n+1}) - k_{p_c} p_t^{n+1} + p^{trial,n+1} (k_{p_c} - k_{p_t})); \\
f_{3,3} &= \frac{\partial f_{3,shear}}{\partial N_v^{n+1}} = 1,
\end{aligned}$$

¹²For the case of apex return on the shear side, $f_{1,1} = 0$.

where k_{p_c} and k_{p_t} are the slopes of p_c and p_t with respect to $\varepsilon_v^{p,n+1}$, so that

$$p_c^{n+1} = p_c^n + k_{p_c} \Delta \varepsilon_v^p; \quad (4.143)$$

$$p_t^{n+1} = p_t^n + k_{p_t} \Delta \varepsilon_v^p. \quad (4.144)$$

If the preconsolidation pressure p_c and tensile intercept p_t are expressed¹³ in exponential form, then

$$p_c^{n+1} = p_c^n \left(1 - \frac{v^{n+1} \Delta \varepsilon_v^p}{\lambda - \kappa} \right); \quad (4.145)$$

$$p_t^{n+1} = p_t^n \left(1 - \frac{v^{n+1} \langle \Delta \varepsilon_v^p \rangle}{\lambda - \kappa} \right) \quad (4.146)$$

, where $\langle \cdot \rangle$ is the Macaulay brackets.

Compression Side Return

The consistency condition for the discrete form of SR4 model yield function on the compression side requires that

$$\Phi_{cap}^{SR4,n+1} = gq^{n+1} - M_{\Phi}^{n+1} p_{\Phi peak}^{n+1} \sqrt{1 - \left(\frac{p^{n+1} - p_{\Phi peak}^{n+1}}{p_{\Phi peak}^{n+1} - p_c^{n+1}} \right)^2} = 0, \quad (4.147)$$

where

$$p_{\Phi peak}^{n+1} = \frac{\eta p_c^{n+1} + p_t^{n+1}}{1 + \eta};$$

$$M_{\Phi}^{n+1} = \frac{q_{\Phi peak}}{p_{\Phi peak}} = -(\eta + 1)^{-\frac{1}{\eta}} \left(1 - \frac{p_t^{n+1}}{p_{\Phi peak}^{n+1}} \right) \tan \beta,$$

which is solved along with

$$\Delta \varepsilon_v^p = 3 \Delta \gamma N_v^{n+1};$$

$$N_v^{n+1} = \frac{M_{\Psi}^{n+1} (p^{n+1} - p_{\Psi crit}^{n+1}) p_{\Psi crit}^{n+1}}{3(p_c^{n+1} - p_{\Psi crit}^{n+1})^2 \sqrt{1 - \left(\frac{p^{n+1} - p_{\Psi crit}^{n+1}}{p_c^{n+1} - p_{\Psi crit}^{n+1}} \right)^2}},$$

¹³Specific volume v is calculated from updated porosity. The values of κ and λ are assumed constant.

where

$$p_{\Psi_{crit}}^{n+1} = \frac{m p_c^{n+1} + p_t^{n+1}}{1 + m};$$

$$M_{\Psi}^{n+1} = \frac{q_{\Psi_{crit}}^{n+1}}{p_{\Psi_{crit}}^{n+1}} = -(m+1)^{-\frac{1}{m}} \left(1 - \frac{p_t^{n+1}}{p_{\Psi_{crit}}^{n+1}} \right) \tan \psi.$$

By substituting the expressions for p^{n+1} and q^{n+1} into the equations above, we obtain

$$\begin{aligned} & \Phi_{cap}^{SR4,n+1}(\Delta\gamma, \Delta\epsilon_v^p) \\ &= g \left(q^{trial,n+1} - 3G\Delta\gamma \right) + \left((m+1)^{-\frac{1}{m}} \left(1 - \frac{p_t^{n+1}}{\left(\frac{m p_c^{n+1} + p_t^{n+1}}{1+m} \right)} \right) \tan \beta \right) \\ & \left(\frac{m p_c^{n+1} + p_t^{n+1}}{1+m} \right) \sqrt{1 - \left(\frac{p^{trial,n+1} - K\Delta\epsilon_v^p - \frac{m p_c^{n+1} + p_t^{n+1}}{1+m}}{\frac{m p_c^{n+1} + p_t^{n+1}}{1+m} - p_c^{n+1}} \right)^2} = 0, \end{aligned} \quad (4.148)$$

which is to be solved with function $f_{2,cap}(\Delta\gamma, \Delta\epsilon_v^p, N_v^{n+1})$

$$f_{2,cap}(\Delta\gamma, \Delta\epsilon_v^p, N_v^{n+1}) = \Delta\epsilon_v^p - 3\Delta\gamma N_v^{n+1} = 0, \quad (4.149)$$

and function $f_{3,cap}(\Delta\epsilon_v^p, N_v^{n+1})$:

$$\begin{aligned} & f_{3,cap}(\Delta\epsilon_v^p, N_v^{n+1}) \\ &= N_v^{n+1} + \frac{(m+1)^{-\frac{1}{m}} \left(\frac{m p_c^{n+1} + p_t^{n+1}}{1+m} - p_t^{n+1} \right) \left(p^{trial,n+1} - K\Delta\epsilon_v^p - \frac{m p_c^{n+1} + p_t^{n+1}}{1+m} \right) \tan \psi}{3 \left(p_c^{n+1} - \frac{m p_c^{n+1} + p_t^{n+1}}{1+m} \right)^2 \sqrt{1 - \left(\frac{p^{trial,n+1} - 3K\Delta\gamma N_v^{n+1} - \frac{m p_c^{n+1} + p_t^{n+1}}{1+m}}{p_c^{n+1} - \frac{m p_c^{n+1} + p_t^{n+1}}{1+m}} \right)^2}} = 0 \end{aligned} \quad (4.150)$$

Similar to the shear side, the unknowns $\Delta\gamma, \Delta\epsilon_v^p, N_v^{n+1}$ for the compression side are solved using Newton-Raphson method by iterating vector \mathbf{x} as follows

$$\mathbf{x}^{i+1} = \mathbf{x}^i - \left[\left(\frac{\partial \mathbf{f}}{\partial \mathbf{x}} \right)^{-1} \Delta \mathbf{x} \right]_{\mathbf{x}=\mathbf{x}^i}, \quad (4.151)$$

where

$$\mathbf{x} = \begin{Bmatrix} \Delta\gamma \\ \Delta\boldsymbol{\varepsilon}_v^p \\ N_v^{n+1} \end{Bmatrix}; \quad \mathbf{f} = \begin{Bmatrix} \Phi_{cap}^{SR4,n+1}(\Delta\gamma, \Delta\boldsymbol{\varepsilon}_v^p) \\ f_{2,cap}(\Delta\gamma, \Delta\boldsymbol{\varepsilon}_v^p, N_v^{n+1}) \\ f_{3,cap}(\Delta\boldsymbol{\varepsilon}_v^p, N_v^{n+1}) \end{Bmatrix}. \quad (4.152)$$

The components of \mathbf{f} for the compression side of SR4 model are as follows

$$\begin{aligned} f_{1,1} &= \frac{\partial \Phi_{cap}^{SR4,n+1}}{\partial \Delta\gamma} = -3gG; \\ f_{1,2} &= \frac{\partial \Phi_{cap}^{SR4,n+1}}{\partial \Delta\boldsymbol{\varepsilon}_v^p} \\ &= -\frac{n(1+n)^{-\frac{1}{n}} \tan \beta}{\sqrt{C_n} (p_c^{n+1} - p_t^{n+1})} (K\Delta\boldsymbol{\varepsilon}_v^p (K + k_{p_t} + (K + k_{p_c})n) + (k_{p_t} + k_{p_c}(n-1) + Kn) p_c^{n+1} \\ &\quad + (K + k_{p_c}) p_t^{n+1} - (K + k_{p_t} + (K + k_{p_c})n) p^{trial,n+1}); \\ f_{1,3} &= \frac{\partial \Phi_{cap}^{SR4,n+1}}{\partial N_v^{n+1}} = 0; \\ f_{2,1} &= \frac{\partial f_{2,cap}}{\partial \Delta\gamma} = -3N_v^{n+1}; \\ f_{2,2} &= \frac{\partial f_{2,cap}}{\partial \Delta\boldsymbol{\varepsilon}_v^p} = 1; \\ f_{2,3} &= \frac{\partial f_{2,cap}}{\partial N_v^{n+1}} = -3\Delta\gamma; \\ f_{3,1} &= \frac{\partial f_{3,cap}}{\partial \Delta\gamma} = 0; \\ f_{3,2} &= \frac{\partial f_{3,cap}}{\partial \Delta\boldsymbol{\varepsilon}_v^p} \\ &= \frac{n(1+n)^{\frac{n-1}{n}} \tan \psi}{3C_m^{3/2} (p_c^{n+1} - p_t^{n+1})^2} (K\Delta\boldsymbol{\varepsilon}_v^p (k_{p_c} - k_{p_t}) - k_{p_t} p_c^{n+1} + k_{p_c} p_t^{n+1} + K(p_t^{n+1} - p_c^{n+1}) \\ &\quad + p^{trial,n+1} (k_{p_t} - k_{p_c})); \\ f_{3,3} &= \frac{\partial f_{3,cap}}{\partial N_v^{n+1}} = 1, \end{aligned} \quad (4.153)$$

where the expressions for C_n and C_m are given by

$$C_n = -\frac{(1+n)(K\Delta\varepsilon_v^p + p_c^{n+1} - p^{trial,n+1})(K\Delta\varepsilon_v^p(1+n) + (n-1)p_c^{n+1} + 2p_t^{n+1} - p^{trial}(1+n))}{(p_c^{n+1} - p_t^{n+1})^2}; \quad (4.154)$$

$$C_m = -\frac{(1+m)(K\Delta\varepsilon_v^p + p_c^{n+1} - p^{trial,n+1})(K\Delta\varepsilon_v^p(1+m) + (m-1)p_c^{n+1} + 2p_t^{n+1} - p^{trial}(1+m))}{(p_c^{n+1} - p_t^{n+1})^2}. \quad (4.155)$$

The pseudocodes for the return-mapping algorithm are all listed in Appendix.

4.7 Elastoplastic-Fracture Model

In the following, rotating crack model and its implementation in elastoplastic-fracture framework are discussed. The advantage of using rotating crack model is that no major change in the existing finite element code is required. In particular, only additional subroutine is needed to perform stress update as required by rotating crack model, based on Rankine failure criterion and a softening law. The implementation of other alternatives (e.g. XFEM [14, 115] and phase-field fracture modelling [112]) on existing finite element code is not straightforward. XFEM requires the incorporation of enrichment function¹⁴ in the finite element approximation. As for phase-field modelling, the nonlinear coupling of displacement and phase fields need to be accounted for [112], which implies that higher computational costs could be incurred.

4.7.1 Rotating Crack Model

Rotating crack model is one of the smeared-type fracture models that was initially developed [42, 77, 48] to study the post-fracture behaviour of reinforced concrete structures. Rotating crack model is based on the Rankine failure criterion; the failure plane is always normal to the most tensile principal stress direction. This means the propagation direction of crack is influenced by the rotation of principal stress, which causes partial closure of existing microcracks and formation of new system of microcracks [77].

¹⁴based on analytical solution of linear elastic fracture mechanics at near-tip field

Let $\boldsymbol{\sigma}_{prp}$ be the principal stress tensor transformed from an effective¹⁵ stress tensor $\boldsymbol{\sigma}$ via an orthogonal transformation tensor \mathbf{Q} , such that

$$\boldsymbol{\sigma}_{prp} = \mathbf{Q}\boldsymbol{\sigma}\mathbf{Q}^T = \begin{bmatrix} \sigma_1 & 0 & 0 \\ 0 & \sigma_2 & 0 \\ 0 & 0 & \sigma_3 \end{bmatrix}. \quad (4.156)$$

Applying Rankine failure criterion, if any of the principal stresses exceeds a critical fracture value (i.e. tensile strength f_t) during elastic stress update, then the principal stress is corrected using softening law to achieve the following Rankine fracture criterion

$$\Phi^{Rankine}(\boldsymbol{\sigma}_{prp}, f_t) = \max(\sigma_1, \sigma_2, \sigma_3) - f_t = 0, \quad (4.157)$$

in which the material is treated as undergoing locally uniaxial tensile failure.

Softening Law

In tensile failure mode, softening law dictates the magnitude of tensile strength reduction per unit of fracture strain ε_f via a softening modulus H_s , such that

$$H_s = -\frac{\partial f_t(\varepsilon_f)}{\partial \varepsilon_f}. \quad (4.158)$$

In the current thesis, the variation of f_t with respect to ε_f is assumed to be linear, so that we may simply express

$$f_t = -H_s \varepsilon_f. \quad (4.159)$$

As illustrated in Figure 4.14, tensile strength is shown to reduce to zero as the fracture strain is driven towards the critical fracture strain $\varepsilon_{f,c}$, which is the point at which discrete crack starts to form.

Furthermore, the area under the plot is defined as the fracture energy density γ_f , which is expressed by

$$\gamma_f = \frac{G_f}{h_c}, \quad (4.160)$$

¹⁵The superscript ' usually appear in effective stress tensor is omitted hereby for notational brevity.

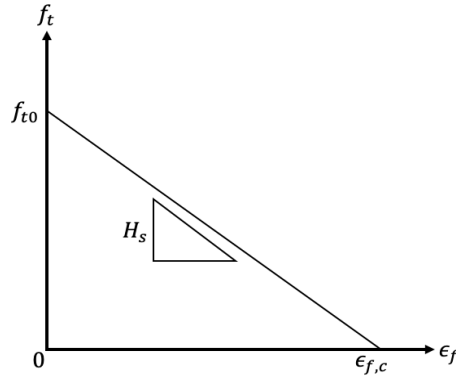


Fig. 4.14 Illustration of linear softening in $f_t - \epsilon_f$ plot, showing tensile strength is reduced to zero when reaching the critical fracture strain $\epsilon_{f,c}$.

where G_f is the specific fracture energy¹⁶, and h_c is the thickness of crack band, which refers to the characteristic size of a single finite element in numerical implementation. It then follows that

$$\gamma_f = \int_0^{\epsilon_{f,c}} f_t d\epsilon_f = \frac{G_f}{h_c}. \quad (4.161)$$

Due to the assumed linearity of softening behaviour, we may now formulate

$$H_s = \frac{f_{t0}^2 h_c}{2G_f}, \quad (4.162)$$

which shows that the softening slope may be determined by the fracture properties of a material.

Similarly, the softening slope needs to be regularised to ensure finite dissipation of specific fracture energy during softening. This is done by allowing

$$G_f = h_c \gamma_f = h_c^{(e)} \gamma_f^{(e)}, \quad (4.163)$$

where $h_c^{(e)}$ is the characteristic length of finite element and $\gamma_f^{(e)}$ is the element fracture energy density. It follows that

$$\gamma_f^{(e)} = \frac{G_f}{h_c^{(e)}} = \frac{f_{t0}^2}{2H_{sr}}, \quad (4.164)$$

¹⁶i.e. energy per unit area required for the formation of discrete crack

where H_{sr} is the regularised softening slope in $f_t - \varepsilon_f$ plane. By rearranging, we may now obtain

$$H_{sr} = \frac{f_{t0}^2 h_c^{(e)}}{2G_f}. \quad (4.165)$$

As the tensile strength reduces, it is assumed that the softening process in the cohesive zone of linear elastic material involves local degradation of elastic properties via Young's modulus and Poisson's ratios. The degraded Young's modulus in principal stress direction i is given by

$$E_i^D = \frac{f_{ti}}{f_{ti,0}} E_i. \quad (4.166)$$

Since the softening process does not immediately decouple the stresses in all principal direction, the Poisson's ratios are allowed to degrade as function of tensile strength.

$$v_{12}^D = v_{21}^D = \frac{f_{t1}}{f_{t1,0}} \frac{f_{t2}}{f_{t2,0}} v; \quad (4.167)$$

$$v_{13}^D = v_{31}^D = \frac{f_{t1}}{f_{t1,0}} v; \quad (4.168)$$

$$v_{23}^D = v_{32}^D = \frac{f_{t2}}{f_{t2,0}} v. \quad (4.169)$$

It is assumed that no degradation of tensile strength takes place in the out-of-plane principal direction for two dimensional problem.

Initial Value Problem

Let a motion be prescribed between a given time t_0 and the next instant of time T . Then, with respect to this motion, the tensile strength $f_t(t)$ is solved using the initial values of tensile strength $f_t(t_0)$ and the history of the total strain tensor $\boldsymbol{\varepsilon}(t)$ for $t \in [t_0, T]$ to satisfy the following constitutive equation

$$\dot{f}_t(t) = -H_{sr} \dot{\varepsilon}_f(t), \quad (4.170)$$

subject to the constraint

$$\Phi^{Rankine} = \max(\sigma_1(t), \sigma_2(t), \sigma_3(t)) - f_t(t) \leq 0. \quad (4.171)$$

Incremental Constitutive Problem

Let a motion be prescribed between a given time t_n and the next instant of time t^{n+1} , such that $\Delta t = t^{n+1} - t^n$ is defined as the time step of the time interval. Then, with respect to this motion, the tensile strength f_t^{n+1} is solved using the initial values of tensile strength f_t^n and the prescribed incremental fracture strain $\Delta \varepsilon_f$ over Δt to satisfy the following algebraic equations

$$f_t^{n+1} = f_t^n - H_{sr} \Delta \varepsilon_f, \quad (4.172)$$

subject to the constraint

$$\Phi^{Rankine} = \max(\sigma_1^{n+1}, \sigma_2^{n+1}, \sigma_3^{n+1}) - f_t^{n+1} \leq 0. \quad (4.173)$$

Softening Slope with respect to Total Strain

In terms of total strain ε , the fracture strain can be expressed by

$$\varepsilon_{f,i} = \varepsilon_i - \varepsilon_{un,i}, \quad (4.174)$$

where i refers to principal stress direction, and $\varepsilon_{un,i}$ is the unloaded strain (Figure 4.15) of the surrounding continuum, which gives rise to the localization nature of fracture opening.

In incremental form, we then have

$$\Delta \varepsilon_i = \Delta \varepsilon_{f,i} + \Delta \varepsilon_{un,i}, \quad (4.175)$$

where $\Delta \varepsilon_{un,i} = \frac{\Delta \sigma_i}{E_i}$.

The use of constant Young's modulus E signifies that the material is linearly elastic before subjected to uniaxial tensile failure.

It then follows that

$$\begin{aligned} \Delta \varepsilon_i &= \Delta \varepsilon_{f,i} + \Delta \varepsilon_{un,i} \\ &= -\frac{\Delta f_{t,i}}{H_{sr,i}} + \frac{\Delta \sigma_i}{E_i} \\ &= -\frac{\Delta \sigma_i}{H_{sr,i}} + \frac{\Delta \sigma_i}{E_i}; \\ \Rightarrow \frac{\Delta \sigma_i}{\Delta \varepsilon_i} &= -\frac{E_i H_{sr,i}}{E_i - H_{sr,i}} = -H_i, \end{aligned} \quad (4.176)$$

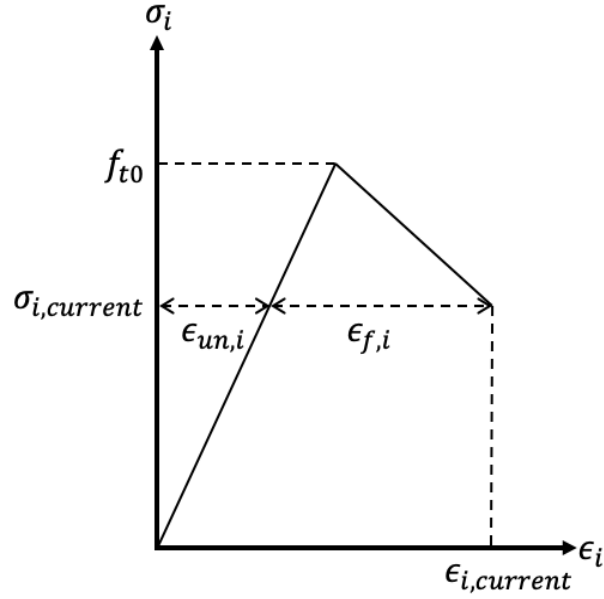


Fig. 4.15 Total strain as sum of fracture strain and elastically unloaded strain during fracture stress update

where H represents the softening slope in $\sigma - \epsilon$ plot.

It is clear that, in order to obtain proper softening response (i.e. $\Delta\sigma_i < 0$), we require that

$$\begin{aligned}
 E - H_{sr} &> 0; \\
 E - \frac{f_{t0}^2 h_c^{(e)}}{2G_f} &> 0; \\
 \Rightarrow h_c^{(e)} &< \frac{2G_f E}{f_{t0}^2} = h_{c,max}.
 \end{aligned} \tag{4.177}$$

In another word, in order to prevent unrealistic “hardening” response, the maximum characteristic size of the element $h_{c,max}$ is bounded by the fracture properties of the material. However, if an element is elongated to a point that the above condition is violated, then instant brittle failure response is assumed.

Trial Stress Computation

The procedure begins with the computation of principal angle θ_p of updated total strain, followed by the transformation of incremental total strain $\Delta\boldsymbol{\epsilon}$ and stress tensor of previous time step $\boldsymbol{\sigma}^n$ into the principal reference frame.

For plane strain problems, the transformation matrix in conjunction with Voigt's notation is given by

$$\mathbf{Q}_{mat,\varepsilon} = \begin{bmatrix} \cos^2 \theta_p & \sin^2 \theta_p & \sin \theta_p \cos \theta_p \\ \sin^2 \theta_p & \cos^2 \theta_p & -\sin \theta_p \cos \theta_p \\ -\sin \theta_p \cos \theta_p & \sin \theta_p \cos \theta_p & \frac{1}{2} \cos 2\theta_p \end{bmatrix}, \quad (4.178)$$

so that we may express

$$\begin{Bmatrix} \Delta \varepsilon_1 \\ \Delta \varepsilon_2 \\ \Delta \gamma_{12} \end{Bmatrix} = \mathbf{Q}_{mat,\varepsilon} \begin{Bmatrix} \Delta \varepsilon_{xx} \\ \Delta \varepsilon_{yy} \\ \Delta \gamma_{xy} \end{Bmatrix}. \quad (4.179)$$

For stress transformation, the transformation matrix is given by

$$\mathbf{Q}_{mat,\sigma} = \begin{bmatrix} \cos^2 \theta_p & \sin^2 \theta_p & \sin 2\theta_p & 0 \\ \sin^2 \theta_p & \cos^2 \theta_p & -\sin 2\theta_p & 0 \\ -\sin \theta_p \cos \theta_p & \sin \theta_p \cos \theta_p & \cos 2\theta_p & 0 \\ 0 & 0 & 0 & 1 \end{bmatrix}, \quad (4.180)$$

so that we may express

$$\begin{Bmatrix} \sigma_1^n \\ \sigma_2^n \\ \sigma_{12}^n \\ \sigma_3^n \end{Bmatrix} = \mathbf{Q}_{mat,\sigma} \begin{Bmatrix} \sigma_{xx}^n \\ \sigma_{yy}^n \\ \sigma_{xy}^n \\ \sigma_{zz}^n \end{Bmatrix}. \quad (4.181)$$

Then, by constructing the following vectors as

$$\Delta \boldsymbol{\varepsilon}^* = \{\Delta \varepsilon_1, \Delta \varepsilon_2, \Delta \varepsilon_3, \Delta \gamma_{12}\}^T; \quad (4.182)$$

$$\boldsymbol{\sigma}^{*,n} = \{\sigma_1^n, \sigma_2^n, \sigma_3^n, \sigma_{12}^n\}^T, \quad (4.183)$$

the stress update during trial stage is performed via degraded constitutive elasticity matrix $\bar{\mathbb{C}}^D$, such that

$$\boldsymbol{\sigma}^{*,trial} = \boldsymbol{\sigma}^{*,n} + \bar{\mathbb{C}}^D \Delta \boldsymbol{\varepsilon}^*. \quad (4.184)$$

The matrix $\bar{\mathbb{C}}^D$ is expressed by

$$\bar{\mathbb{C}}^D = k \begin{bmatrix} C_{11}^D & C_{12}^D & C_{13}^D & 0 \\ C_{12}^D & C_{22}^D & C_{23}^D & 0 \\ C_{13}^D & C_{23}^D & C_{33}^D & 0 \\ 0 & 0 & 0 & \frac{G}{k} \end{bmatrix}, \quad (4.185)$$

where

$$\begin{aligned} k &= \frac{E}{E_1^D E_2^D v_{12}^D (v_{12}^D + 2v_{13}^D v_{23}^D) + E_1^D E (v_{13}^D)^2 + E (E_2^D (v_{23}^D)^2 - E)}; \\ C_{11}^D &= E_1^D (E_2^D (v_{23}^D)^2 - E); \\ C_{12}^D &= -E_1^D E_2^D (v_{12}^D + v_{13}^D v_{23}^D); \\ C_{13}^D &= -E_1^D (E_2^D v_{12}^D v_{23}^D + v_{13}^D E); \\ C_{22}^D &= E_2^D (E_1^D (v_{13}^D)^2 - E); \\ C_{23}^D &= -E_2^D (E_1^D v_{12}^D v_{13}^D + v_{23}^D E); \\ C_{33}^D &= (E_1^D E_2^D (v_{12}^D)^2 - E^2); \\ G &= \frac{E}{2(1 + \nu)}. \end{aligned}$$

Stress Correction Computation

Subsequent to the evaluation of $\boldsymbol{\sigma}^{*,trial}$ using Rankine failure criterion, the stress update procedure (if needed) depends on the direction of softening. If the stress and strain components are related via a compliance matrix \mathbb{D} , such that

$$\begin{Bmatrix} \varepsilon_1 - \varepsilon_{01} \\ \varepsilon_2 - \varepsilon_{02} \\ \varepsilon_3 - \varepsilon_{03} \end{Bmatrix} = \mathbb{D} \begin{Bmatrix} \sigma_1 \\ \sigma_2 \\ \sigma_3 \end{Bmatrix}, \quad (4.186)$$

where

$$\mathbb{D} = \begin{bmatrix} \frac{1}{E_1^D} & -\frac{v_{12}^D}{E} & -\frac{v_{13}^D}{E} \\ -\frac{v_{12}^D}{E} & \frac{1}{E_2^D} & -\frac{v_{23}^D}{E} \\ -\frac{v_{13}^D}{E} & -\frac{v_{23}^D}{E} & \frac{1}{E} \end{bmatrix}, \quad (4.187)$$

then we assume the following method of stress update formulations.

If softening takes place in principal direction 1, then σ_2 and σ_3 are updated as follows

$$\begin{Bmatrix} \varepsilon_1 - \varepsilon_{01} \\ -\varepsilon_{02} \\ -\varepsilon_{03} \end{Bmatrix} = \mathbb{D} \begin{Bmatrix} f_{i1} \\ \sigma_2 \\ \sigma_3 \end{Bmatrix}, \quad (4.188)$$

from which

$$\begin{aligned} -\varepsilon_{02} &= -\frac{\nu_{12}^D}{E} f_{i1} + \frac{1}{E_2^D} \sigma_2 - \frac{\nu_{23}^D}{E} \sigma_3; \\ -\varepsilon_{03} &= -\frac{\nu_{13}^D}{E} f_{i1} - \frac{\nu_{23}^D}{E} \sigma_2 + \frac{1}{E} \sigma_3. \end{aligned} \quad (4.189)$$

By solving the simultaneous equations for σ_2 and σ_3 and taking derivatives with respect to f_{i1} , we obtain the following expressions

$$\frac{\partial \sigma_2}{\partial f_{i1}} = \frac{E_2^D f_{i1} f_{i2} f_{i2,0} \nu (1 + \nu)}{f_{i1,0} (E f_{i2,0}^2 - E_2^D (f_{i2} \nu)^2)}; \quad (4.190)$$

$$\frac{\partial \sigma_3}{\partial f_{i1}} = \frac{f_{i1} \nu (E f_{i2,0}^2 + E_2^D \nu f_{i2}^2)}{f_{i1,0} (E f_{i2,0}^2 - E_2^D (f_{i2} \nu)^2)}. \quad (4.191)$$

Then, the stress update procedures for softening in principal direction 1 are as follows

$$f_{i1}^{n+1} = f_{i1}^n + \Delta f_{i1} = f_{i1}^n - \frac{E_1 H_{sr1}}{E_1 - H_{sr1}} \Delta \varepsilon_1; \quad (4.192)$$

$$E_1^{D,n+1} = E_1^{D,n} + \frac{\Delta f_{i1}}{f_{i1,0}} E_1; \quad (4.193)$$

$$\varepsilon_{f1}^{n+1} = \varepsilon_{f1}^n + \frac{\Delta f_{i1}}{H_{sr1}}; \quad (4.194)$$

$$\sigma_1^{n+1} = \sigma_1^{trial} + \Delta f_{i1}; \quad (4.195)$$

$$\sigma_2^{n+1} = \sigma_2^{trial} + \frac{\partial \sigma_2}{\partial f_{i1}} \Delta f_{i1} = \sigma_2^{trial} + \frac{E_2^D f_{i1}^{n+1} f_{i2} f_{i2,0} \nu (1 + \nu)}{f_{i1,0} (E f_{i2,0}^2 - E_2^D (f_{i2} \nu)^2)} \Delta f_{i1}; \quad (4.196)$$

$$\sigma_3^{n+1} = \sigma_3^{trial} + \frac{\partial \sigma_3}{\partial f_{i1}} \Delta f_{i1} = \sigma_3^{trial} + \frac{f_{i1}^{n+1} \nu (E f_{i2,0}^2 + E_2^D \nu f_{i2}^2)}{f_{i1,0} (E f_{i2,0}^2 - E_2^D (f_{i2} \nu)^2)} \Delta f_{i1}. \quad (4.197)$$

If softening takes place in principal direction 2, then σ_1 and σ_3 are updated as follows

$$\begin{Bmatrix} -\varepsilon_{01} \\ \varepsilon_2 - \varepsilon_{02} \\ -\varepsilon_{03} \end{Bmatrix} = \mathbb{D} \begin{Bmatrix} \sigma_1 \\ f_{t2} \\ \sigma_3 \end{Bmatrix}, \quad (4.198)$$

from which

$$-\varepsilon_{01} = \frac{1}{E_1^D} \sigma_1 - \frac{\nu_{12}^D}{E} f_{t2} - \frac{\nu_{13}^D}{E} \sigma_3; \quad (4.199)$$

$$-\varepsilon_{03} = -\frac{\nu_{13}^D}{E} f_{t1} - \frac{\nu_{23}^D}{E} \sigma_2 + \frac{1}{E} \sigma_3. \quad (4.200)$$

Following the similar procedures as above, we obtain the following partial derivatives

$$\frac{\partial \sigma_1}{\partial f_{t2}} = \frac{E_1^D f_{t1} f_{t2} f_{t1,0} \nu (1 + \nu)}{f_{t2,0} (E f_{t1,0}^2 - E_1^D (f_{t1} \nu)^2)}; \quad (4.201)$$

$$\frac{\partial \sigma_3}{\partial f_{t2}} = \frac{f_{t2} \nu (E f_{t1,0}^2 + E_1^D \nu f_{t1}^2)}{f_{t2,0} (E f_{t1,0}^2 - E_1^D (f_{t1} \nu)^2)}. \quad (4.202)$$

Then, the stress update procedures for softening in principal direction 2 are as follows

$$f_{t2}^{n+1} = f_{t2}^n + \Delta f_{t2} = f_{t2}^n - \frac{E_2 H_{sr2}}{E_2 - H_{sr2}} \Delta \varepsilon_2; \quad (4.203)$$

$$E_2^{D,n+1} = E_2^{D,n} + \frac{\Delta f_{t2}}{f_{t2,0}} E_2; \quad (4.204)$$

$$\varepsilon_{f2}^{n+1} = \varepsilon_{f2}^n + \frac{\Delta f_{t2}}{H_{sr2}}; \quad (4.205)$$

$$\sigma_2^{n+1} = \sigma_2^{trial} + \Delta f_{t2}; \quad (4.206)$$

$$\sigma_1^{n+1} = \sigma_1^{trial} + \frac{\partial \sigma_1}{\partial f_{t2}} \Delta f_{t2} = \sigma_1^{trial} + \frac{E_1^D f_{t1} f_{t2}^{n+1} f_{t1,0} \nu (1 + \nu)}{f_{t2,0} (E f_{t1,0}^2 - E_1^D (f_{t1} \nu)^2)} \Delta f_{t2}; \quad (4.207)$$

$$\sigma_3^{n+1} = \sigma_3^{trial} + \frac{\partial \sigma_3}{\partial f_{t2}} \Delta f_{t2} = \sigma_3^{trial} + \frac{f_{t2}^{n+1} \nu (E f_{t1,0}^2 + E_1^D \nu f_{t1}^2)}{f_{t2,0} (E f_{t1,0}^2 - E_1^D (f_{t1} \nu)^2)} \Delta f_{t2}. \quad (4.208)$$

If softening takes place in both principal directions, then σ_3 is updated as follows

$$\begin{Bmatrix} \varepsilon_1 - \varepsilon_{01} \\ \varepsilon_2 - \varepsilon_{02} \\ -\varepsilon_{03} \end{Bmatrix} = \mathbb{D} \begin{Bmatrix} f_{t1} \\ f_{t2} \\ \sigma_3 \end{Bmatrix}, \quad (4.209)$$

from which

$$-\varepsilon_{03} = -\frac{v_{13}^D}{E} f_{t1} - \frac{v_{23}^D}{E} f_{t2} + \frac{1}{E} \sigma_3. \quad (4.210)$$

Then, the partial derivatives of σ_3 with respect to f_{t1} and f_{t2} are simply given by

$$\frac{\partial \sigma_3}{\partial f_{t1}} = \frac{f_{t1} \mathbf{v}}{f_{t1,0}}; \quad (4.211)$$

$$\frac{\partial \sigma_3}{\partial f_{t2}} = \frac{f_{t2} \mathbf{v}}{f_{t2,0}}. \quad (4.212)$$

Then, the stress update procedures for softening in both principal directions are as follows

$$f_{t1}^{n+1} = f_{t1}^n + \Delta f_{t1} = f_{t1}^n - \frac{E_1 H_{sr1}}{E_1 - H_{sr1}} \Delta \varepsilon_1; \quad (4.213)$$

$$f_{t2}^{n+1} = f_{t2}^n + \Delta f_{t2} = f_{t2}^n - \frac{E_2 H_{sr2}}{E_2 - H_{sr2}} \Delta \varepsilon_2; \quad (4.214)$$

$$E_1^{D,n+1} = E_1^{D,n} + \frac{\Delta f_{t1}}{f_{t1,0}} E_1; \quad (4.215)$$

$$E_2^{D,n+1} = E_2^{D,n} + \frac{\Delta f_{t2}}{f_{t2,0}} E_2; \quad (4.216)$$

$$\varepsilon_{f1}^{n+1} = \varepsilon_{f1}^n + \frac{\Delta f_{t1}}{H_{sr1}}; \quad (4.217)$$

$$\varepsilon_{f2}^{n+1} = \varepsilon_{f2}^n + \frac{\Delta f_{t2}}{H_{sr2}}; \quad (4.218)$$

$$\sigma_1^{n+1} = \sigma_1^{trial} + \Delta f_{t1}; \quad (4.219)$$

$$\sigma_2^{n+1} = \sigma_2^{trial} + \Delta f_{t2}; \quad (4.220)$$

$$\sigma_3^{n+1} = \sigma_3^{trial} + \frac{f_{t1}^{n+1} \mathbf{v}}{f_{t1,0}} \Delta f_{t1} + \frac{f_{t2}^{n+1} \mathbf{v}}{f_{t2,0}} \Delta f_{t2}. \quad (4.221)$$

Finally, the updated stress components are transformed back to the local reference system via the inverse of matrix $\mathbf{Q}_{mat,\sigma}$, given by

$$\mathbf{Q}_{mat,\sigma}^{-1} = \begin{bmatrix} \cos^2 \theta_p & \sin^2 \theta_p & -\sin 2\theta_p & 0 \\ \sin^2 \theta_p & \cos^2 \theta_p & \sin 2\theta_p & 0 \\ \sin \theta_p \cos \theta_p & -\sin \theta_p \cos \theta_p & \cos 2\theta_p & 0 \\ 0 & 0 & 0 & 1 \end{bmatrix}, \quad (4.222)$$

so that we may express

$$\begin{Bmatrix} \sigma_{xx}^n \\ \sigma_{yy}^n \\ \sigma_{xy}^n \\ \sigma_{zz}^n \end{Bmatrix} = \mathbf{Q}_{mat,\sigma}^{-1} \begin{Bmatrix} \sigma_1^n \\ \sigma_2^n \\ \sigma_{12}^n \\ \sigma_3^n \end{Bmatrix}. \quad (4.223)$$

The updated stress components can now be evaluated using elastoplastic yield criterion, if present.

4.7.2 Implementation with Elastoplastic Models

Representation in Meridional and Deviatoric Planes

Before proceeding to further discussion about implementation with elastoplastic models, it is useful to, firstly, visualize the Rankine failure criterion in meridional $p - q$ plane. Recall from (4.10) that Mohr-Coulomb yield function can also be expressed in invariant forms

$$\Phi_{invariant}^{MC} = \left(\cos \theta - \frac{1}{\sqrt{3}} \sin \theta \sin \phi \right) \sqrt{J_2(\mathbf{s})} + p(\boldsymbol{\sigma}) \sin \phi - c \cos \phi.$$

By expressing (Figure 4.16) cohesion as $c = f_t \tan \phi$ and using the relation $q = \sqrt{3J_2}$, we obtain

$$\Phi_{f_t}^{MC} = \left(\cos \theta - \frac{1}{\sqrt{3}} \sin \theta \sin \phi \right) q + \sqrt{3}(p - f_t) \sin \phi = 0. \quad (4.224)$$

Then, by allowing $\phi = \frac{\pi}{2}$ (Rankine failure condition), we arrive at the following expression of Lode-angle dependent Rankine failure model

$$q = \frac{\sqrt{3}(f_t - p)}{\cos \theta - \frac{1}{\sqrt{3}} \sin \theta}. \quad (4.225)$$

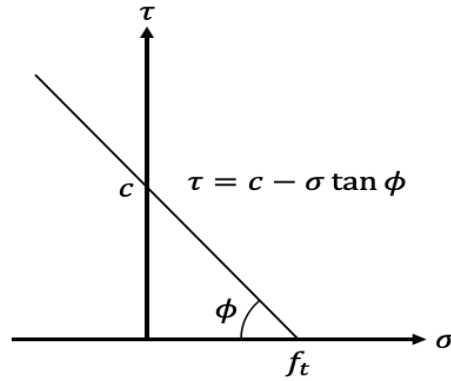


Fig. 4.16 Failure criterion based on Mohr-Coulomb model

Figure 4.17 shows the variation of Rankine state boundary line as the Lode angle changes from $\theta = -\frac{\pi}{6}$ (pure extension) to $\theta = \frac{\pi}{6}$ (pure compression). In particular, for pure exten-

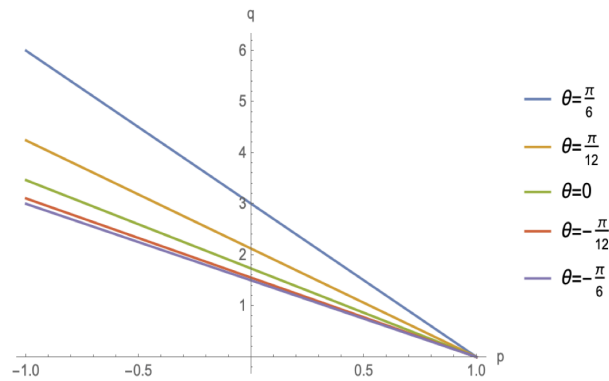


Fig. 4.17 Rankine state boundary line becomes steeper as Lode angle θ changes from $\theta = -\frac{\pi}{6}$ to $\theta = \frac{\pi}{6}$.

sion condition whereby $\theta = -\frac{\pi}{6}$, we obtain the following simple Rankine state boundary expression

$$q = \frac{3}{2}(f_t - p). \quad (4.226)$$

In deviatoric plane, the variable radius of the state boundary locus is given by

$$\rho_s^{f_t} = \sqrt{\frac{2}{3}}q = \frac{\sqrt{2}(f_t - p) \sin \phi}{\cos \theta - \frac{1}{\sqrt{3}} \sin \theta \sin \phi}. \quad (4.227)$$

Figure 4.18 shows how the size of Rankine state boundary locus increases with tensile strength f_t .

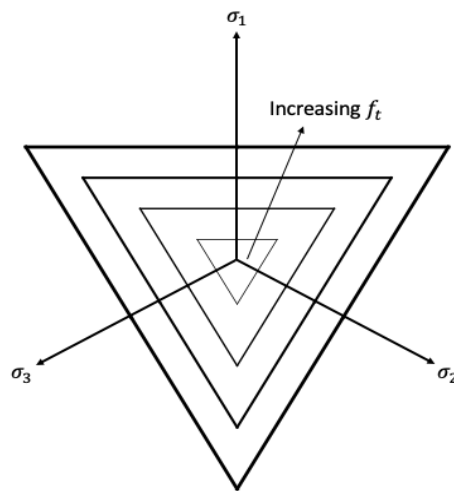


Fig. 4.18 Increasing size of Rankine state boundary locus with tensile strength f_t

Elastoplastic-Fracture Evaluation Stages

In the current work, as shown in Figure 4.19, if rotating crack model is activated, the computation of trial stress state is followed by the evaluation of principal stress components using Rankine failure criterion. If violated, softening law is applied to pull the stress state back to the Rankine state boundary locus. Then, the updated stress state is evaluated using any elastoplastic yield criterion. The advantage of this method is high modularity; the fracture model can be used along with almost any elastoplastic model.

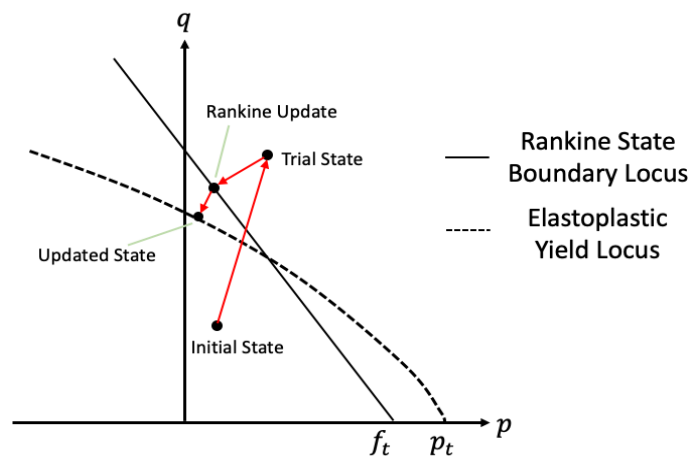


Fig. 4.19 Increasing size of Rankine state boundary locus with tensile strength f_t

Coupling of Strength Parameters

It is hypothesised that the reduction of tensile strength f_t within cohesive zone is the manifestation of the degradation of bonding among material particles. It follows that, in the context of elastoplastic model, strength parameter such as cohesion d in the modified Drucker-Prager model should also degrade. Hence, it is taken hereby that degradation of tensile strength and cohesion should take place concurrently.

A simple model in the form of dimensionless equation is used to couple f_t and d

$$\int_{d_0}^d \frac{d(d)}{d} = \eta_1 \int_{f_{t0}}^{f_t} \frac{df_t}{f_t};$$

$$\Rightarrow d = d_0 \left(\frac{f_t}{f_{t0}} \right)^{\eta_1}, \quad (4.228)$$

where $\eta_1 \geq 0$ is a constant controlling the slope in d - f_t plot (Figure 4.20).

Sublinear behaviour is exhibited for $\eta_1 < 1$ and supralinear behaviour is exhibited for $\eta_1 > 1$. No coupling exists for $\eta_1 = 0$.

In discretised form¹⁷, we then have

$$d^{n+1} = d^n \left(1 + \eta_1 \frac{\Delta f_t}{f_t^{n+1}} \right). \quad (4.229)$$

If softening takes place in more than one principal direction, then we have

$$d^{n+1} = d^n \left(1 + \eta_1 \left(\frac{\Delta f_{t1}}{f_{t1}^{n+1}} + \frac{\Delta f_{t2}}{f_{t2}^{n+1}} \right) \right). \quad (4.230)$$

Upon the completion of elastoplastic stress update and if $\eta_1 > 0$, similar update can also be done for tensile strength via

$$f_t^{n+1} = f_t^n \left(1 + \frac{\Delta d}{\eta_1 d^{n+1}} \right). \quad (4.231)$$

Apart from considering the effect of coupled tensile strength-cohesion, another form of coupled strength phenomenon to be considered is the orthotropic softening. In this case, the reduction of tensile strength in one principal direction will cause the degradation of tensile strength in other principal directions. In view of this, a simple model is presented as follows. In rotating crack model, if softening takes place in principal direction i , then orthotropic

¹⁷ derived from $\frac{\partial d}{\partial f_t} = \frac{\eta d}{f_t}$

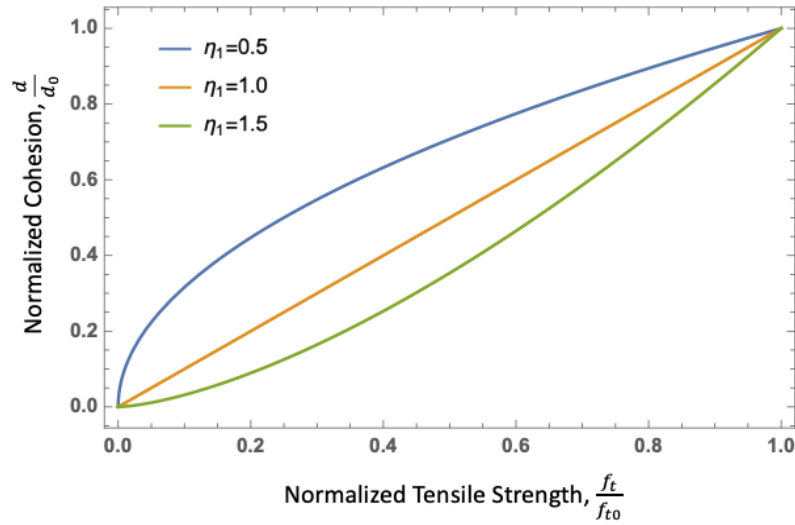


Fig. 4.20 Influence of coupling constant η on the slope of d - f_t plot. $\eta < 0$ for sublinear behaviour and $\eta > 0$ for supralinear behaviour.

softening in principal directions j and k is realised via a coupling constant $\eta_2 \geq 0$

$$\begin{aligned} f_{ij}^{n+1} &= f_{ij}^n + \eta_2 \Delta f_{ti}; \\ f_{tk}^{n+1} &= f_{tk}^n + \eta_2 \Delta f_{ti}. \end{aligned} \quad (4.232)$$

4.8 Single Element Test

4.8.1 Elastoplastic Models

Modified Drucker-Prager Model

One key difference of the current modified Drucker-Prager model compared with the standard version is the presence of π -plane correction factor g . The aim of this test to demonstrate how g regularises the yield surface size in response to a variety of loading conditions. To demonstrate this, a single element, having material properties listed in Table 4.1, is loaded biaxially under compressional and extensional loading conditions, subjected to boundary conditions illustrated in Figure 4.21. Both cohesion and dilation angle are linearly reduced to 0 when the effective plastic strain accumulates to 1.0.

For compressional loading condition, the top boundary is prescribed with vertically downward displacement of -1.0m , whereas for extensional loading condition, the boundary is prescribed with vertically upward displacement 1.0m . Three cases of confining pressure p_{conf} are considered for each loading condition. For compressional loading,

Properties	Value
Porosity	0.2
Young's modulus (GPa)	10
Poisson's ratio	0.30
Cohesion (MPa)	20.0
Friction parameter β ($^{\circ}$)	50
Dilation parameter β ($^{\circ}$)	50
π -plane correction parameter β_0	0.60
π -plane correction parameter α	0.25

Table 4.1 Material properties for modified Drucker-Prager model range test

$p_{conf} = \{-1, -3, -5\}$ MPa, whereas for extensional loading, $p_{conf} = \{-5, 0, 5\}$ MPa. The time step size is 10^{-5} s with a total simulation time of 1.0s.

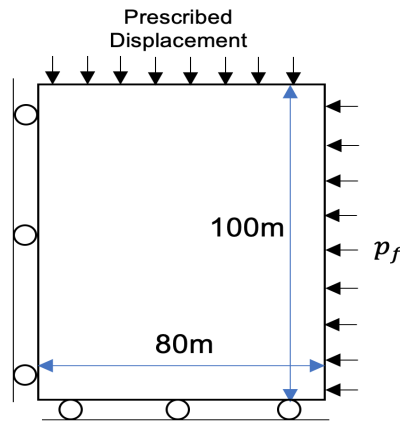


Fig. 4.21 Illustration of boundary conditions applied on a single element. The top boundary is prescribed with vertically downward displacement for compressional loading, and vertically upward displacement for extensional loading. Confining pressure p_{conf} is fixed throughout the loading process.

All results are plotted on a meridional $p - q$ plane and illustrated in Figure 4.22. The key outcome is that the yield surface size under extensional loading condition is smaller than the compressional counterpart due to difference in the value of g . Lower g leads to larger yield surface, and vice versa. The same effect can also be alternatively visualised in Figure 4.23. Note that, the outcome of this test is not only applicable to the Drucker-Prager model, but also to any elastoplastic model that considers the effect of g in a similar fashion.

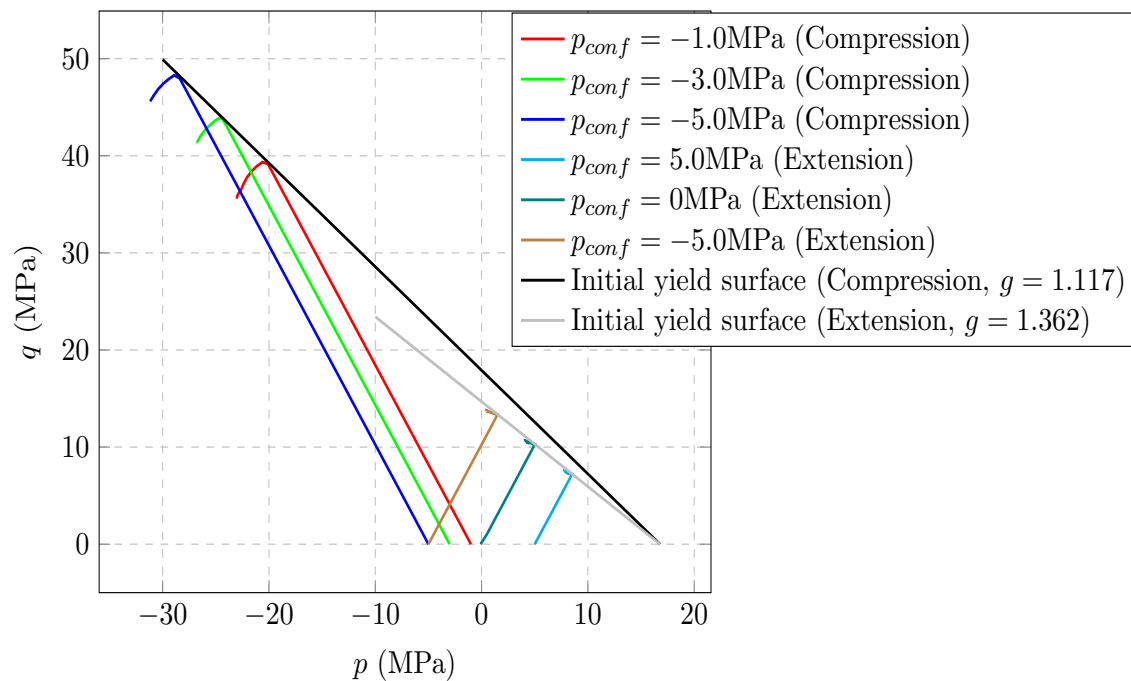


Fig. 4.22 Stress paths of each element initially loaded with different confining pressures p_{conf} . Lower π -plane correction factor g results in larger elastic domain under compressional loading condition, and vice versa for extensional loading condition.

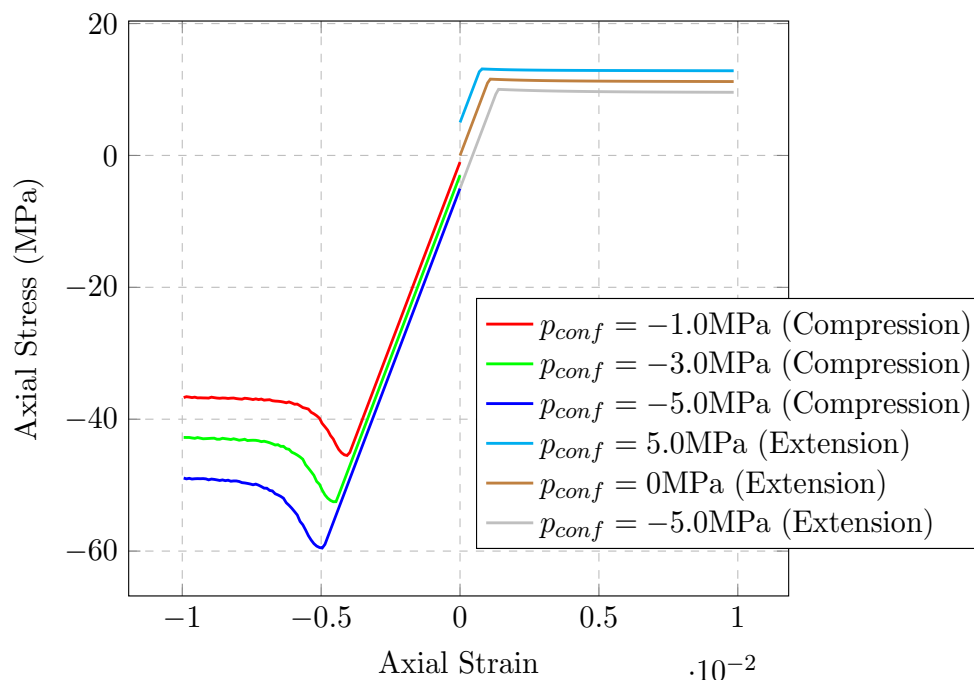


Fig. 4.23 The effect of π -plane correction factor can also be visualised in terms of stress-strain response of the test specimen. The key highlight is that the magnitude of yield stress of extensional loading is different from that of compressional loading.

SR4 Model

In large-scale geomechanical simulation, it is not untypical to encounter deformation related to plastic compaction due to burial and lateral earth pressure, as well as the corresponding accumulation of pore fluid pressure. Such phenomenon cannot be replicated in the current Drucker-Prager model due to the lack of cap model. Instead, SR4 model is used since the evolution of its yield surface depends on both pre-consolidation pressure p_c as well as tensile intercept p_t .

In this test, conventional triaxial compression (CTC) and triaxial extension (TXE) tests are simulated using 4-noded linear element in axisymmetric conditions (Figure 4.24) using material properties suited for SR4 model listed in Table 4.2 and illustrated in Figure 4.25. The element width is given as $R = 80\text{m}$, whereas the element height is given as $H = 100\text{m}$.

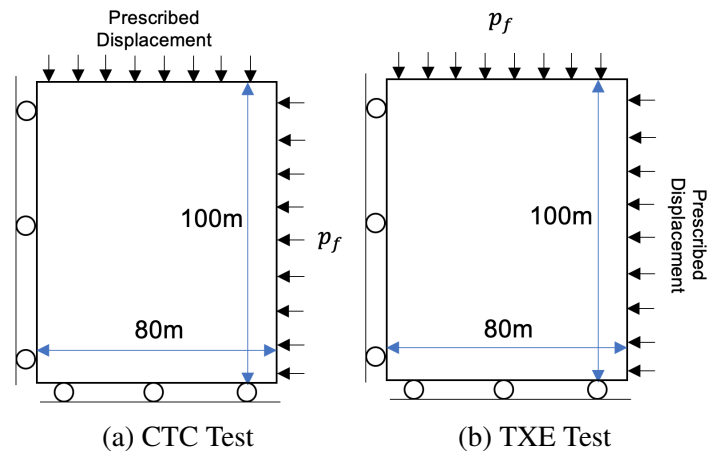


Fig. 4.24 Axisymmetric illustration of conventional triaxial compression (CTC) and triaxial extension (TXE) tests for SR4 model

The aim is to study differences in the way the stress path is led to critical state condition in the following tests with varying confining pressure $p_{conf} = \{0.1, 0.3, 1.0, 1.5\}$ MPa. In both CTC and TXE tests, the displacement is prescribed linearly until critical state condition is attained. The latter is characterised by constant mean effective stress p' , deviatoric stress q , and porosity n . The time step size is 10^{-4} Ma over a period of 1 Ma.

All results are presented in terms of deviatoric stress q , mean effective stress p' , volumetric strain ε_v , axial strain ε_a and radial strain ε_r . The calculation of the strain parameters are as

Properties	Value
Grain density (kg/m ³)	2700
Young's modulus (GPa)	10
Poisson's ratio	0.3
Material length scale (m)	80.0
Friction parameter β (°)	65.4
Dilation parameter ψ (°)	60.0
Exponent n	1.6
Exponent m	1.6
π -plane β_0	0.6
π -plane β_1	0.6
π -plane α	0.25
p_{c0} (MPa)	-3.0
p_{t0} (MPa)	0.01

Table 4.2 Material properties of SR4 model used for CTC and TXE tests

follows

$$\varepsilon_a = \ln \left(\frac{H + u_y}{H} \right) \quad (4.233)$$

$$\varepsilon_r = \ln \left(\frac{R + u_x}{R} \right) \quad (4.234)$$

$$\varepsilon_v = 2\varepsilon_r + \varepsilon_a \quad (4.235)$$

, where u_y and u_x are vertical and horizontal displacements, respectively.

The results for CTC and TXE tests are shown in Figure 4.26-4.27 and Figure 4.28-4.29, respectively. Overall, towards critical state condition, it is demonstrated that

- All strains eventually plateau out when plotted against deviatoric stress q .
- Stress path reaches the peak point of final yield surface through hardening or softening stress paths.
- Higher p_{conf} tends to drive stress path towards the compression side of the initial yield surface, causing the expansion of yield surface via higher q .
- Lower p_{conf} tends to drive stress path towards the shear side of the initial yield surface, causing the shrinkage of yield surface via lower q .
- The slope of CTC stress path is 3 whereas the slope of TXE stress path is 1.5. Therefore, stress path in RTE condition has higher tendency to cause plastic compaction than the stress path in CTC condition does.

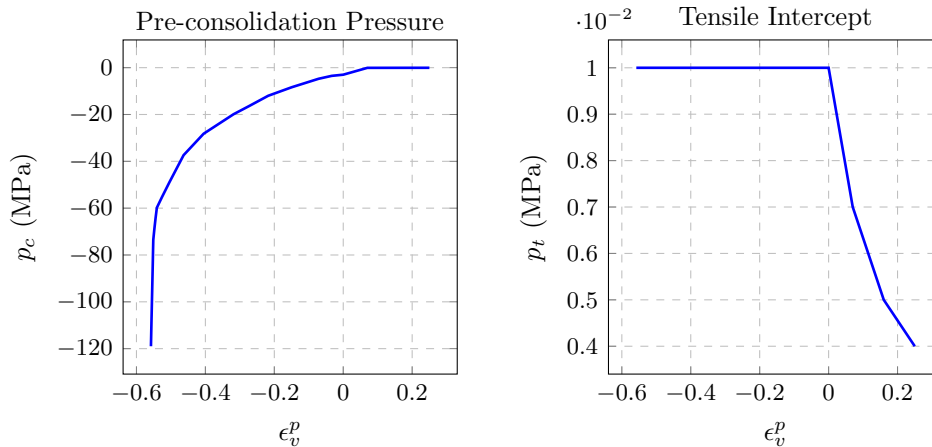


Fig. 4.25 Hardening properties for SR4 elastoplastic model

The results demonstrate how the nature of deformation is affected by initial confining pressure and the size of yield surface via a capped elastoplastic model such as SR4. In the case of sedimentary evolution, these outcomes could lead towards better understanding of the nature of stratigraphy deformation. On the subsurface layers, if the confining pressure is sufficiently low such that most stress paths reach at the shear side of yield surface, localised shear deformation leading towards the formation of fault is expected. Porosity enhancement is also predicted due to the increase of volumetric plastic strain. On the other hand, for deeper layers where confining pressure is relatively high, it is expected that most stress paths will reach at the compaction side of the yield surface. As a result, the stratigraphy layers will exhibit ductile behaviour and diffuse plastic strain distribution. Porosity loss is predicted in this case due to the decrease of volumetric plastic strain. In addition, fluid overpressure might be accumulated in the vicinity if the overall compaction rate is higher than the flow drainage rate.

In view of the explanation above, the standard and modified Drucker-Prager model (without cap model) will predict inaccurate result if the deformation is predominantly compressive in nature since no cap model is present to account for plastic compaction and the resulting porosity loss.

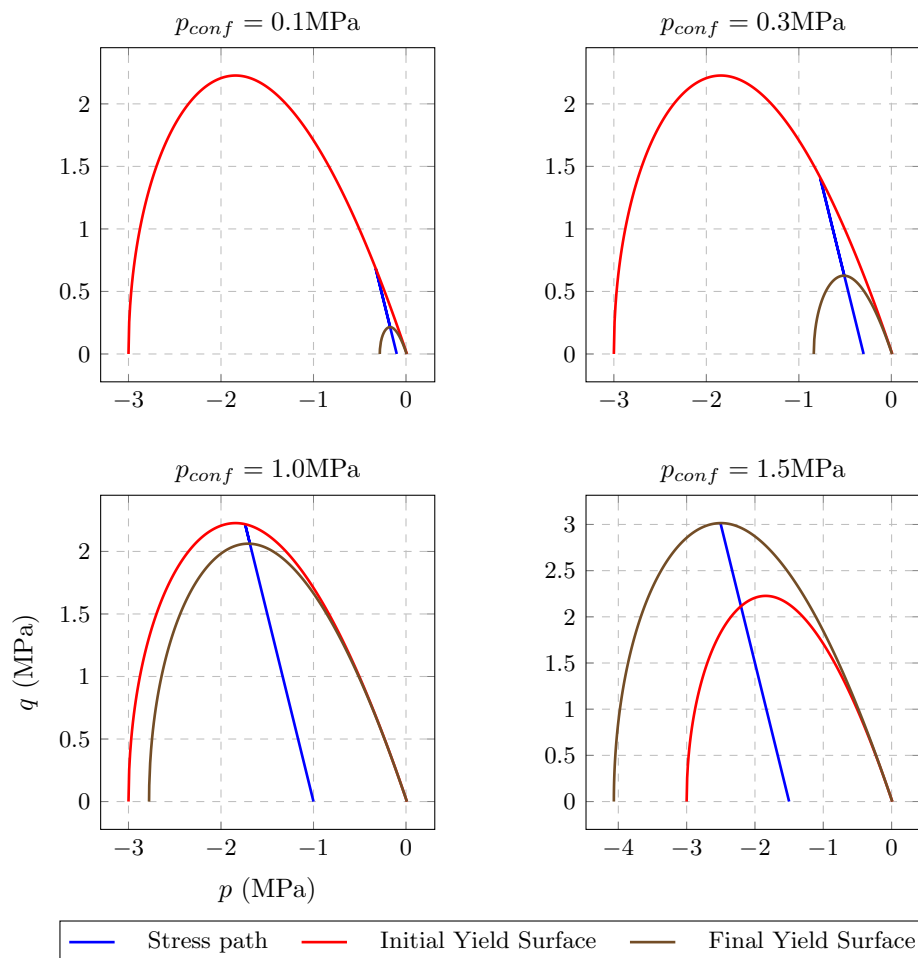


Fig. 4.26 Effect of confining pressure p_{conf} on the final yield surface under CTC condition at fixed initial pre-consolidation pressure (-3MPa). For low confining pressure (0.1-1.0MPa), the stress path approaches the shear side of initial yield surface, resulting in the shrinkage of yield surface towards critical state condition. For high confining pressure (1.5MPa), the stress path approaches the compression side of initial yield surface, resulting in the expansion of yield surface towards critical state condition.

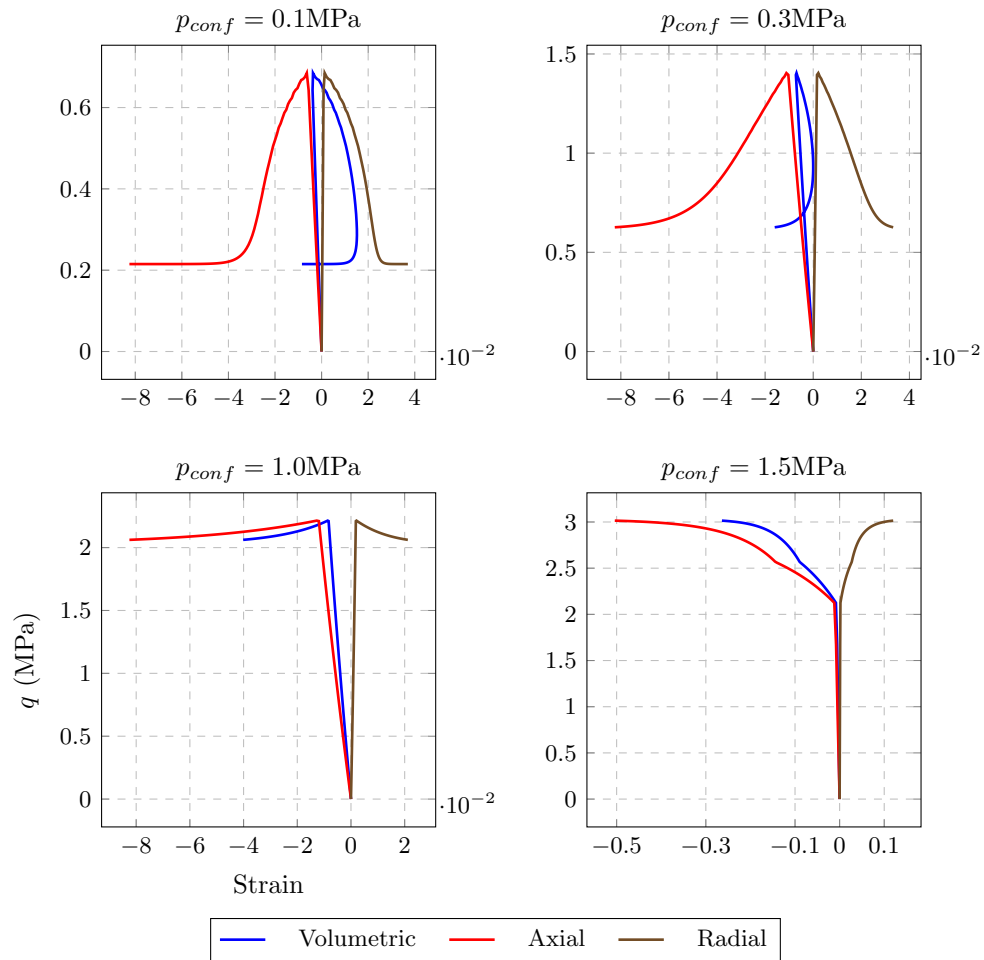


Fig. 4.27 Effect of confining pressure p_{conf} on the evolution of volumetric, axial, and radial strains under CTC condition. Positive radial strain, negative volumetric and axial strains recovered. Strain hardening is observed for $p_{conf} = 1.5 \text{ MPa}$, which corresponds to expansion of yield surface.

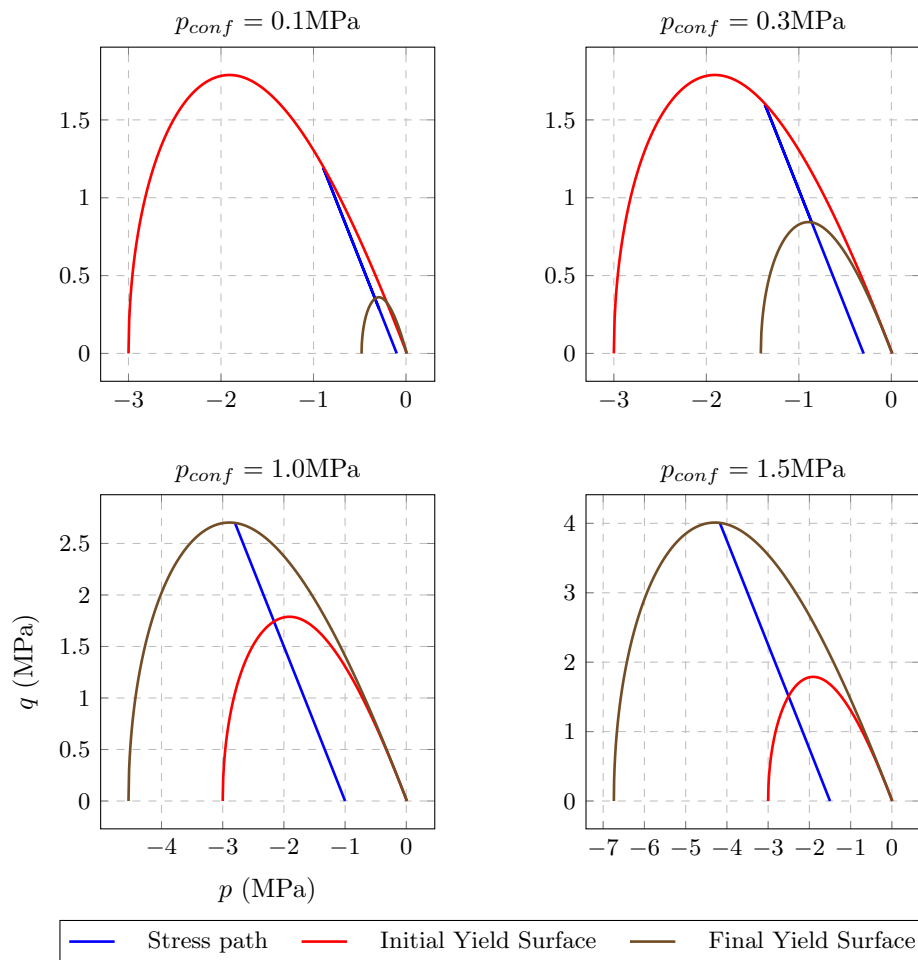


Fig. 4.28 Effect of confining pressure p_{conf} on the final yield surface under TXE condition at fixed initial pre-consolidation pressure (-3MPa). For low confining pressure (0.1-0.3MPa), the stress path approaches the shear side of initial yield surface, resulting in the shrinkage of yield surface towards critical state condition. For high confining pressure (1.0-1.5MPa), the stress path approaches the compression side of initial yield surface, resulting in the expansion of yield surface towards critical state condition. Note that, because the stress path slope in TXE condition is lower than the CTC counterpart, plastic compression takes place at relatively lower confining pressure (i.e. $p_{conf} = 1.0\text{MPa}$), compared to CTC case.

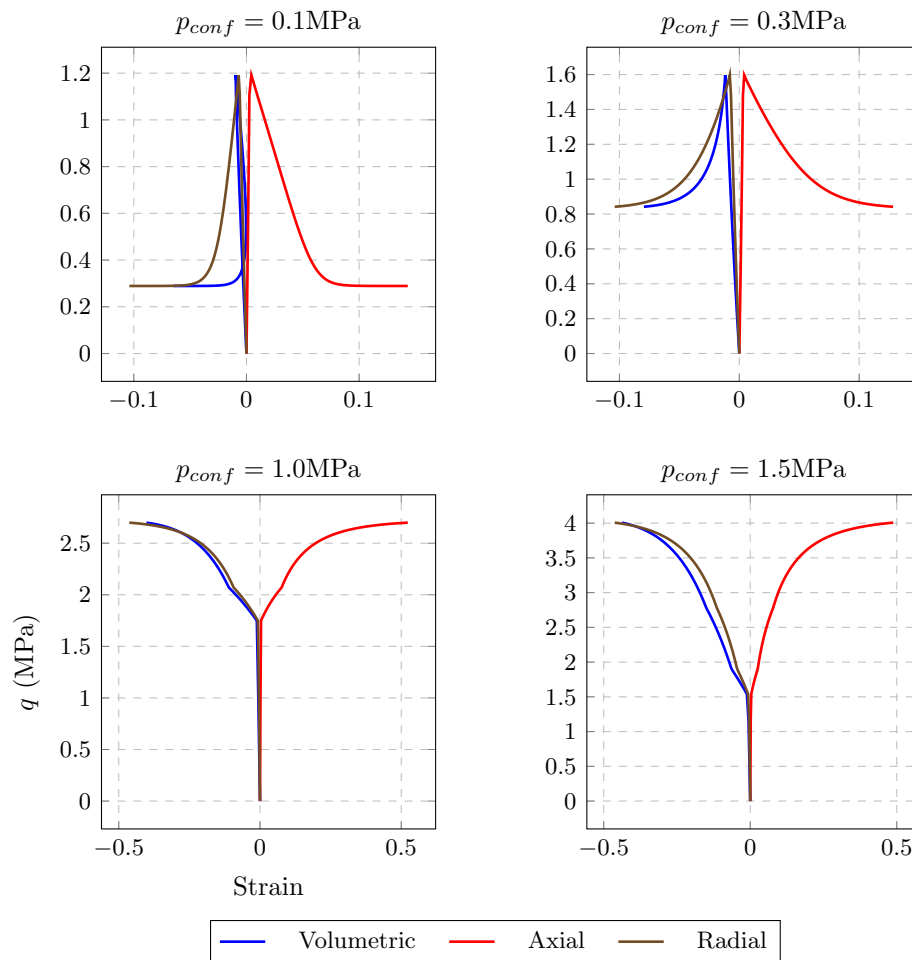


Fig. 4.29 Effect of confining pressure p_{conf} on the evolution of volumetric, axial, and radial strains under TXE condition. Positive axial strain, negative volumetric and radial strains recovered. Strain hardening is observed for $p_{conf} = 1.0\text{MPa}$ and $p_{conf} = 1.5\text{MPa}$, which corresponds to expansion of respective yield surface.

4.8.2 Elastoplastic-Fracture Model

The desiderata of this test is to demonstrate the effect of coupled strength which is proposed in the current elastoplastic-fracture model. A block (size 1m x 1m, with material properties listed in Table 4.3) is subjected to prescribed displacement on its right boundary (Figure 4.30). The cohesion is reduced linearly to 0 as the effective plastic strain $\bar{\epsilon}^p$ attains 1.0. Two simulation groups are considered: monotonic and cyclic loadings.

Properties	Value
Porosity	0.35
Young's modulus (GPa)	20
Poisson's ratio	0.20
Cohesion (MPa)	1.0
Friction parameter β ($^\circ$)	30.164
Dilation parameter β ($^\circ$)	30.164
π -plane correction parameter β_0	0.60
π -plane correction parameter α	0.25
Tensile strength f_t (MPa)	1.0
Fracture energy G_f (Pa.m)	200

Table 4.3 Material properties for elastoplastic-fracture 1D element demonstration

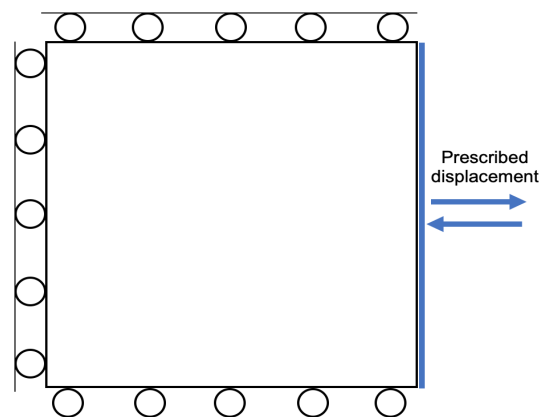
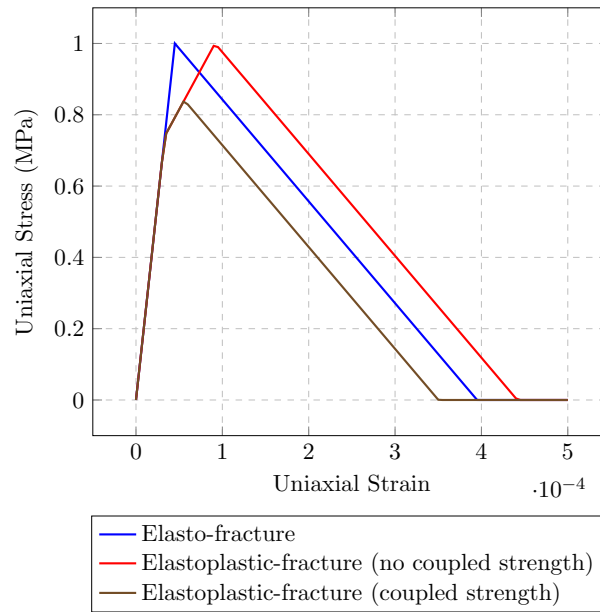
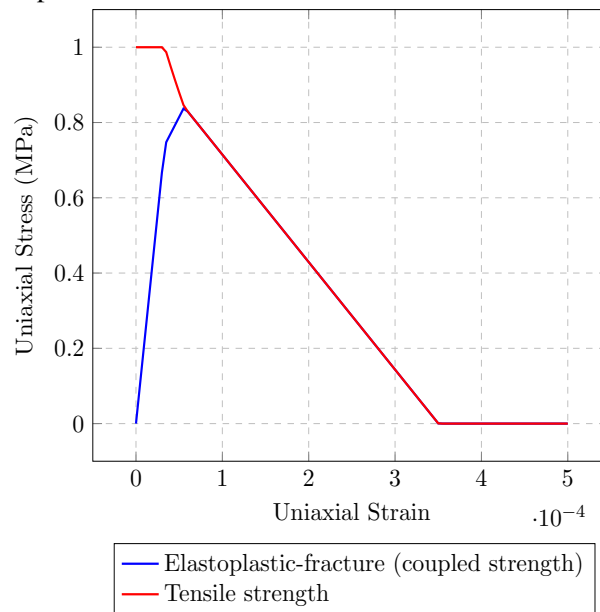


Fig. 4.30 A block of size 1m by 1m is subjected to prescribed displacement on the right side under the boundary conditions as illustrated in the figure

The results for monotonic loading are summarised in Figure 4.31. A total displacement of 0.5mm is loaded in 1.0s. It is noted that, without considering the coupling effect of tensile strength-cohesion, the final critical fracture strain is larger than the quasi-brittle model. The coupled strength effect is introduced by setting $\eta_1 = 0.0001$, thereby reducing the tensile strength as plastic deformation takes place. Assuming constant fracture energy, the final critical fracture strain is smaller than the quasi-brittle model.



(a) Comparison of stress-strain behaviour for different scenario



(b) Reduction of tensile strength during plastic deformation

Fig. 4.31 Effect of coupled tensile strength-cohesion on the stress-strain constitutive behaviour under monotonic loading condition

As for the second simulation group, the same model is used but the right boundary is now prescribed with cyclic displacement, as listed in Table 4.4. Three values of η_1 are tested: 0.0001, 0.00005, and 0.00001. The results are displayed in Figure 4.32. Smaller η_1 contributes to larger change in tensile strength, which explains the tensile strength is close to

the yield stress for the smallest η_1 in the plot. The plastic deformation during compression also triggers another tensile strength reduction due to the degradation of cohesion. When the block is subjected to extension again, the block associated with the lowest η_1 fails at much lower tensile strength compared to the one before compression.

Time (s)	Horizontal Displacement (mm)
0.00	0.000
0.25	0.125
0.50	-0.050
1.00	0.500

Table 4.4 Prescribed cyclic displacement

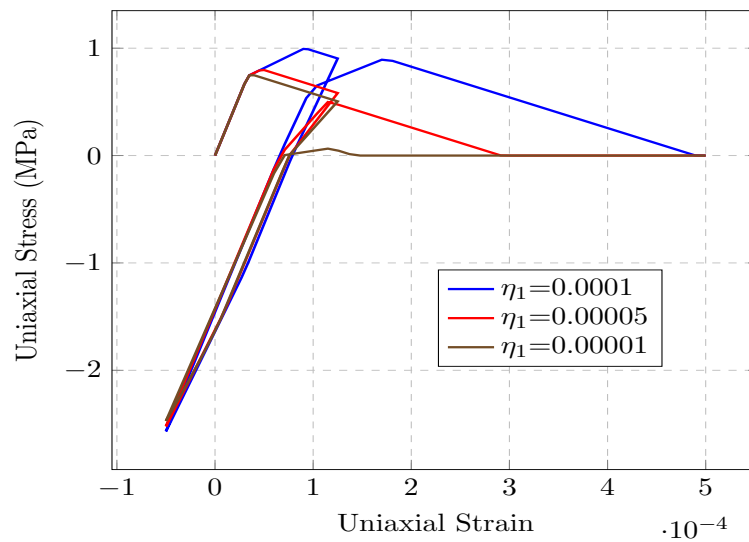


Fig. 4.32 Stress-strain behaviour due to cyclic loading at different level of η_1

Chapter 5

Numerical Examples: Lab-scale Test Simulations

5.1 Introduction

This chapter presents a series of numerical tests with the aim of measuring the performance of the current codes to predict the global material response (e.g. limit load of bearing capacity, size effect on borehole collapse pressure) as well as development of local material response (e.g. crack initiation/propagation/coalescence, spatial/temporal evolution of pore fluid pressure in hydromechanical analysis, and the development of strain localisation in thrust fault formation). To achieve the objectives, all numerical results are compared with available analytical solutions (bearing capacity of strip footing, uniaxial consolidation and sedimentation of soil column) and experimental observations (crack propagation and coalescence, influence of size effect on borehole instability, uniaxial consolidation with variable permeability, and formation of thrust fault).

5.2 Bearing Capacity of Strip Footing

5.2.1 Introduction

In this example, a settlement analysis of a strip footing problem (Figure 5.1) is simulated. Strip footing is used to spread the weight of overlying wall across the soil it makes contact with. Drucker-Prager model is used to model the soil behaviour, and the predicted limit load

is compared against Prandtl's solution [138], given by

$$\frac{P_{lim}}{c} = \cot \phi \left(\frac{1 + \sin \phi}{1 - \sin \phi} e^{\pi \tan \phi} - 1 \right). \quad (5.1)$$

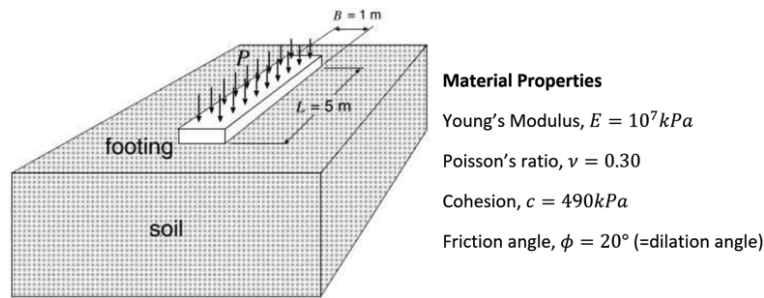


Fig. 5.1 Problem definition of strip footing using Drucker-Prager model [54]

It is known that the application of Prandtl's solution is very limited in the design practice. One of the limitations is that the bearing capacity is zero for cohesionless material. This is equivalent to assuming that the soil is weightless. Nonetheless, the desiderata is only to investigate the performance of Drucker-Prager model under the constraints of Prandtl's solution:

- The model is treated as plane strain problem.
- Associative plastic flow model is assumed, i.e. $\beta = \psi$.
- Cohesion d and friction angle β are constants.
- The π -plane correction factor is unity, i.e. $g = 1$.

Since the material properties (cohesion c and friction angle ϕ) are given in the context of Mohr-Coulomb model, their equivalent values (d and β) in $p - q$ plane as required by the current Drucker-Prager model requires further assumptions. In the following simulations, the effect of the following two separate idealisations are considered:

1. Predicting identical limit load as Mohr-Coulomb criterion under plane strain conditions
2. Predicting limit load by assuming that Drucker-Prager yield locus coincides with the outer edges of the Mohr-Coulomb yield locus

5.2.2 Model Setup and Material Parameters

Due to geometric symmetry, only half of the full domain is simulated. A square block (Figure 5.2) of length 5m is discretised using 4-noded standard linear elements in three mesh sizes, i.e. 0.1m , 0.0625m , 0.05m . The corresponding critical time steps are, respectively, $4(10^{-5})\text{s}$, $2.5(10^{-5})\text{s}$, and $2(10^{-5})\text{s}$. In the current simulation, the time step size for all models is set as 10^{-5}s , producing 100000 time steps in 1s .

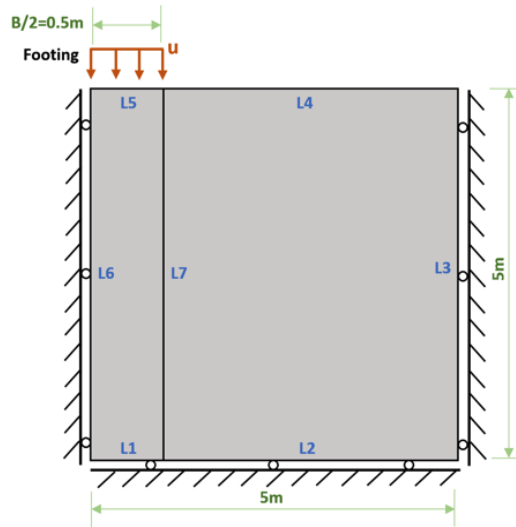
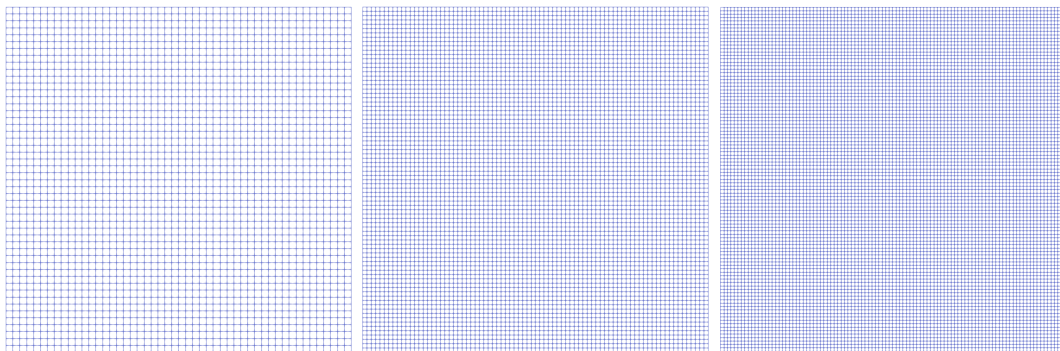


Fig. 5.2 Geometry and boundary conditions of strip footing simulation domain



(a) Mesh size = 0.1m , (b) Mesh size = 0.0625m , (c) Mesh size = 0.05m ,
2500 elements 6400 elements 10000 elements

Fig. 5.3 Different mesh sizes to be simulated in the strip footing problem

The block is modelled such that the left and right boundaries are constrained in horizontal direction, while the bottom boundary is constrained in vertical direction. The left boundary represents the symmetry line of the full model. A displacement boundary condition u is prescribed on L5, so that u increases linearly from 0 to 5mm in 1s .

The given material properties are

$$\phi = 20^\circ; \quad c = 490kPa.$$

If the Drucker-Prager model is to predict identical limit load as Mohr-Coulomb criterion under plane strain conditions, then using (4.29), we obtain

$$\beta = 30.16^\circ; \quad d = 782.4kPa.$$

If Drucker-Prager yield locus coincides with the outer edges of the Mohr-Coulomb yield locus, then using (4.22), we obtain

$$\beta = 37.67^\circ; \quad d = 1039.4kPa.$$

By having $g = 1$ and constant material parameters (independent of $\bar{\epsilon}^p$), the Drucker-Prager model is now simplified as

$$\Phi = q + p \tan \beta - d. \quad (5.2)$$

5.2.3 Results

It is clear from the outcome (Figure 5.4) that the plane strain assumption outperforms the Mohr-Coulomb outer edge assumption. The latter predicts relatively high value of P_{lim}/c (≈ 34.85), which is about 35% above the Prandtl's solution. Such finding is also reported in [54]. On the other hand, given the same mesh size and time step size, the error given by the plane strain assumption is about 0.12% (Figure 5.5). As the mesh size decreases, the numerical solution approaches the analytical solution asymptotically. Such convergence behaviour is illustrated in Figure 5.6.

As shown in Figure 5.7 and 5.8, the similarity between the contour of plastic strain (as well as its rate) and the Prandtl's failure mechanism indicates that the soil behaviour under the assumption of Prandtl's solution is successfully predicted by Drucker-Prager model. The reason that the plastic strain rate at 0.6s resembling the one at 1.0s implies that the bearing capacity has been reached and the failure mechanism is now dictated by the limit load. In fact, the time evolution of vertical stress begins to plateau at around 0.45s.

Figure 5.9 reveals the discontinuity of vertical stress between the surface subjected to settlement and the one without. It is observed in Figure 5.10 that the region immediately subjected to compressive stress condition undergoes downward velocity and displacement. These vectors then progressively change direction towards the top surface that is not subjected

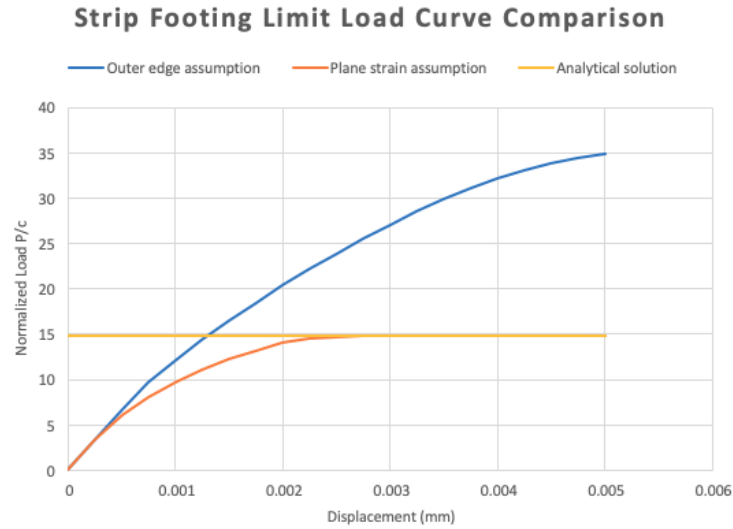


Fig. 5.4 Comparison of outer edge assumption and plane strain assumption

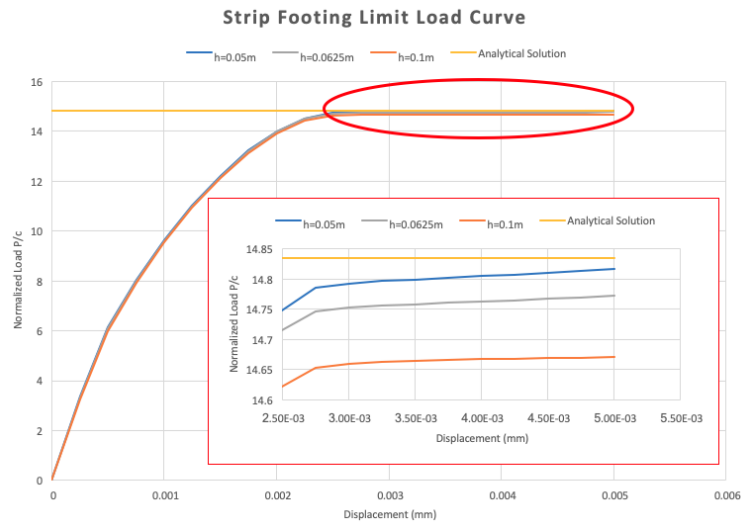


Fig. 5.5 Numerical solution approaching Prandtl’s solution asymptotically as mesh size decreases

to the applied load. Such phenomenon is only active in the region bounded by the plastic strain¹ resembling logarithmic spiral as observed in Figure 5.7.

¹In all results presented in this thesis, legends containing the keyword 'Node' imply that nodal values are derived from the volume-/area-averaged using cell values surrounding the node. For 2D results, the nodal value at node i , represented by s_i , is given by

$$s_i = \frac{\sum_I^{nelm} s_I A_I}{\sum_I^{nelm} A_I},$$

where $nelm$ is the total number of elements surrounding node i and A_I is the area of element I .

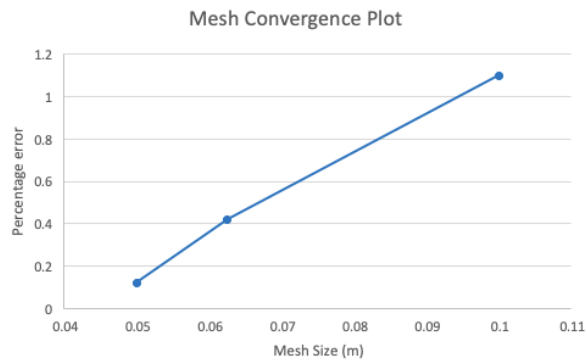


Fig. 5.6 Mesh convergence plot for plane strain assumption

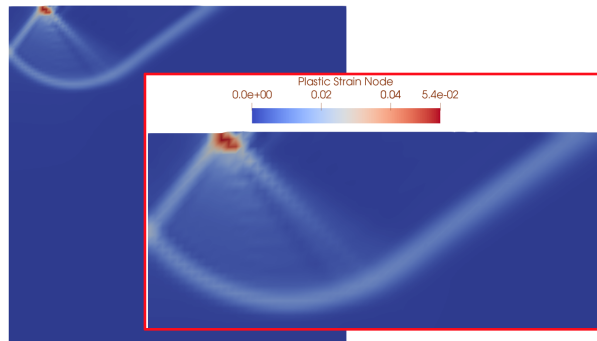


Fig. 5.7 Plastic strain contour when $u = 5mm$

Although the aforementioned results are not new, this test shows that the Drucker-Prager subroutine in ParaGeo solver produces excellent result for the plane strain problem with the correct conversion of cohesion c and friction angle ϕ into its equivalent values (d and β) in $p - q$ meridional plane.

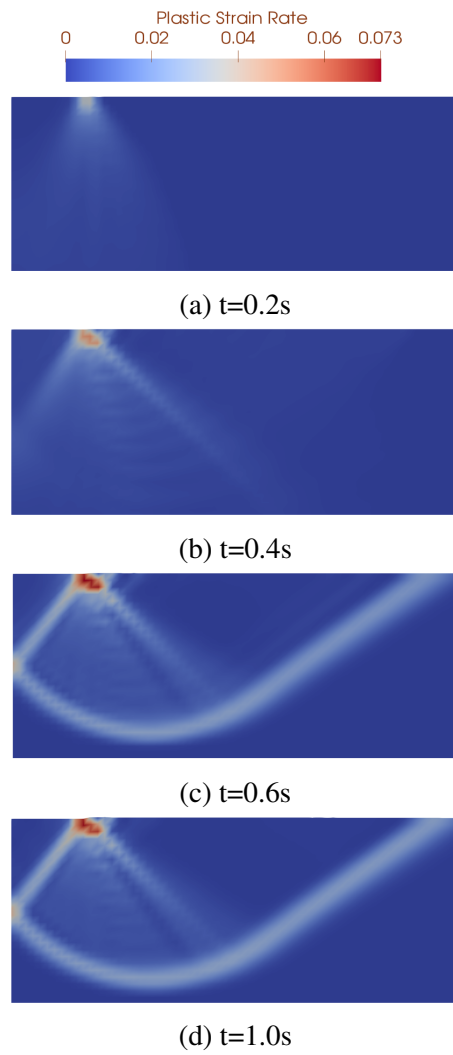


Fig. 5.8 Evolution of plastic strain rate as settlement increases

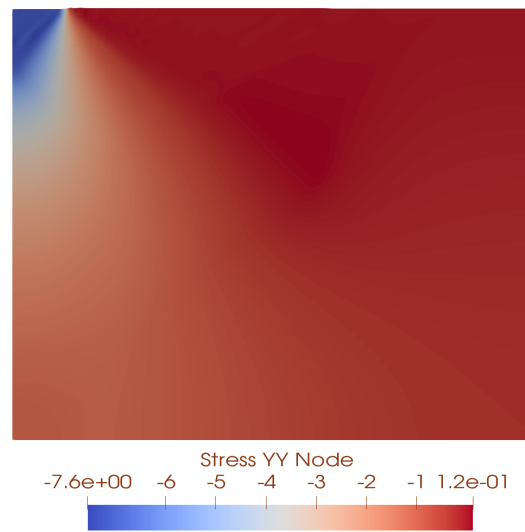
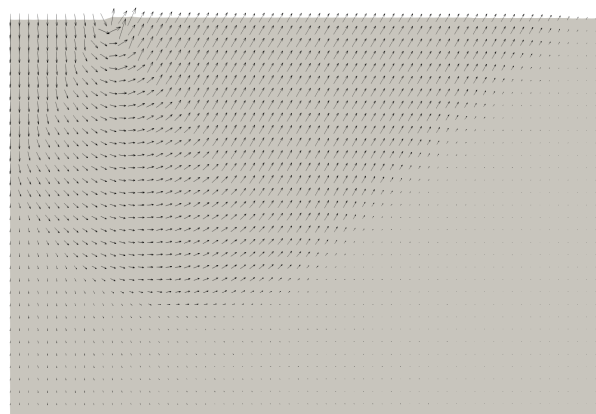
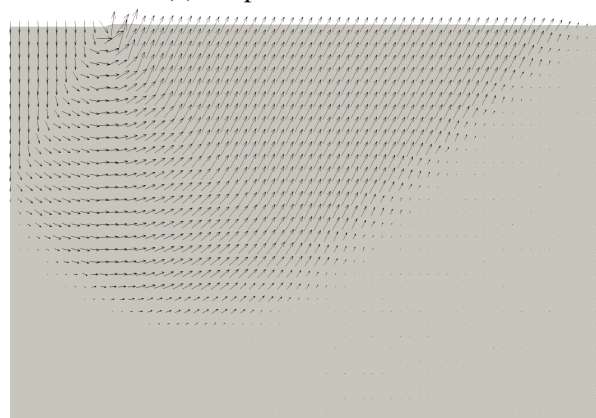


Fig. 5.9 Vertical stress σ_{yy} as failure progresses during limit load



(a) Displacement vector



(b) Velocity vector

Fig. 5.10 Displacement and velocity vectors during failure of strip footing

5.3 Crack Propagation and Coalescence in a Specimen with Pre-existing Inclined Fault

5.3.1 Introduction

Evolution of geologic activities is inevitably accompanied by the formation of discontinuities, such as faults. Given the appropriate stress condition in the environment, new cracks may form and propagate further to coalesce with other cracks. This results in the reduction [148] of overall strength, and subsequently causes the instability of natural slope [64, 73]. Extensive experimental [86, 166, 185, 186, 148, 62, 102, 184, 133, 168, 190, 30, 18, 19, 141] and simulation [158, 159, 51, 176, 159, 148, 62, 20] studies on the coalescence of crack with other fractures have been conducted. The fracture criteria used for the formation of crack include maximum tangential stress [66], maximum energy release rate [88] and minimum energy density theory [156], whereas damage model [141] and F-criterion [155] are applied for modelling crack coalescence.

The goal of the current simulation study is to simulate the initiation and propagation of wing crack and secondary crack (Figure 5.11) originated from a pre-existing inclined fracture and the coalescence behaviour under compressive stress condition. Rotating crack model is used to simulate Mode I failure (tensile wing crack), whereas elastoplastic model can be used to capture Mode II failure (secondary crack). In the following simulation studies, the rock model is assumed to be isotropic².

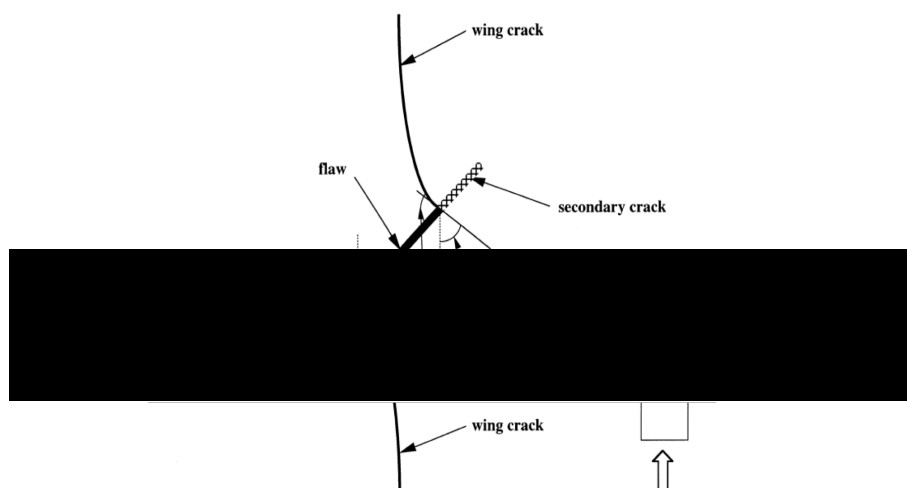


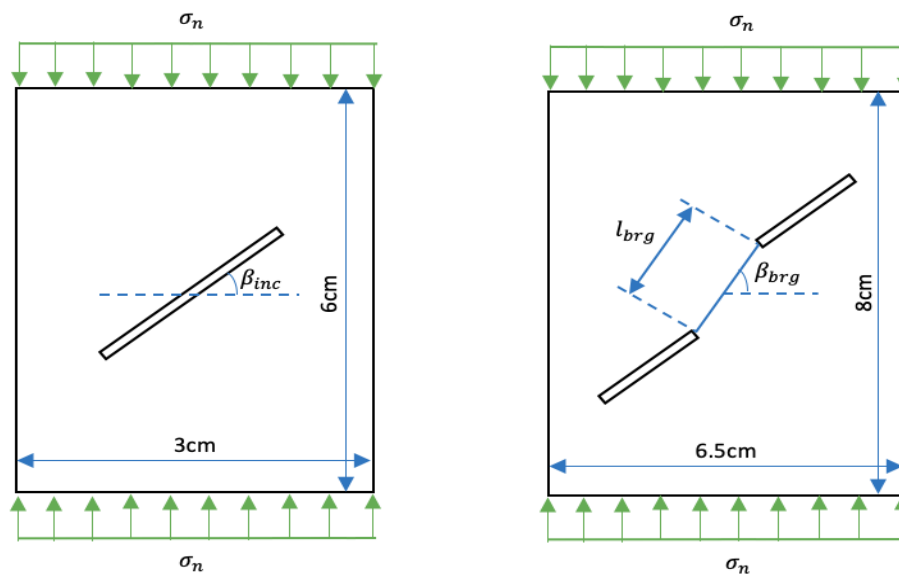
Fig. 5.11 Illustration of crack type in the vicinity of pre-existing fracture under compressive stress condition. Figure obtained from [19].

²Tensile strength being $f_{t1} = f_{t2} = f_t$

5.3.2 Rock Specimen Types

There are two types of rock specimen to be considered:

- Type 1 Specimen: With single pre-existing fracture
- Type 2 Specimen: With two pre-existing fractures



(a) Type 1 rock specimen with single pre-existing fracture (b) Type 2 rock specimen with two pre-existing fractures

Fig. 5.12 Types of rock specimen used in the current study

With reference to Figure 5.12, Type 1 specimen is used to simulate the formation of cracks with the influence of the inclination angle (β_{inc}) and cohesive strength (d) of the material. Type 2 specimen is used to simulate the coalescence of cracks by varying the bridge angle (β_{brd}).

In the following, the rock specimen is firstly assumed to be quasi-brittle so that it behaves as elasto-brittle material. This is effectively achieved by setting an unreasonably high value of cohesive strength so that the stress path can only reach the Rankine yield surface before Drucker-Prager yield surface. The material properties are listed in Table 5.1. All specimen are monotonically loaded with σ_n at a rate of 10GPa/s until full fracture with a time step size of 10^{-6} s.

The effect of cohesive strength will also be considered for Type 1 and Type 2 rock specimens. The corresponding initial elastoplastic properties (unless specified otherwise) are listed in Table 5.2. It is assumed that when reaching 1% of effective plastic strain, cohesion

Material properties	Value
Grain density (kg/m^3)	2710
Young's modulus (GPa)	3.3
Poisson's ratio	0.19
Material length scale (mm)	0.5
Uniaxial tensile strength (MPa)	3.17
Fracture energy, G_f (Pa.m)	1.0

Table 5.1 Properties of quasi-brittle material

d_0 reduces linearly to 0, β_0 to 15° , and ψ_0 to 0° . Note that non-associative plastic flow is applied here.

Material properties	Value
Cohesion, d_0 (MPa)	9.0
Friction angle, β_0 ($^\circ$)	17.8
Dilation angle, ψ_0 ($^\circ$)	17.8

Table 5.2 Initial properties of elastoplastic material

5.3.3 Test 1: Formation of Tensile Wing Crack

In this test, only Type 1 rock specimen is used. The length of the pre-existing fracture is 1.5cm, with an aperture size of 0.1mm. The inclination angle is 45° . The purpose of this test is to benchmark the nature of the formation of tensile wing crack. It should be fail due to tensile failure, and should propagate following curvilinear path towards the direction parallel with the major principal stress.

These characteristics are observed in the simulation results (Figure 5.13). Before new crack is formed, stress concentration is already observed at the upper right and bottom left tips of the pre-existing fractures. When the principal stress in this localised region reaches the value of tensile strength, softening take places before full fracture is obtained. As the loading continues, the softening process changes its path towards the direction of external loading, thus forming curvilinear propagation path which is the main characteristic of tensile wing crack. During this process, maximum principal stress 1 is observed to overlap with the propagation path. We thus deduce that the wing crack is indeed a manifestation of localised tensile failure.

Highly localised compressive stress field is observed at the tip of pre-existing fracture (Figure 5.14). It is situated adjacent to the starting point of tensile wing crack. The compressive stress field in this region is correlated to the spalling phenomenon as observed in some

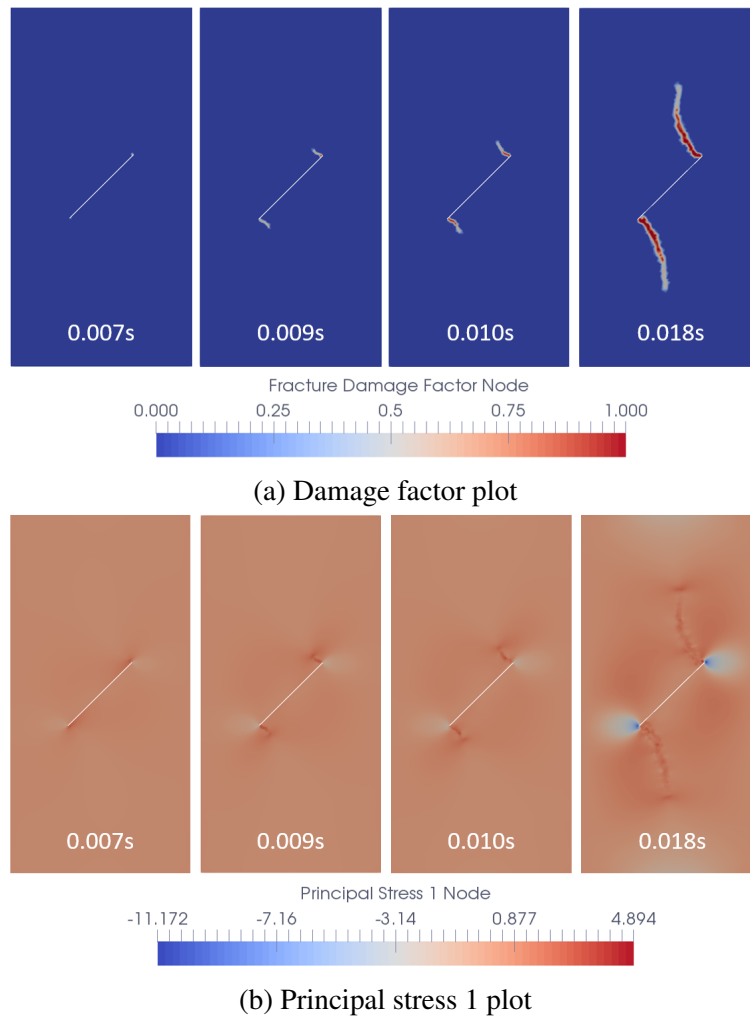


Fig. 5.13 Formation of tensile wing crack. Direction of crack propagation becoming increasingly parallel to the loading direction.

test cases [19], which is not modelled in the current plane strain models. Also, concomitant to the formation and propagation of tensile wing crack is the horizontal expansion of the specimen during compression (Figure 5.15). The displacement contour and the velocity vector indicate the pre-cursor of the direction of final rupture.

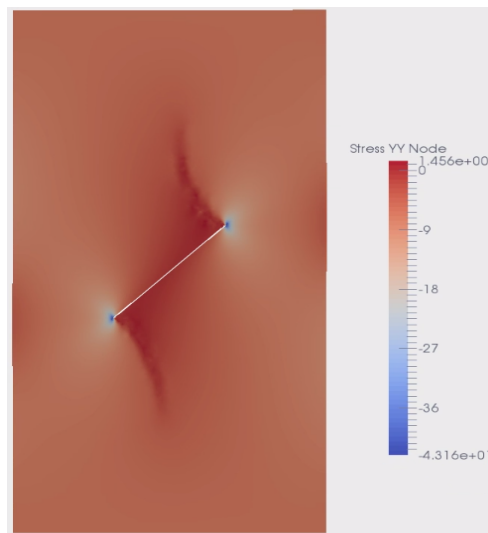
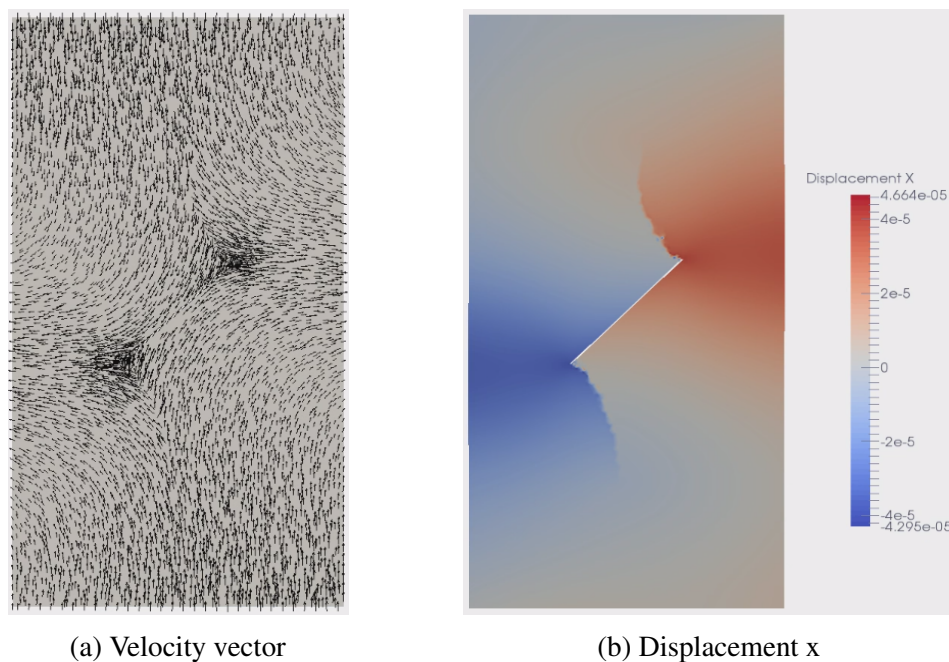


Fig. 5.14 Highly compressive stress field at the tip of pre-existing fracture



(a) Velocity vector

(b) Displacement x

Fig. 5.15 Displacement and velocity field at time 0.018s

The crack pattern is qualitatively comparable to the experimental results by [176], as shown in Figure 5.16. This is despite the fact that different terminology is used; they refer tensile wing crack as secondary crack, which is formed due to shear failure [19]. In this example, localised tensile failure has been successfully captured in a domain that is subjected to compressive stress condition. Overall, this test has demonstrated that the rotating crack

model coded in ParaGeo is able to take into account the rotation of principal stress as new crack is formed.

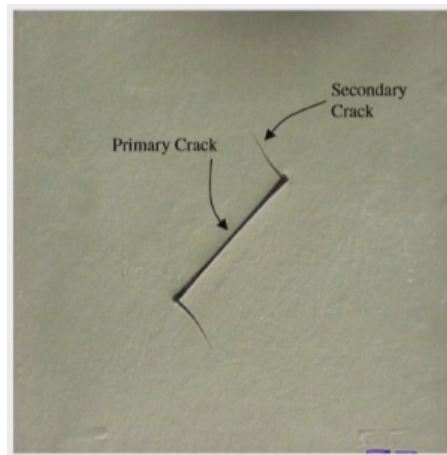


Fig. 5.16 Tensile wing crack created in experiment by [176].

5.3.4 Test 2: Effect of Inclination Angle

It is experimentally observed [176] that the initiation point of tensile wing crack shifts towards the centre of the pre-existing fracture as the inclination angle (β_{inc}) decreases. The goal of this test is to verify the ability of the current code to capture this phenomenon. Same material properties and modelling setup are used, except that the inclination angle is varied (0° , 15° , 30° , 45° and 60°).

The numerical result generally agrees with the experimental findings. When β_{inc} is in the range of $30^\circ - 60^\circ$ (Figure 5.17-5.19), there is no noticeable change of the initiation point of tensile wing crack. However, for $\beta_{inc} = 15^\circ$ (Figure 5.20) and $\beta_{inc} = 0^\circ$ (Figure 5.21), the origin of tensile wing crack has shifted towards the centre of the pre-existing fracture.

As the inclination angle decreases, the effect of external loading gradually extends to the centre of the pre-existing fracture. This can be visualised in Figure 5.23 by the evolution of principal stress 1 as β_{inc} decreases. Since tensile wing crack is the manifestation of tensile failure, its nucleation point has to follow the migration of the largest principal stress 1. The implication is that the overall strength of rock specimen becomes sensitive to the migration of principal stress 1. Figure 5.22 shows the vertical stress to initiate cracking for a given inclination angle. It is observed that $\beta_{inc} = 45^\circ$ corresponds to the weakest rock specimen. Such finding agrees with the laboratory result conducted by [176].

The result of Test 2 is qualitatively supported by experimental observation. It shows that the current code is able to capture the phenomenon whereby the initiation point of tensile

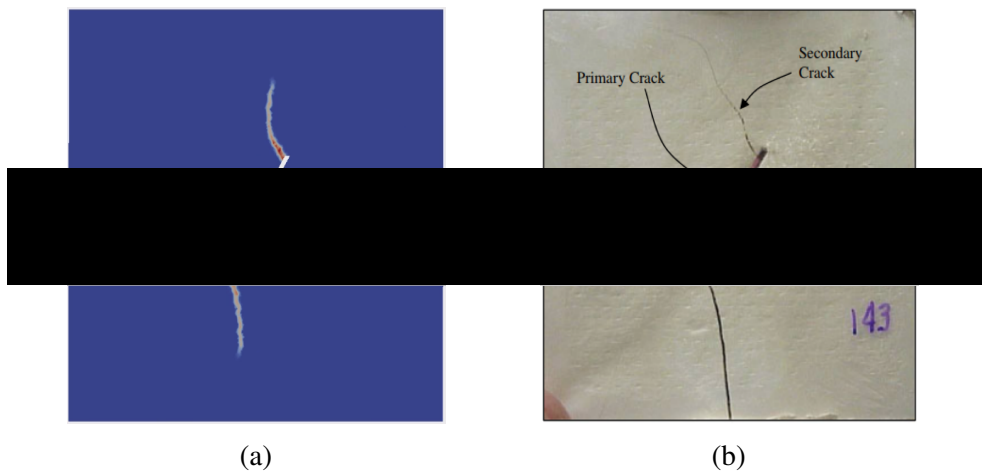


Fig. 5.17 $\beta_{inc} = 60^\circ$. (a) Damage factor (b) Figure obtained from [176]

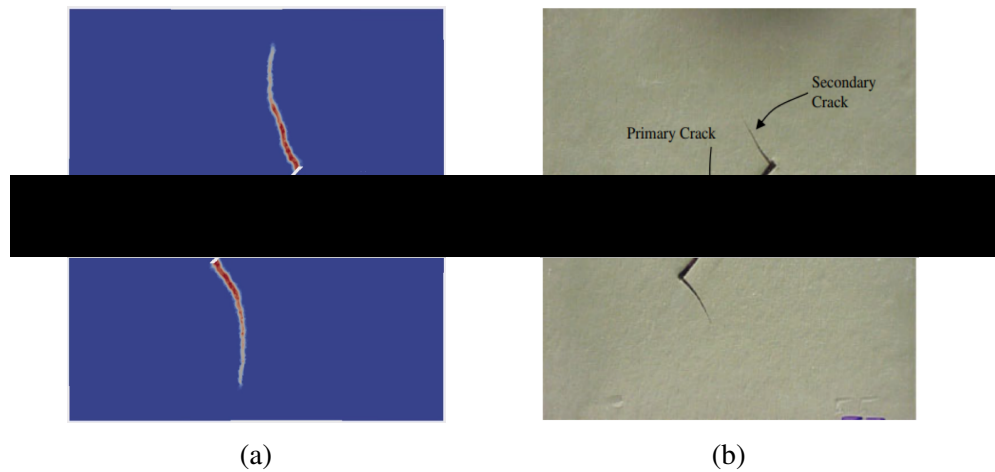


Fig. 5.18 $\beta_{inc} = 45^\circ$. (a) Damage factor (b) Figure obtained from [176]

wing crack shifts towards the centre of the pre-existing fracture as the inclination angle decreases due to the migration of principal stress 1 field.

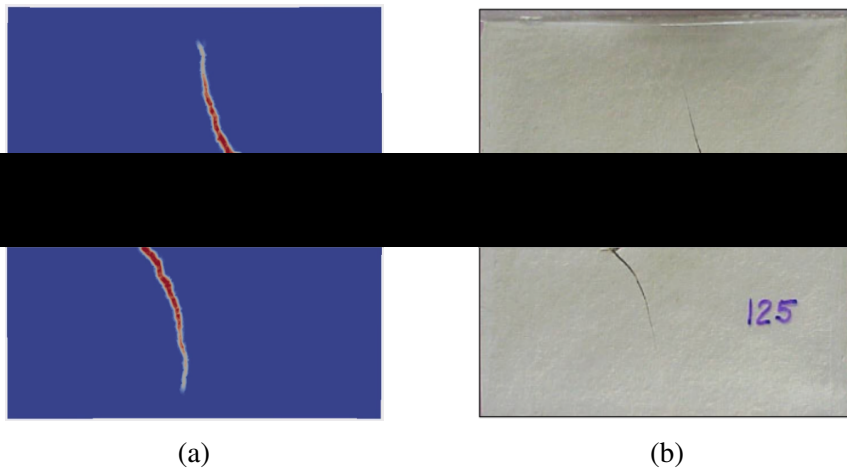


Fig. 5.19 $\beta_{inc} = 30^\circ$. (a) Damage factor (b) Figure obtained from [176]

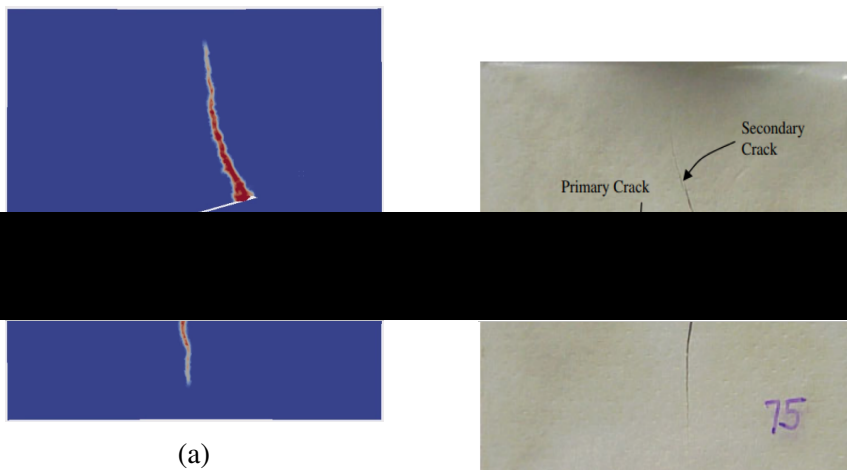


Fig. 5.20 $\beta_{inc} = 15^\circ$. (a) Damage factor (b) Figure obtained from [176]

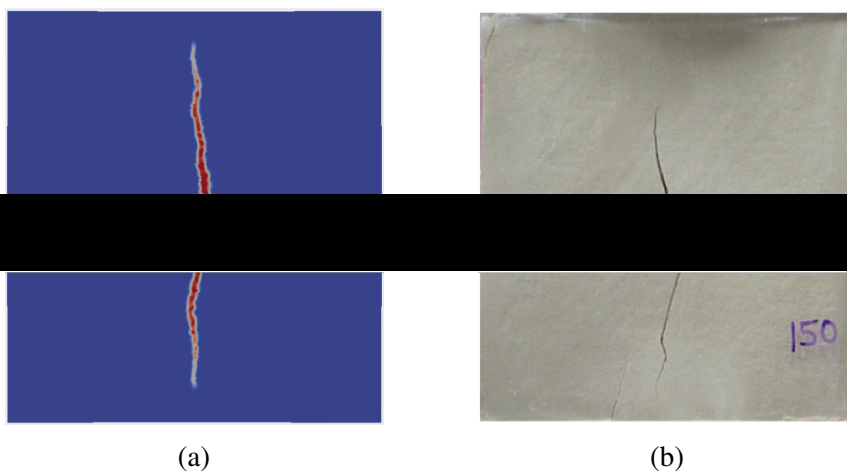


Fig. 5.21 $\beta_{inc} = 0^\circ$. (a) Damage factor (b) Figure obtained from [176]

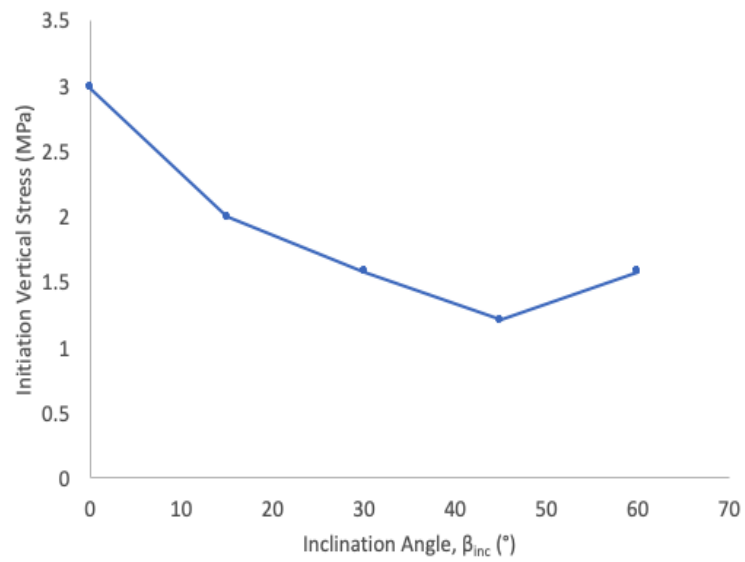


Fig. 5.22 $\beta_{inc} = 45^\circ$ corresponds to the lowest strength of rock specimen. Such finding agrees with the laboratory result conducted by [176].

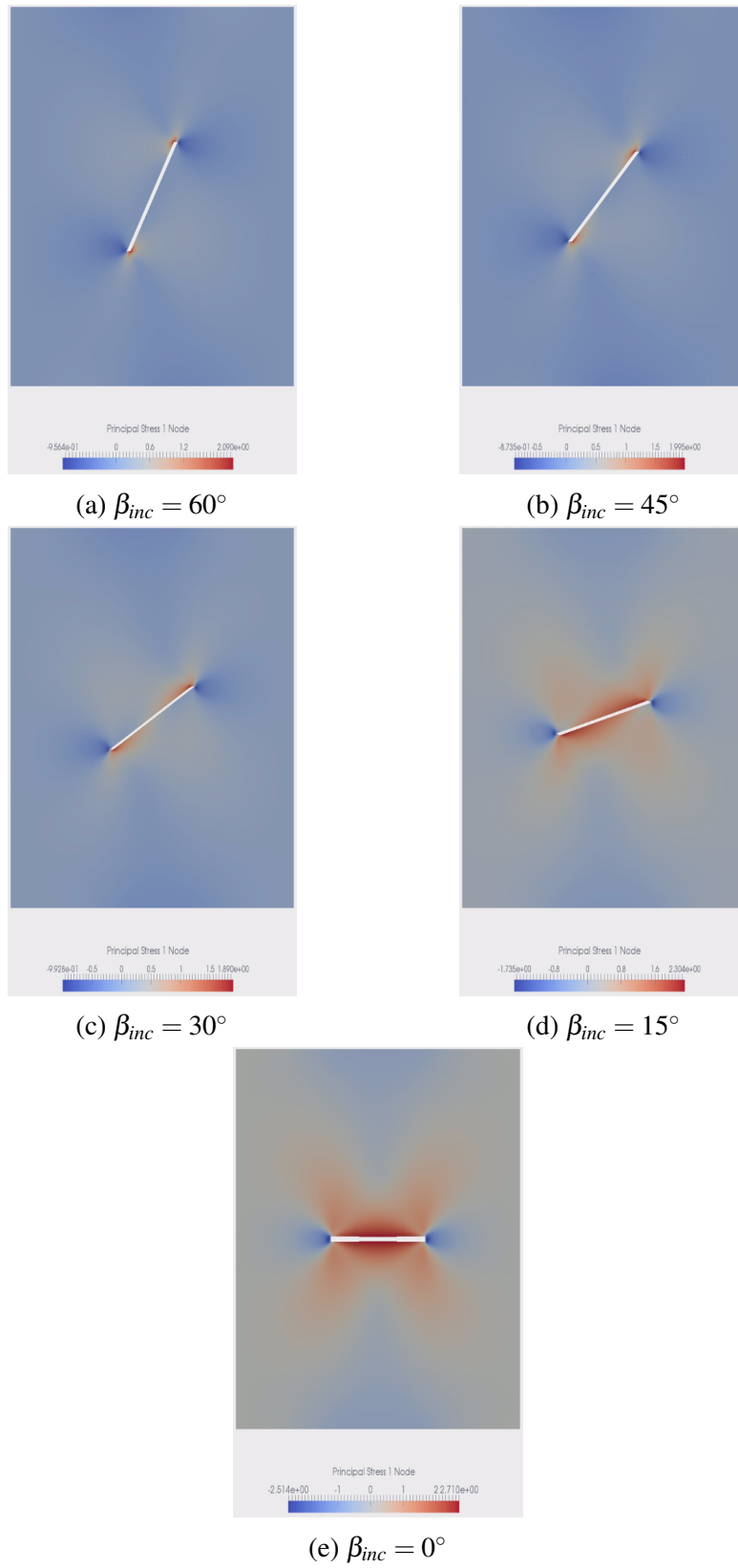


Fig. 5.23 The migration of principal stress 1 as the inclination angle decreases

5.3.5 Test 3: Effect of Cohesive Strength on Secondary Crack

In the previous tests, the material is assumed to be quasi-brittle. Secondary crack (Figure 5.24), which is a manifestation of shear failure [19], does not appear in the simulation result. This is because the material used in the simulation is assigned with unreasonably high cohesive strength.

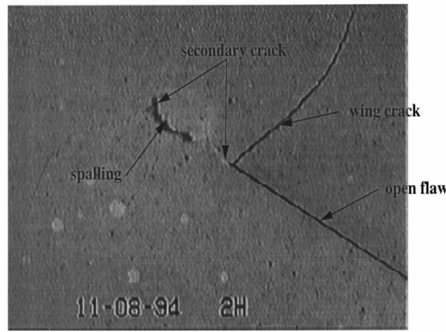


Fig. 5.24 Secondary crack observed in experimental test by [19]

Experiments on the failure behaviour of sample with relatively low cohesive strength have been conducted by [167]. Samples of kaolinite clay were tested, whereby the water content is varied to manipulate the shear strength. All inclination angles of pre-existing fracture ranging from $15^\circ - 75^\circ$ were tested. The key finding is that ductile sample fails at a lower crack propagation angle (β_{inc2}) than a brittle sample does.

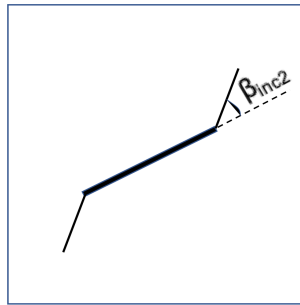


Fig. 5.25 Crack propagation angle as defined in [167]

The goal of this numerical test is to simulate the influence of cohesive strength on the failure behaviour of rock specimen. This is achieved by applying elastoplastic-fracture framework that is discussed in the previous chapter. The coupling factor of cohesion and tensile strength is set as $\eta_1 = 0.01$, whereas the orthotropic tensile strength coupling factor is set as $\eta_2 = 1.0$. In the current simulation, four cases of cohesive strength are considered:

5MPa, 10MPa, 15MPa, and 20MPa. All other detail of material parameters are available in Section 5.3.2. In the following, the load-displacement curves for all specimen are presented. Next, the progressive failure pattern of specimen with initial cohesive strength $d_0 = 10\text{MPa}$ are described, followed by the final failure pattern of all specimen. Lastly, the change of crack propagation angle in response to varying d_0 is demonstrated.

The load-displacement curves from the numerical result shown in Figure 5.26 reflect the constitutive behaviour of specimen with varying initial cohesive strength. All specimen, except for the one with $d_0 = 20\text{MPa}$, are shown to fail at limit load, which is close to their respective initial cohesive strength. The specimen with $d_0 = 20\text{MPa}$ has not failed uncontrollably for the given loading history because its yield surface is sufficiently large.

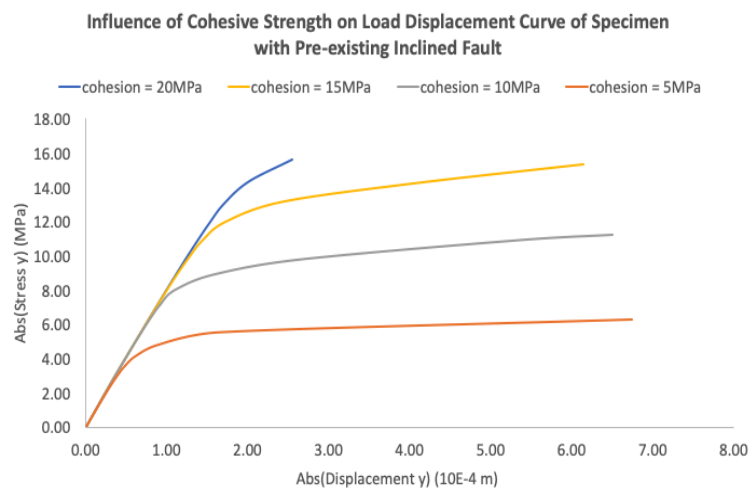


Fig. 5.26 Load displacement curve for specimen with varying initial cohesive strength

Figure 5.27 shows the progressive crack propagation pattern as the external load increases monotonically from the top and bottom boundaries. Unlike previous tests, secondary cracks are also observed after the stable growth of tensile wing crack. Via coupling factor η_1 , plastic deformation reduces local tensile strength, which effectively increases the tendency for tensile failure. Figure 5.28 and 5.29 show that secondary cracks is mostly confined in localised plastic shear zone. The pattern of secondary crack in the numerical result agrees with the physical observation [19], in which the crack originates from the tip of pre-existing fracture and propagates in shear mode. In addition, Figure 5.30 displays large horizontal displacement with higher loading. It can be inferred that the failure mechanism towards final rupture of the specimen at later stage is dominated by increasingly severe shear localisation in secondary crack, rather than the propagation of tensile wing crack. This reasoning is supported by Figure 5.27, in which secondary crack propagates much faster than tensile wing crack.

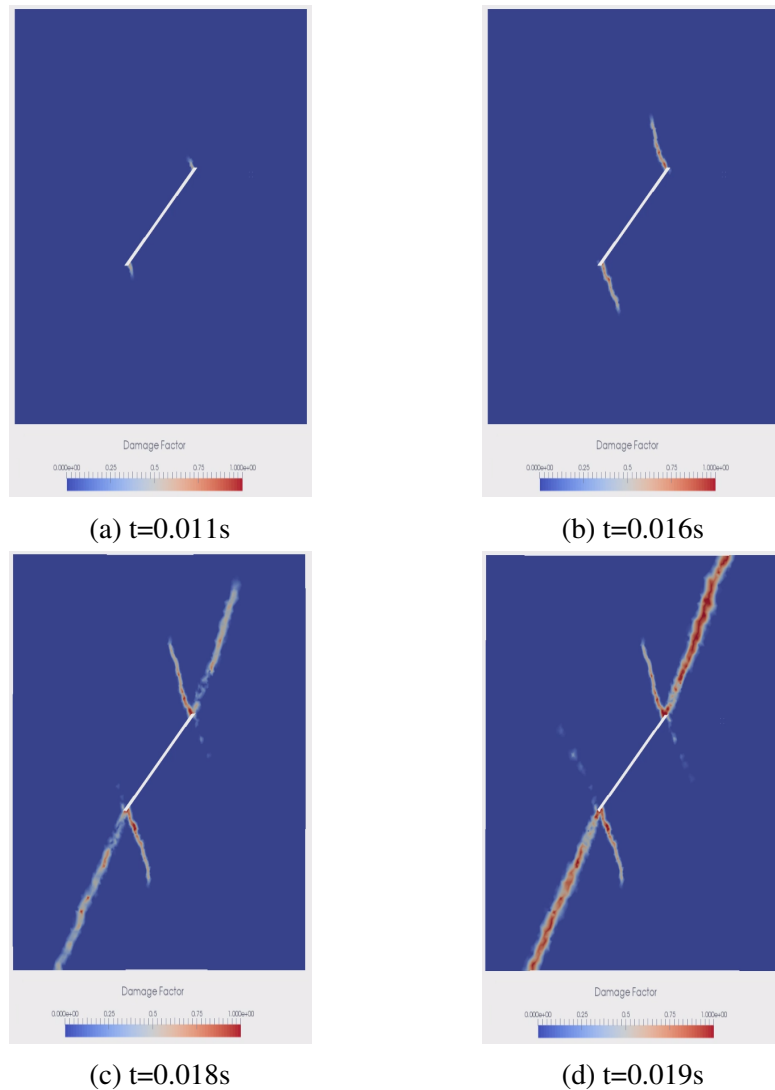


Fig. 5.27 Tensile wing crack and secondary crack propagation of specimen with $\beta_{inc} = 45^\circ$ and initial cohesion as 10MPa

It is important that the constitutive model should be able to reflect the influence of cohesive strength on the behaviour of crack propagation. As shown in Figure 5.31, with the increase of cohesive strength, the propagation of secondary crack tends to approach the direction of external loading. Such propagation behaviour resembles that of tensile wing crack. Hence, it is inferred that, even with the presence of secondary crack, the overall mechanism is increasingly dominated by brittle failure as the cohesive strength increases. On the other hand, at lower cohesive strength, the overall mechanism should be dominated by ductile failure. Figure 5.32 clearly shows that the localisation of shear zone becomes more evident with decreasing cohesive strength.

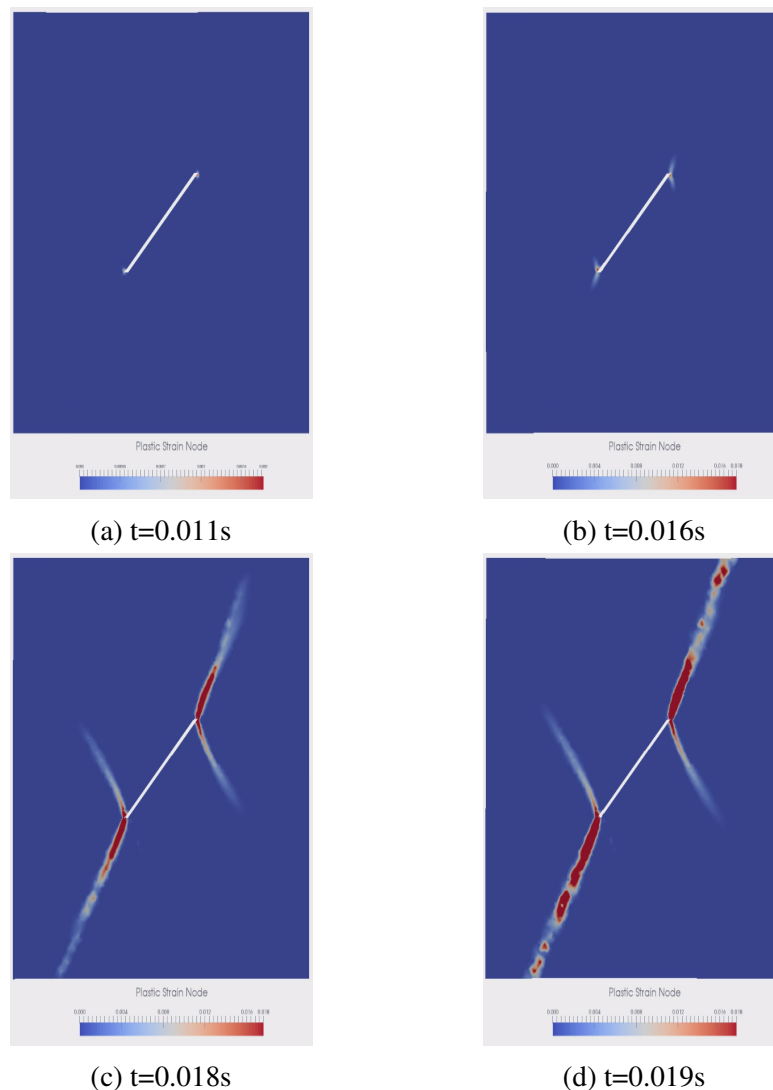


Fig. 5.28 Evolution of plastic strain in specimen with $\beta_{inc} = 45^\circ$ and initial cohesion as 10MPa

In addition, experiments [167] also showed that ductile specimen fails at lower crack propagation angle (β_{inc2}) than that of a brittle specimen. A sample data corresponding to 45° of pre-existing fracture is digitally extracted from [167] and presented in Figure 5.33. As water content increases, the Mohr's circle is driven closer to the yield surface. This effect could be duplicated by manipulating the initial cohesive strength in numerical settings. As the material becomes weaker, the crack propagation angle β_{inc2} becomes lower. This effect is also clearly reproduced, albeit in a slightly different presentation style, in Figure 5.34. For a brittle material, the major crack propagation is led by tensile wing crack and therefore β_{inc2} should be larger than that of a ductile material. The latter is dominated by the propagation

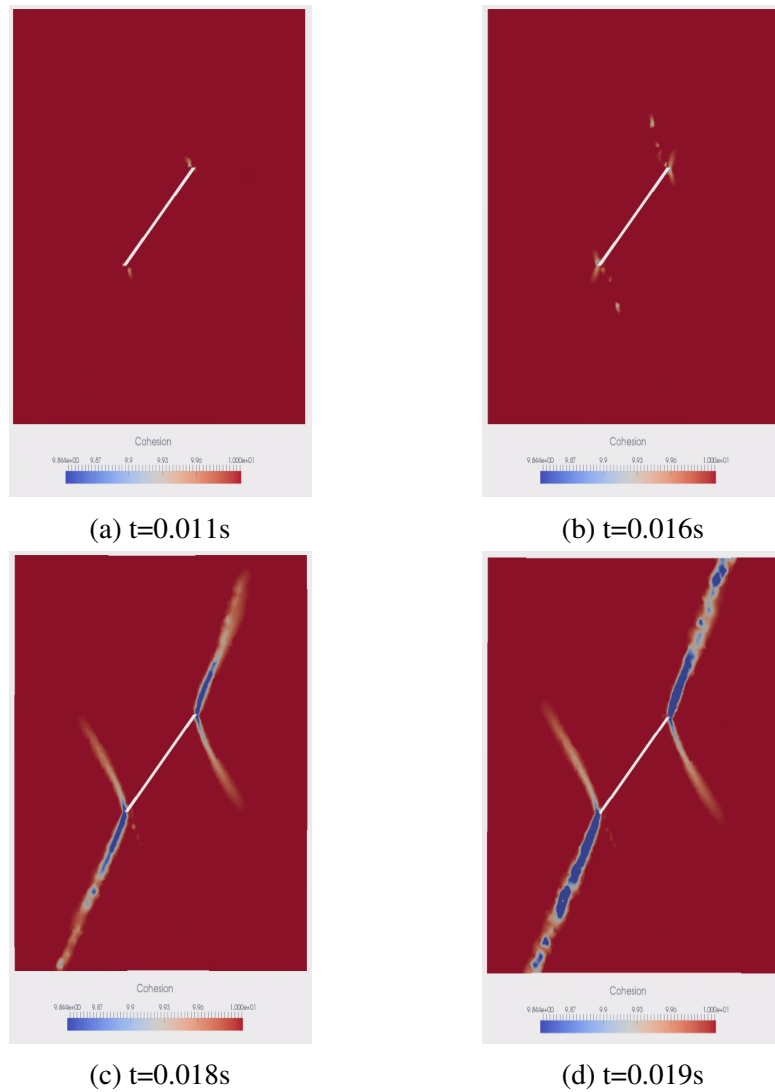


Fig. 5.29 Evolution of cohesive strength in specimen with $\beta_{inc} = 45^\circ$ and initial cohesion as 10MPa

of secondary crack, which is characterised by small value of β_{inc2} . Overall, the numerical results so far have shown that the constitutive model is able to describe the crack propagation behaviour for both ductile and brittle materials.

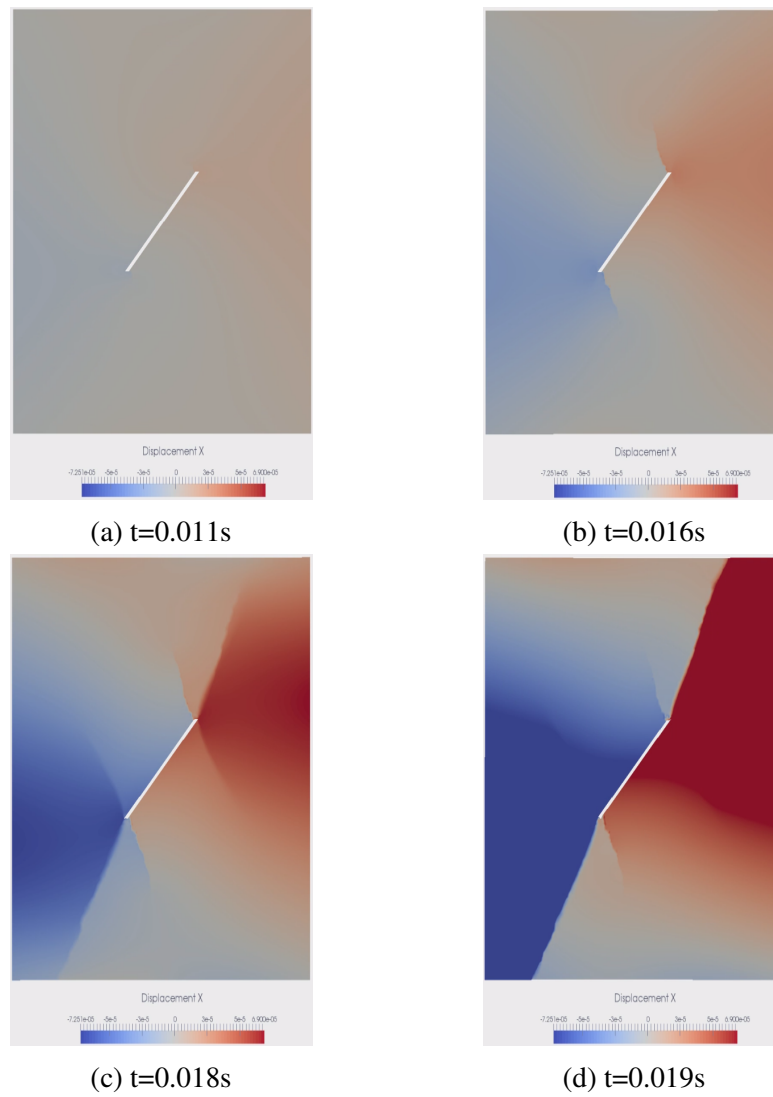


Fig. 5.30 Horizontal displacement of specimen with $\beta_{inc} = 45^\circ$ and initial cohesion as 10MPa

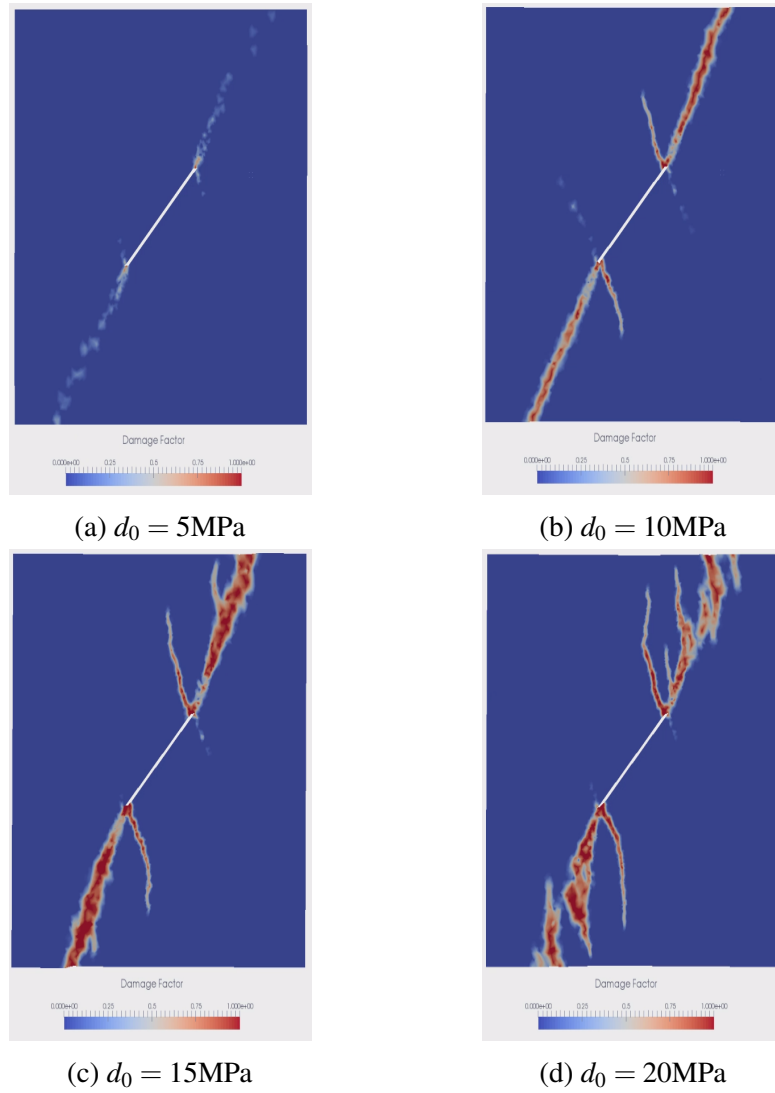


Fig. 5.31 Crack propagation pattern for specimen with different initial cohesive strength

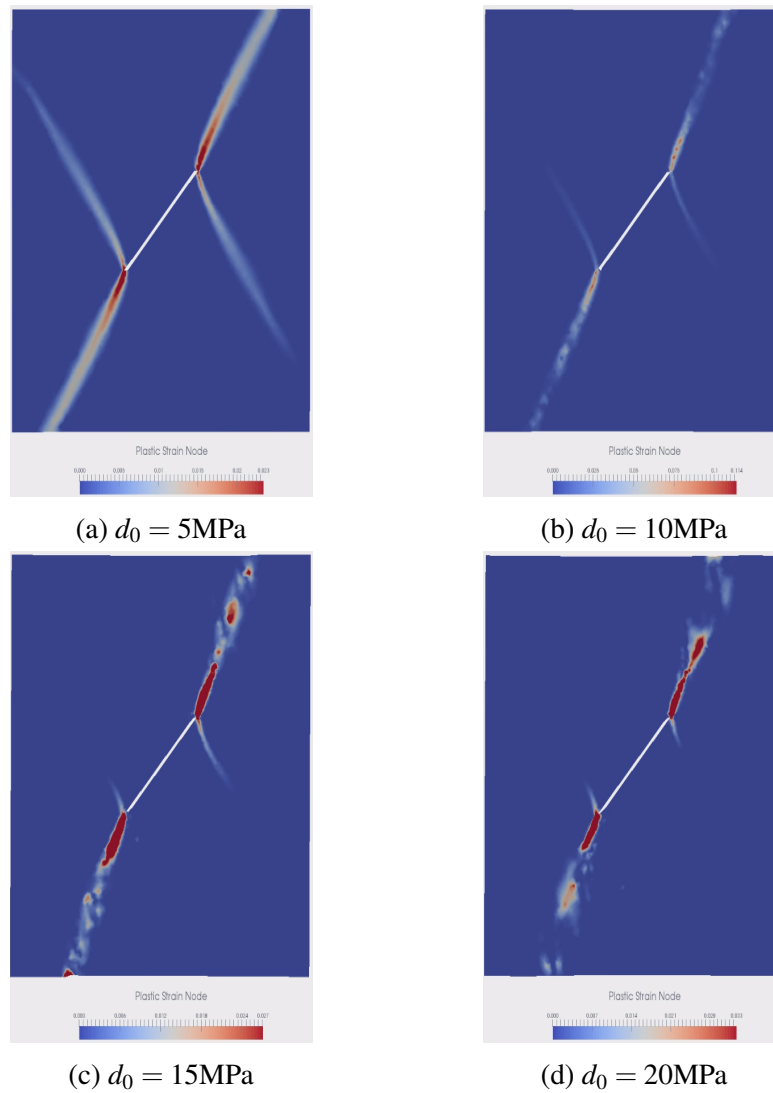


Fig. 5.32 Plastic strain distribution for specimen with different initial cohesive strength

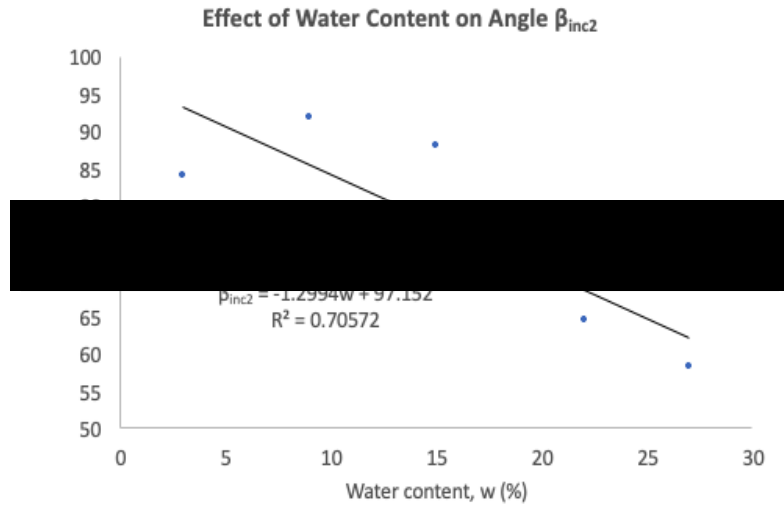


Fig. 5.33 (Tested on specimen having 45° of inclination angle) Crack propagation angle decreases as water content is increased. Experimental data obtained from [167].

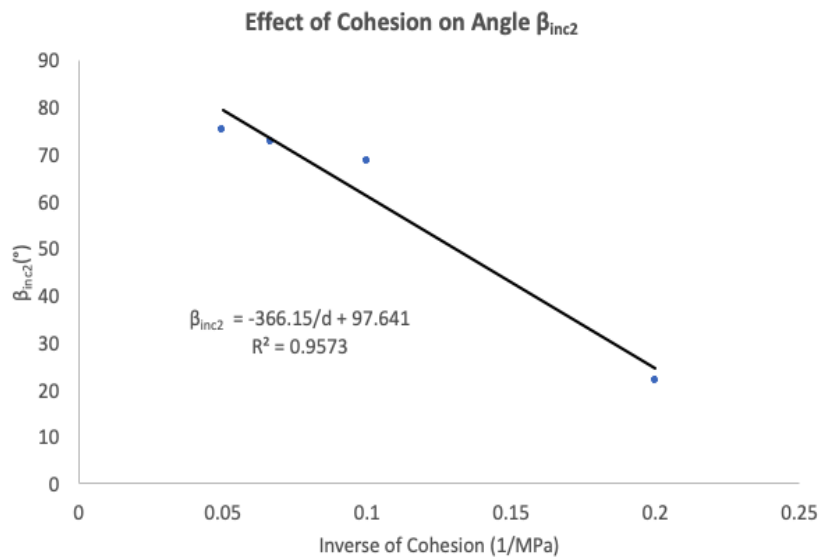


Fig. 5.34 Crack propagation angle β_{inc2} decreases with initial cohesive strength

5.3.6 Test 4: Effect of Bridge Angle on Crack Coalescence

As mentioned in the introduction, the formation of fault within rocks is inevitable throughout geological evolution. The presence of these discontinuities reduces the material strength by propagating new cracks as well as coalescing with other propagating cracks. In all previous tests, the focus is placed on the formation of new cracks using Type 1 rock specimen. In the current test, the goal is to simulate the coalescence of propagating cracks using Type 2 rock specimen under uniaxial compression, following the setup by [114]. In particular, the bridge angle (β_{brg}) is varied ($45^\circ, 90^\circ, 120^\circ$) in order to observe the changes in the coalescence behaviour of propagating cracks. The results are presented by following the order of $\beta_{brg} = 45^\circ, 90^\circ$ and 120° .

Figure 5.35 shows the damage factor plot for specimen with $\beta_{brg} = 45^\circ$. In the beginning, the crack propagation starts with the formation of tensile wing crack at the tips of individual faults. Then, the outer tensile wing cracks grow further when secondary cracks are being developed. The latter rapidly curves towards the direction of external loading. In addition, there are patches of tensile failure zone connecting the pre-existing fractures. Note that, the evolution of damage factor is a measure of how much tensile softening has taken place before full fracture is developed. Since the material is defined with finite cohesive strength, it is then necessary to also investigate the evolution of cohesive strength within the material, which is shown in Figure 5.36.

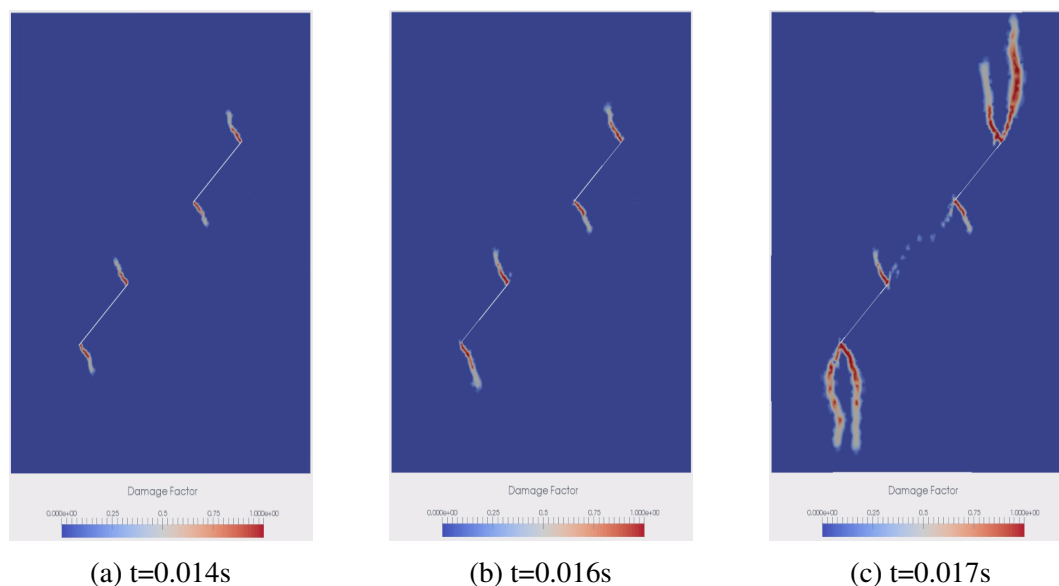


Fig. 5.35 Evolution of damage factor for Type 2 rock specimen with $\beta_{brg} = 45^\circ$

The evolution of cohesive strength clearly demonstrates the progressive growth of secondary cracks and the associated coalescence that takes place between the pre-existing

fractures. The latter is not quite pronounced in the damage factor contour, showing that shear failure is more dominant than tensile failure in the coalescence mechanism.

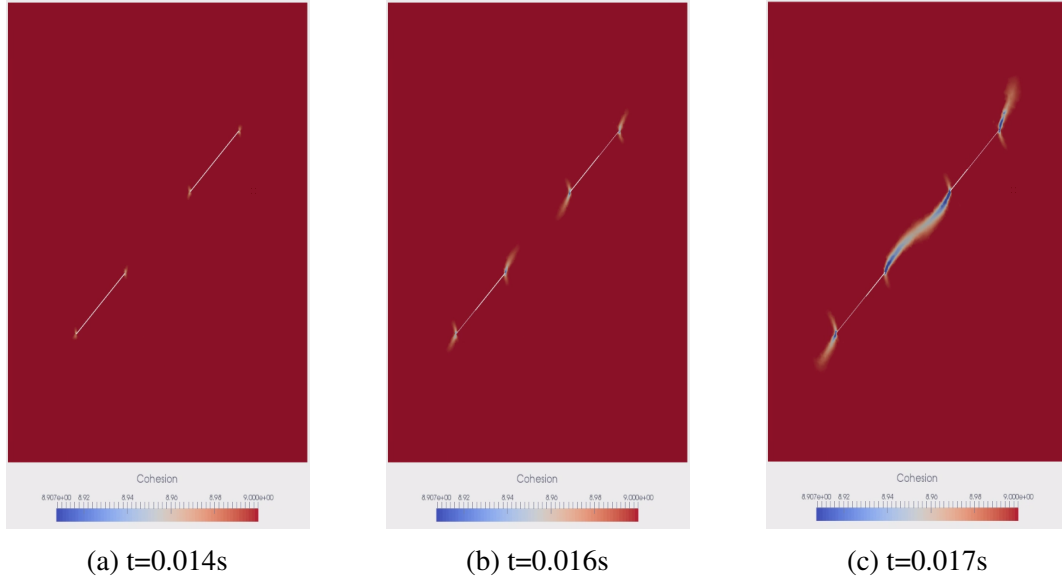


Fig. 5.36 Evolution of cohesive strength for Type 2 rock specimen with $\beta_{brg} = 45^\circ$

While the contour plots of cohesive strength and damage factor provide the insights about the failure mechanism (e.g. shear failure or tensile failure) that is taking place in the specimen, the tensile strength contour allows us to visualise the overall condition of specimen strength, as shown in Figure 5.37. The reason is that, as cohesion is updated, the tensile strength is reduced accordingly via the coupling factor η_1 . At the same time, the development of tensile failure can also be traced by updating the tensile strength. Hence, the tensile strength plot combines the propagation of tensile wing crack and secondary crack as well as the coalescence of the propagating cracks. The observation as depicted in Figure 5.37 is close to Type I coalescence as defined by [19], in which the coalescence is achieved via the linkage of internal secondary cracks through shearing mechanism. Although the numerical results show some additional cracks, the salient feature of this type of coalescence are successfully reproduced and comparable to experimental observation by [19] and [114] in Figure 5.38.

For specimen with $\beta_{brg} = 90^\circ$ whereby the pre-existing fractures come closer in horizontal direction, the coalescence mechanism is slightly different than the case with $\beta_{brg} = 45^\circ$. Figure 5.39 shows the evolution of damage factor whereby tensile wing cracks are developed at initial stage and coalescence takes place at later stage. On the other hand, the evolution of cohesive strength in Figure 5.40 shows that the coalescence is not directly attained via secondary cracks. This result is close to Type II coalescence as defined by [19], in which the

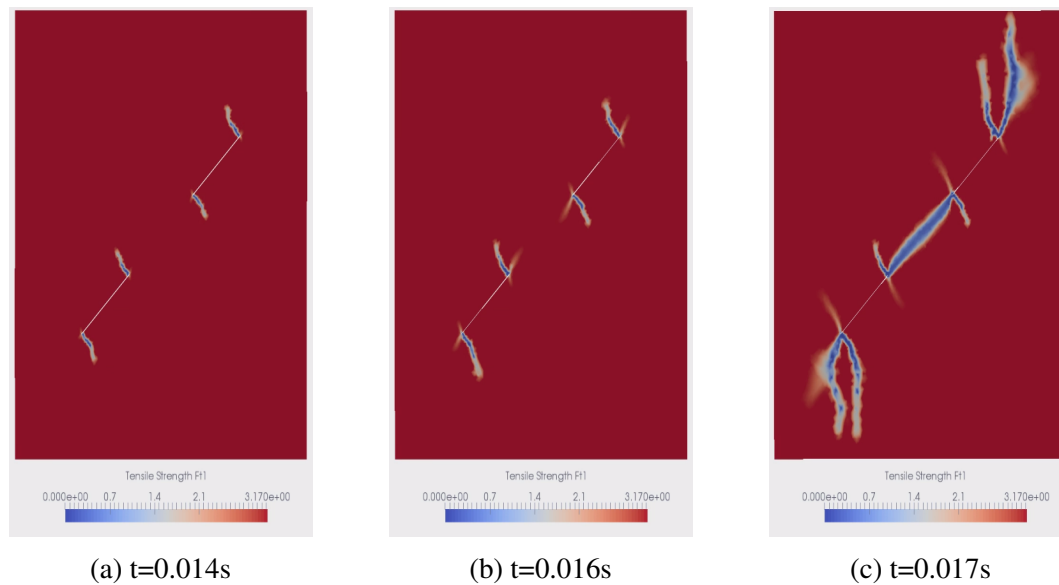
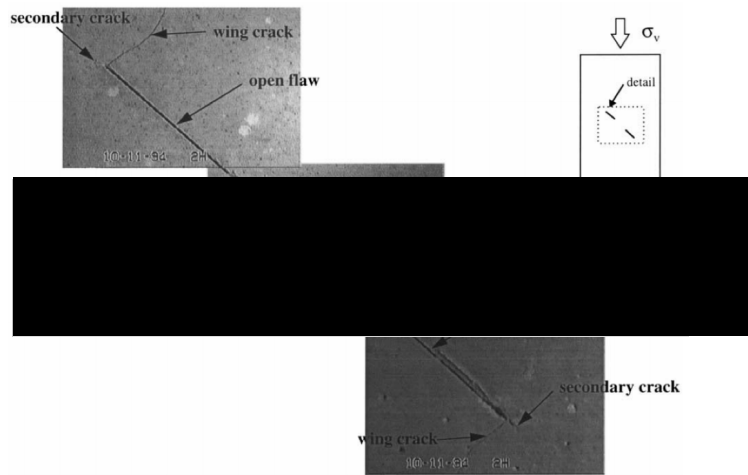


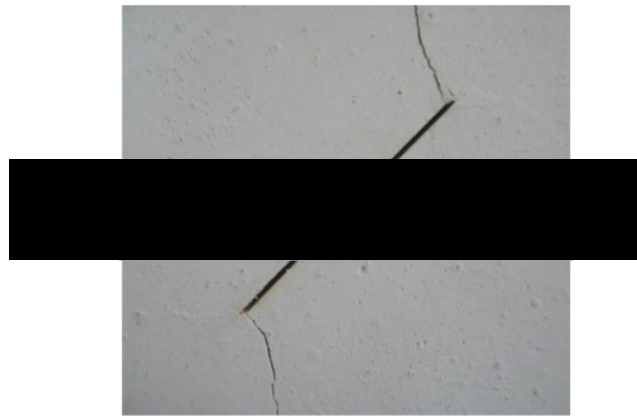
Fig. 5.37 Evolution of tensile strength f_{t1} for Type 2 rock specimen with $\beta_{brg} = 45^\circ$

coalescence is achieved by linking the secondary cracks from the inner tips of pre-existing fractures through a secondary tensile crack. The tensile crack is clearly shown in Figure 5.39. Finally, using tensile strength plot, the overall condition of material strength is able to be visualised and compared with the experimental observations by [19] and [114] as shown in Figure 5.42.

Lastly, for specimen with $\beta_{brg} = 120^\circ$ whereby the two pre-existing fractures overlap, the predicted coalescence style appears to differ slightly from that of [114]. First of all, the damage factor plot (Figure 5.43) shows the development of tensile wing crack at initial stage. The internal tensile wing cracks from both pre-existing fractures approach one another before coalescence takes place in another location at later stage. By comparing the cohesion plot (Figure 5.44) and damage factor plot, it can be concluded that the coalescence is achieved through a secondary tensile crack that connects the secondary cracks emanating from the left tips of both pre-existing fractures. As shown in Figure 5.46, the predicted coalescence style resembles that of [141] than [114]. At the moment, it is impossible to numerically recover the crack propagation and coalescence styles in exactly the same manner as experimental observations. However, the key thing that both sides agree on is that as the bridge angle β_{brg} increases, the coalescence transitions from being dominated by shear failure to tensile failure.



(a) Figure obtained from [19]



(b) Figure obtained from [114]

Fig. 5.38 Crack pattern for specimen with $\beta_{brg} = 45^\circ$.

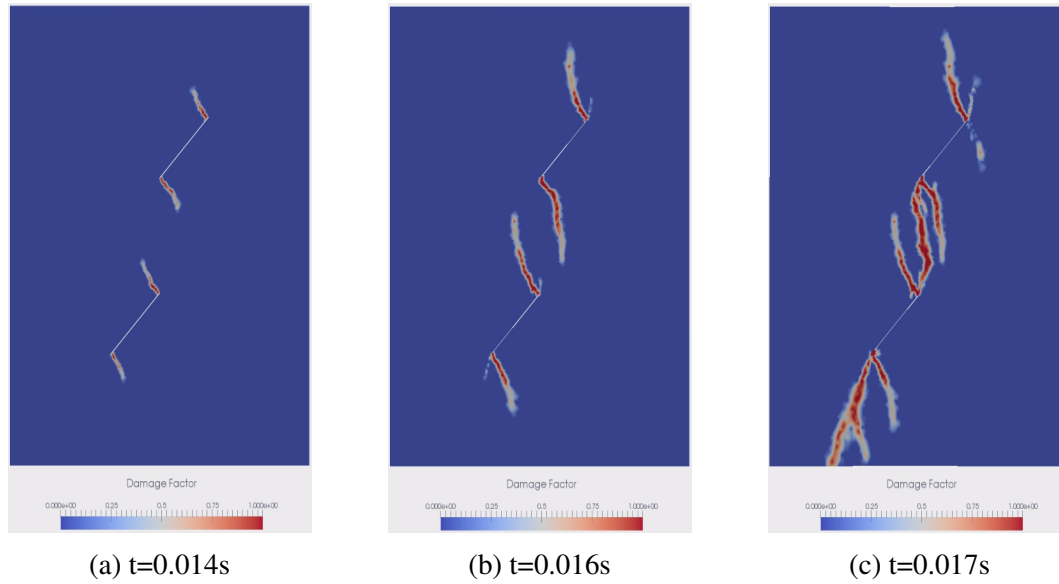


Fig. 5.39 Evolution of damage factor for Type 2 rock specimen with $\beta_{brg} = 90^\circ$

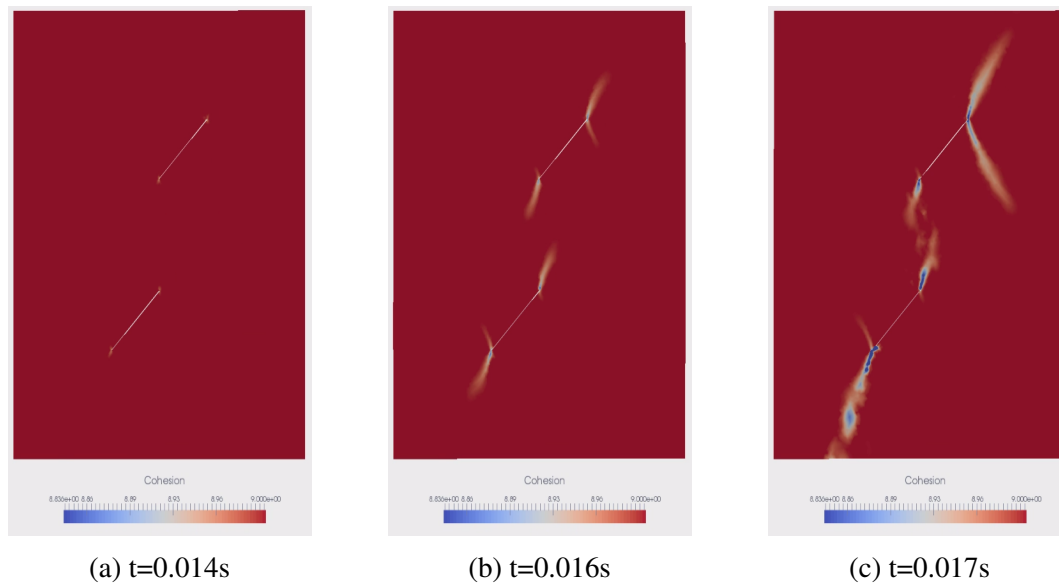


Fig. 5.40 Evolution of cohesive strength for Type 2 rock specimen with $\beta_{brg} = 90^\circ$

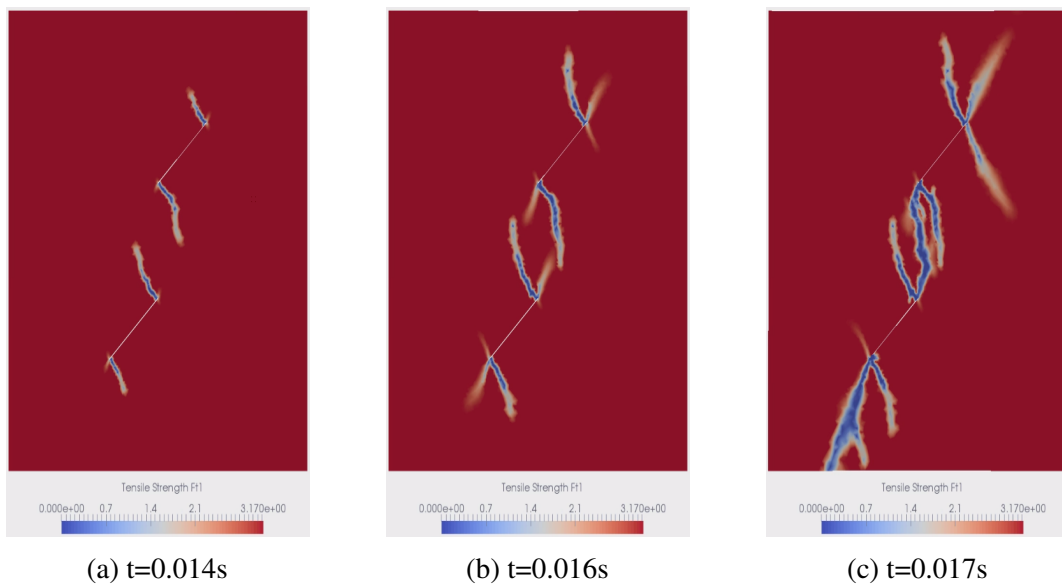


Fig. 5.41 Evolution of tensile strenght for Type 2 rock specimen with $\beta_{brg} = 90^\circ$

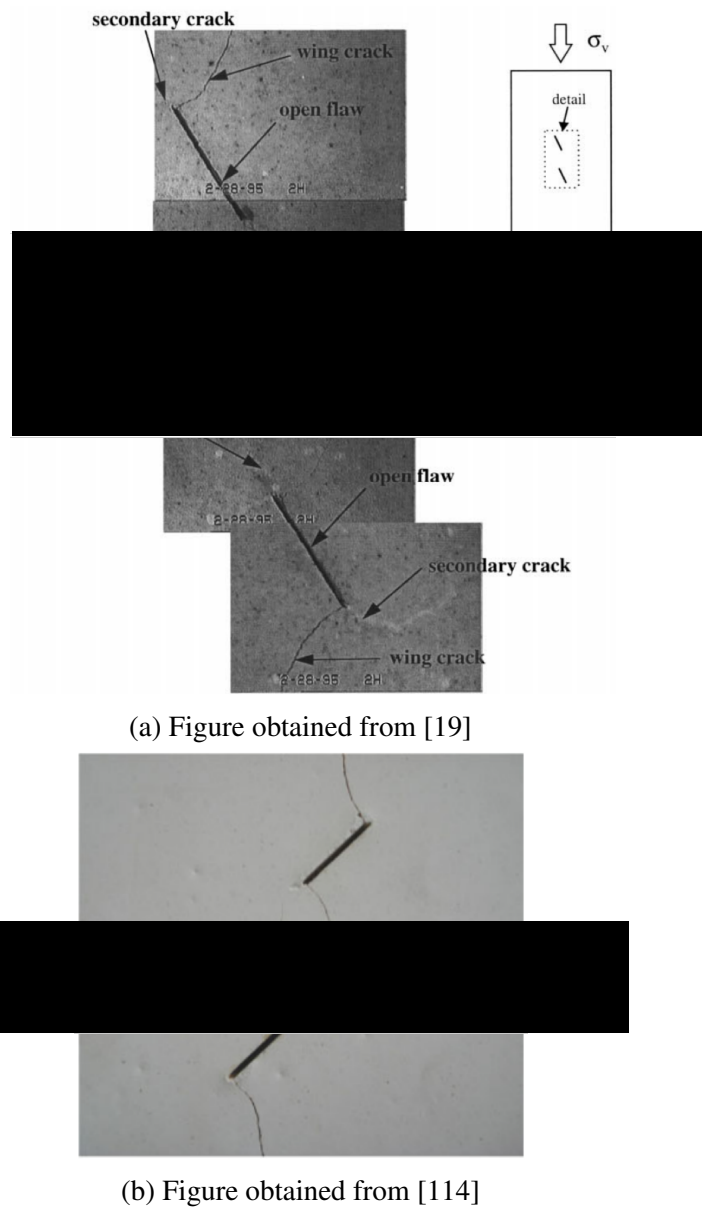


Fig. 5.42 Crack pattern for specimen with $\beta_{brg} = 90^\circ$.

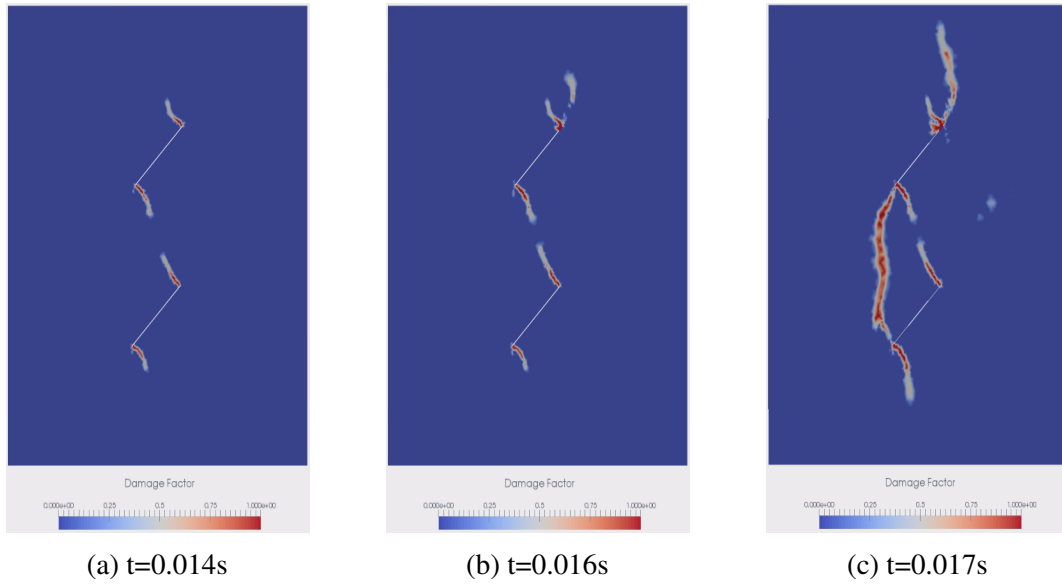


Fig. 5.43 Evolution of damage factor for Type 2 rock specimen with $\beta_{brg} = 120^\circ$

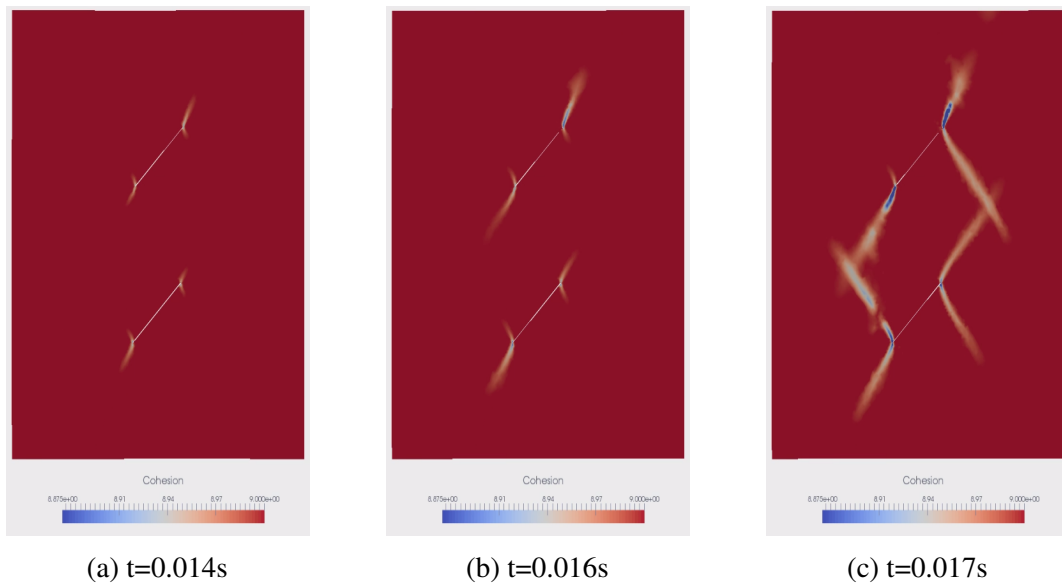


Fig. 5.44 Evolution of cohesive strength for Type 2 rock specimen with $\beta_{brg} = 120^\circ$

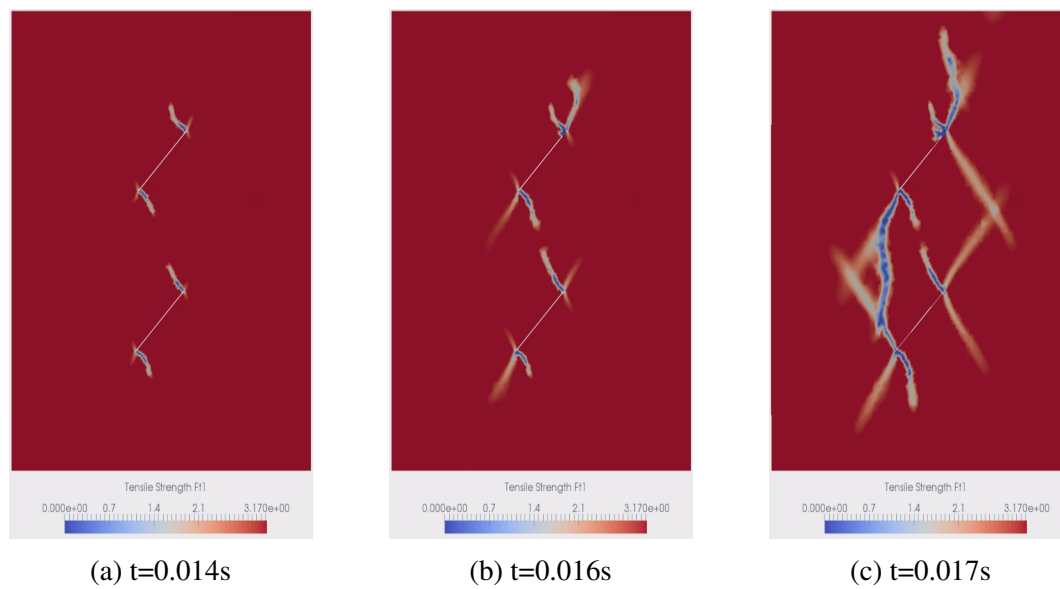
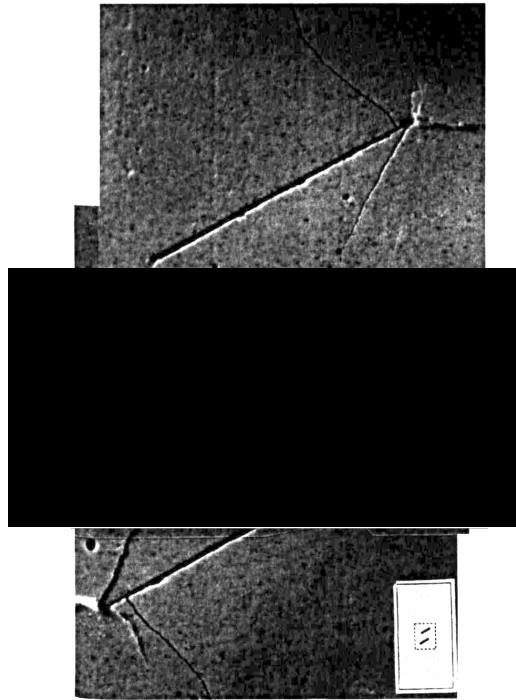
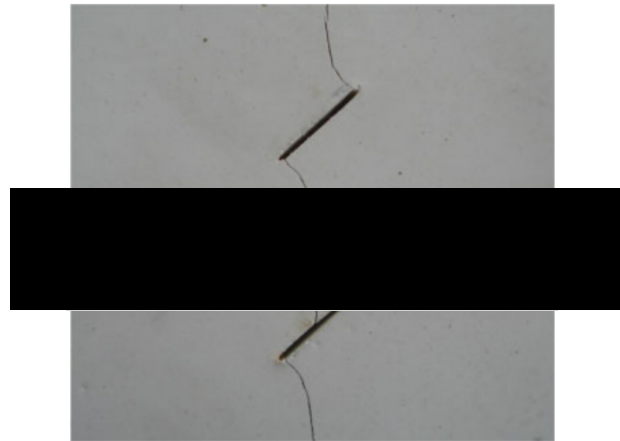


Fig. 5.45 Evolution of tensile strength f_{t1} for Type 2 rock specimen with $\beta_{brg} = 120^\circ$



(a) Figure obtained from [141]



(b) Figure obtained from [114]

Fig. 5.46 Crack pattern for specimen with $\beta_{brg} = 120^\circ$.

5.3.7 Concluding Remarks

From the numerical tests, it can be concluded that the current constitutive model performs well in capturing the salient features that are demonstrated in experimental observations. In particular, the formation of tensile wing crack and secondary crack, as well as the coalescence behaviour in response to changes in geometrical parameters (i.e. inclination angle β_{inc} and bridge angle β_{brg}) are developed in a way that matches the published findings at macroscopic level. In the next numerical example, the constitutive model is assessed for its ability to capture the size effect on the limit load of a specimen made of the same material.

5.4 Influence of Size Effect on Borehole Instability

5.4.1 Introduction

It is crucial that an algorithm of constitutive model should be able to scale accordingly the material response (e.g. limit load) with respect to the structural size [11]. Such phenomenon is termed as size effect, which is a manifestation of the nonlinear dependence on material characteristic length scale [50]. The argument is that a larger structure contains higher elastic energy and therefore tends to exhibit brittle response during fracture. Vice versa, for a smaller structure made of the same material, the failure mechanism is dominated by ductile response.

This is important for the application of computational geomechanics since the large scale simulation is mostly modelled based on the material properties measured at laboratory scale. Several modelling techniques have been proposed³ to reproduce size effects in numerical results, including Cosserat continuum [126, 132], gradient plasticity model [125], non-local continuum [67, 8–10] and fracture energy regularisation methods [50]. The latter technique is applied in the current thesis because of the ease in implementation, and the ability to reproduce size effect as well as to regularise Mode I and Mode II localisation [50].

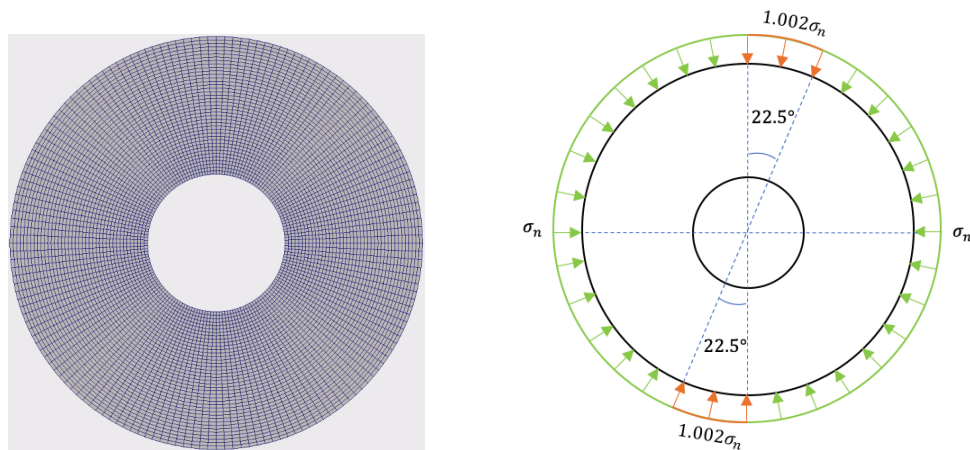
In this numerical test, the goal is to assess the ability to reproduce size effect within the framework of modified Drucker-Prager model. The simulation case study is the prediction of borehole collapse pressure that comes in different sizes. The outcome will be compared qualitatively with the experimental results by [169] and [68].

5.4.2 Modelling Setup

Four sizes of borehole cross section are considered in the current numerical test. Each of the model is created with an outer to inner diameter ratio of 3. The inner diameter of the

³See [50] for review

models are 20, 100, 200, and 400mm. The domain is discretised using 4-noded standard linear elements. There are 160 divisions along the inner circumference and 40 divisions along the radial direction. External load is applied at the outer circumference, with a small perturbation of 0.2% applied in the region shown in Figure 5.47. A loading rate of 100MPa/s (or 100.2MPa at the perturbed region) is applied until final rupture takes place. The material properties (modified from [132]) and hardening properties are summarised in Table 5.3 and 5.4.



(a) Discretised domain of borehole cross section
(b) Boundary condition on the domain of thick-walled cylinder. $\sigma_n = 100\text{MPa}$

Fig. 5.47 Geometry and boundary conditions of borehole cross section

Material properties	Value
Young's modulus (GPa)	25.0
Poisson's ratio	0.2
Material characteristic length scale (mm)	0.05
Cohesion, d_0 (MPa)	27.7
Friction angle ($^\circ$)	34
Dilation angle ($^\circ$)	34

Table 5.3 Initial properties of elastoplastic material

Effective plastic strain	0.0	1.0
Cohesion, d_0 (MPa)	27.7	0.0
Friction angle ($^\circ$)	34	34
Dilation angle ($^\circ$)	34	34

Table 5.4 Hardening properties for borehole breakout simulation

5.4.3 Results

The regularisation technique using fracture energy approach is shown to be effective in scaling the material response for different specimen size. Figure 5.48 shows the evolution of mean stress with the increase of normalised displacement⁴. Each plot ceases at a stress level corresponding to their final rupture. The results show that the size effect is evidently pronounced; it is clear that larger specimen fails at lower mean stress, and vice versa. In particular, the collapse pressure of specimen with inner diameter of 400mm is almost half of specimen with inner diameter of 10mm. A more direct representation of size effect is given by Figure 5.49, showing the predicted collapse pressure for each specimen size.

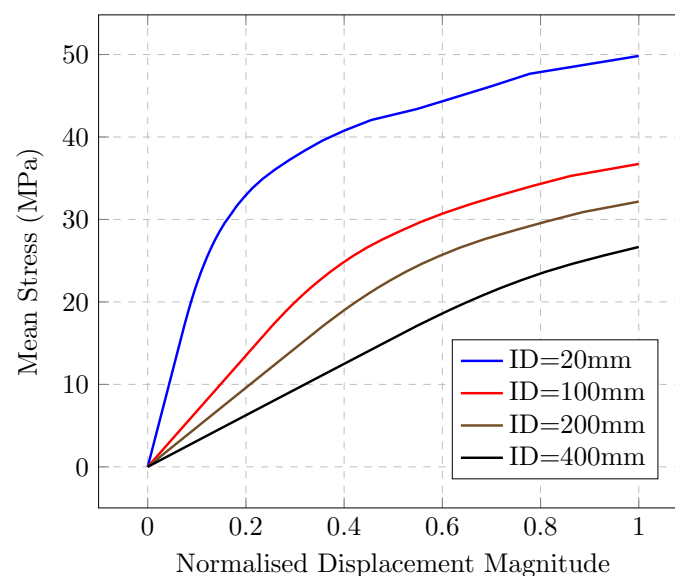


Fig. 5.48 Mean stress-displacement curve for specimen of different sizes

The localised deformation of borehole rupture for each specimen size is shown in Figure 5.50. For smaller specimen, a more ductile response is observed in the final rupture form. This is characterised by a longer propagation trajectory of shearing failure initiated from the outer wall that intersects with the one originating from the inner wall [50]. On the other hand, for larger specimen, brittle response is observed during breakout, which is characterised by axial splitting mechanism. Similar finding was observed by [68] when testing Berea sandstone, as depicted in Figure 5.52. In addition, it is revealed in Figure 5.51 that the kinematics is more localised within the wedge of axial splitting for larger specimen. Although no data is accessible to the author to confirm this finding yet, it is still expected that, for a smaller specimen, the displacement contour is more diffuse within the active region due to higher ductility.

⁴with respect to final displacement magnitude $(u_{rupture}^2 + v_{rupture}^2)^{1/2}$

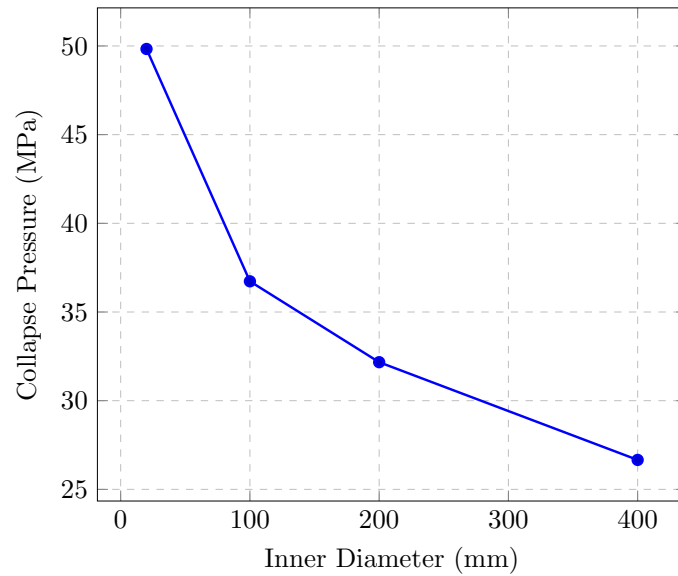


Fig. 5.49 Dependence of collapse pressure on the specimen size

More simulation studies on borehole breakout could have been done. For example, the elastoplastic-fracture constitutive framework can be used to simultaneously capture tensile and shear failure within the cross section of borehole. This will give rise to more accurate modelling of nonlinear fracture mechanics when the elastoplastic yield criterion and tensile failure criterion are both considered when predicting the material response [50].

However, in this numerical test, the main goal is to validate if the constitutive model can scale the material response according to the specimen size. It has been shown that the size effect on material strength is successfully captured via the use of regularisation technique based on fracture energy approach.

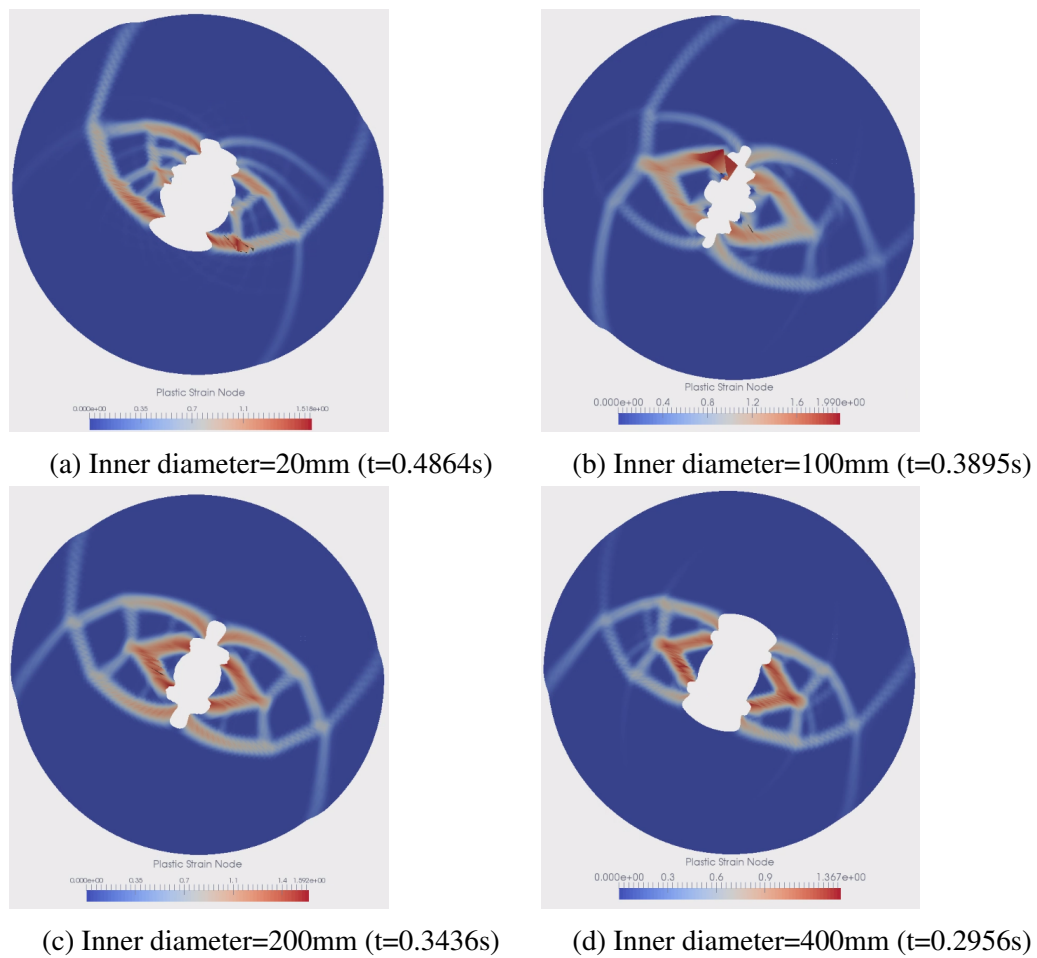


Fig. 5.50 Plastic strain contour of specimen with different size during final rupture

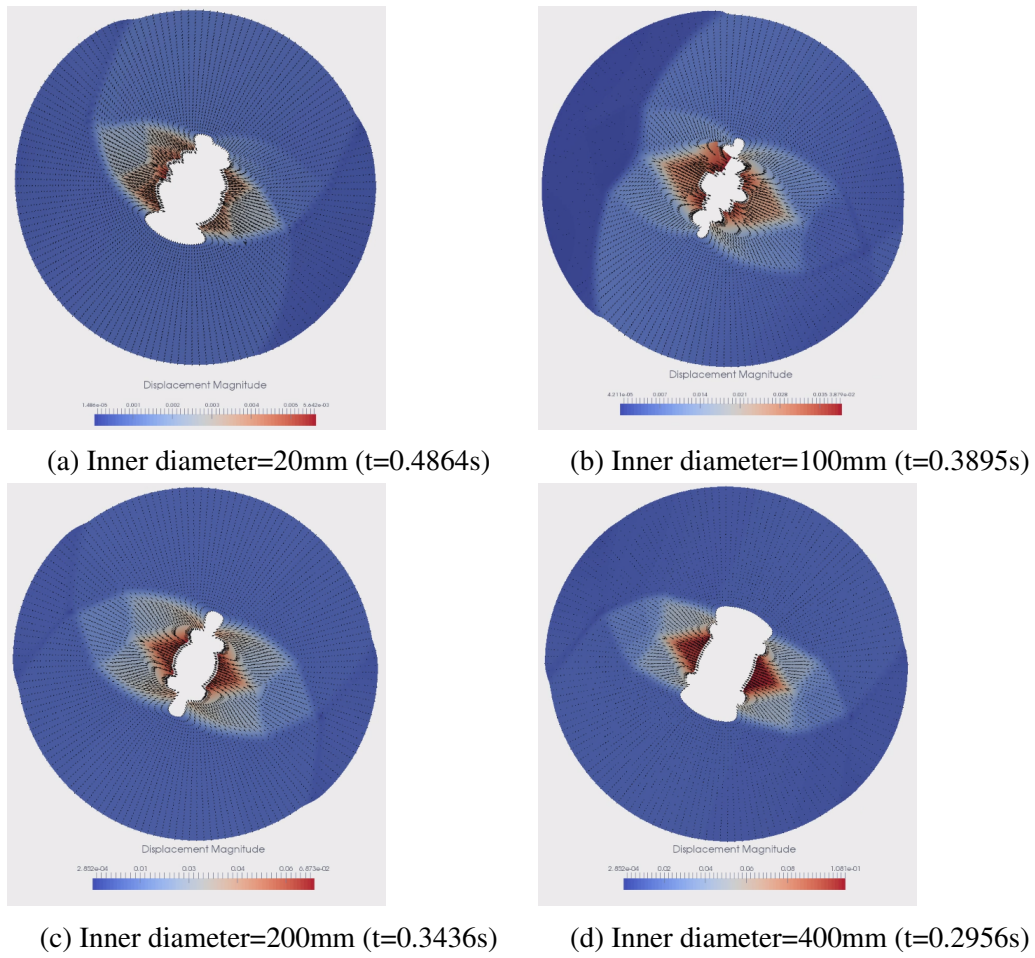


Fig. 5.51 Displacement contour and vector plot for each specimen during borehole breakout stage

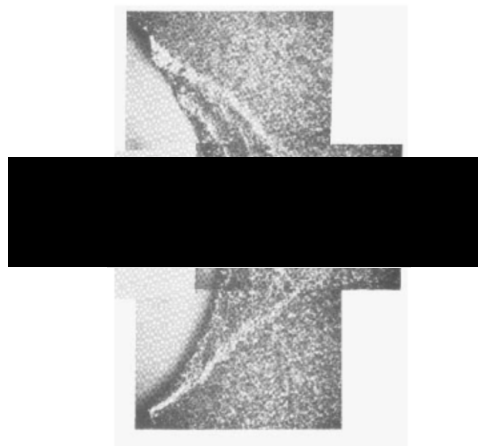


Fig. 5.52 Axial splitting of brittle Berea sandstone. Figure obtained from [68].

5.5 Uniaxial Consolidation and Sedimentation of Soil Column

5.5.1 Uniaxial Consolidation of Soil Column

Terzaghi's Solution

In this test, the main objective is to simulate the consolidation of a 50m high soil column due to a sudden change in the drainage condition at the top surface. The predicted evolution of pore pressure along the column height is compared against Terzaghi's analytical solution.

In the initial configuration, the soil is fully saturated with an initial pore pressure of 1 MPa with no flow allowed through any boundary. Gravity is neglected, allowing comparison with a classical analytical solution. The effective stress is zero so that the total mean stress in the column is 1 MPa. Equilibrium in the initial configuration is achieved by applying a 1 MPa mechanical stress to the top boundary of the model. At time $t=0$, the boundary condition of the top surface is changed to allow free drainage, resulting in a gradual dissipation of pore pressure in the model. The model is analysed in uniaxial strain conditions; i.e. the vertical sides of the model are constrained in the horizontal direction, and the base of the model is constrained in the vertical direction.

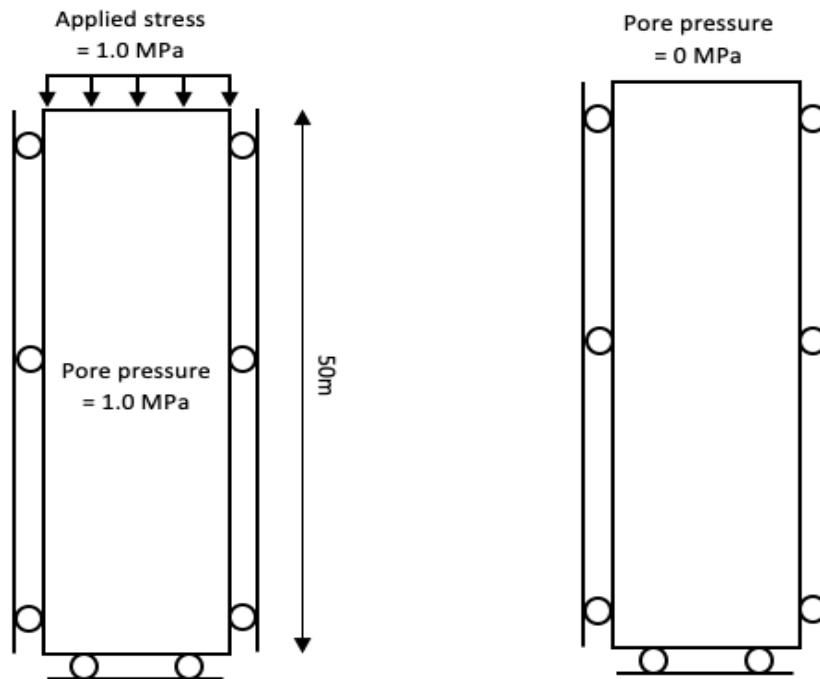
The column is discretised by a mesh structured mesh of 40 linear quadrilateral elements. The solution time step size is $0.2(10^{-6})$ year, with a factor of critical time step as 0.7. The material properties are listed in Table 5.5. The hydromechanical solution is solved using fixed stress coupling algorithm. The termination time is 1.34 years, with 67000 porous flow steps and 68109955 mechanical steps.

The analytical solution of Terzaghi's problem is given by

$$\frac{p}{p_0} = \frac{4}{\pi} \sum_{j=1}^{\infty} \left(\frac{(-1)^{j-1}}{2j-1} \cos \left[(2j-1) \frac{\pi}{2} \left(\frac{z}{h} \right) \right] \right) \left(-(2j-1)^2 \frac{\pi^2 c_v t}{4 h^2} \right), \quad (5.3)$$

where p_0 is the initial pore pressure, z is the spatial height, h is the soil column height, and the expression c_v is given by

$$c_v = \frac{k}{\mu m_v}, \quad (5.4)$$



(a) Initial condition: Zero effective mean (b) Boundary condition: At $t = 0$, The top stress. Externally applied stress is balanced surface boundary condition is prescribed with by the pore pressure. No drainage from the zero pore pressure and remains so throughout domain is allowed. the simulation test.

Fig. 5.53 Initial and boundary conditions of soil column for solving Terzaghi's solution

from which k is the hydraulic permeability, μ is the fluid dynamic viscosity, and m_v is defined as

$$m_v = \frac{(1 + \nu)(1 - 2\nu)}{(1 - \nu)E}. \quad (5.5)$$

Material properties	Value
Young's modulus (MPa)	50.0
Poisson's ratio	0.0
Grain density (kg/m^3)	2700
Porosity	0.5
Hydraulic permeability (m^2)	$1.18(10^{-15})$
Fluid viscosity (MPa.year)	$3.17(10^{-17})$
Fluid density (kg/m^3)	1000

Table 5.5 Material properties for Terzaghi's benchmark test

Figure 5.54 shows agreement between the analytical and numerical solutions of pore pressure evolution along the soil column height. As the applied stress is removed and a boundary condition of zero pore pressure is prescribed at the top surface, a sudden finite pore pressure gradient is developed to activate the fluid drainage. Figure 5.55 verifies the effective vertical stress near the column top surface increases in compaction condition during the dissipation of pore fluid pressure. The fluctuation of total vertical stress in the beginning of time is due to the sudden change of equilibrium at the top surface (i.e. zero pore pressure), which can be mitigated by applying smaller times step size.

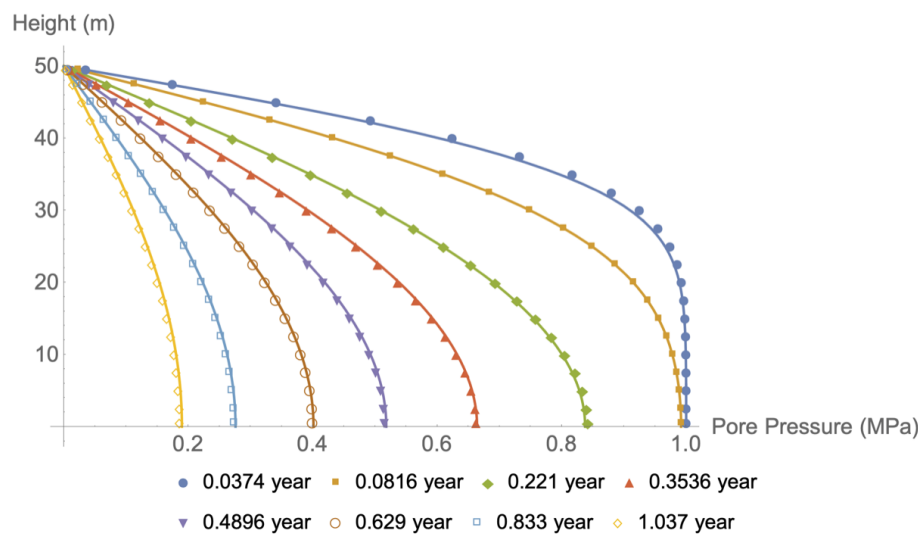


Fig. 5.54 Comparison of analytical (line plot) and numerical (dotted plot) prediction of pore pressure evolution during consolidation of fully saturated soil column. Time step size = $0.2(10^{-6})$.

Experimental Comparison with Porosity-Dependent Permeability

The uniaxial consolidation test above is extended to comparison with experimental [100] findings whereby the effect of porosity-dependent permeability is considered. A kaolin sample (width: 25.4cm, height: 37cm) is tested in a Rowe consolidation test, with material properties given in Table 5.6. The porosity-dependent permeability plot is converted using the void ratio-hydraulic conductivity plot provided. It should be noted that the hydraulic conductivity plot was a “hypothetical graph” [100], since the void ratio-permeability data and other nonlinear material parameters are available. In this test, it is assumed that the data (Figure 5.56) is converted based on simple equation $k = K \frac{\mu}{\rho g}$, whereby k is isotropic permeability and K is isotropic hydraulic conductivity, and that the analysis is based on linear elastic model. Similar outcome is obtained as that of [100]’s numerical prediction against

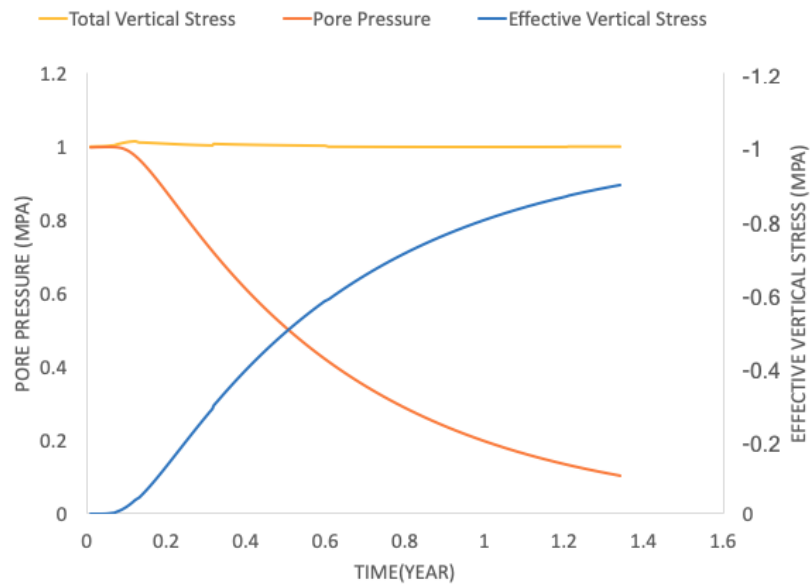
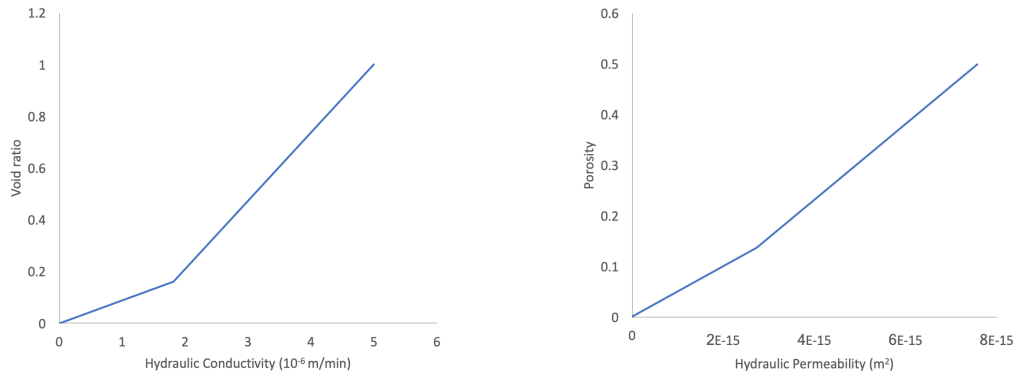


Fig. 5.55 Evolution of pore pressure and effective mean stress near the column top surface

experimental finding. Model with porosity-dependent permeability provides better global fitting than the fixed permeability model, although the latter provides very good prediction of pore pressure towards the end of simulation time. In this test, the main thing is not about predicting the details of consolidation process of this kaolin sample because the available data is very limited and only linear elastic analysis can be done, but to show the possibility of enhancing general accuracy by using nonlinear porosity-dependent permeability model.

Material properties	Value
Young's modulus (MPa)	2.07
Poisson's ratio	0.2
Grain density (kg/m^3)	2650
Initial porosity	0.5

Table 5.6 Material properties for Terzaghi's benchmark test



(a) Void ratio-hydraulic conductivity plot obtained from [100] via electronic conversion using Engauge Digitizer

(b) Porosity-hydraulic permeability plot converted assuming water properties: $\mu_f = 8.9(10^{-4})$ Pa.s, $\rho_f = 1000$ kg/m³

Fig. 5.56 Properties of fluid conductivity and permeability

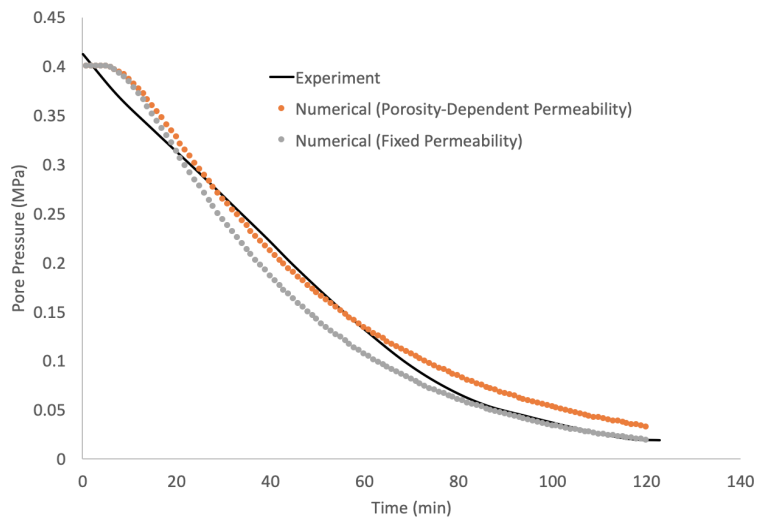


Fig. 5.57 Comparison of pore pressure evolution

5.5.2 Sedimentation of Soil Column

Modelling Description and Analytical Solution

This test is extended from the uniaxial consolidation example by considering overpressure build up and dissipation during sedimentation. The layer sedimentation algorithm available in ParaGeo, which deposits new layer with discrete thickness, is utilised. The advantage of this algorithm compared to Eulerian boundary algorithm⁵ is that general intersection of the new sediment layer with existing sediment is possible.

The objective is to simulate the sedimentation and consolidation of 1000m of sediment over a period of 1.0 Ma. Only 20m of pre-existing sediment is represented and sedimentation is represented by the layer sedimentation algorithm.

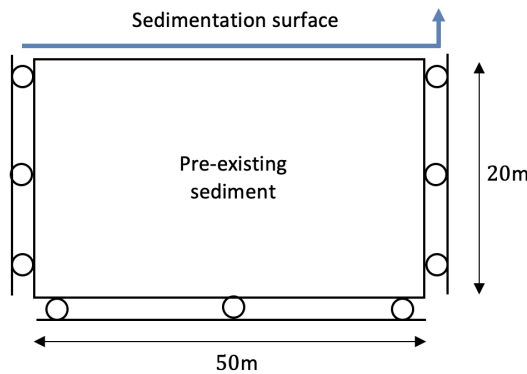


Fig. 5.58 Geometry of the initial model. The top surface is subjected to sedimentation with (a) high sedimentation rate (1000m/Ma) and (b) low sedimentation rate (500m/Ma)

The model is analysed in uniaxial strain conditions; i.e. the vertical sides of the model are constrained in the horizontal direction, and the base of the model is constrained in the vertical direction. Gravity is the only load type and the top surface of the model is prescribed zero pore pressure, i.e. free drainage, resulting in a gradual dissipation of pore pressure in the model. The gravity load for the pre-existing sediment is applied over 0.1 Ma and then sedimentation of the column takes place between 0.1 and 1.1 Ma for high sedimentation rate (1000m/Ma), and between 0.1 and 2.1 Ma for low sedimentation rate (500m/Ma). Standard linear 3-noded element is used with a target element size of 20m. Adaptive remeshing is activated in conjunction with to the sedimentation process. Remeshing is triggered at a distortion of 15% with the objective of maintaining the element size at 20m. The flow time step size is 0.001 Ma, while the geomechanical time step is $0.2(10^{-5})$ Ma. Fixed stress coupling algorithm is used. The material properties used are listed in Table 5.7.

⁵which allows continuous deposition process

Material properties	Value
Young's modulus (MPa)	64.62
Poisson's ratio	0.3
Grain density (kg/m ³)	2833
Porosity	0.4
High hydraulic permeability (m ²)	10 ⁻¹⁸
Low hydraulic permeability (m ²)	10 ⁻¹⁹
Fluid viscosity (MPa.Ma)	3.171(10 ⁻²³)
Fluid density (kg/m ³)	1000

Table 5.7 Material properties for uniaxial consolidation test

For this problem, the analytical solution is given by [72], where the fluid overpressure p_{ovp} is given by

$$p_{ovp} = \gamma' w_b t - \frac{\gamma'}{\sqrt{\pi c_v t}} e^{-\frac{z^2}{4c_v t}} \int_0^\infty \xi \tanh\left(\frac{w_b \xi}{2c_v}\right) \cosh\left(\frac{z\xi}{2c_v}\right) e^{-\frac{\xi^2}{4c_v t}} d\xi, \quad (5.6)$$

where z is the spatial height, c_v is identical to (5.4), w_b is the sedimentation rate (m/Ma), and γ' is defined by

$$\gamma' = (\rho_{bulk} - \rho_{fluid}) g. \quad (5.7)$$

Two groups of test are conducted. The first group assesses the effect of hydraulic permeability with a constant sedimentation rate (1000m/Ma), whereas the second group assesses the effect of sedimentation rate with constant hydraulic permeability (10⁻¹⁹). In all the following plots, results are shown only at the onset of sedimentation.

Effect of Hydraulic Permeability

For a given sedimentation rate, it is expected that material with lower permeability accumulates higher pore pressure than one with higher permeability. Figure 5.59 shows the quantitative comparison between the analytical solution and numerical predictions. Good agreement is obtained. Note that, beyond duration of 1.0Ma is when sedimentation process ceases. This is the point when the analytical solution is not valid. Major fluid drainage starts to take place, and thus the pore pressure at the column base begins to subside. As expected, higher dissipation rate occurs in material with higher hydraulic permeability. Figure 5.60 shows the pore pressure variation with depth at the end of sedimentation process. Towards the base of the column, the numerical result approaches the analytical solution. Some deviations are observed in the vicinity of top surface. This is due to the layer sedimentation algorithm

used. As the top surface with discrete thickness is newly deposited, it requires some extra time for the pore pressure to build up. In contrast, if it were to be Eulerian boundary algorithm which continuously deposits new layer at the top surface, the deviation is expected to be smaller since pore pressure buildup is continuously developed. However, as mentioned previously, the current layer sedimentation algorithm is still preferred due to its ability to intersect with general top surface of pre-existing sediment with complicated topology.

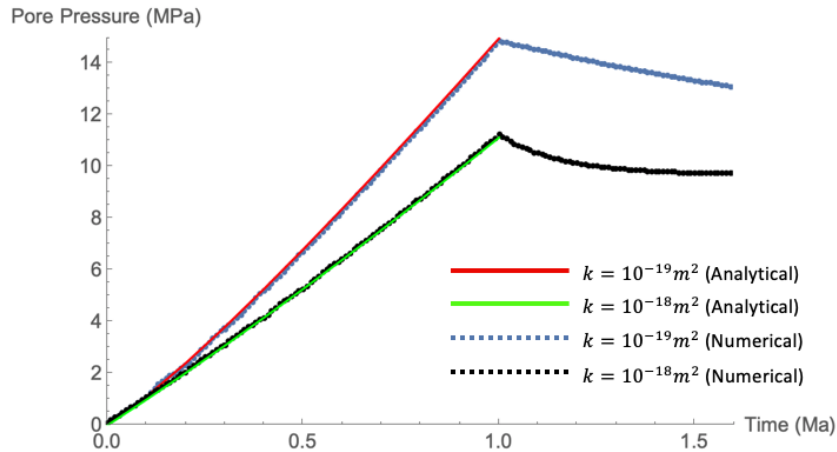


Fig. 5.59 Comparison of pore pressure evolution at the column base during sedimentation for different hydraulic permeabilities

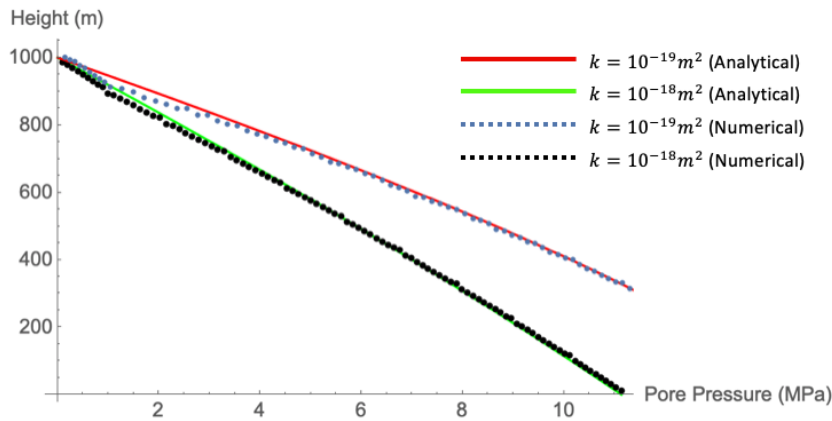


Fig. 5.60 Comparison of pore pressure variation with depth at 1.1 Ma for different hydraulic permeabilities

Effect of Sedimentation Rate

On the other hand, Figure 5.61 shows the pore pressure evolution at the column base with constant hydraulic permeability but different sedimentation rate. Good agreement between

analytical solution and numerical results are obtained as well. At lower sedimentation rate, it is expected to take longer duration to reach the peak pore pressure. Even then, the peak value is still lower than the higher rate counterpart due to continuous fluid discharge from the top surface. Figure 5.62 shows the pore pressure variation with depth at the end of sedimentation process. Similarly, better agreement is obtained near the column base, whereas deviation is observed in the vicinity of top surface due to the choice of layer sedimentation algorithm.

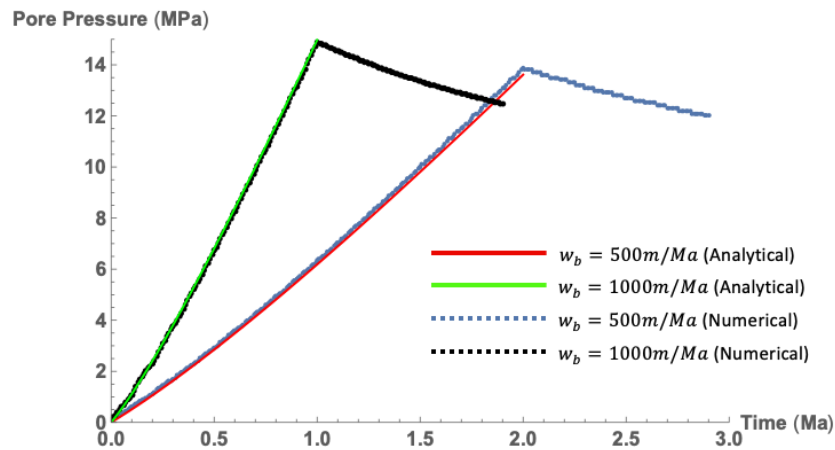


Fig. 5.61 Comparison of pore pressure evolution at the column base during sedimentation for different sedimentation rates

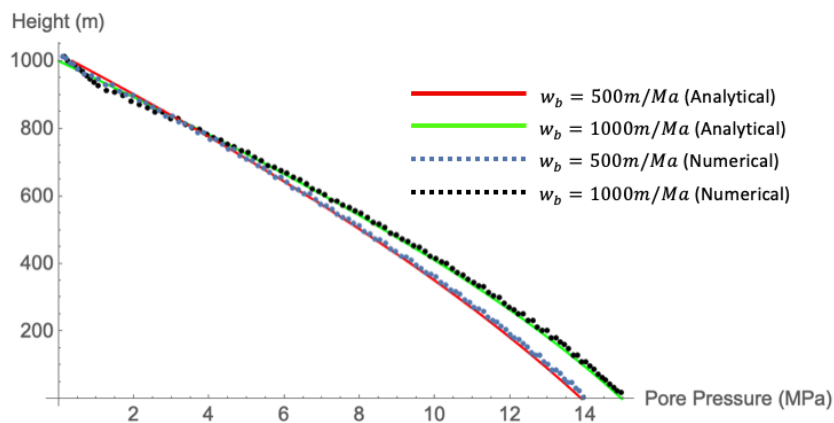


Fig. 5.62 Comparison of pore pressure variation with depth at 2.1 Ma for different sedimentation rates

5.6 Influence of Pore Pressure on Thrust Fault Formation

5.6.1 Introduction

A model of laboratory scale containing four sand layers is prescribed with pore fluid pressure at the base, and subsequently pushed by a sliding wall on one of its sides to form thrust faults. The goal of this test is to investigate changes in the pattern of thrust fault formation under the influence of pore pressure. The model is designed in accordance to the experimental work by [38], who uses compressed air as pore fluid⁶. The consequence of the choice of air as pore fluid in the modelling work is that no coupling volume strain between seepage and mechanical fields is considered as it is assumed air contributes negligible loading to the volumetric strain of the solid grains surrounding the pore space. Furthermore, it is also assumed that the sand material can be modelled using Drucker-Prager model, so that all plastic deformation are dilative in nature and are represented in terms of shear localisation.

The experimental setup by [38] is described as follows and illustrated in Figure 5.63. A sandbox model is placed in a rectangular box (300mm long, 200mm wide, 100mm high), which is bounded by transparent plexiglass. A pressure chamber, acting as a compressed air reservoir, is put under the base of the sand layers to provide uniform fluid pressure distribution. The feasibility of using compressed air as pore fluid to overpressurize the base layer of a sandbox model has been verified [36]. Furthermore, a sieve is placed in between the pressure chamber and basal sand layer. It has the right mesh size that is sufficiently small to prevent the granular material from falling into the chamber, yet sufficiently large to allow compressed air flow through the porous media. A sliding wall on the right side of the model is pushed by a piston that is displaced horizontally by a motor-driven screw jack. A total displacement of 100mm is completed in 30 minutes.

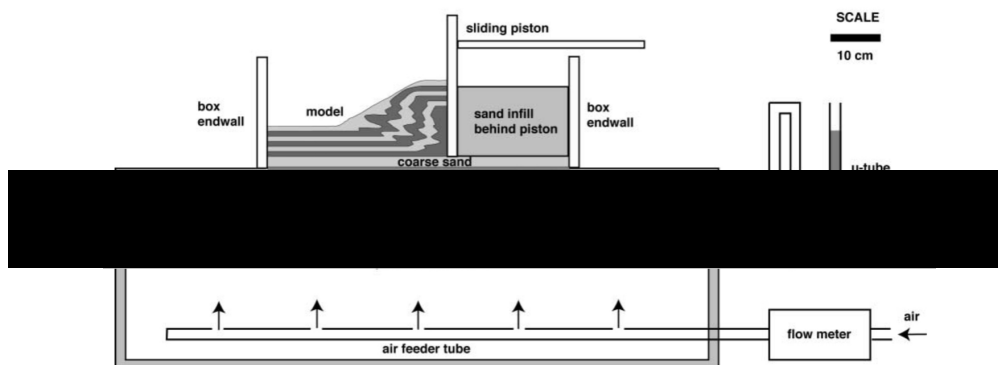


Fig. 5.63 Experimental setup by Cobbold et al. [38]

⁶The fluid is assumed to obey Darcy's law.

5.6.2 Modelling Setup and Material Properties

The initial discretised simulation model is shown in Figure 5.64. It is discretised into 12394 elements with 6490 nodes. The default mesh size is 2mm with a time step size of $6(10^{-3})$ s. Adaptive remeshing utility of ParaGeo is activated. For side walls, the mesh size is kept constant at 5mm throughout the loading history. For sand layers, the meshes are updated according to the evolution of effective plastic strain $\bar{\epsilon}^p$, as shown in Table 5.8.

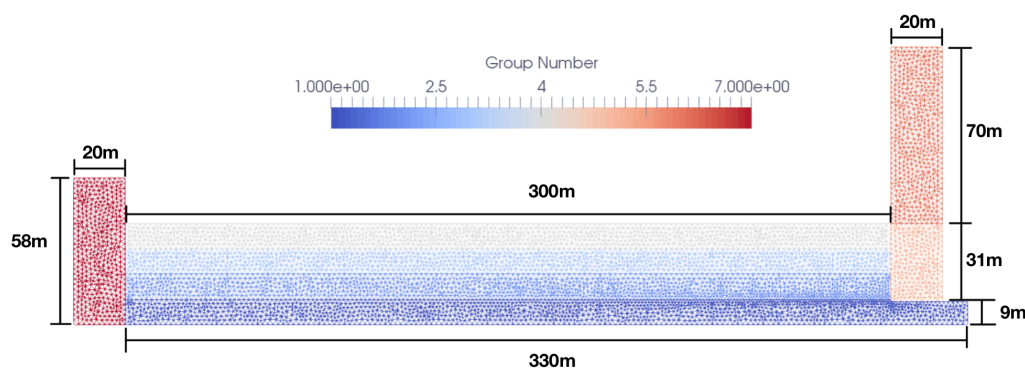


Fig. 5.64 Dimension of model geometry

Effective plastic strain	0.00	0.10	0.20	0.30	0.40	0.50
Element size (mm)	2.00	1.30	0.90	0.65	0.50	0.50

Table 5.8 Adaptive remeshing as function of effective plastic strain

There are four types of boundary condition to be taken into account, i.e. displacement, mechanical loading, pore pressure and contact. Figure 5.65 illustrates the boundary conditions applied to the simulation domain.

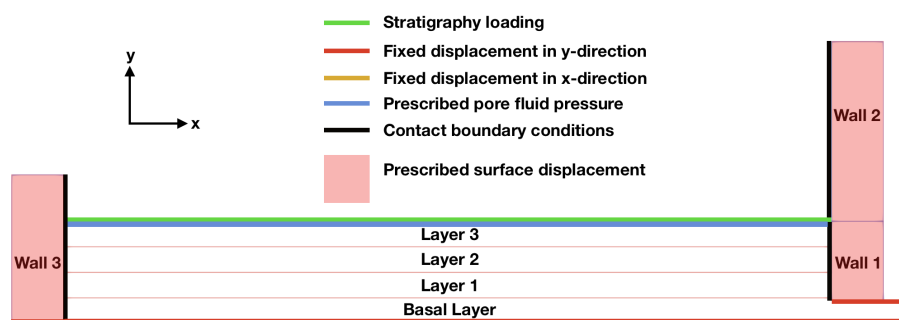


Fig. 5.65 Prescribed boundary conditions

In terms of **displacement** boundary conditions, the bottom of basal layer, and of Wall 3, as well as the part of basal layer in contact with Wall 1 are all fixed in y direction, whereas

the right side of basal layer is fixed in x direction. In addition, the surface of Wall 3 is fixed in x and y directions, while on the right side, the surfaces of Wall 1 and Wall 2 are prescribed a total displacement of 100mm in x direction at a velocity of $-\frac{1}{18}$ mm/s. The simultaneous displacement of Wall 1 and Wall 2 represents the movement of sliding wall.

In terms of **mechanical loading** boundary conditions, the whole domain is subjected to gravitational force. In addition, a stratigraphy load of 5 Pa, representing sedimentary load in sandbox scale, is applied at the top surface of Layer 3.

Pore pressure boundary conditions are applied in Case 2-4⁷. The value at the top surface of Layer 3 is always zero throughout the simulation period. Pore fluid pressure gradient across the sand layers is generated by prescribing pore pressure (Table 5.9) at the bottom surface of basal layer.

Case	2	3	4
Pore Pressure (Pa)	98.1	196.2	294.3

Table 5.9 Cases with different prescribed basal pore pressure

To prescribe **contact** boundary conditions, it is convenient to firstly group some lines into several geometry sets, as illustrated in Figure 5.66. Using the geometry sets, it is easier to prescribe possible interaction between contacted surfaces, as shown in Table 5.10. The contact property, as shown in Table 5.11, determines the level of compressional and tangential penalty parameters (or, stiffness) that are applied to the contacted surfaces. Contacts between Block 3 and LHS as well as Block 1 and RHS are expected to undergo high compressional condition, and so high penalty parameter value is used. Conversely, contact between Block 2 and Top is expected to undergo relatively lower compressional condition, and thus lower penalty parameter is used. It is assumed that the sand layers are sufficiently long to prevent the contact between Block 3 and Top from taking place.

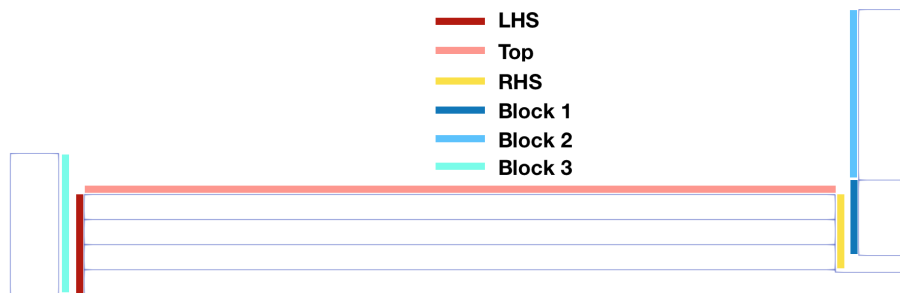


Fig. 5.66 Geometry sets of simulation model

⁷Case 1 represents dry case

Interaction	Geometry Set 1	Geometry Set 2	Contact Property Set
1	Block 1	RHS	1
2	Block 2	RHS, Top	2
3	Block 3	LHS, Top	1

Table 5.10 Surface interaction for contact boundary condition

Contact Property Set	Comp. Penalty (10^4)	Tang. Penalty (10^3)	Friction Coefficient
1	10	30	0.1
2	1	2	0.1

Table 5.11 Compressional/Tangential penalty and friction coefficient

There are two simulation groups to run in this study, as shown in Table 5.12. Group 1⁸ simulates the condition where all sand layers are having similar hydraulic permeabilities, whereas Group 2 includes a material that is about 4 orders of magnitude lower in terms of hydraulic permeability in Layer 1 compared to its counterpart in Group 1. In each group, all cases of prescribed pore pressure (Table 5.9) are considered. The walls on both sides of sand layer are treated as rigid bodies. The material properties used in this study are given in Appendix C.

Layer Order	Group 1	Group 2
Basal Layer	Sand 1	Sand 1
Layer 1	Sand 2	Sand 3
Layer 2	Sand 2	Sand 2
Layer 3	Sand 2	Sand 2

Table 5.12 Simulation groups

5.6.3 Solution Control and Loading Stages

The coupling between pore fluid and solid is solved using incremental staggered scheme. The fluid field is firstly solved with a time step of 0.3s, followed by solving the geomechanical field within the same fluid step. However, the geomechanical time step is $6(10^{-3})$ s. Furthermore, because air is used as pore fluid, it essentially contributes negligible loading to the volumetric strain of the solid surrounding the pore space. Hence, no coupling of volume strain between the two fields is considered.

For each simulation group, the first stage is stress initialization. In this stage, gravitational force is applied to the sandbox model by linearly ramping up the gravity acceleration from

⁸Group 1 corresponds to Series A experiment of Cobbold's work [38]

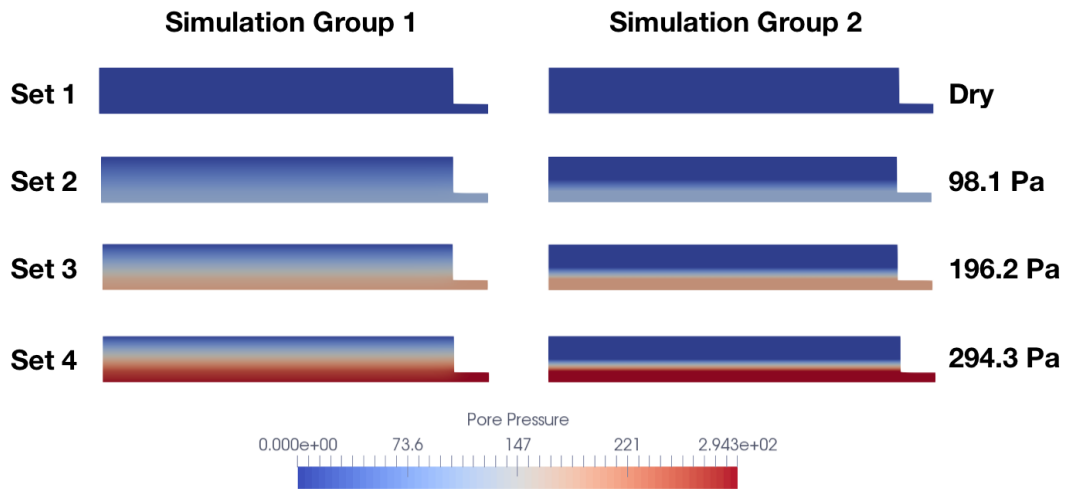


Fig. 5.67 Pore pressure contour before the displacement of sliding wall

0m/s² to 9.81m/s² in 30s. This is followed by pore pressure initialization stage. Depending on the case (referring to Table 5.9), this process also linearly ramps up the pore pressure beneath the Basal Layer from zero to the prescribed level in 30s. The pore pressure contour for each simulation group is shown in Figure 5.67. It is evident that there is significant discontinuity of pore pressure distribution in Group 2 because of the low permeability of Sand 3. Finally, the third stage is when the sliding wall begins to push the sand layers, covering 100mm in 1800s.

5.6.4 Results

Simulation results from Group 1 are compared with Cobbold's illustrated results in Figure 5.68. The character w represents the hydraulic head of water.

Some important features [38] are recovered from the simulation results. Firstly, as basal pore pressure increases, the sand layers gradually feature undulating deformation style, especially on the free surface. As pore pressure increases (Figure 5.69), effective stress naturally decreases, thus driving the corresponding Mohr's circle increasingly closer to the yield surface. Consequently, as shown in Figure 5.70, this increases the tendency of initiating thrust formation in the form of strain localization. Furthermore, Figure 5.70 also shows that the detachment length at the bottom of Layer 1 increases significantly with pore pressure.

In terms of $p - q$ plot of Layer 1, Figure 5.71 shows that higher pore pressure corresponds to plastic yielding at lower effective stress. This observation is complemented by Figure 5.72, which alternatively shows the migration of the median of stress point distribution towards lower effective stress region as pore pressure increases.

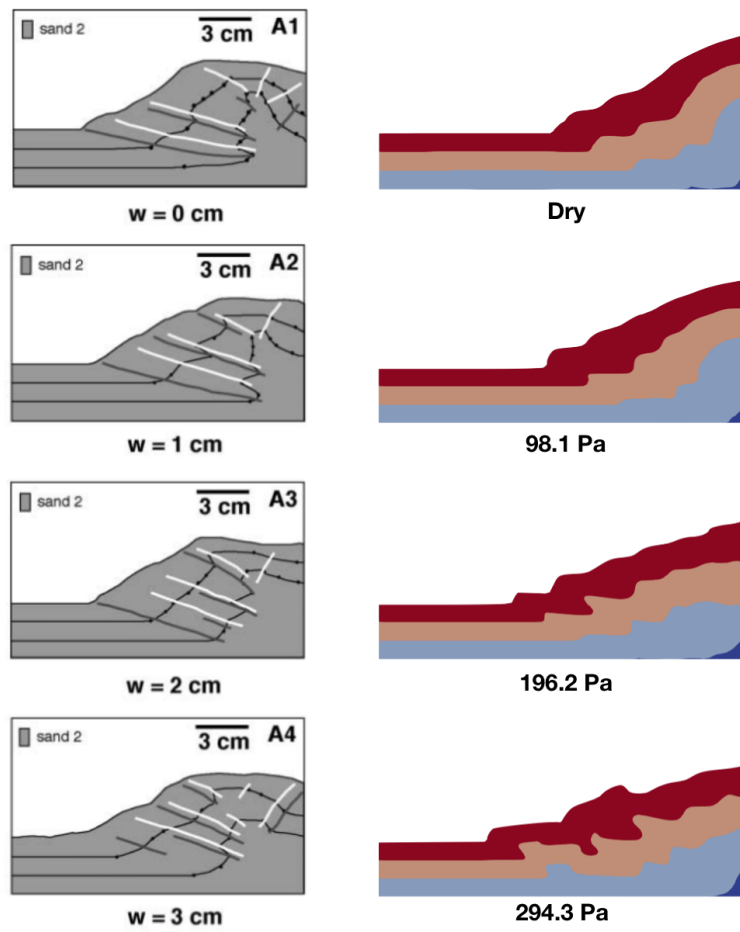


Fig. 5.68 Comparison between simulation and Cobbold's [38] results

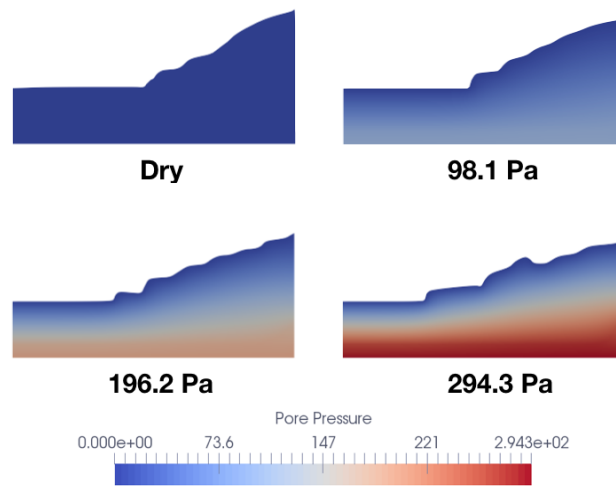


Fig. 5.69 Pore pressure contour in final configurations (Group 1)

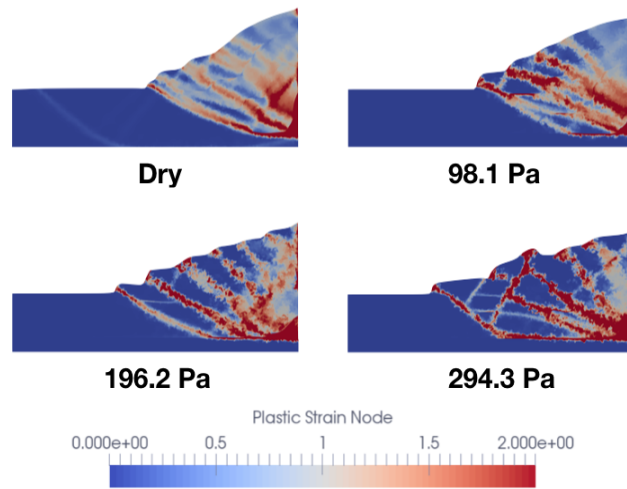


Fig. 5.70 Plastic strain development (Group 1)

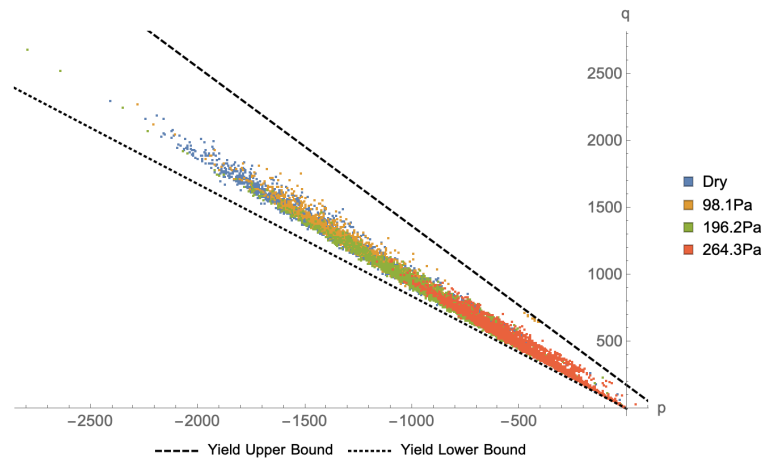


Fig. 5.71 Cloud plotting of yielding points in Layer 1 (Group 1)

Another important influence of pore pressure as discussed in [38] is about the topological evolution of the top surface. Figure 5.73 shows higher pore pressure is associated with shallower top surface slope as well as higher displacement of forethrust build-up. This result is consistent with the experimental observation [38].

In Group 2 simulation results, similar trends are also recovered. In this simulation group, Layer 1 consists of Sand 3 that is about 4 orders of magnitude lower in terms of hydraulic permeability compared with its counterpart (Sand 2) in Group 1. As shown in Figure 5.74, waviness of the sand layers is also observed due to the influence of pore pressure.

The deformation configuration in Case 4 (294.3 Pa) is mainly caused by the large detachment at the bottom of Layer 1. Because of low permeability of Sand 3, a large portion of pore fluid is trapped within the layer, and thus lowering the effective stress in the region.

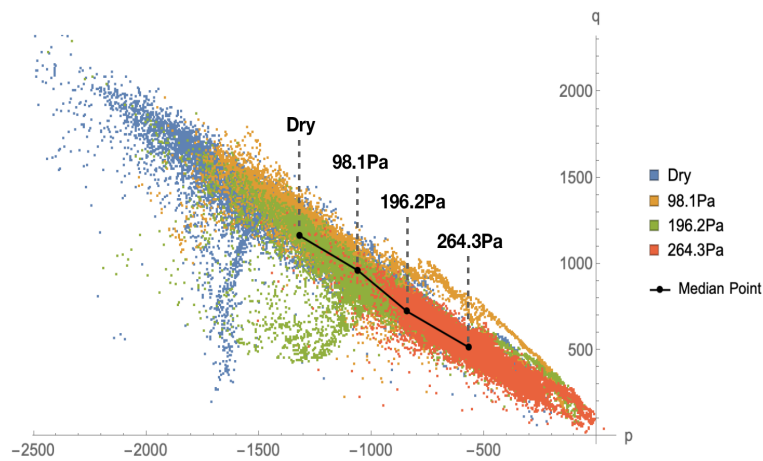


Fig. 5.72 Cloud plotting of stress points (elastic state) in Layer 1 (Group 1)

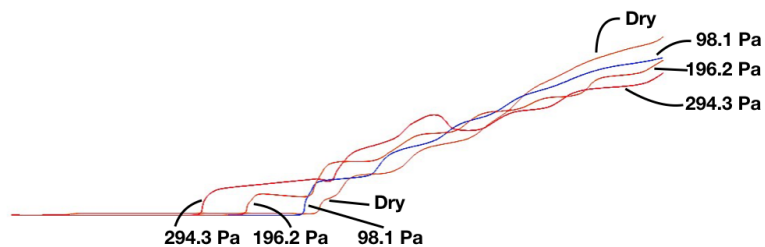


Fig. 5.73 Topological evolution of top surface due to pore pressure (Group 1)

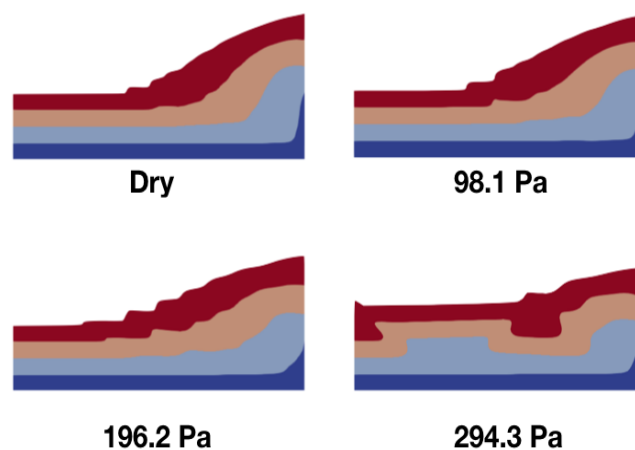


Fig. 5.74 Deformation style of sand layers (Group 2)

This condition will rapidly assist in the initiation and propagation of the basal detachment (Figure 5.75). The incipient formation of graben in Case 4 is also another indication of accelerated basal detachment.

In terms of $p - q$ plot, similar behaviour as observed in Group 1 simulation is also noted in the current Group 2 simulation. Figure 5.76 shows that higher pore pressure corresponds

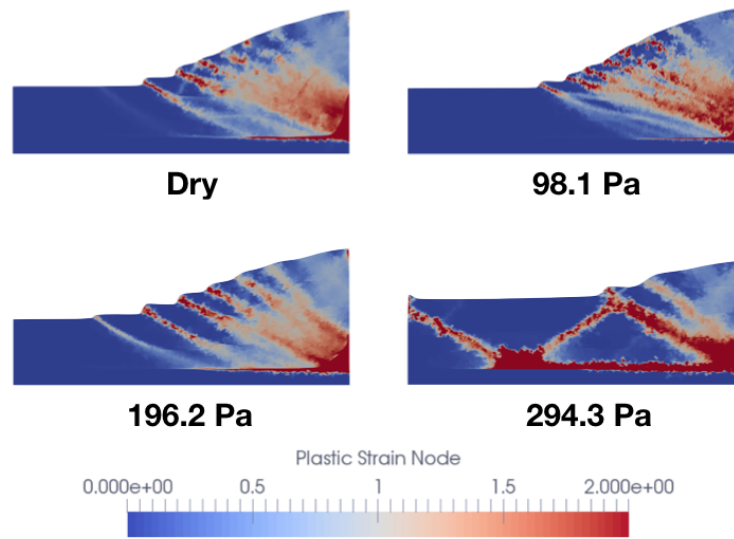


Fig. 5.75 Plastic strain development (Group 2)

to plastic yielding at lower effective stress. Figure 5.77 also demonstrates the migration of the median of stress point distribution towards lower effective stress region as pore pressure increases.

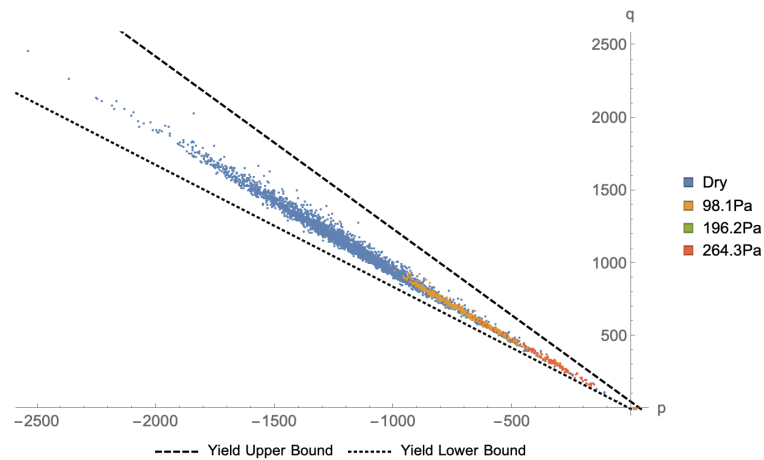


Fig. 5.76 Cloud plotting of yielding points in Layer 1 (Group 2)

However, one notable difference between Figure 5.71 and Figure 5.76 is that the latter shows immediate reduction of effective stress when low permeability material (i.e. Sand 3) subjected to pore pressure is introduced. This finding shows the important influence of hydraulic permeability to the deformation style of sand layers.

Finally, the topological evolution of the top surface in Group 2 under the influence of pore pressure is shown Figure 5.78. Higher pore pressure is associated with shallower top

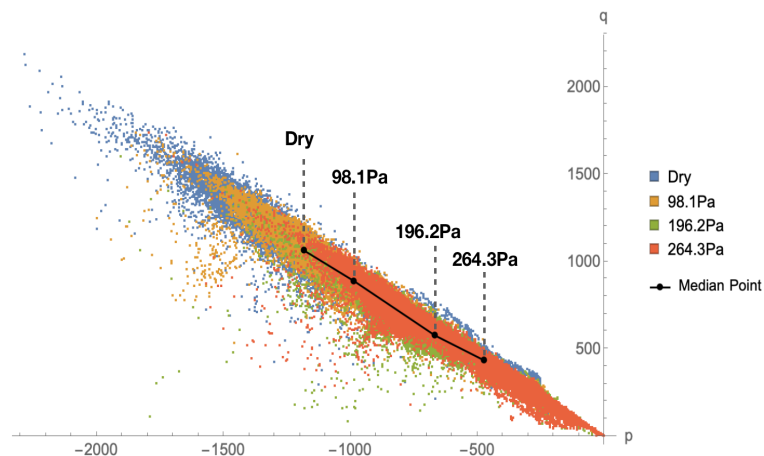


Fig. 5.77 Cloud plotting of stress points (elastic state) in Layer 1 (Group 2)

surface slope as well as higher displacement of forethrust build-up. In comparison with Group 1, Figure 5.79 demonstrates that, given the same pore pressure, material with lower permeability will also visibly decrease the top surface slope.

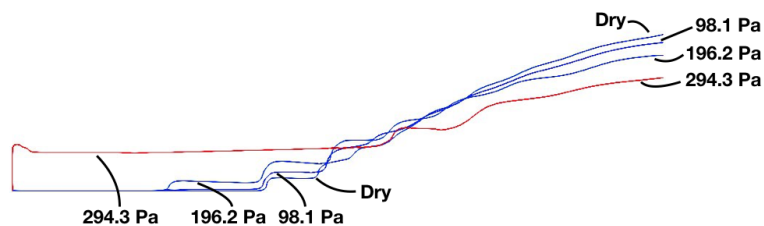


Fig. 5.78 Topological evolution of top surface due to pore pressure (Group 2)

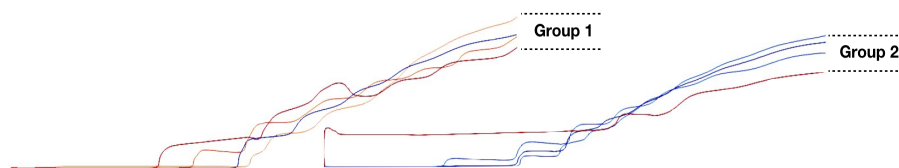


Fig. 5.79 Comparison of top surface slope between Group 1 and Group 2 simulations

5.6.5 Concluding Remarks

Both simulation results from Group 1 and Group 2 successfully recover the important influence of pore pressure when a system of sand layers is subjected to thrusting. When the Basal Layer is prescribed with high pore pressure, the resulting deformation configuration

demonstrates undulating features across sand layers, especially at the top surface. The waviness is a direct consequence of the basal detachment caused by fluid overpressure. In addition, shallower top surface as well as higher displacement of forethrust build-up are also attributable to fluid overpressure condition.

The effect of hydraulic permeability is simulated in Group 2. Given the same level of pore pressure, it is predicted that lower permeability also contributes to larger basal detachment as well as shallower top surface in the final deformation configuration.

5.7 Hydraulic Fracture due to Fluid Injection

5.7.1 Modelling Setup

In this simulation test, a $20m \times 25m$ block is subjected to fluid injection on a small surface at the left boundary as illustrated in Figure 5.80. The objective is to induce hydraulic fracture within the domain, whereby its top and bottom boundaries are constrained in vertical direction and the left and right boundaries are constrained in horizontal direction. An initial fracture with small aperture is pre-defined. It is assumed to be linear elastic and relatively permeable (i.e. $k_x = k_y = 10^{-9}m^2$) with respect to the surrounding medium. Fluid flux is introduced at the boundary of the initial fracture, with an increase from 0 to $0.2m^3/s$ in 0.1s, and stays constant for a duration of 0.4s. The augmentation of hydraulic permeability due to fracture is realised through a simple multiplier model, which depends on the surrounding normal stress. In the current test, the permeability multiplier changes linearly from 1000 to 100 when the surrounding normal stress decreases from 0 MPa to -2.0 MPa. The whole domain is discretised into 9090 elements. The maximum element size has a dimension of $0.225m \times 0.28125m$, whereas the smallest element size has a dimension of $0.2m \times 0.04m$. The geomechanical and seepage field time step sizes are set, respectively, as $10^{-6}s$ and $10^{-4}s$.

5.7.2 Simulation Groups

Two simulation groups are considered. Assuming elasto-fracture constitutive behaviour, the first group studies the effect of the ratio of horizontal permeability (k_x) to vertical permeability (k_y) on the behaviour of hydraulic fracturing. This is relevant to the geomechanical conditions, in which transversely isotropic properties are usually assumed across different stratigraphic layers. In this test group, the vertical permeability is set as constant ($10^{-14}m^2$), whereas the horizontal permeabilities are varied: $10^{-10}m^2$, $10^{-12}m^2$ and $10^{-14}m^2$.

On the other hand, the second group considers elastoplastic-fracture behaviour with and without the cohesion-tensile strength coupling effect. The cohesion is set as 1MPa,

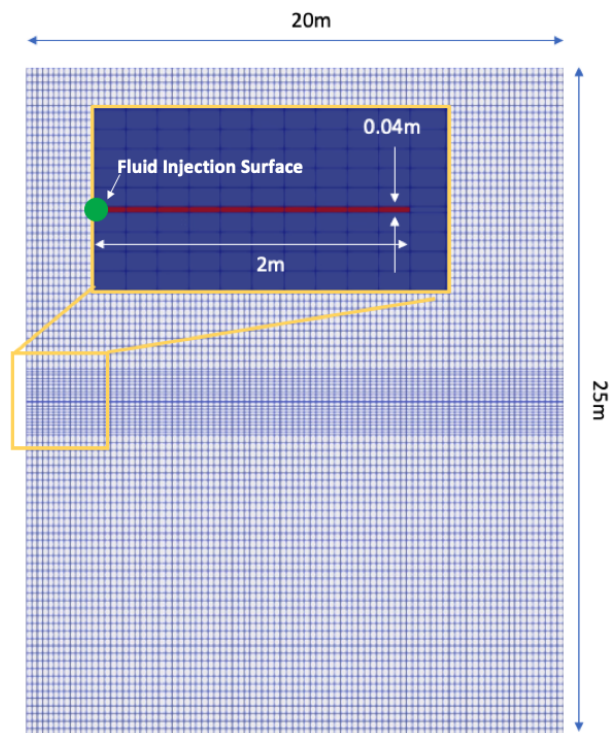


Fig. 5.80 Geometry and spatial discretisation

linearly driven to 0 when the effective plastic strain attains 1.0. Associative plastic flow model is assumed; the friction and dilation angles are set as 30.164° . For the case where cohesion-tensile strength coupling effect is considered, the value of η_1 is set as 0.01. Other common material properties are listed in Table 5.13.

Material Properties	Value
Porosity	0.35
Grain density (kg/m^3)	2300
Young's modulus (GPa)	20
Poisson's ratio	0.20
Uniaxial tensile strength (MPa)	1.0
Fracture energy, G_f (Pa.m)	200
Fluid density (kg/m^3)	1000
Fluid viscosity (MPa.s)	$8.9(10^{-10})$

Table 5.13 Properties of quasi-brittle material

5.7.3 Results: 1st Simulation Group

The effect of k_x/k_y is markedly pronounced in the pore fluid pressure distribution as shown in Figure 5.81. In the isotropic case ($k_x/k_y = 1$), the pore pressure distribution tends to be radial. On the other hand, for the case with the highest k_x/k_y , the pore pressure distribution is evidently biased towards horizontal direction. The change of pore pressure distribution due to the variation of k_x/k_y as observed in the simulation results is expected, since the fluid flow is spontaneously in favour of path with the least hydraulic resistance. Therefore, with higher k_x/k_y , the pore pressure tends to migrate horizontally. If Rankine criterion⁹ is violated, fracture develops. Driven by the augmentation of hydraulic permeability, the crack propagation path may develop further for higher k_x/k_y (Figure 5.82, 5.83). Given that the fluid flux stays constant after $t = 0.1s$, the global pore pressure should be maximum at the final time for the isotropic permeability model, since the fluid stays relatively closer to the source due to shorter propagation path. This phenomenon is reflected by the vertical displacement contour in Figure 5.84; high pore pressure is correlated to higher vertical displacement. The uneven distribution of vertical displacement in the vicinity of initial fracture for low k_x is due to the high pore pressure accumulated by the surrounding medium. Because the accumulation rate is higher than the dissipation rate, the surrounding medium tends to cause the closure of the initial fracture. The mechanical loading contributed by pore pressure can also be visualised in the form of volumetric strain (Figure 5.85-5.87). A sample element that is positioned along the propagation path is investigated. The key observation is that, as k_x/k_y increases, the distribution of volumetric strain tends to shift away from the initial fracture tip, with an apparent reduction in the peak volumetric strain (Figure 5.88). The effect of k_x/k_y on the pore pressure evolution at the initial fracture tip is also revealed in Figure 5.89. The pore pressure progresses towards the first peak momentarily before starting to decline due to hydraulic fracture. For low permeability cases ($k_x = 10^{-14}m^2$, and $k_x = 10^{-12}m^2$), the pore pressure increases again due to relatively higher hydraulic resistance in the subsequent propagation path.

5.7.4 Results: 2nd Simulation Group

In the second simulation group, the effect of elastoplastic-fracture model is considered in the hydraulic fracturing test. With the current modelling setup and the choice of material properties, the difference between elasto-fracture and elastoplastic-fracture models in terms of pore pressure contour is hardly discernible. Therefore, the same sample element is investigated only for its stress-strain constitutive behaviour. As shown in Figure 5.90, there

⁹the effect of breakdown (or activation) pressure is not considered in the current test

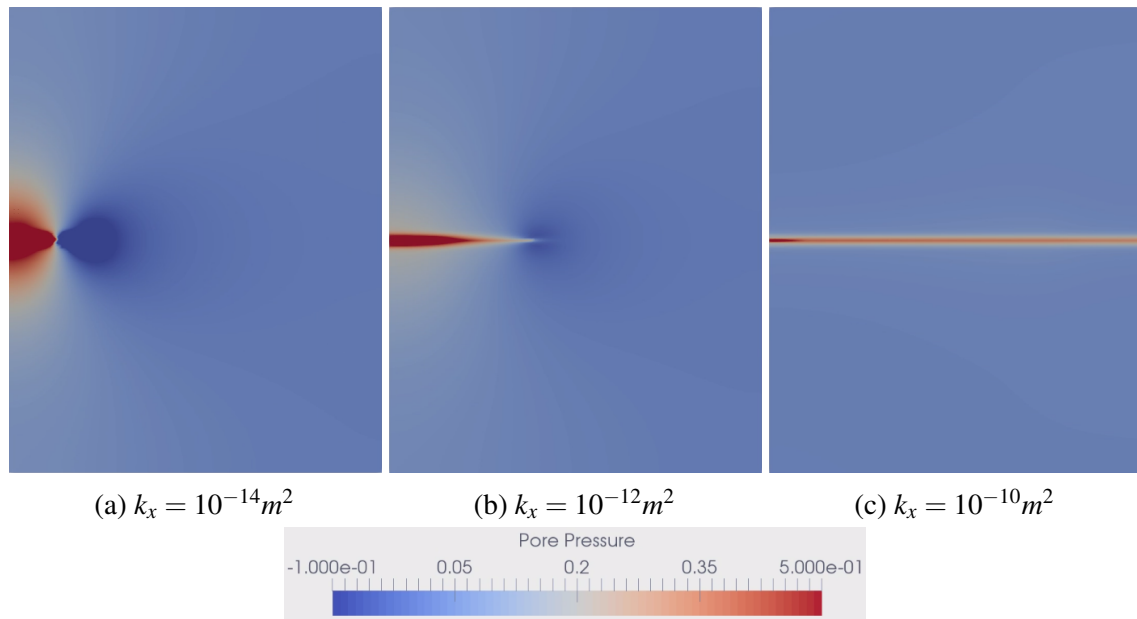


Fig. 5.81 Pore pressure distribution for different permeabilities at fixed $k_y = 10^{-14} m^2$ at $t = 0.5s$

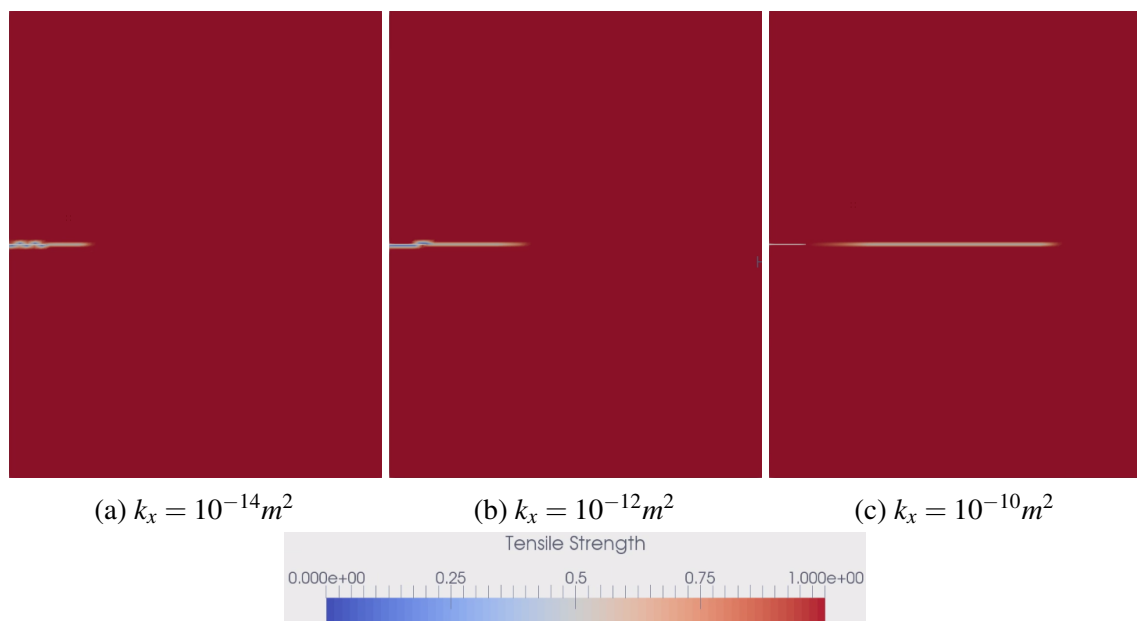


Fig. 5.82 Tensile strength distribution for different permeabilities at fixed $k_y = 10^{-14} m^2$ at $t = 0.5s$

is however noticeable difference in terms of strain at which the softening starts to take place. It is clear that the effect of plastic deformation delays the initiation of softening process. However, with the effect of cohesion-tensile strength coupling via factor η_1 , the softening

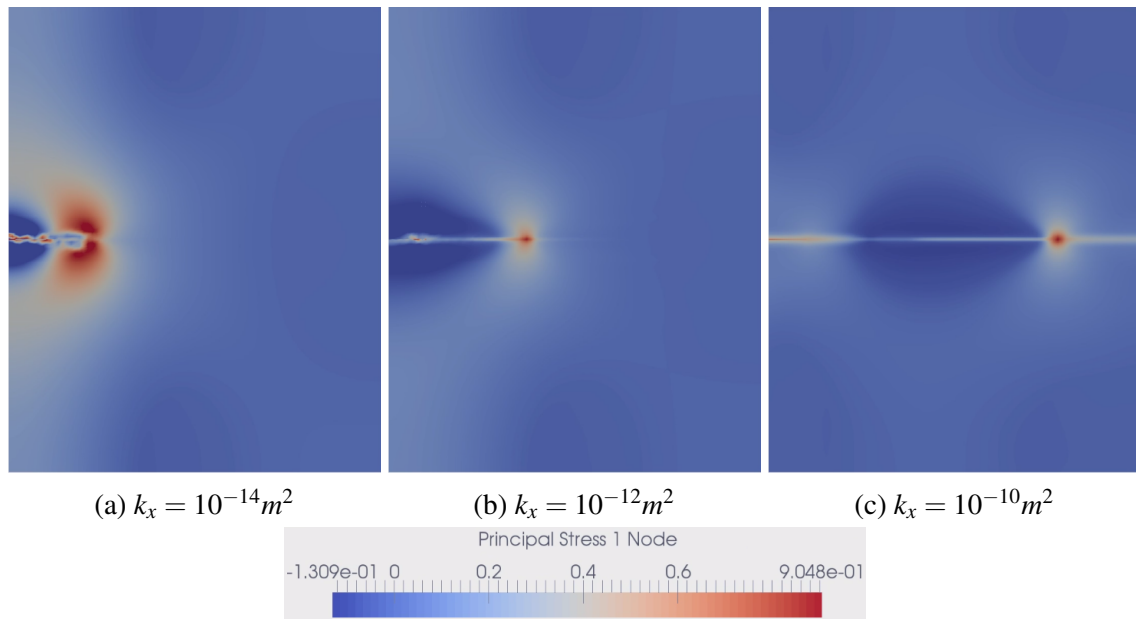


Fig. 5.83 Principal stress 1 distribution for different permeabilities at fixed $k_y = 10^{-14} m^2$ at $t = 0.5s$

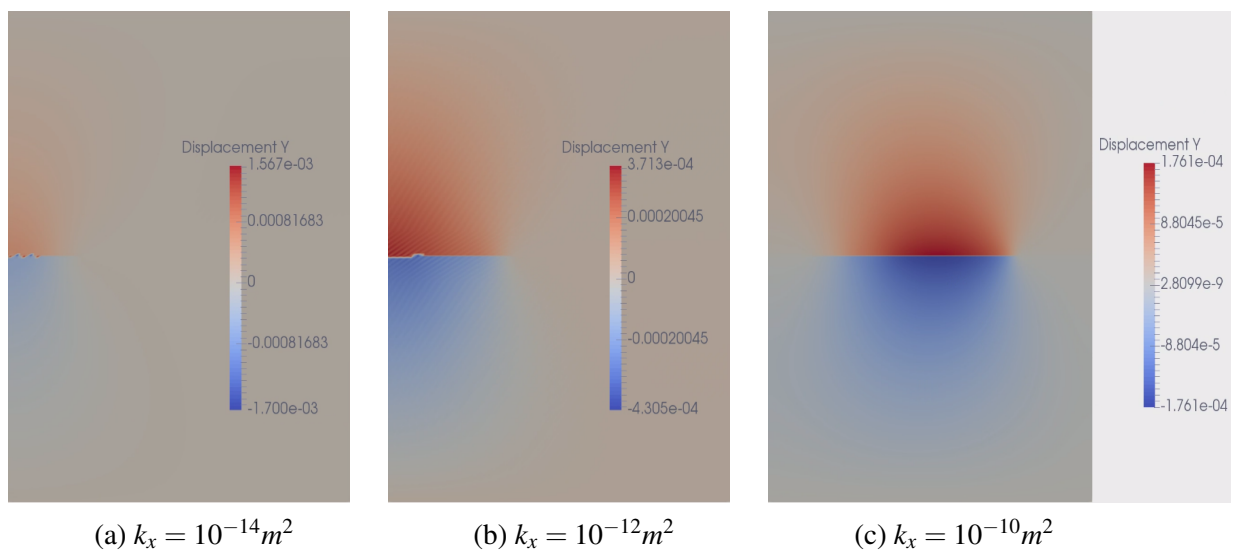


Fig. 5.84 Vertical (y) displacement for different permeabilities at fixed $k_y = 10^{-14} m^2$ at $t = 0.5s$

process is further delayed and takes place at a lower tensile strength. The effect of η_1 is magnified in Figure 5.91, in which the reduction of tensile strength is complemented by the reduction of cohesion.

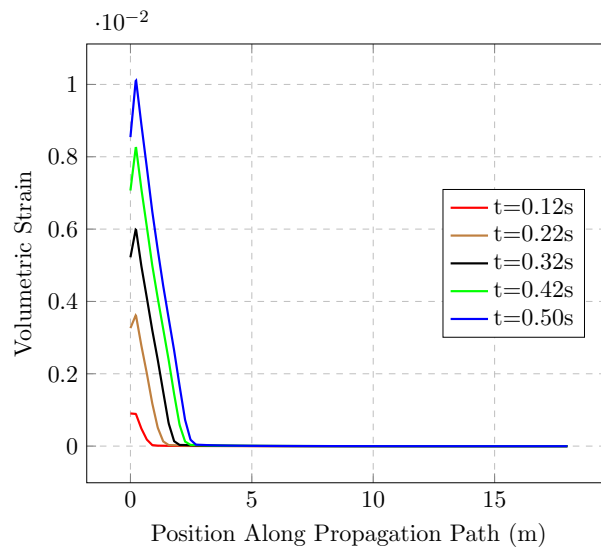


Fig. 5.85 Volumetric strain evolution of a sample element near initial fracture tip for $k_x = 10^{-14}m^2$

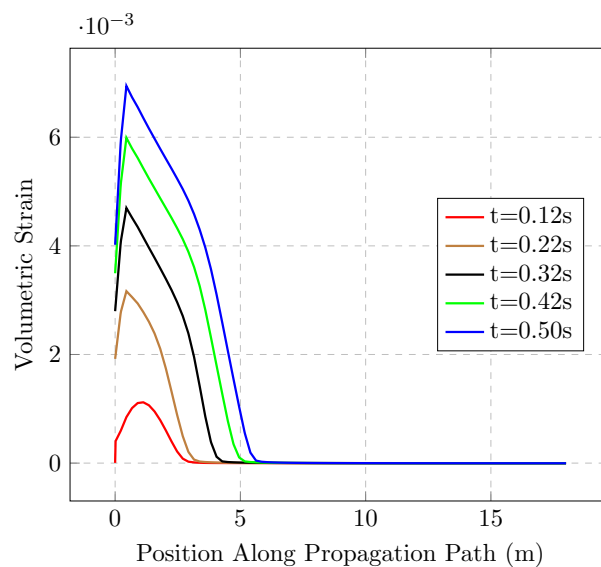


Fig. 5.86 Volumetric strain evolution of a sample element near initial fracture tip for $k_x = 10^{-12}m^2$

5.7.5 Concluding Remarks

It is acknowledged hereby that smoother plots could have been obtained, had all the points been recorded at a more refined time step size. The key thing of this simulation test is to demonstrate the capability of the elastoplastic-fracture model with coupled cohesion-tensile strength to work in a flow-mechanical simulation, with the consideration of anisotropic

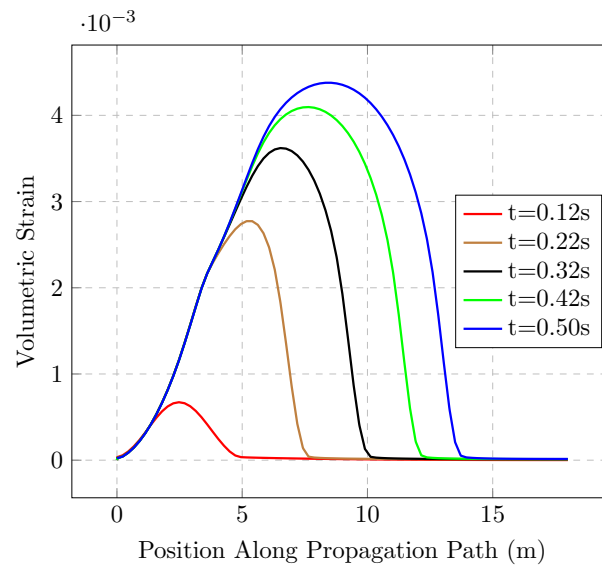


Fig. 5.87 Volumetric strain evolution of a sample element near initial fracture tip for $k_x = 10^{-10} m^2$

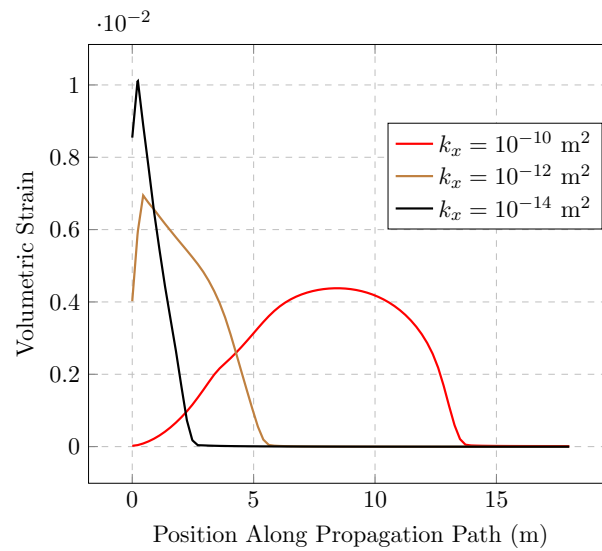


Fig. 5.88 Volumetric strain evolution of a sample element near initial fracture tip for different k_x at final simulation time $t = 0.5s$

hydraulic permeability. A successful demonstration of this test is crucial to the field-scale simulation of geomechanical importance.

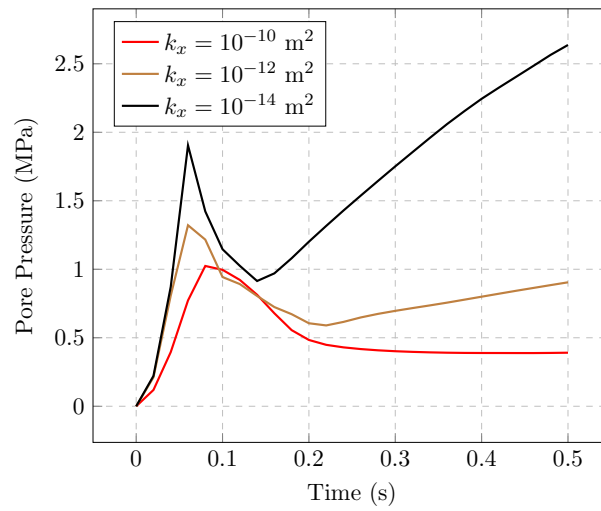


Fig. 5.89 Pore pressure evolution at the initial fracture tip for different k_x and fixed k_y

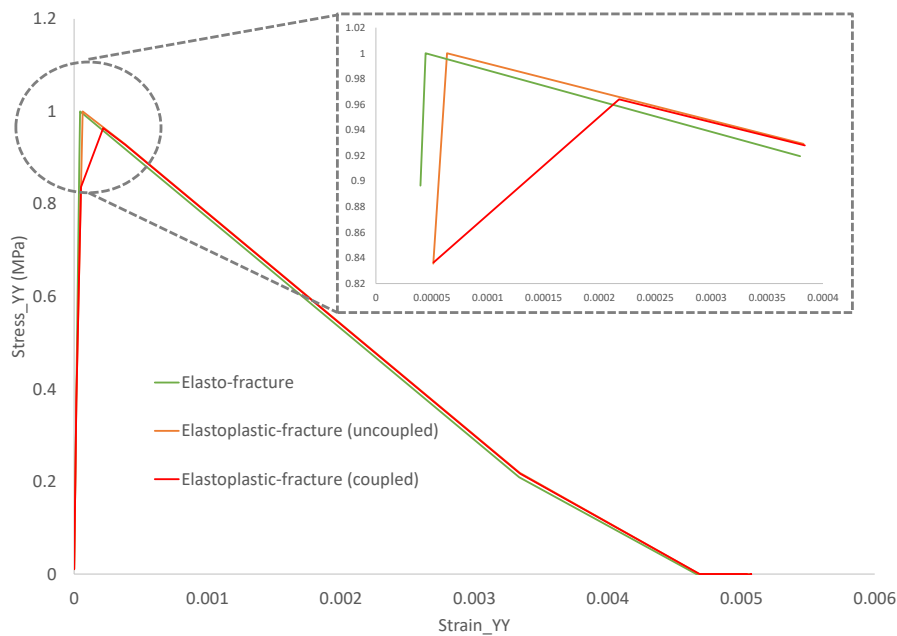


Fig. 5.90 Effect of cohesion-tensile strength coupling on the initiation of stress softening. The coupling factor η_1 is set as 0.01.

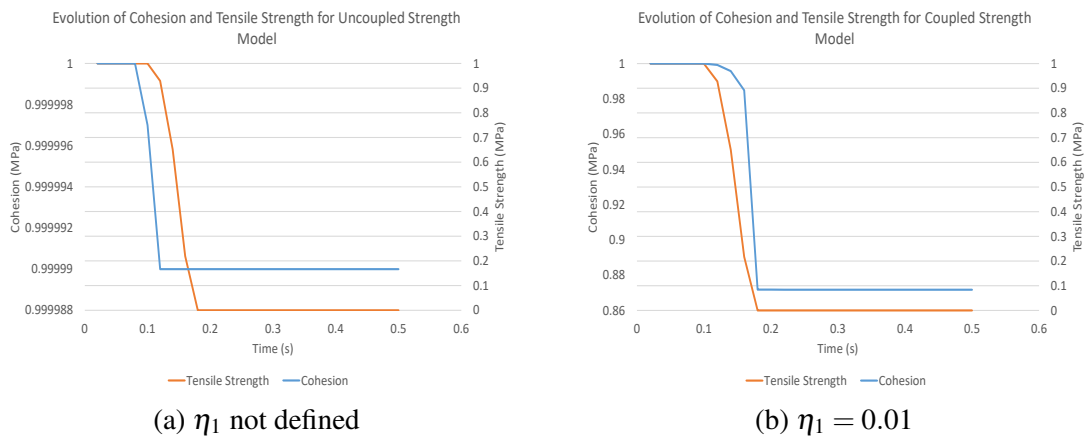


Fig. 5.91 The reduction of tensile strength contributes to the reduction of cohesion via the cohesion-tensile strength coupling factor η_1 .

Chapter 6

Basin Scale Simulation: Gravity Spreading in Prograding Delta due to Overpressure

6.1 Introduction

6.1.1 Background

The formation of continental passive margins is generally associated with a combination of gravity-induced deformations due to the presence of weak basal layer, characterised by extensional-type faults at proximal regions and compressional-type faults at distal regions [142, 151]. Specifically at distal regions, deepwater fold and thrust belts are the results of the evolution of seaward progradation departing from upslope extensional structures along a decollement layer under the influence of gravitational force over geological time scale [142].

6.1.2 Decollement Layer

The weak basal strength in the decollement layer could be due to abnormally low friction coefficient [123], the presence of viscous salt layer [53] or highly overpressured shale layer [144]. Regions that have been identified to be detaching over salt layer include northern Gulf of Mexico and Mississippi fan [188, 143, 142], Atlantic margins of Mauritania and Angola [28, 69] and Nile deepsea fan [71, 103]. On the other hand, regions that are known to be detaching over highly overpressured shale layer include Niger delta [181, 122, 41, 87, 43, 26], Amazon fan [39], Mexican ridges [183] and Baram Delta [172]. Although shale and salt

tectonics may coexist in the same sedimentary basin [89], such complicated nature is not considered in the present study.

6.1.3 Overpressure Generation

For the case of highly overpressured shale layer, the associated generation mechanisms [130, 157] can be caused by disequilibrium compaction of solid matrix due to burial and tectonic loadings as well as any non-mechanical process that increases the volume of pore fluid.

Disequilibrium compaction happens [120, 128] when the outflow fluid velocity from the pore space is lower than the compression rate of the pore volume, causing the transfer of the compressive load to the fluid and the subsequent reduction of the effective stress in the solid matrix. This mechanical compaction is a function of bulk compressibility as it is linked to the grain rearrangement to form denser packing [89]. The associated time scale is represented by characteristic diffusion time scale [120]

$$t_d = \frac{L^2 \beta_b(n) \mu_f}{k_0}, \quad (6.1)$$

where L is characteristic length, β_b is bulk compressibility, μ_f is single-phased fluid viscosity, and k_0 is the reference permeability.

If the sedimentation time scale is represented by t_s , it then follows that disequilibrium compaction happens when $t_d \gg t_s$. On the contrary, if t_d is less than t_s , it implies that the diffusion rate is higher than the overpressure generation rate.

However, gravitational deformation of a prograding delta is unlikely to be solely caused by the mechanism of disequilibrium compaction, unless an unreasonably large bulk compressibility¹ is considered [89]. To remain using normal value of bulk compressibility, a viscous compaction model, representing the salt behaviour, has been applied instead [89].

In cases where viscous compaction might not be applicable (e.g. Niger Delta shale tectonics), deltaic destabilisation under gravity can still be triggered by pore pressure generation mechanism, including thermal dilation, mineralogical transformation (e.g. from smectite to illite at temperature 70-150°C [117, 119, 12, 13, 130, 157]), capillary seals [31] as well as hydrocarbon generation. It is further suggested by [7] that thermogenic gas production is the most efficient overpressure generation mechanism.

¹around $8(10^{-7}) \text{ Pa}^{-1}$

6.1.4 Feedback Mechanism

If sedimentary progradation is caused by the mobilisation of highly overpressured shale layer, then the continuity of the process relies on the further development of fluid overpressure generation, which can be explained in the form of feedback mechanism [157].

Under sufficiently high pressure and temperature, solid kerogen is transformed into oil and gas via the destruction of cohesive bonds between grains. The transformation of solid kerogen into oil and gas involves the destruction of cohesive bonds between the grains. The resulting increased compressibility of the solid matrix readily transfers the overburden weight to the generated fluid. In an environment of low permeability, high overpressure can rapidly build up, close to the overburden weight [118, 116]. The resultant high overpressure weakens the solid matrix and thus enhances basal detachment, causing the advance of thrust front that are typically characterised by listric development at the base. Subsequent burial caused by further sedimentation at the top surface will continue to catalyse the source rock maturation process.

6.1.5 Nigeria Delta Field

Background

As previously mentioned, Niger Delta is an example of prograding delta believed to be caused by an underlying highly overpressured shale layer. In the following, some background and the characteristic structures of Niger Delta are introduced.

Sitting at the southern Benue trough, the progradation in Niger Delta [37] has started since Eocene (56 to 33.9 million years ago). The delta is characterised by thin-skinned structures, which become increasingly listric towards flat-lying faults in the underlying source rock layer [52]. The latter is the manifestation of slope instability due to overpressured shale [60, 52, 27]. The process of seaward sediment progradation is concurrent at basin scale with the progressively basinward migration of the front of overpressured domain [124], subjected to the evolving sliding friction between overpressured and normally pressured shale boundaries as well as the sedimentary wedge [108, 175].

The geological structures due to large-scale gravity deformation triggered by fluid overpressure can be categorised into three main zones, namely extensional province, transitional province, and compressional province [52, 43].

The extensional province of Niger Delta displays [37] basinward dipping, listric normal growth faults, whereas the compressional province, located at the distal part of the delta in deep water, features basinward fold and thrust imbricate geological structures [52, 81, 1, 2, 87, 43, 44, 15, 16, 26]. The transitional province, lying in the middle of extensional

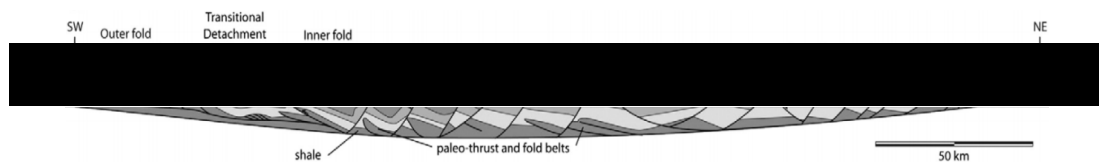


Fig. 6.1 Figure obtained from [37], showing extensional, transitional and compressional province along a generic cross section of Niger Delta.

and compressional domains, is characterised by inner fold and thrust belts superimposed with younger extensional faults [124]. The whole transitional structure can be treated as a prograding shelf [37].

In general, Niger Delta consists of three stratigraphic groups, which are Benin formation, Agbada formation and Akata formation [37]:

- Benin formation: The top layer forming the ocean seabed; predominantly of continental and fluvial origin.
- Agbada formation: The middle layer, which is about 3km thick or more, serves as hydrocarbon reservoir rock, which has little or no overpressure. The sediment materials are of clastic nature, which is very different from the underlying Akata formation [121].
- Akata formation: The bottom layer, which houses 3-4km thick overpressured hydrocarbon source rock. The thickness is not uniform; it ranges from 7km-thick in the extensional region to 2km-thick in the compressional region [124].

Characteristic Structures

The formation of thin-skinned thrust wedges and stratigraphic folds that are developed sequentially towards the ocean, are caused by lateral shortening and vertical thickening under tectonic compression over overpressured shale layer in the vicinity of Akata formation [37]. The structures are characterised [81, 87, 1, 2, 121, 43, 44, 15, 16, 98, 26, 85] by fore- and back-thrusts with small apical angles, complemented by the associated hanging wall anticlines and flat-bottomed synclines. It is also noted that all thrusts originate from the Akata formation. As shown in Figure 6.2, the basal detachment is not only confined to the top surface of Akata formation, but also capable of taking place at up to certain depths within the formation. The depth at which detachment takes place depends on several factors, such as sediment burial depth, thermal gradient and the richness of the source rock.

With reference to Figure 6.2, the left figure shows that sharp basal detachment develops from within the Akata formation and the faults propagate to the surface in a listric nature [37]. The location of the basal detachment indicates that overpressure is maximal in the

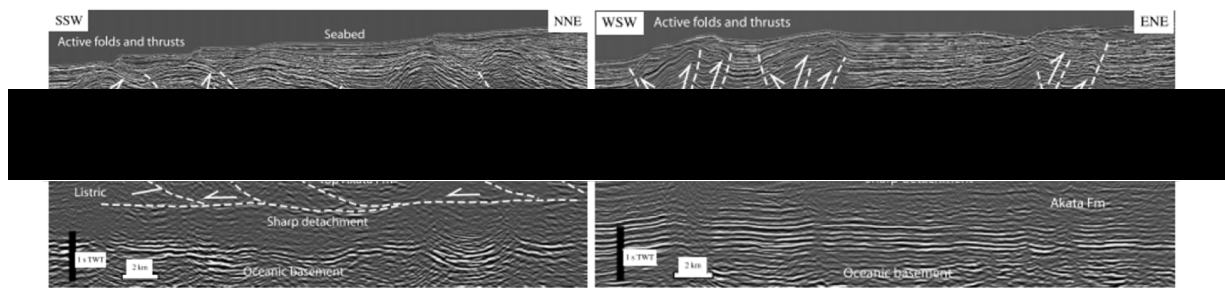


Figure 3 (Southern lobe)

Figure 4 (Western lobe)

Fig. 6.2 Figure obtained from [37], showing the seismic profiles and interpretation of Southern lobe (left) and Western lobe (right) in Niger Delta.

region. This observation suggests that overpressured generating mechanism occurs within Akata Formation [40]. On the other hand, the right figure shows the propagation of thrust faults from the surface of Akata formation to the top surface over shorter listric segments, suggesting high pore fluid pressure gradient across the stratigraphic interval and so, Agbada formation could act as sealing layer to the underlying Akata formation. Regardless of the depth at which detachment takes place, it is a good indication that high fluid overpressure plays important role in triggering large tectonic motion under gravitational force [124].

The overpressured condition [60, 81] of Akata formation can be inferred from low reflectivity in the seismic profile [121]. The low seismic reflectivity can also exclude the possibility of the existence of salt layer in Niger Delta. It is argued [121] that low seismic interval velocity indicates low bulk density in the formation, which can only be sustained by high fluid overpressure. Furthermore, direct evidence of hydrocarbon via drilling and mud volcanoes have also been reported [65, 76].

In fact, hydraulic vents (Figure 6.3) can be recognised [37] from some of the examples of seismic profiles. They are situated within hanging wall anticlines of thrust fault originating from Akata formation. The profiles show that the content of the hydraulic vent is seismically transparent. Also, it can be interpreted from the sharp edge surrounding the vent that the content is more likely to be fluid than gas.

Since the vent is connected to the listric fault originating from Akata formation, it can be inferred [37] that high fluid discharge has taken place through the thrust faults due to large seepage force. In October 2004, Petrobas performed [37] drilling in Niger Delta and concluded that while the pore pressure in Agbada formation is quasi-hydrostatic, high overpressure in near Akata formation was detected. Such discovery is important as it confirms that overpressure is not produced until reaching the Akata formation.

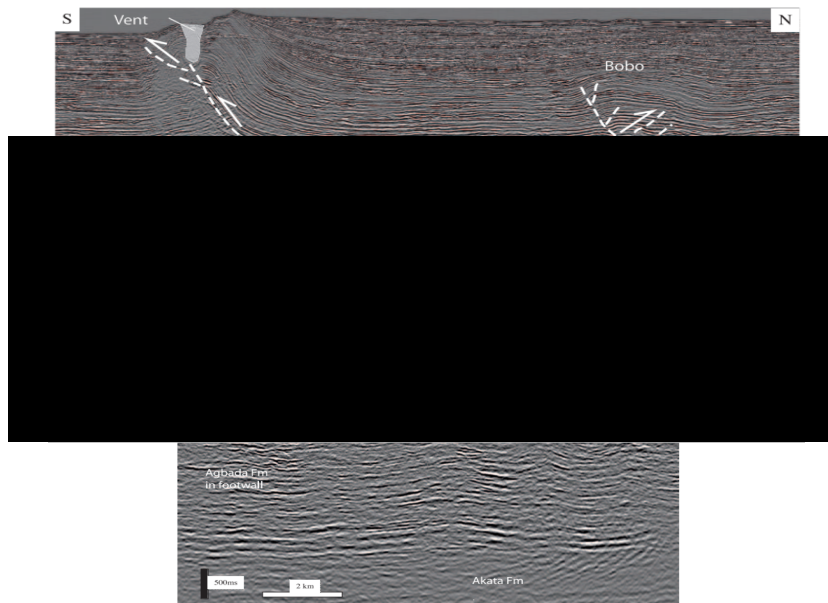


Fig. 6.3 Figures obtained from [37], showing the seismic profile of vents identified in Niger Delta.

6.2 Some Previous Modelling Studies

6.2.1 Sedimentary Progradation using Sandbox Models

Using analog modelling technique, [124] simulates sedimentary progradation by controlling the overpressure injection window beneath basal layer using compressed air. Three models of 1.8m in length are prepared for this experiment. In Model 1, the overpressure injection window extends according to the length of the sedimentary progradation, whereas in Model 2 and 3, an overpressure injection window of fixed length translates according to the sedimentary progradation. Model 3 differs from Model 2 by having a coarse sand layer interbedded with two fine sand layers at its base.

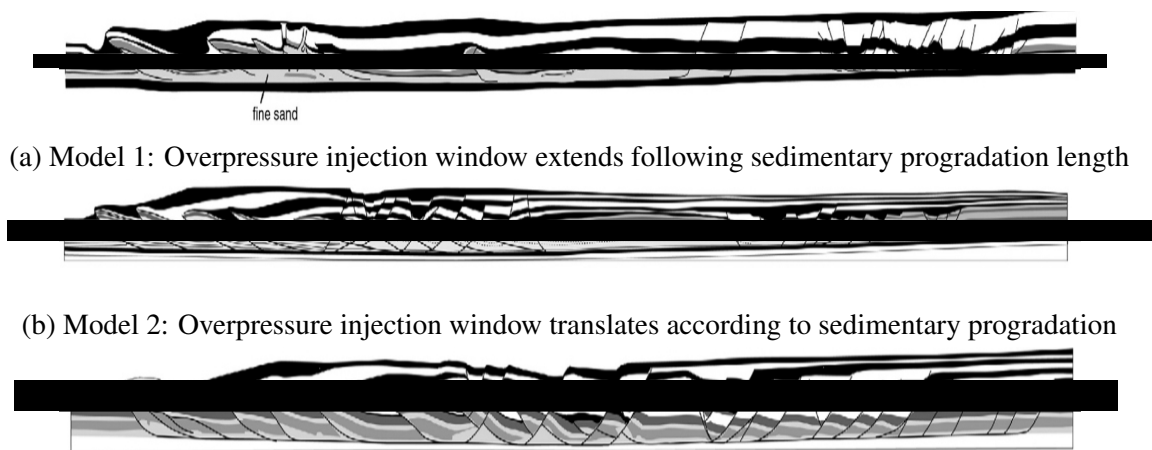
The following procedure outlines how sedimentary progradation was applied in all the sandbox models:

1. Fluid (compressed air) pressure is increased in the base, over which gravitational deformation is expected to take place.
2. As extensional faults are developed, new layer of sediment is filled on top of the fault surface to simulate synkinematic sedimentation.
3. The increment of fluid pressure and synkinematic sedimentation processes are stopped when no further faults are formed.

4. Then, a new sediment wedge is deposited to simulate sedimentary progradation.
5. Fluid pressure is increased again and the procedure above is repeated. The fluid injection window is extended to cover the base of the newly prograded sediment.

As shown in Figure 6.4, the outcome from all models shares some of the patterns as observed in the field:

- Three distinct zones are identified: Extensional (demonstrating basinward verging normal faults), transitional and compressional zones.
- Detachments root on a decollement layer.
- When fluid overpressure is high, fine sand layer becomes fluidised and results in the thickening of the detachment layer in a ductile manner.



(a) Model 1: Overpressure injection window extends following sedimentary progradation length

(b) Model 2: Overpressure injection window translates according to sedimentary progradation

(c) Model 3: Same as Model 2, but with a coarse sand layer interbedded with two fine sand layers at the base

Fig. 6.4 Figures obtained from [124], showing the fault patterns obtained from three different sandbox models

In the extensional zone, all models demonstrate basinward-verging normal faults. However, whereas the pore pressure injection window translates with the progradation direction in Model 2 and 3, it is observed in Model 1 that the continuous exposure to high overpressure in the extensional zone has caused the fine sand layer to migrate towards the distal part. In reality, despite the reduced influence of disequilibrium compaction (lower sedimentation rate compared to the distal part) in the extensional zone, the continued overpressure in this region is justified by acknowledging the contribution by potential hydrocarbon generation mechanism.

In the transition region of Model 1, a large flat dome made up of fine sand is formed. It is noted that the faults developed within the dome does not propagate towards the overburden. Similar structure, known as broad detachment fold, is also spotted in Niger Delta. In contrast, in Model 2 and 3, the transition region is characterised by paleo-thrust at the bottom (resulted from shelf progradation) that is intersected by normal faults associated with extension above the thrusts. The latter is also modelled by [108, 109].

In the compressional region, fluidization of fine sand layer has caused the thickening of the base of fore thrusts in all models. However, in Model 1, sand volcanoes are formed in the compressional region, reflecting high degree of overpressure in the low permeability fine sand layer. Such pipe-like structures are also observed in passive margin and overpressured deltas [173, 76, 59]. At basin scale, mud volcanoes are formed in compressive stress regime, where local pore fluid pressure exceeds the fracturing pressure [58]. On the other hand, basal detachment in the compressional region is more evident (characterised by the formation of young active thrusts at the distal section) in Model 2 and 3 compared to Model 1, with Model 3 having more back-thrusts than Model 2. The latter is attributed to the additional upper decollement layer [124]. In addition, at the distal part of Model 3, a pop-up is formed, which is expected when decollement layer is very weak. This could mean that, along the whole sedimentary margin, the fluid overpressure level may be the highest in this location.

Overall, the sandbox models provide useful insights regarding the formation and propagation of each fault. While the use of compressed air may help mobilising the base layer via the reduction of effective mean stress, the use of granular material with low cohesion however means that fluid overpressure can hardly be contained.

In addition, with such laboratory length scale, the material is unlikely to be subjected to mechanical loading which leads to plastic compaction. The latter is an important measure of porosity loss and its rate influences the generation rate of fluid overpressure. This importance is highlighted by [128]. In the study, disequilibrium compaction is simulated [128] as a combined effect of sedimentary and tectonic loadings in a column of 400m in thickness and 4000m in height to investigate the influences of mechanical stress and the corresponding evolution of porosity on the generation of overpressure. The finding confirms that high fluid dissipation rate is associated with high porosity loss.

6.2.2 Influence of Fluid Overpressure on Deformation

The profound impact of fluid overpressure is further demonstrated by [129] in the simulation of fold and thrust structures in northwest Borneo. Two models with identical geometry, constitutive models and boundary conditions are run in drained and coupled analysis modes, respectively. As shown in Figure 6.5, two different outcomes are obtained for the shale layer.

In the coupled model, the presence of overpressure locally shifts the stress path towards the shear side of the yield surface as lateral shortening increases, resulting in strain localization. In contrast, such shift of stress path can never be reproduced in drained model, where only hydrostatic pore pressure is present all the time in the whole domain. Therefore, in the drained condition example by [129], the stress path keeps approaching the compression side of the yield surface when subjected to tectonic compression, resulting in more diffuse plastic deformation.

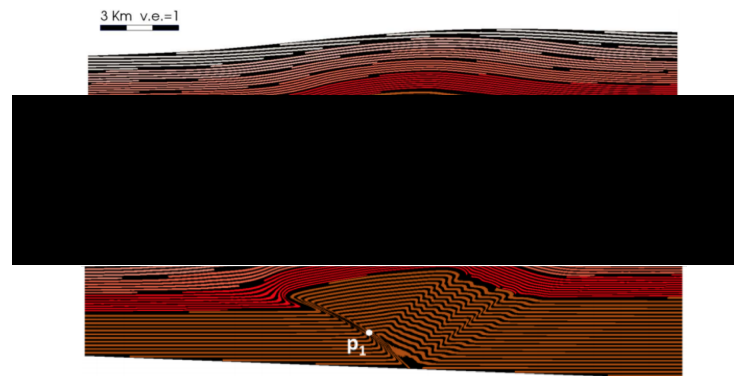


Fig. 6.5 Figure obtained from [129]. The structure at the top was generated under drained conditions, whereas the structure at the bottom was generated under coupled hydro-mechanical conditions. This comparison highlights the importance of accounting for overpressure generation in simulating fold and thrust faults.

6.2.3 Sedimentary Progradation via Mechanical and Viscous Compaction Mechanisms

Two relevant studies are briefly summarised hereby. The first study [120] simulates sedimentary progradation over highly overpressured shale without accounting for isostatic compensation, whereas the second study [89] does. In both cases, fluid overpressure is generated by disequilibrium as well as viscous compaction mechanisms.

In the first study, it is concluded that deltaic instability is triggered only when the pore pressure reaches close to lithostatic pressure, i.e. Hubbert-Rubey pore pressure parameter $\lambda_{HR} \approx 0.95$. Purely disequilibrium compaction model exhibits $\lambda_{HR} < 0.95$ and downward velocity vector, indicating gravitational stability due to simultaneous dissipation of pore fluid pressure. On the other hand, for another model with viscous and mechanical (disequilibrium) compactions, the velocity vector of the progradation front is pointing forward, indicating that gravitational instability of the delta is caused by very high basal overpressure ratio, that is $\lambda_{HR} \geq 0.95$.

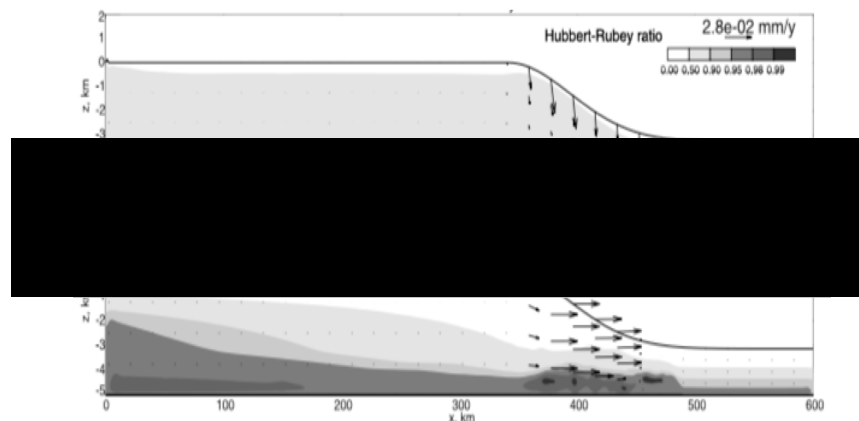


Fig. 6.6 Figures obtained from [120], showing the distribution of Hubbert-Rubey pore pressure parameter along with solid-matrix velocity vector in a purely disequilibrium compaction model (top), and in a model with disequilibrium and viscous compaction mechanisms (bottom).

In the second study, deltaic gravity instability over highly overpressured shale with simultaneous sedimentary progradation is simulated based on lithospheric model (Figure 6.7). The actual domain that is considered in the simulation covers all but the continental and oceanic crusts, thus leaving only the top section which is assumed to be in isostatic equilibrium. To achieve correct isostatic balance, traction boundary condition is prescribed at the bottom of the top section so that geologically realistic curved shape sedimentary basin is formed in response to the load contributed by progradation sedimentation.

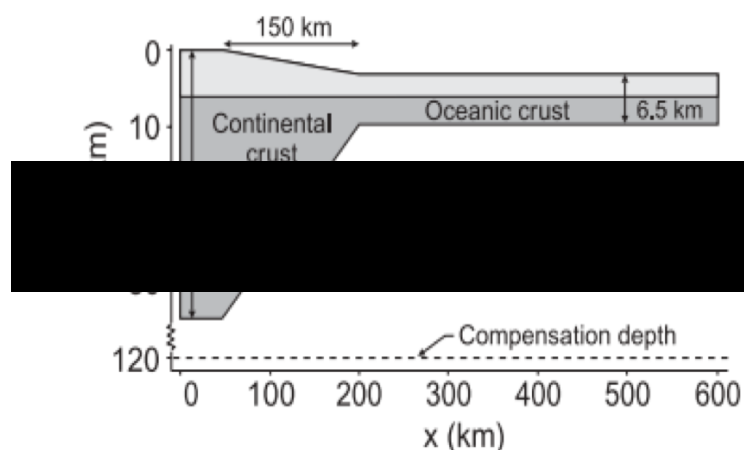


Fig. 6.7 Figures obtained from [89], showing a lithospheric model to account for isostatic equilibrium.

The delta is comprised of sand-dominated material and shale. Sand-dominated material, modelled by Drucker-Prager elastoplastic model, has a friction angle of 30° and relatively

moderate hydraulic permeability. On the other hand, shale, modelled by Bingham viscoplastic model, has a friction angle of 10° and relatively low hydraulic permeability. The permeability², as a function of porosity n , is defined according to the following equation

$$k = k_0 \left(\frac{n}{n_0} \right)^m, \quad (6.2)$$

with $m = 5$ for shale, and $m = 3$ for sand-dominated material.

For example, for $k_0 = 10^{-18} \text{ m}^2$ and $n_0 = 0.1$, we observe in Figure 6.8 the permeability-porosity trend for shale and sand-dominated material as defined in [89].

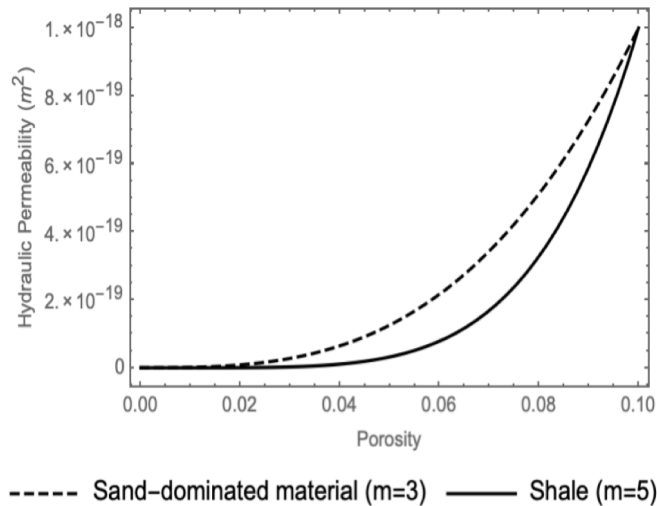


Fig. 6.8 Permeability-porosity trend based on (6.2), with $k_0 = 10^{-18} \text{ m}^2$ and $n_0 = 0.1$

During initialization stage (0-30 Ma) of the simulation (Figure 6.9), shale is deposited on the slope whereas sand is deposited on the shelf. The basin deforms accordingly in response to the continuous sedimentation loading on the surface. The resulting progradation occurs at a rate of 0.75cm/year.

In the stress relaxation stage (30-50 Ma), deltaic progradation (Figure 6.10) continues with synkinematic sedimentation of sand layers on the shelf and slope. Although progressive shale thickening is observed in the compressional region, the autochthonous nature of the layer is preserved; it is found relatively close to the place of initial deposition. During this period, the translation of shale slug equivalent to about 100km seaward is recorded.

²However, it is worth mentioning that while the formation of faults can be correlated to augmentation of hydraulic permeability, there are several other possible factors that could counter the augmentation effect, such as cataclasis which produces mineral grains that may undergo cementation in the pores under proper temperature and burial depths. Furthermore, the transformation of smectite to illite may also release some solutes that readily precipitate and occlude the effective fluid pathway [117, 119, 12, 13, 130, 157].

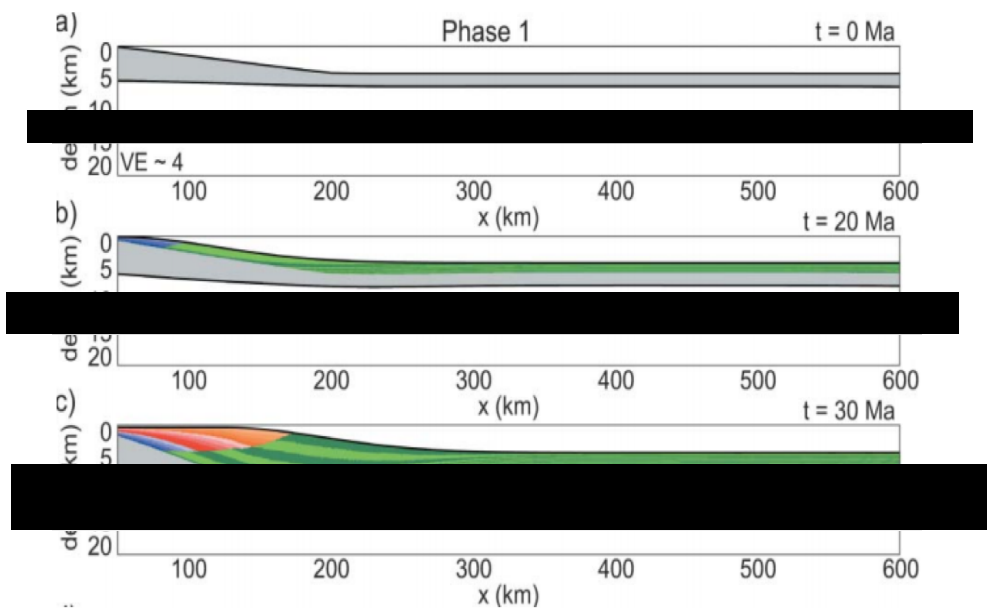


Fig. 6.9 Figures obtained from [89], showing the evolution of basal deformation during initialisation stage.

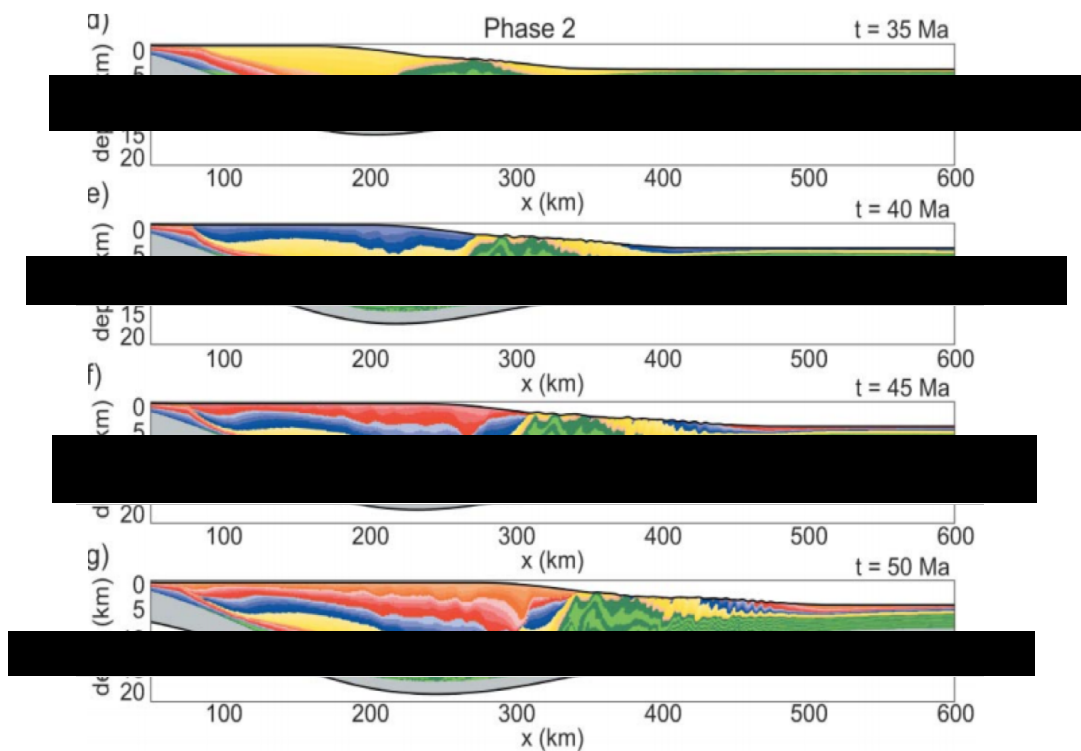


Fig. 6.10 Figures obtained from [89], showing the evolution of sedimentary deformation deposited at different times during stress relaxation stage.

In this stage, the mobilization of basinward shale layer (driven by gravity as well as the shape of the basin) causes noticeable extensional strain in the upslope and compressional strain in the downslope. The evolution continues with the seaward propagation of distal fold and thrust belt. In addition, high degree of overpressure ($\lambda_{HR} \approx 0.98$) close to basin demonstrates the extent of mobilization of shale layer. The increase of sedimentary basin thickness is a spontaneous manifestation of isostatic adjustment. Such phenomenon contributes to high pore fluid pressure in the basin up to a certain extent. In the shortening domain where pore pressure distribution is reminiscent of thrust faults, it is found that the highest pore fluid pressure reflects the highest shortening rate.

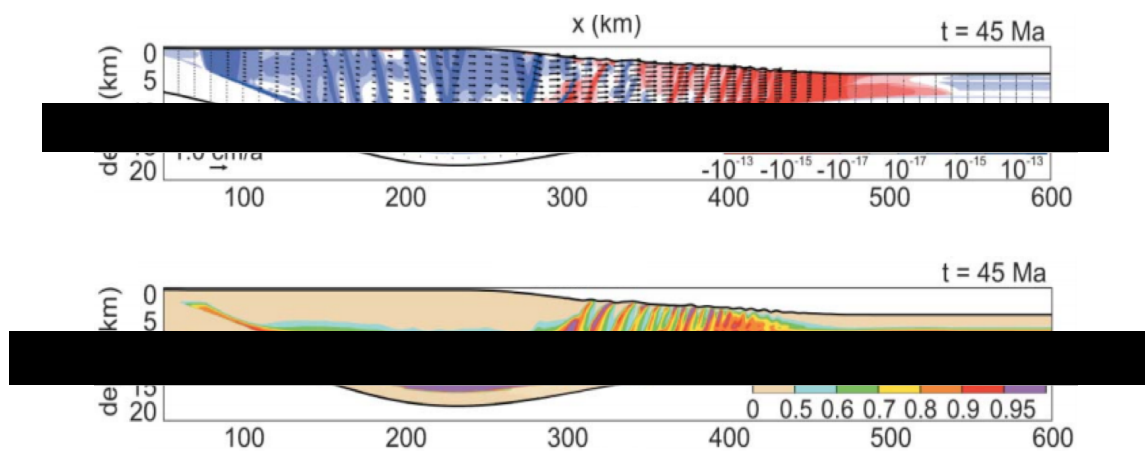


Fig. 6.11 Figures obtained from [89], showing the horizontal strain rate as well as Hubbert-Rubey pore pressure distribution in the delta towards the end of stress relaxation stage

From the simulation, small critical angle (sum of bathymetric slope angle α and detachment dip angle β), which is comparable to the outer fold and thrust belt of Niger Delta [15] is recovered, signifying weak basal strength due to high fluid overpressure in the simulation. However, the basal detachment in the simulation occurs at the base of shale layer. This is contrary to the field observation in Niger Delta, where the detachment tends to occur at the surface or subsurface of Akata formation.

6.2.4 Key Aspects of Literature Findings

Based on the literature findings above, there are several aspects that need to be appreciated in the modelling of sedimentary progradation due to gravitational instability.

- Simulation should be done based on coupled flow-geomechanical analysis instead of drained analysis due to the important influence of fluid overpressure on the overall geological deformation.

- Simulation should produce, at least, two distinct regions (extensional and compressional) along the model domain with the corresponding fault patterns.
- Major faults should track down to the decollement layer, where significant detachment occurs due to large fluid overpressure.
- During progradation, the velocity vector of the progradation front should point forward, indicating gravitational instability of the delta.
- The surface slope angle should decay gradually during progradation, signifying weak basal strength.

6.3 Modelling Setup

6.3.1 Geometry and Boundary Conditions

In this feasibility study, the objective is to simulate gravitational deformation in a prograding delta using SR4 rate-independent elastoplastic model with prescribed pore pressure beneath shale layer under coupled flow-geomechanical analysis using a 160km-long model. The general description of the model, including the boundary condition, is illustrated in Figure 6.12, while the corresponding dimensions are listed in Table 6.1.

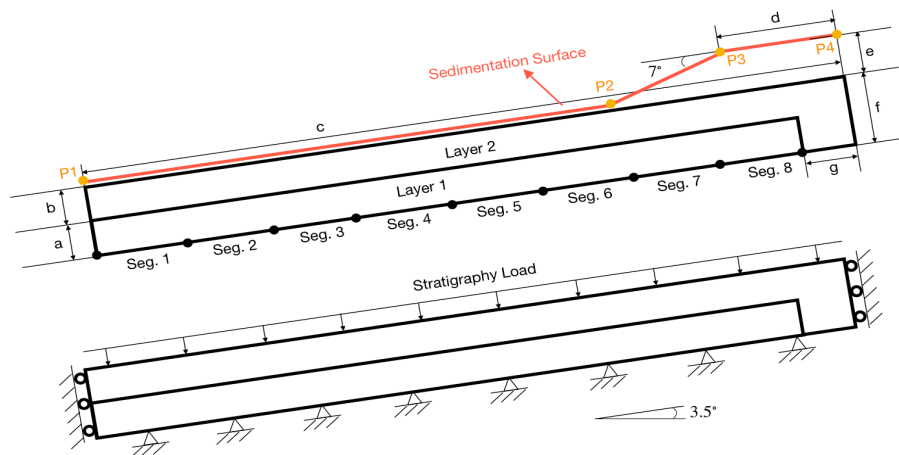


Fig. 6.12 Description of geometry and boundary conditions for 160km model of prograding delta

The model is initially constructed such that no pre-existing fault is assumed in the material. Instead of applying full thickness of shale layer (~2-7km), Layer 1 is treated as the mobile part of shale layer, where basal detachment is assumed to actively take place.

Geometry Parameter	Value (m)
a	800
b	400
c	160000
d	10000
e	2000
f	1200
g	7500
Segment 1-2 (each)	20000
Segment 3-8 (each)	18750
Sediment minimum thickness	200

Table 6.1 Geometry values for 160km model with reference to Figure 6.12

Layer 2 is treated as a pre-existing overburden layer. A stratigraphy load of 2.0MPa is prescribed at the top surface of Layer 2, and of all subsequent newly deposited layers. Seven new sedimentation layers are deposited at different simulation time (refer Table 6.2) in a synkinematic manner. The choice of basal angle and sediment surface slope angle follows the analog setup by [124]. The pore fluid distribution is assumed to increase from Segment 8 towards lower segments progressively according to Table 6.3. Different levels of pore fluid pressure are prescribed on different segments at different times³. Liquid water is assumed to represent pore fluid in the current study.

Layer	Sim. Time (Ma)	P_1	P_2	P_3	P_4
1	1.0-1.1	598.88	8861.20	11552.80	12163.29
2	1.1-1.2	798.51	8789.57	11929.77	12662.36
3	1.2-1.3	998.13	8717.94	12306.75	13161.42
4	1.3-1.4	1197.76	8646.31	12683.72	13660.49
5	2.4-2.5	1517.16	7044.76	11351.33	14159.56
6	3.5-3.6	0.00	4401.15	11728.30	14658.63
7	5.6-5.7	1716.79	3046.52	11006.39	15157.69

Table 6.2 Coordinates for new deposition layer at different simulation time. Each new layer is defined by 4 points (i.e. P_1 - P_4) with reference to Figure 6.12.

Note that, for the purpose of convenience, the prescription of pore pressure at the base in the current isothermal study represents the effect of any non-mechanical pore pressure generation mechanisms as described earlier.

³It is known that the time scale of pore pressure distribution is different than that of the development of geological deformation. In view of this, prescription of basal pore pressure, instead of fluid flux, is preferred in this feasibility study, which focuses on its influence on the effective mean stress and on the subsequent global destabilisation.

Simulation time (Ma)	Seg. 2	Seg. 3	Seg. 4	Seg. 5	Seg. 6	Seg. 7	Seg. 8
1.4-1.9	20	20	20	20	20	20	65
1.9-2.5	20	20	20	20	20	65	65
2.5-3.6	20	20	20	20	65	65	40
3.6-4.6	20	20	20	65	65	40	40
4.6-5.7	20	20	65	65	40	40	40
5.7-6.7	20	65	65	40	40	40	40
6.7-7.7	65	65	40	40	40	40	40
7.7-8.7	80	65	40	40	40	40	40

Table 6.3 Prescription of pore fluid pressure (MPa) at different segments of shale base layer at different simulation times

The model, which is 160km-long, is initially discretised into 6375 elements (, each having characteristic size of 300m) with 3729 nodes. The criteria for adaptive remeshing is based on plastic strain and its rate, as shown in Table 6.4-6.6. The time step size for flow field is $0.5(10^{-2})$ Ma, whereas for geomechanical field, the time step size is $0.5(10^{-4})$ Ma. In the final results, the total coupling and mechanical time steps are, respectively, 8040 and 1250225, with a total simulation time of 8.7Ma.

Plastic Strain	0	60
Plastic Strain Rate (Ma^{-1})	0	60
Element Size (m)	300	300

Table 6.4 Adaptive remeshing criteria for shale layer

Plastic Strain	0	2
Element Size (m)	300	80

Table 6.5 Adaptive remeshing criteria based on plastic strain for overburden layer

Plastic Strain Rate (Ma^{-1})	0	5
Element Size (m)	300	80

Table 6.6 Adaptive remeshing criteria based on plastic strain rate for overburden layer

6.3.2 Material Properties

In the following, the material properties used for shale and overburden materials are listed in Table 6.7-6.8. The evolution of the yield function is governed by plastic volumetric strain,

such that

$$p_c = p_{c0} \exp \left[-\frac{v \varepsilon_v^p}{\lambda - \kappa} \right]; \quad (6.3)$$

$$p_t = p_{t0} \exp \left[-\frac{v \varepsilon_{v,max}^p}{\lambda - \kappa} \right], \quad (6.4)$$

where p_{c0} and p_{t0} are, respectively, reference pre-consolidation pressure and tensile intercept in $p - q$ meridional plane; v is the specific volume, given by $\frac{1}{1-n_0}$ where n_0 is reference porosity; λ is the slope of normal compression line; κ is the slope of unloading-reloading line; and $\varepsilon_{v,max}^p$ is the maximum dilational volumetric plastic strain. In the current study, it is assumed for both materials that $\lambda = 0.2$ and $\kappa = 0.02$ for $-0.6 \leq \varepsilon_v^p \leq 0.27$.

Overburden Properties	Value
Density (kg/m ³)	2700
Reference porosity	0.45
Reference Young's modulus (GPa)	10
Poisson's ratio	0.30
Bulk modulus at deposition (MPa)	100
Initial tensile intercept (MPa)	0.01
Initial pre-consolidation pressure (MPa)	-10
Friction parameter β (°)	60
Dilation parameter ψ (°)	53
π -plane parameter β_0	0.60
π -plane parameter β_1	0.60
π -plane parameter α	0.25
SR4 yield function exponent n	1.6
SR4 potential function exponent m	1.6
Regularisation characteristic length (m)	80.0

Table 6.7 SR4 material parameters and properties for overburden

The porosity-depth correlation assumes a simple form given by Sclater-Christie[152]

$$n = n_0 \exp[-cz], \quad (6.5)$$

where c is a material constant and z represents depth.

For shale, $c = 0.00055$ is hypothetically chosen to reduce initial porosity of 0.3 to 0.033 at depth of 4km. On the other hand, for overburden material, $c = 0.0006$ is hypothetically chosen to reduce initial porosity of 0.45 to 0.041 at depth of 4km.

Shale Properties	Value
Density (kg/m ³)	2260
Reference porosity	0.30
Reference Young's modulus (GPa)	10
Poisson's ratio	0.30
Bulk modulus at deposition (GPa)	10.0
Initial tensile intercept (MPa)	0.10
Initial pre-consolidation pressure (MPa)	-15
Friction parameter β (°)	34.7
Dilation parameter ψ (°)	30.0
π -plane parameter β_0	0.60
π -plane parameter β_1	0.60
π -plane parameter α	0.25
SR4 yield function exponent n	1.6
SR4 potential function exponent m	1.6
Regularisation characteristic length (m)	80.0

Table 6.8 SR4 material parameters and properties for shale

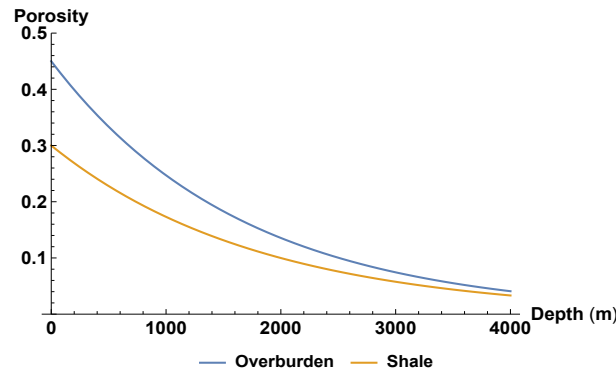


Fig. 6.13 Porosity-depth relationship for overburden and shale according to Scalter-Christie correlation

The properties of hydraulic permeability assumes the correlation as used by [89]

$$k = k_0 \left(\frac{n}{n_0} \right)^m ,$$

with $m = 5$ for shale, and $m = 3$ for overburden material. The value of k_0 for shale and overburden materials are, respectively, $10^{-16}m^2$ and $10^{-10}m^2$. It is noted that $10^{-16}m^2$ is the ceiling value for shale material according to the Figure 2 of [120].

6.4 Results

During initialisation stage, the pre-existing layers are loaded for 1Ma before applying four new sedimentation layers in sequential manner. The duration of each sedimentation stage is 0.1Ma, leading to a total initialisation duration of 1.4Ma. Then, different segments of the shale layer base are prescribed with pore pressure at different simulation time according to Table 6.3.

The effect of pore pressure on the stability of delta is illustrated in Figure 6.18 using Hubbert-Rubey ratio λ_{HR} , i.e. Pore pressure/Lithostatic stress. When λ_{HR} is low, the delta appears to be at quiescent state. As $\lambda_{HR} \rightarrow 1$, the horizontal (leftward) velocity gradually increases, indicating incipient deltaic progradation. This is accompanied by the reduction of surface slope at the continental shelf, which is a sign of weak basal strength. This is caused by the reduction of frictional resistance as a large portion of overburden weight is now supported by pore fluid. It should be noted that every progradation that takes place in the simulation is triggered when the λ_{HR} ratio is close to 1.

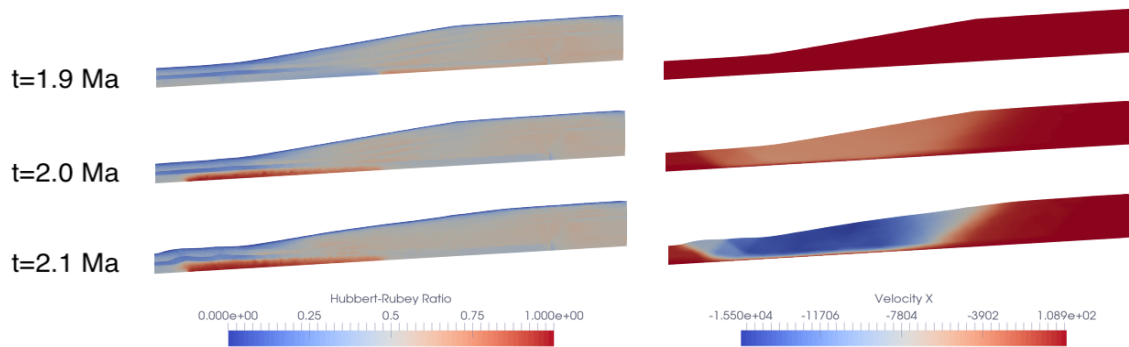


Fig. 6.14 Incipient deltaic progradation as Hubbert-Rubey pore pressure ratio λ_{HR} is close to 1.

The complex development of faults during progradation resulted from gravitational deformation and the simulation time at which each new sedimentation layer is deposited are illustrated in Figure 6.15. The total simulation time is 8.7Ma.

In the early period, it is noticed that a forethrust is firstly established. Subsequent layer suppresses further development of this thrust fault, while contributing to the overall delta progradation. For each progradation process, new fore-thrusts are formed ahead by squeezing the mobile shale layer forward. The process is repeated when another layer of sedimentation is deposited. By now, the previously formed forethrusts have become inner fold and thrust belts while the outer fold and thrust belts are simultaneously formed at the distal part of the delta (i.e. left boundary).

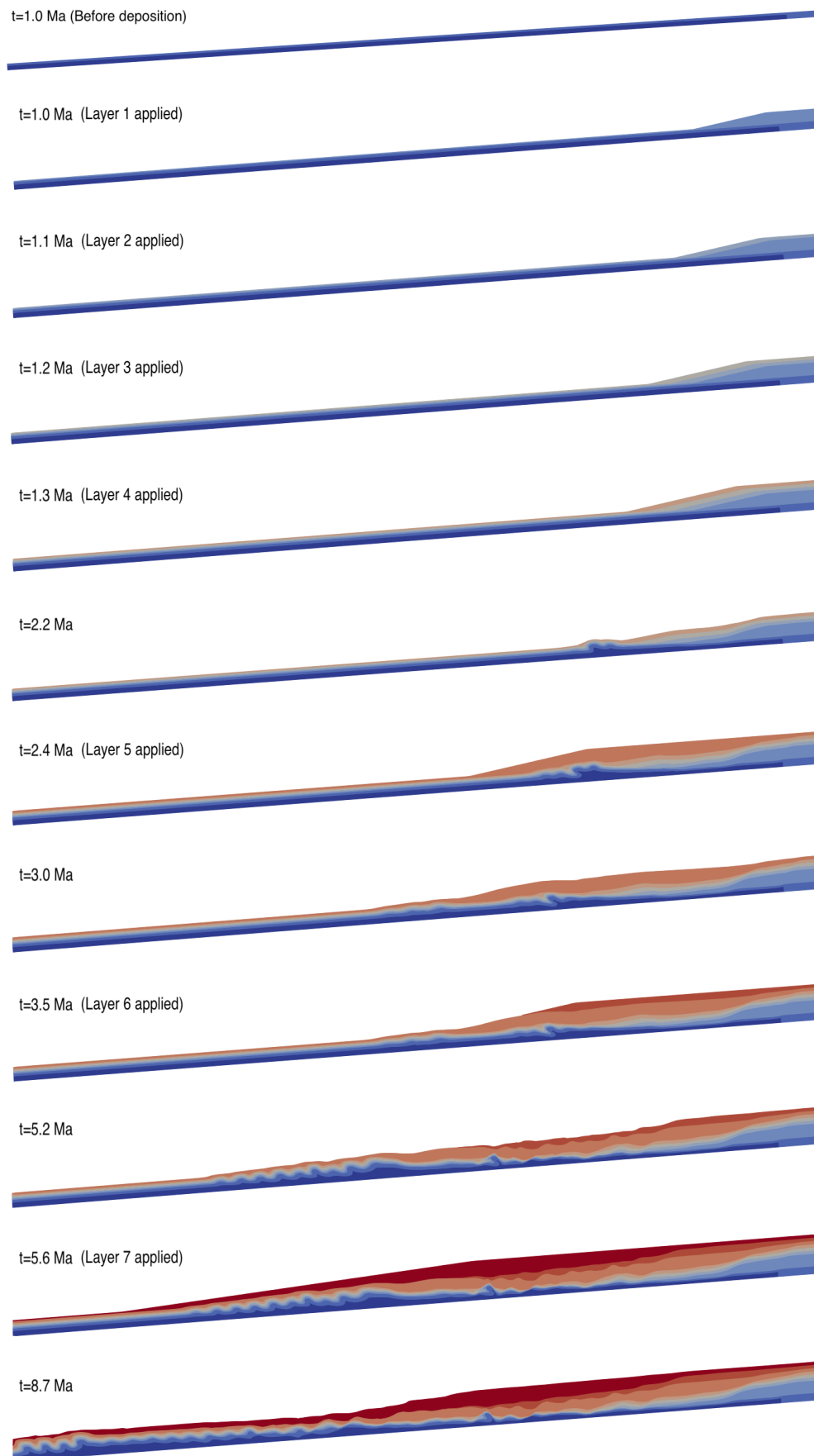


Fig. 6.15 Prograding delta due to basal fluid overpressure with synkinematic sedimentation

Overall, by referring to Figure 6.16-6.17, some key features observed in the field are reproduced in the results by the end of simulation time. Firstly, the plastic strain distribution can be observed along the base, which indicates the formation of decollement layer where basal detachment actively occurs due to high fluid overpressure. Furthermore, three different structural zones are simultaneously formed amid synkinematic sedimentation process: extensional, transition, and compressional zones.

In the extensional zone, basinward-dipping, concave upwards normal faults are successfully replicated. These listric normal faults are directly resulted from frictional detachment in the shale layer due to high fluid overpressure. Ahead of the extensional region is diapir, which is already suppressed by younger sedimentation layers. The diapir consists of paleo-fore thrust that is formed at $t = 2.2\text{Ma}$ (as shown in Figure 6.15). The diapir marks the beginning of transition zone, which is characterised by a series of detachment folds and basinward verging thrust faults within inner fold and thrust belts. In the transition zone, it can be seen that the buried forethrusts within inner fold and thrust belts are superimposed by young extensional faults, of which some of them extend to the top sedimentation layer [1]. Further into deepwater domain, four asymmetric basinward-verging fore-thrusts are observed in the outer fold and thrust belts, which are located at the distal part of the delta.



Fig. 6.16 Plastic strain development during progradation

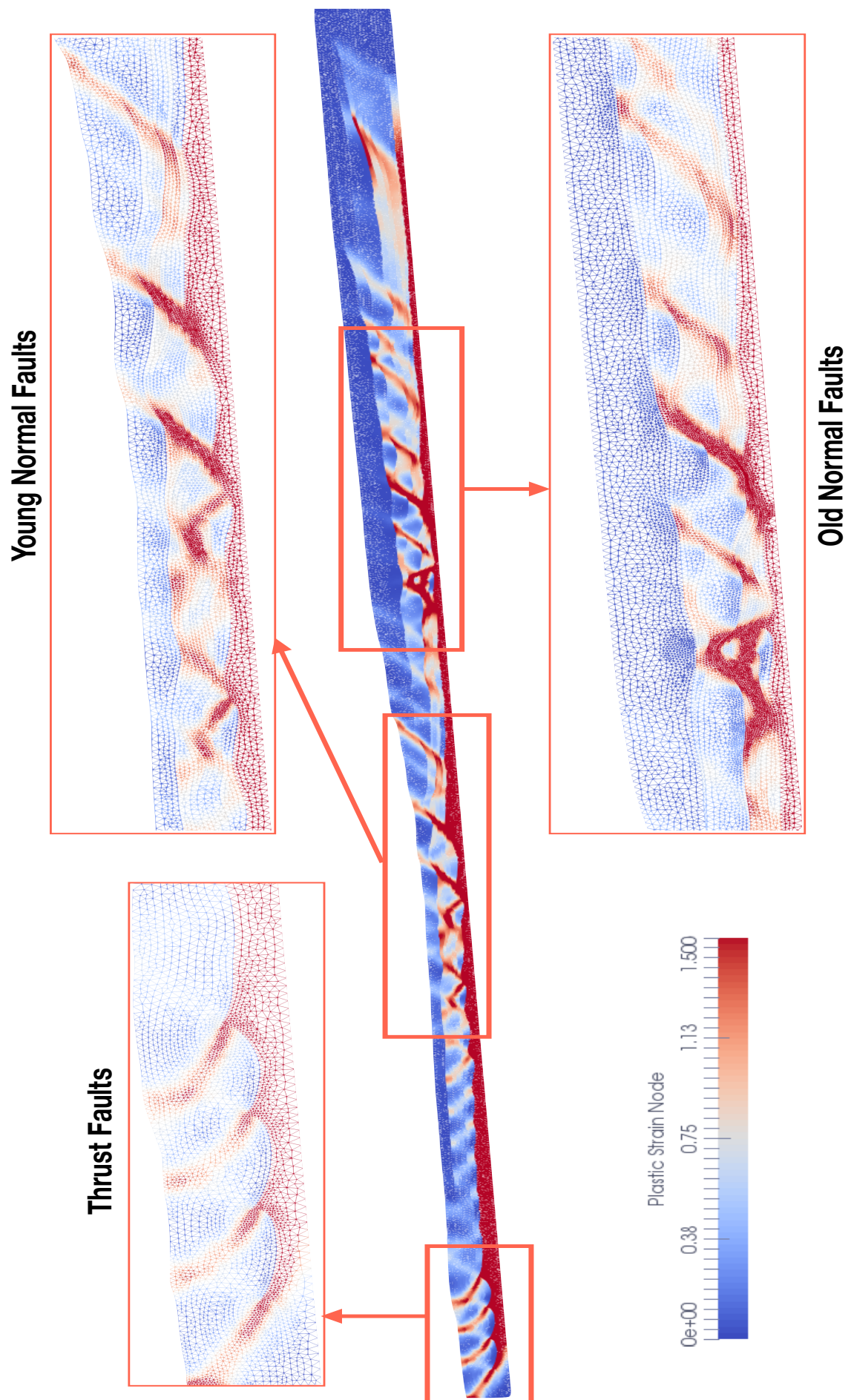


Fig. 6.17 Plastic strain as representation of faults. Fore-thrust faults in compressional domain, and concave-upward normal faults in extensional domain

Figure 6.18 shows, at final simulation time $t = 8.7\text{Ma}$, the pore pressure distribution over the whole delta as well as the depth-dependent distribution in a selected region within compressional domain. The pore pressure in the extensional domain is slightly higher than that in the transition domain due to higher hydrostatic counterpart. In the depth-dependent pore pressure plot, it is clear that the distribution is hydrostatic in the subsurface layers before increases abruptly over small range of depth to a high level of pore pressure, which is commonly observed in the field (Figure 6.19).

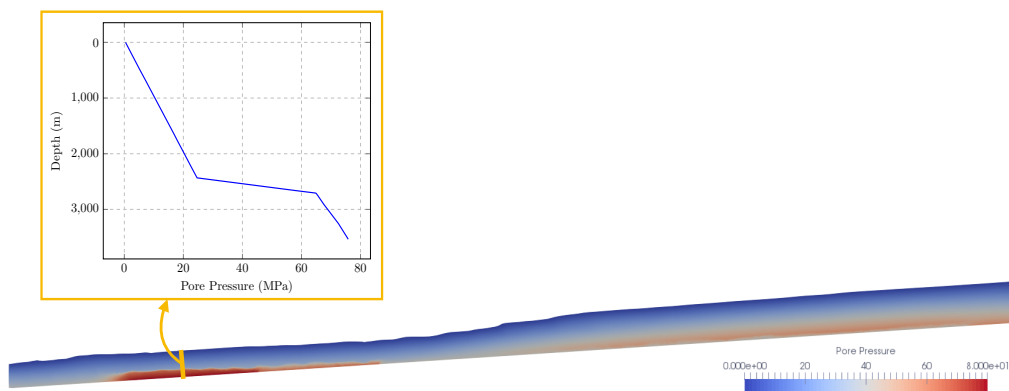


Fig. 6.18 Pore pressure distribution during at final simulation time $t = 8.7\text{Ma}$

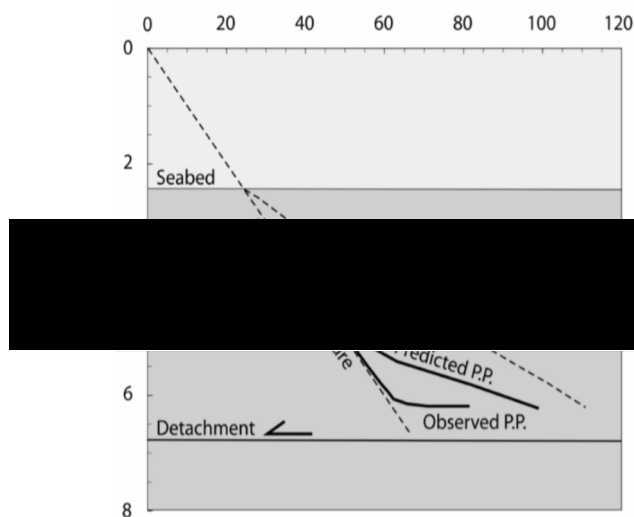


Fig. 6.19 Figure obtained from [37], showing the large deviation from hydrostatic distribution towards higher value of pore pressure as depth approaches shale layer

On the other hand, the distribution of velocity vector illustrated in Figure 6.20 reflects that region of active motion translates basinward as progradation takes place. This is deduced from the observation that early extensional zone is now relatively static. Furthermore, in the magnified figures of compressional and extensional zones, it is clear that delta instability is associated with basinward-pointing velocity vectors as observed in the outer fold and thrust belts as well as in the region of young normal faults. This agrees with the findings by [120].

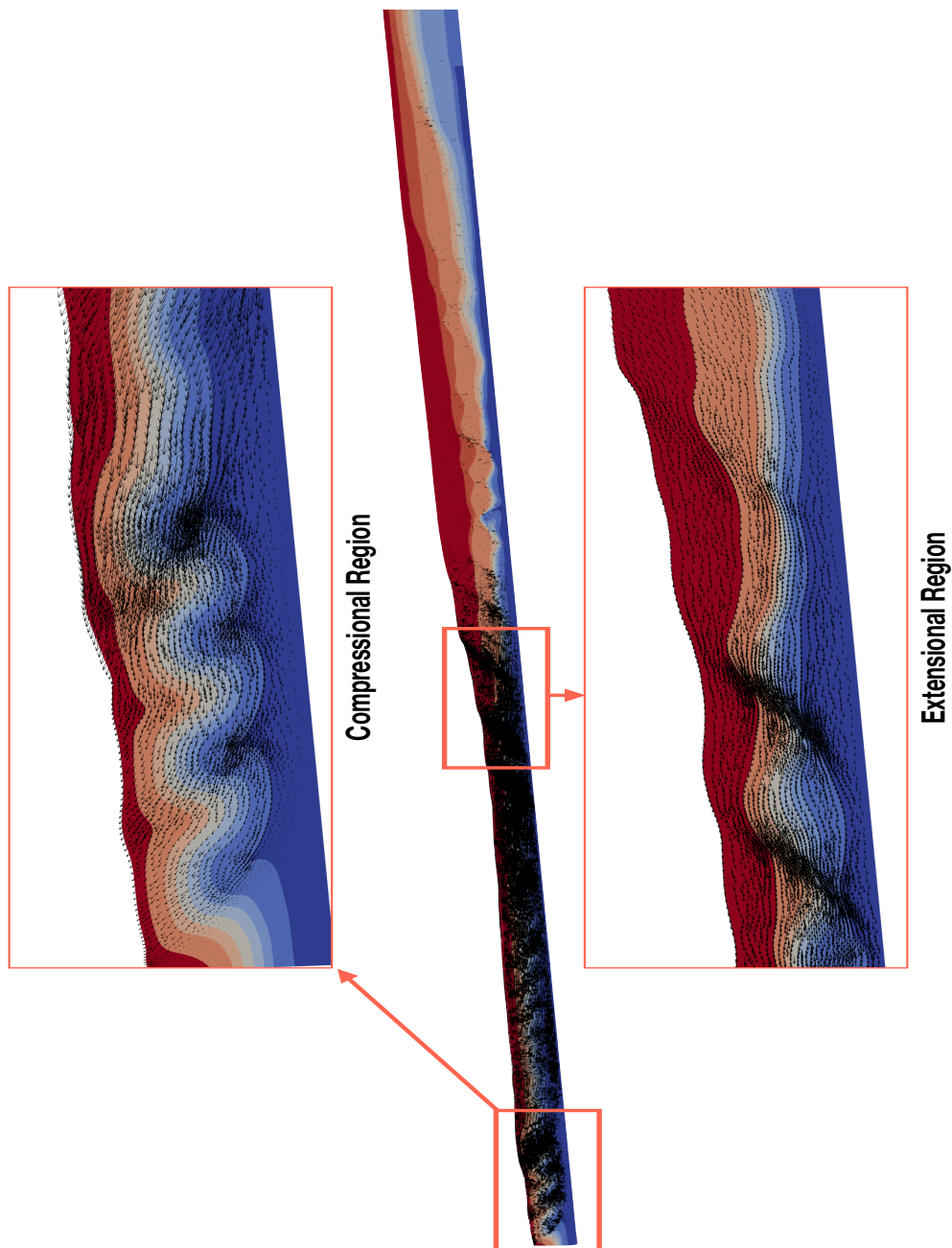


Fig. 6.20 Magnified velocity vectors in both compressional and extensional region

The displacement contour in Figure 6.21 reveals difference in terms of distribution between extensional and compressional domains. For both horizontal and vertical displacement, the distribution is smooth across stratigraphy layers in the compressional domain. In the case of extensional domain, the distribution is, on the contrary, discontinuous. In particular for horizontal displacement, the distribution reflects the chronological order of sedimentation layers; old layers are more horizontally displaced than the younger layers.

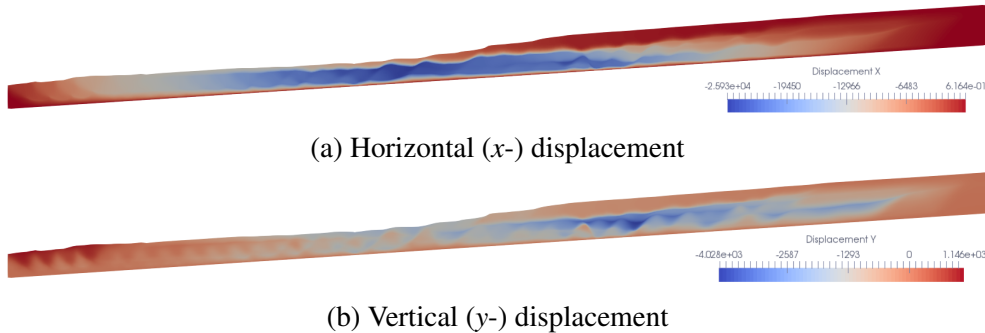


Fig. 6.21 Displacement components at final simulation time $t = 8.7\text{Ma}$

By analysing the displacement contours for both directions and the velocity vector plots, it is likely that extensional zone (which is associated with rifting deformation) tend to have high rate of progradation and subsidence in the early period, but low rate in the later period. On the other hand, smooth displacement distribution in the compressional zone reflects that the progradation and subsidence rates are relatively low in the early period. The rate only increases in the later period, as can be seen from the velocity vector plots in Figure 6.20.

Lastly, the bulk compressibility of the model is found to range from $1.34(10^{-10})\text{Pa}^{-1}$ to $6.94(10^{-10})\text{Pa}^{-1}$, which is within the realistic range [120] from 10^{-10}Pa^{-1} to 10^{-8}Pa^{-1} .

6.5 Concluding Remarks

This feasibility study demonstrates the possibility of simulating delta progradation without relying on any rate-dependent constitutive model. By prescribing pore pressure at the base of shale layer and sequentially depositing new sedimentation layer at different simulation times, the final result encompasses faults that are characteristic in the field observation. In particular, basinward-dipping normal faults are found in the extensional zone and fore-thrusts are observed in compressional zone. Delta instability is triggered by high Hubbert-Rubey ratio (close to 1) and identified by basinward-pointing velocity vectors in the active region. The current model can be further enhanced by considering more realistic factors, such as thermal effect on the constitutive models, augmentation of hydraulic permeability that depends on

plastic strain rate, etc. to provide more useful insights regarding the evolution of sedimentary basin.

Chapter 7

Conclusions

The main objective of this thesis is to develop a coupled geomechanical/flow-modelling framework suitable for the simulation of basin-scale evolution over geological time frames, with focus on constitutive modelling of pressure-sensitive geomaterials. The developed constitutive models have been applied on a range of benchmark examples, and a large-scale geomechanical problem. In the followings, a summary of achievements and conclusions are listed.

7.1 Dry Case: Elastoplastic-Fracture Model

The standard Drucker-Prager model has been enhanced by applying Lode angle-dependent π -plane correction factor in the yield function. The implication is that the Drucker-Prager yield surface is no longer circular in π -plane; it allows higher yield stress under compression-dominant loading condition and lower yield stress under extension-dominant loading. In addition, the hardening properties, such as cohesion, friction angle, and dilation angle, are now dependent on the evolution of effective plastic strain. The presence of dilation angle means that non-associative potential plastic flow function has been generally employed in the current framework. Lastly, regularisation technique based on fracture energy approach is adopted to ensure finite energy dissipation during softening. With the adoption of regularisation technique, it has been successfully demonstrated that the modified Drucker-Prager model predicts lower collapse pressure in a larger specimen (, and vice versa) in size effect benchmark example.

Next, an elastoplastic-fracture framework has been developed by combining the modified Drucker-Prager model and rotating crack model, with the consideration of coupling between cohesion and tensile strength. It should be noted that the proposed framework is not restricted only to the Drucker-Prager model, but to any general elastoplastic model including SR4.

Multi-step stress update is adopted in this framework; evaluation of stress state using Rankine failure criterion, followed by elastoplastic yield criterion. A series of simulation tests have been performed with the focus on the initiation, propagation, and coalescence of cracks in a specimen with pre-existing inclined fault. Experimental findings, such as the formation of tensile wing crack in quasi-brittle material, the development of secondary crack that is of shear origin in a soft material, coalescence of propagating cracks as well as the effects of fault inclination and bridge angles are all reproduced in the simulation results with good agreement.

7.2 Elastoplastic-Fracture Model Coupled with Flow Field

In coupled field problem, the modified Drucker-Prager model is firstly used to model thrust fault formation in granular material under the influence of pore pressure, without considering fracture model. Results have been compared with the findings from sandbox model testing. Good agreement was obtained: As basal pore pressure increases, more thrust faults are formed, and the surface slope in the final configuration are lower. These findings indicate lower effective mean stress and weaker basal strength. The overall result provides confidence in simulating larger model at basin scale.

Next, a problem of hydraulic fracture due to fluid injection is simulated by considering anisotropic distribution of hydraulic permeability. For elasto-fracture materials, the results obtained are in agreement with the expectation. Distribution of pore fluid pressure tends to be radial in isotropic permeability case compared to anisotropic permeability case. In the latter case, the crack tends to propagate further with the highest concentration of stress in the propagating tip. The results obtained from elastoplastic-fracture materials are very similar to the elasto-fracture materials, except that plastic yielding precedes softening due to fracture at a lower tensile strength. Overall, the developed elastoplastic-fracture framework based on multi-step stress update algorithm yields some promising results and the potential for the application in more complex problems.

7.3 Prograding Delta due to Gravitational Instability Triggered by Overpressured Shale Layer with Synkinematic Sedimentation

In this large-scale simulation, SR4 model is used. It is demonstrated that characteristic fault patterns have been successfully reproduced in both extensional and compressional

regions of the prograding delta in terms of plastic strain. In particular, extensional region is characterised by basinward-dipping normal faults while the compressional region is characterised by basinward-verging fore-thrust faults. Due to the effect of synkinematic sedimentation, young normal faults are observed to overlap with buried paleo-thrust faults, which is consistent with the field observation.

7.4 Recommendations for Further Research

- **Plastic strain-based permeability augmentation.** In the last basin-scale simulation, no fracture model is considered. Hydraulic permeability augmentation algorithm based on plastic strain and plastic strain rate is needed to ensure the proper distribution of pore fluid pressure. This is essential for the modelling of fluid migration that is greatly dependent on the formation of fore-thrust faults. Furthermore, depth-dependent fracturing pressure should be taken into account in the future algorithm.
- **Coupled geomechanical/flow/thermal modelling framework.** This requires an integrated modelling framework that properly accounts for the coupling between the reaction, transport and mechanical dynamic evolution of the geophysical rock formation. Loose sediment is deposited at the surface; e.g. sand or clay, and due to continued burial evolves into lower porosity lithified sandstone via a combination of mechanically and chemically driven processes. This transformation alters the material characteristics of the sediment and has a first-order effect on the evolution of geological structure, strongly influencing the likelihood of fault and fracture formation and fluid migration. The classical “structured soil” framework will be extended to incorporate both generation and degradation of structure via non-mechanical processes. This theory adopts the concept of “sedimentation” and “post-sedimentation” structure, where sedimentation structure corresponds to structure derived from mechanical driven consolidation, and post-sedimentation structure includes creep, thixotropy, cementation and other microstructural processes. The approach will be based on the formulation of multi-reaction evolution laws for the state boundary surface.
- **Prediction of landslide.** The constitutive models that are developed should not be restricted only to the modelling of large-scale evolution that is measured over geological time. These models can be extended¹ to the applications of predicting landslides and the impact of earthquakes, which should be part of catastrophe modelling project that can assist governments making risk-informed decision prior to actual disasters.

¹accounting for partially saturated soil condition

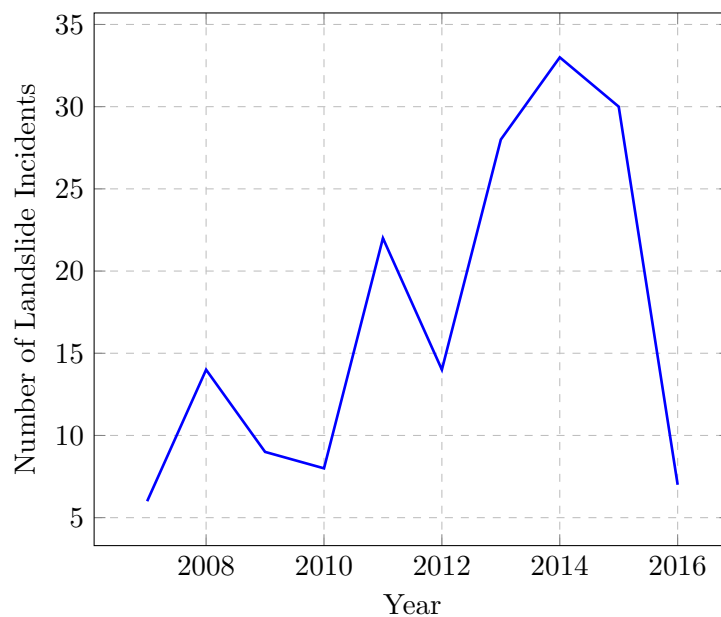


Fig. 7.1 Increasing trend of landslide happening in Malaysia in recent years. Data obtained from [95, 96].

In Malaysia², for instance, the author is concerned about the increasing trend in the number of landslide in recent years (Figure 7.1) that has put the country into the list of top 10 countries especially prone to landslides in the world. In the context of geomechanics, any robust constitutive model should be able to assist us in identifying specific vulnerabilities in places prone to landslides and earthquake, planning better engineering strategies for mitigation of the risk, and understanding the economic impacts should the worst scenario happens.

²Author's country of origin

References

- [1] Ajakaiye, D. and Bally, A. (2002a). Course manual and atlas of structural styles on reflection profiles from the Niger Delta. *American Association of Petroleum Geologists, Continuing Education Course Note Series*, 41.
- [2] Ajakaiye, D. and Bally, A. (2002b). Some structural styles on reflection profiles from offshore Niger Delta. *Search and Discovery*, 10031:1–6.
- [3] Akai, K. and Mori, H. (1967). Study on the failure mechanism of a sandstone under combined compressive stresses. *Transactions of the Japan Society of Civil Engineers*, 1967(147):11–24.
- [4] Allen, P. A. and Allen, J. R. (2013). *Basin analysis: principles and applications*. Wiley-Blackwell.
- [5] Allwardt, J. R., Michael, G. E., Shearer, C. R., Heppard, P. D., and Ge, H. (2009). 2D modeling of overpressure in a salt withdrawal basin, Gulf of Mexico, USA. *Marine and Petroleum Geology*, 26(4):464–473.
- [6] Babeyko, A., Sobolev, S., Trumbull, R., Oncken, O., and Lavier, L. (2002). Numerical models of crustal scale convection and partial melting beneath the Altiplano-Puna plateau. *Earth and Planetary Science Letters*, 199(3-4):373–388.
- [7] Barker, C. (1990). Calculated Volume and Pressure Changes During the Thermal Cracking of Oil to Gas in Reservoirs. *AAPG Bulletin*, 74:1254–1261.
- [8] Bazant, Z., Belytschko, T., and Chang, T. (1984). Continuum theory for strain-softening. *Journal of Engineering Mechanics*, 110:1666–1692.
- [9] Bazant, Z. and Lin, F. (1988). Nonlocal Smeared Cracking Model for Concrete Fracture. *Journal of Structural Engineering*, 114:2493–2510.
- [10] Bazant, Z. and Pijaudier-Cabot, G. (1988). Nonlocal Continuum Damage, Localization Instability and Convergence. *Journal of Applied Mechanics*, 55:287–293.
- [11] Bazant, Z. P., Lin, F., and Lippmann, H. (1993). Fracture energy release and size effect in borehole breakout. *Int. J. for Num. and Anal. Meth. Geomech.*, 17:1–14.
- [12] Bekins, B., McCaffrey, A. M., and Dreiss, S. J. (1994). Influence of kinetics on the smectite to illite transition in the Barbados accretionary prism. *Journal of Geophysical Research: Solid Earth*, 99(B9):18147–18158.

- [13] Bekins, B. A., McCaffrey, A. M., and Dreiss, S. J. (1995). Episodic and constant flow models for the origin of low-chloride waters in a modern accretionary complex. *Water Resources Research*, 31(12):3205–3215.
- [14] Belytschko, T. and Black, T. (1999). Elastic crack growth in finite elements with minimal remeshing. *International Journal for Numerical Methods in Engineering*, 45(5):601–620.
- [15] Bilotti, F., Shaw, J., Cupich, R., and Lakings, R. (2005). Detachment fold, Niger Delta. In: Shaw, J.H., Connors, C. and Suppe, J. (eds) *Seismic interpretation of contractional fault-related folds. American Association of Petroleum Geologists, Studies in Geology*, 53:103–104.
- [16] Bilotti, F. and Shaw, J. H. (2005). Deep-water Niger Delta fold and thrust belt modeled as a critical-taper wedge: The influence of elevated basal fluid pressure on structural styles. *AAPG Bulletin*, 89(11):1475–1491.
- [17] Bjorlykke, K. (1993). Fluid flow in sedimentary basins. *Sedimentary Geology*, 86(1-2):137–158.
- [18] Bobet, A. (2000). The initiation of secondary cracks in compression. *Engineering Fracture Mechanics*, 66(2):187–219.
- [19] Bobet, A. and Einstein, H. (1998a). Fracture coalescence in rock-type materials under uniaxial and biaxial compression. *International Journal of Rock Mechanics and Mining Sciences*, 35(7):863–888.
- [20] Bobet, A. and Einstein, H. (1998b). Numerical modeling of fracture coalescence in a model rock material. *International Journal of Fracture*, 92:221–252.
- [21] Bolas, H. M. N., Christian, H., and Teige, G. M. G. (2004). Origin of overpressures in shales: Constraints from basin modeling. *AAPG Bulletin*, 88.
- [22] Bolas, H. M. N., Hermanrud, C., Schutter, T. A., and Teige, G. M. G. (2008). Is stress-insensitive chemical compaction responsible for high overpressures in deeply buried North Sea chalks? *Marine and Petroleum Geology*, 25(7):565–587.
- [23] Borgesson, L., Chijimatsu, M., Fujita, T., Nguyen, T., Rutqvist, J., and Jing, L. (2001). Thermo-hydro-mechanical characterisation of a bentonite-based buffer material by laboratory tests and numerical back analyses. *International Journal of Rock Mechanics and Mining Sciences*, 38(1):95–104.
- [24] Both, J. W., Kumar, K., Nordbotten, J. M., and Radu, F. A. (2019). Anderson accelerated fixed-stress splitting schemes for consolidation of unsaturated porous media. *Computers and Mathematics with Applications*, 77(6):1479–1502.
- [25] Braun, J., Thieulot, C., Fullsack, P., Dekool, M., Beaumont, C., and Huisman, R. (2008). DOUAR: A new three-dimensional creeping flow numerical model for the solution of geological problems. *Physics of the Earth and Planetary Interiors*, 171(1-4):76–91.

- [26] Briggs, S. E., Davies, R. J., Cartwright, J. A., and Morgan, R. (2006). Multiple detachment levels and their control on fold styles in the compressional domain of the deepwater west Niger Delta. *Basin Research*, 18(4):435–450.
- [27] Brun, J.-P. and Choukroune, P. (1983). Normal faulting, block tilting, and decollement in a stretched crust. *Tectonics*, 2(4):345–356.
- [28] Brun, J.-P. and Fort, X. (2004). Compressional salt tectonics (Angolan margin). *Tectonophysics*, 382(3-4):129–150.
- [29] Buitter, S. J. H., Huismans, R. S., and Beaumont, C. (2008). Dissipation analysis as a guide to mode selection during crustal extension and implications for the styles of sedimentary basins. *Journal of Geophysical Research*, 113(B6).
- [30] Cao, P., Liu, T., Pu, C., and Lin, H. (2015). Crack propagation and coalescence of brittle rock-like specimens with pre-existing cracks in compression. *Engineering Geology*, 187:113–121.
- [31] Cathles, L. (2001). Capillary seals as a cause of pressure compartmentation in sedimentary basins. In: Fillon R.H., Rosen, P., et al. (eds) *Petroleum Systems of Deepwater Basins: Global and Gulf of Mexico Experience. 21st Annual Bob F. Perkins Research Conference, Gulf Coast Section of the Society of Economic Paleontologists and Mineralogists*, pages 561–571.
- [32] Chan, T., Khair, K., Jing, L., Ahola, M., Noorishad, J., and Viollod, E. (1995). International Comparison of Coupled Thermo-Poro-Mechanical Models of a Multiple-Fracture Benchmark Problem: DECOVALEX Phase I, Benchmark Test 2. *Int. J. Rock Mech. Min. Sci.*, 32:435–452.
- [33] Chen, H., Teufel, L., and Lee, R. (1995). Coupled Fluid Flow and Geomechanics in Reservoir Study - I. Theory and Governing Equations. *SPE Annual Technical Conference and Exhibition*.
- [34] Chen, W.-F. and Mizuno, E. (1990). *Nonlinear Analysis in Soil Mechanics. Theory and Implementation*. Elsevier.
- [35] Chin, L. and Thomas, L. (1999). Fully Coupled Analysis of Improved Oil Recovery by Reservoir Compaction. *SPE Annual Technical Conference and Exhibition*.
- [36] Cobbold, P. and Castro, L. (1999). Fluid Pressure and Effective Stress in Sandbox Models. *Tectonophysics*, 301:1–19.
- [37] Cobbold, P., Clarke, B., and Loseth, H. (2009). Structural consequences of fluid overpressure and seepage forces in the outer thrust belt of Niger Delta. *Petroleum Geoscience*, 15:3–15.
- [38] Cobbold, P., Durand, S., and Mourgues, R. (2001). Sandbox Modelling of Thrust Wedges with Fluid-Assisted Detachments. *Tectonophysics*, 334:245–258.
- [39] Cobbold, P., Mourgues, R., and Boyd, K. (2004). Mechanism of thin-skinned detachment in the Amazon Fan: Assessing the importance of fluid overpressure and hydrocarbon generation. *Marine and Petroleum Geology*, 21(8):1013–1025.

- [40] Cobbold, P. and Rodrigues, N. (2007). Seepage forces, important factors in the formation of horizontal hydraulic fractures and bedding-parallel fibrous veins. *Geofluids*, 7:313–332.
- [41] Cohen, H. A. and McClay, K. (1996). Sedimentation and shale tectonics of the northwestern Niger Delta front. *Marine and Petroleum Geology*, 13(3):313–328.
- [42] Cope, R. J., Rao, P. V., Clark, L. A., and Norris, P. (1980). Modelling of reinforced concrete behaviour for finite element analysis of bridge slabs. *Numerical Methods for Nonlinear Problems*, 1:457–470.
- [43] Corredor, F., Shaw, J., and Bilotti, F. (June 2005a). Structural styles in the deep-water fold and thrust belts of the Niger Delta. *American Association of Petroleum Geologists*, 89(6):753–780.
- [44] Corredor, F., Shaw, J., and Suppe, J. (2005b). Shear fault-bend fold, deep water Niger Delta. In: Shaw, J.H., Connors, C. and Suppe, J. (eds) *Seismic interpretation of contractional fault-related folds*. American Association of Petroleum Geologists, *Studies in Geology*, 53:87–92.
- [45] Corredor, F., Shaw, J. H., and Bilotti, F. (2005c). *Tectonic Structures drawn over a seismic profile of the Niger Delta Basin*.
- [46] Crisfield, M. (1991). *Non-linear Finite Element Analysis of Solids and Structures. Volume 2: Advanced Topics*. John Wiley and Sons.
- [47] Crisfield, M. (1997). *Non-linear finite element analysis of solids and structures. Volume 2: Advanced Topics*. John Wiley and Sons.
- [48] Crisfield, M. A. and Wills, J. (1987). Numerical comparisons involving different concrete models. *IABSE Reports 54 Coll. Comp. Mech. Of Reinforced Concrete*, pages 177–187.
- [49] Crook, A. (2016). *ParaGeo Documentation*. ThreeCliffs Geomechanical Analysis Ltd.
- [50] Crook, A., Willson, S., Yu, J., and Owen, D. (2003). Computational modelling of the localized deformation associated with borehole breakout in quasi-brittle materials. *Journal of Petroleum Science and Engineering*, 38(3-4):177–186.
- [51] Cundall, P. A. and Strack, O. D. L. (1979). A discrete numerical model for granular assemblies. *Geotechnique*, 29:47–65.
- [52] Damuth, J. E. (1994). Neogene gravity tectonics and depositional processes on the deep Niger Delta continental margin. *Marine and Petroleum Geology*, 11(3):320–346.
- [53] Davis, D. M. and Engelder, T. (1985). The role of salt in fold-and-thrust belts. *Tectonophysics*, 119(1-4):67–88.
- [54] de Souza Neto, E., Peric, D., and Owen, D. (2008). *Computational methods for plasticity*. Wiley.

- [55] Dean, R. H., Gai, X., Stone, C. M., and Minkoff, S. E. (2003). A Comparison of Techniques for Coupling Porous Flow and Geomechanics. *SPE Reservoir Simulation Symposium*.
- [56] Desai, C. S. and Salami, M. R. (1987). A constitutive model and associated testing for soft rock. *International Journal of Rock Mechanics and Mining Sciences*, 24:299–307.
- [57] Detournay, C. and Dzik, E. (2006). Nodal mixed discretization for tetrahedral elements. In *4th International FLAC Symp. Numer. Model. GeoMechanics, Madrid, Itasca Consulting Group, Inc.*, pages 07–02.
- [58] Deville, E., Battani, A., Guerlais, S., Lallemand, S., Mascle, A., Prinzhofer, A., and Schmitz, J. (2004). Processes of mud volcanism vs shale diapirism: Integrated structural, thermal and geochemical approach in the Barbados-Trinidad compressional system. *24th CSSEPM Research Conference on Salt Sediment Interactions and Hydrocarbon Prospectivity, Houston, Texas*, pages 868–891.
- [59] Deville, E., Guerlais, S.-H., Callec, Y., Gribouard, R., Huyghe, P., Lallemand, S., Mascle, A., Noble, M., and Schmitz, J. (2006). Liquefied vs stratified sediment mobilization processes: Insight from the South of the Barbados accretionary prism. *Tectonophysics*, 428(1-4):33–47.
- [60] Doust, H. and Omatsola, E. (1989). Niger Delta. In: *Edwards, J.D., Santogrossini, P.A. (Eds.), Divergent/Passive Margin Basins: AAPG Mem.*, 48:201–238.
- [61] Drucker, D. C. and Prager, W. (1952). Soil mechanics and plastic analysis or limit design. *Quarterly of Applied Mathematics*, 10(2):157–165.
- [62] Dyskin, A., Sahouryeh, E., Jewell, R., Joer, H., and Ustinov, K. (2003). Influence of shape and locations of initial 3-d cracks on their growth in uniaxial compression. *Engineering Fracture Mechanics*, 70(15):2115–2136.
- [63] Earle, S. (accessed 27-Sept-2019). Rock cycle diagram. *Opentextbc.ca*.
- [64] Einstein, H., Veneziano, D., Baecher, G., and O'Reilly, K. (1983). The effect of discontinuity persistence on rock slope stability. *International Journal of Rock Mechanics and Mining Sciences and Geomechanics Abstracts*, 20(5):227–236.
- [65] Ekweozor, C. and Daukoru, E. (1994). Northern delta depobelt portion of the Akata-Agbada petroleum system, Niger Delta, Nigeria. In: *Magoon, L.B. and Dow, W.G. (eds) The Petroleum System - from source to trap. American Association of Petroleum Geologists Memoir*, 460:599–613.
- [66] Erdogan, F. and Sih, G. C. (1963). On the crack extension in plates under plane loading and transverse shear. *Journal of Basic Engineering*, 85(4):519.
- [67] Eringen, A. (1966). A unified theory of thermomechanical materials. *International Journal of Engineering Science*, 4:179–202.
- [68] Ewy, R. and Cook, N. (1990). Deformation and fracture around cylindrical openings in rock: II. Initiation, growth and interaction of fractures. *Int. J. Mech. Min. Sci. Geomech. Abstr.*, 27(5):409–427.

- [69] Fort, X., Brun, J.-P., and Chauvel, F. (2004). Salt tectonics on the Angolan margin, synsedimentary deformation processes. *AAPG Bulletin*, 88(11):1523–1544.
- [70] Fredrich, J. T. and Wong, T.-F. (1986). Micromechanics of thermally induced cracking in three crustal rocks. *Journal of Geophysical Research: Solid Earth*, 91(B12):12743–12764.
- [71] Gaullier, V., Mart, Y., Bellaiche, G., Mascle, J., Vendeville, B. C., and Zitter, T. (2000). Salt tectonics in and around the Nile deep-sea fan: insights from the PRISMED II cruise. *Geological Society, London, Special Publications*, 174(1):111–129.
- [72] Gibson, R. (1958). The progress of consolidation in a clay layer increasing in thickness with time. *Geotechnique*, 8:171–182.
- [73] Goodman, R. and Kieffer, D. (2000). Behavior of rock in slopes. *Journal of Geotechnical and Geoenvironmental Engineering*, 126(8):675–684.
- [74] Goult, N. R. (2004). Mechanical compaction behaviour of natural clays and implications for pore pressure estimation. *Petroleum Geoscience*, 10:73–79.
- [75] Gradmann, S., Beaumont, C., and Albertz, M. (2009). Factors controlling the evolution of the Perdido Fold Belt, northwestern Gulf of Mexico, determined from numerical models. *Tectonics*, 28(2).
- [76] Graue, K. (2000). Mud volcanoes in deepwater Nigeria. *Marine and Petroleum Geology*, 17(8):959–974.
- [77] Gupta, A. K. and Akbar, H. (1984). Cracking in reinforced concrete analysis. *J. Struct. Engng*, 110(8):1735–1746.
- [78] Gutierrez, M. and Lewis, R. (1998). The Role of Geomechanics in Reservoir Simulation. *SPE/ISRM Rock Mechanics in Petroleum Engineering*.
- [79] Gutierrez, M. and Makurat, A. (1997). Coupled HTM modelling of cold water injection in fractured hydrocarbon reservoirs. *International Journal of Rock Mechanics and Mining Sciences*, 34(3-4).
- [80] Gutierrez, M. and Wangen, M. (2005). Modeling of compaction and overpressuring in sedimentary basins. *Marine and Petroleum Geology*, 22(3):351–363.
- [81] Haack, R., Sundararaman, P., Diedjomahor, J., Xiao, H., Gant, N., May, E., and Kelsch, K. (2000). Niger delta petroleum systems, Nigeria. In: Mello, M.R. and Katz, B.J. (eds), *Petroleum systems of South Atlantic margins. American Association of Petroleum Geologists Memoir*, 73:213–232.
- [82] Hansom, J. and Lee, M. K. (2005). Effects of hydrocarbon generation, basal heat flow and sediment compaction on overpressure development: a numerical study. *Petroleum Geoscience*, 11(4):353–360.
- [83] Hantschel, T. and Kauerauf, A. I. (2009). *Fundamentals of basin and petroleum systems modeling*. Springer.

- [84] Hashiguchi, K. (1995). Short communication on the linear relations of V-Inp and Inv-Inp for isotropic consolidation of soils. *Int. J. Numer. Anal. Methods Geomech.*, 19:367–376.
- [85] Higgins, S., Davies, R. J., and Clarke, B. (2007). Antithetic fault linkages in a deep water fold and thrust belt. *Journal of Structural Geology*, 29(12):1900–1914.
- [86] Hoek, E. and Bieniawski, Z. (1965). Brittle fracture propagation in rock under compression. *International Journal of Fracture Mechanics*, 1(3).
- [87] Hooper, R. J., Fitzsimmons, R. J., Grant, N., and Vendeville, B. C. (2002). The role of deformation in controlling depositional patterns in the south-central Niger Delta, West Africa. *Journal of Structural Geology*, 24(4):847–859.
- [88] Hussian, M., Pu, E., and Underwood, J. (1974). Strain energy release rate for a crack under combined mode i and mode ii. in- fracture analysis. *ASTM STP 560. American Society for Testing and Materials*, pages 2–28.
- [89] Ings, S. J. and Beaumont, C. (2010). Continental margin shale tectonics: Preliminary results from coupled fluid-mechanical models of large-scale delta instability. *Journal of the Geological Society*, 167(3):571–582.
- [90] Jha, B. and Juanes, R. (2007). A Locally Conservative Finite Element Framework for the Simulation of Coupled Flow and Reservoir Geomechanics. *SPE Annual Technical Conference and Exhibition*.
- [91] Kim, J., Tchelepi, H., and Juanes, R. (2011a). Stability and convergence of sequential methods for coupled flow and geomechanics: Drained and undrained splits. *Computer Methods in Applied Mechanics and Engineering*, 200(23-24):2094–2116.
- [92] Kim, J., Tchelepi, H., and Juanes, R. (2011b). Stability and convergence of sequential methods for coupled flow and geomechanics: Fixed-stress and fixed-strain splits. *Computer Methods in Applied Mechanics and Engineering*, 200(13-16):1591–1606.
- [93] Kim, J., Tchelepi, H. A., and Juanes, R. (2011c). Rigorous Coupling of geomechanics and multiphase flow with strong capillarity. *SPE Reservoir Simulation Symposium*.
- [94] Kim, J., Tchelepi, H. A., and Juanes, R. (2011d). Stability, Accuracy and Efficiency of Sequential Methods for Coupled Flow and Geomechanics. *SPE Reservoir Simulation Symposium*.
- [95] Kirschbaum, D., Adler, R., Hong, Y., Hill, S., and Lerner-Lam, A. (2010). A global landslide catalog for hazard applications: method, results, and limitations. *Natural Hazards*, 52(3):561–575.
- [96] Kirschbaum, D., Stanley, T., and Zhou, Y. (2015). Spatial and temporal analysis of a global landslide catalog. *Geomorphology*.
- [97] Klerck, P. (2000). The Finite Element Modelling of Discrete Fracture in Quasi-Brittle Materials. *Ph.D. Thesis, University of Wales, Swansea*.

- [98] Krueger, S. and Grant, N. (2006). Evolution of fault-related folds in the contractional toe of the deepwater niger delta. paper presented at the aapg annual convention, 9-12 april, houston, texas. *Search and Discovery*, 40201.
- [99] Laske, G. and Masters, G. (1997). A global digital map of sediment thickness. *EOS Trans. AGU*, 78, F483.
- [100] Lewis, R. W. and Shrefler, B. A. (1998). *The finite element method in the static and dynamic deformation and consolidation of porous media*. Wiley, 2 edition.
- [101] Lewis, R. W. and Sukirman, Y. (1993). Finite element modelling of three-phase flow in deforming saturated oil reservoirs. *International Journal for Numerical and Analytical Meth. Geomech.*, 17:577–598.
- [102] Li, Y.-P., Chen, L.-Z., and Wang, Y.-H. (2005). Experimental research on pre-cracked marble under compression. *International Journal of Solids and Structures*, 42(9-10):2505–2516.
- [103] Loncke, L., Gaullier, V., Mascle, J., Vendeville, B., and Camera, L. (2006). The Nile deep-sea fan: An example of interacting sedimentation, salt tectonics, and inherited subsalt paleotopographic features. *Marine and Petroleum Geology*, 23(3):297–315.
- [104] Luo, X. and Vasseur, G. (1992). Contributions of Compaction and Aquathermal Pressuring to Geopressure and the Influence of Environmental Conditions (1). *AAPG Bulletin*, 76.
- [105] Luo, X., Vasseur, G., Pouya, A., Lamoureux-Var, V., and Poliakov, A. (1998). Elasto-plastic deformation of porous media applied to the modelling of compaction at basin scale. *Marine and Petroleum Geology*, 15(2):145–162.
- [106] Mainguy, M. and Longuemare, P. (2002). Coupling Fluid Flow and Rock Mechanics: Formulations of the Partial Coupling Between Reservoir and Geomechanical Simulators. *Oil and Gas Science and Technology*, 57(4):355–367.
- [107] Marchina, P. and Onaisi, A. (2005). Reservoir-Geomechanics Coupled Simulations: A Powerful Tool for Well Design and Operation in an HP-HT Environment. *SPE/IADC Drilling Conference*.
- [108] McClay, K. R., Dooley, T., and Lewis, G. (1998). Analog modeling of progradational delta systems. *Geology*, 26(9):771.
- [109] McClay, K. R., Dooley, T., and Zamora, G. (2003). Analogue models of delta systems above ductile substrates. *Geological Society, London, Special Publications*, 216(1):411–428.
- [110] Meredith, P. G., Main, I. G., Clint, O. C., and Li, L. (2012). On the threshold of flow in a tight natural rock. *Geophysical Research Letters*, 39(4).
- [111] Merxhani, A. (2016). An introduction to linear poroelasticity.
- [112] Miehe, C., Hofacker, M., and Welschinger, F. (2010). A phase field model for rate-independent crack propagation: Robust algorithmic implementation based on operator splits. *Computer Methods in Applied Mechanics and Engineering*, 199(45-48):2765–2778.

- [113] Minkoff, S. E., Stone, C., Bryant, S., Peszynska, M., and Wheeler, M. F. (2003). Coupled fluid flow and geomechanical deformation modeling. *Journal of Petroleum Science and Engineering*, 38(1-2):37–56.
- [114] Mirzaei, H., Kakaie, R., Jalali, S., Shariati, M., and Hassani, B. (2010). Experimental investigation of crack propagation and coalescence in rock-like materials under uniaxial compression. *International Society for Rock Mechanics and Rock Engineering, ISRM International Symposium - EUROCK 2010, 15-18 June, Lausanne, Switzerland*.
- [115] Moes, N., Dolbow, J., and Belytschko, T. (1999). A finite element method for crack growth without remeshing. *International Journal for Numerical Methods in Engineering*, 46(1):131–150.
- [116] Moore, J. and Tobin, H. (1997). Estimated fluid pressure of the Barbados accretionary prism and adjacent sediments. *Proc. Ocean Drill. Program Sci. Results*, 156:229–238.
- [117] Moore, J. C., MASCLE, A., TAYLOR, E., ANDREIEFF, P., ALVAREZ, F., BARNES, R., BECK, C., BEHRMANN, J., BLANC, G., and BROWN, K. e. a. (1988). Tectonics and hydrogeology of the northern Barbados Ridge: Results from Ocean Drilling Program Leg 110. *Geological Society of America Bulletin*, 100(10):1578–1593.
- [118] Moore, J. C., Shipley, T. H., Goldberg, D., Ogawa, Y., Filice, F., Fisher, A., Jurado, M.-J., Moore, G. F., Rabaute, A., and Yin, H. e. a. (1995). Abnormal fluid pressures and fault-zone dilation in the Barbados accretionary prism: Evidence from logging while drilling. *Geology*, 23(7):605.
- [119] Moore, J. C. and Vrolijk, P. (1992). Fluids in accretionary prisms. *Reviews of Geophysics*, 30(2):113.
- [120] Morency, C., Huismans, R. S., Beaumont, C., and Fullsack, P. (2007). A numerical model for coupled fluid flow and matrix deformation with applications to disequilibrium compaction and delta stability. *Journal of Geophysical Research*, 112(B10).
- [121] Morgan, R. (2003). Prospectivity in ultradeep water: the case for petroleum generation and migration within the outer parts of the Niger Delta apron. *Geological Society, London, Special Publications*, 207(1):151–164.
- [122] Morley, C. K. and Guerin, G. (1996). Comparison of gravity-driven deformation styles and behavior associated with mobile shales and salt. *Tectonics*, 15(6):1154–1170.
- [123] Mourgues, R. and Cobbold, P. R. (2006). Thrust wedges and fluid overpressures: Sandbox models involving pore fluids. *Journal of Geophysical Research: Solid Earth*, 111(B5):n/a–n/a.
- [124] Mourgues, R., Lecomte, E., Vendeville, B., and Raillard, S. (2009). An experimental investigation of gravity-driven shale tectonics in progradational delta. *Tectonophysics*, 474:643–656.
- [125] Muhlhaus, H. and Alfantis, E. (1991). A variational principle for gradient plasticity. *International Journal of Solids and Structures*, 28:845–857.

- [126] Muhlhaus, H. and Vardoulakis, I. (1987). The thickness of shear bands in granular materials. *Geotechnique*, 37:271–283.
- [127] Nguyen, T., Borgesson, L., Chijimatsu, M., Rutqvist, J., Fujita, T., Hernelind, J., Kobayashi, A., Ohnishi, Y., Tanaka, M., and Jing, L. (2001). Hydro-mechanical response of a fractured granitic rock mass to excavation of a test pit - the Kamaishi Mine experiment in Japan. *International Journal of Rock Mechanics and Mining Sciences*, 38(1):79–94.
- [128] Obradors-Prats, J., Rouainia, M., Aplin, A. C., and Crook, A. J. (2017a). Assessing the implications of tectonic compaction on pore pressure using a coupled geomechanical approach. *Marine and Petroleum Geology*, 79:31–43.
- [129] Obradors-Prats, J., Rouainia, M., Aplin, A. C., and Crook, A. J. L. (2017b). Hydromechanical Modeling of Stress, Pore Pressure, and Porosity Evolution in Fold-and-Thrust Belt Systems. *Journal of Geophysical Research: Solid Earth*, 122(11):9383–9403.
- [130] Osborne, M. and Swarbrick, R. (1997). Mechanisms for Generating Overpressure in Sedimentary Basins: A Reevaluation. *American Association of Petroleum Geologists Bulletin*, 81:1023–1041.
- [131] Owen, D. and Hinton, E. (1980). *Finite elements in Plasticity: Theory and practice*. Pineridge.
- [132] Papanastasiou, P. and Vardoulakis, I. (1992). Numerical treatment of progressive localization in relation to borehole stability. *International Journal for Numerical and Analytical Methods in Geomechanics*, 16(6):389–424.
- [133] Park, C. and Bobet, A. (2009). Crack coalescence in specimens with open and closed flaws: A comparison. *International Journal of Rock Mechanics and Mining Sciences*, 46(5):819–829.
- [134] Petrunin, A. and Sobolev, S. (2008). Three-dimensional numerical models of the evolution of pull-apart basins. *Physics of the Earth and Planetary Interiors*, 171(1-4):387–399.
- [135] Pietruszczak, S. and Mroz, Z. (1981). Finite element analysis of deformation of strain-softening materials. *International Journal for Numerical Methods in Engineering*, 17(3):327–334.
- [136] Poliakov, A. N. B., Podladchikov, Y. Y., Dawson, E. C., and Talbot, C. J. (1996). Salt diapirism with simultaneous brittle faulting and viscous flow. *Geological Society, London, Special Publications*, 100(1):291–302.
- [137] Popov, A. and Sobolev, S. (2008). SLIM3D: A tool for three-dimensional thermomechanical modeling of lithospheric deformation with elasto-visco-plastic rheology. *Physics of the Earth and Planetary Interiors*, 171(1-4):55–75.
- [138] Prandtl, L. (1921). Über die Eindringungsfestigkeit (Harte) plastischer Baustoffe und die Festigkeit von Schneiden. *Zeitschrift für angewandte Mathematik und Mechanik*, 1(1):15–20.

- [139] Rahman, N. A. and Lewis, R. W. (1999). Finite element modelling of multiphase immiscible flow in deforming porous media for subsurface systems. *Computers and Geotechnics*, 24(1):41–63.
- [140] Rebecca M., B. (2002). A review of useful theorems involving proper orthogonal matrices referenced to three-dimensional physical space. *Sandia National Laboratories*.
- [141] Reyes, O. and Einstein, H. (1991). Failure mechanisms of fractured rock - a fracture coalescence model. *International Journal of Rock Mechanics and Mining Sciences and Geomechanics Abstracts*, 29(4):217.
- [142] Rowan, M., Peel, F., and Vendeville, B. (2004). Gravity-driven Fold Belts on Passive Margins. *AAPG Memoir*, 82:157–182.
- [143] Rowan, M. G. (1997). Three-dimensional geometry and evolution of a segmented detachment fold, Mississippi Fan fold belt, Gulf of Mexico. *Journal of Structural Geology*, 19(3-4):463–480.
- [144] Rubey, W. W. and King Hubbert, M. (1959). Role of fluid pressure in mechanics of overthrust faulting. *Geological Society of America Bulletin*, 70(2):167.
- [145] Rutqvist, J., Birkholzer, J., Cappa, F., and Tsang, C. F. (2007). Estimating maximum sustainable injection pressure during geological sequestration of CO₂ using coupled fluid flow and geomechanical fault-slip analysis. *Energy Conversion and Management*, 48(6):1798–1807.
- [146] Rutqvist, J., Birkholzer, J., and Tsang, C.-F. (2008). Coupled reservoir-geomechanical analysis of the potential for tensile and shear failure associated with CO₂ injection in multilayered reservoir-caprock systems. *International Journal of Rock Mechanics and Mining Sciences*, 45(2):132–143.
- [147] Rutqvist, J., Borgesson, L., Chijimatsu, M., Kobayashi, A., Jing, L., Nguyen, T., Noorishad, J., and Tsang, C. F. (2001). Thermohydromechanics of partially saturated geological media: governing equations and formulation of four finite element models. *International Journal of Rock Mechanics and Mining Sciences*, 38(1):105–127.
- [148] Sagong, M. and Bobet, A. (2002). Coalescence of multiple flaws in a rock-model material in uniaxial compression. *International Journal of Rock Mechanics and Mining Sciences*, 39(2):229–241.
- [149] Schneider, F. and Hay, S. (2001). Compaction model for quartzose sandstones application to the Garn Formation, Haltenbanken, Mid-Norwegian Continental Shelf. *Marine and Petroleum Geology*, 18(7):833–848.
- [150] Schneider, F., Potdevin, J., Wolf, S., and Faille, I. (1996). Mechanical and chemical compaction model for sedimentary basin simulators. *Tectonophysics*, 263(1-4):307–317.
- [151] Schultz-Ela, D. (2001). Excursus on gravity gliding and gravity spreading. *Journal of Structural Geology*, 23(5):725–731.

- [152] Selater, J. and Christie, P. A. F. (1980). Continental stretching: An explanation of the post-mid-cretaceous subsidence of the central north sea basin. *Journal of Geophysical Research: Solid Earth*, 85(B7):3711–3739.
- [153] Settari, A. and Mourits, F. (1998). A Coupled Reservoir and Geomechanical Simulation System. *SPE Journal*, 3(03):219–226.
- [154] Settari, A. T. and Walters, D. A. (1999). Advances in Coupled Geomechanical and Reservoir Modeling With Applications to Reservoir Compaction. *SPE Reservoir Simulation Symposium*.
- [155] Shen, B. and Stephansson, O. (1994). Modification of the g-criterion for crack propagation subjected to compression. *Engineering Fracture Mechanics*, 47(2):177–189.
- [156] Sih, G. C. (1974). Strain-energy-density factor applied to mixed mode crack problems. *International Journal of Fracture*, 10(3):305–321.
- [157] Swarbrick, R., Osborne, M., and Yardley, G. (2002). Comparison of overpressure magnitude resulting from the main generating mechanisms, in Pressure Regimes in Sedimentary Basins and Their Prediction, edited by A.R. Huffman and G.L. Bowers. *AAPG Mem.*, 76:1–12.
- [158] Tang, C. and Kou, S. (1998). Crack propagation and coalescence in brittle materials under compression. *Engineering Fracture Mechanics*, 61(3-4):311–324.
- [159] Tang, C., Lin, P., Wong, R., and Chau, K. (2001). Analysis of crack coalescence in rock-like materials containing three flaws. part ii- numerical approach. *International Journal of Rock Mechanics and Mining Sciences*, 38(7):925–939.
- [160] Taylor, D. W. (1948). *Fundamentals of Soil Mechanics*. Wiley.
- [161] Teige, G., Hermanrud, C., Wensaas, L., and Bolas, H. N. (1999). The lack of relationship between overpressure and porosity in North Sea and Haltenbanken shales. *Marine and Petroleum Geology*, 16(4):321–335.
- [162] Thomas, L., Chin, L., Pierson, R., and Sylte, J. (2003). Coupled Geomechanics and Reservoir Simulation. *SPE Journal*, 8(04):350–358.
- [163] Tran, D., Nghiem, L., and Buchanan, L. (2005). Improved Iterative Coupling of Geomechanics With Reservoir Simulation. *SPE Reservoir Simulation Symposium*.
- [164] Tran, D., Settari, A., and Nghiem, L. (2004). New Iterative Coupling Between a Reservoir Simulator and a Geomechanics Module. *SPE/ISRM Rock Mechanics Conference*.
- [165] Ungerer, P., Burrus, J., Doligez, B., and Chenet, P. Y. (1990). Basin Evaluation by Integrated Two-Dimensional Modeling of Heat Transfer, Fluid Flow, Hydrocarbon Generation, and Migration. *AAPG Bulletin*, 74:309–335.
- [166] Vallejo, L. (1988). The brittle and ductile behaviour of clay samples containing a crack under mixed mode loading. *Theoretical and Applied Fracture Mechanics*, 10(1):73–78.
- [167] Vallejo, L. E. (1987). The influence of fissures in a stiff clay subjected to direct shear. *Géotechnique*, 37(1):69–82.

- [168] Vallejo, L. E., Shettima, M., and Alaasmi, A. (2013). Unconfined compressive strength of brittle material containing multiple cracks. *International Journal of Geotechnical Engineering*, 7(3):318–321.
- [169] van den Hoek, P., Smit, D., Kooijman, A., de Bree, P., Kenter, C., and Khodaverdian, M. (1994). Size dependency of hollow cylinder stability. *Eurock, Balkema, Rotterdam*, 94.
- [170] Van Eekelen, H. A. M. (1980). Isotropic yield surfaces in three dimensions for use in soil mechanics. *International Journal for Numerical and Analytical Methods in Geomechanics*, 4:89–101.
- [171] van Genuchten, M. T. (1980). A Closed-form Equation for Predicting the Hydraulic Conductivity of Unsaturated Soils. *Soil Science Society of America Journal*, 44(5):892.
- [172] Van Rensbergen, P. and Morley, C. (2000). 3D Seismic study of a shale expulsion syncline at the base of the Champion delta, offshore Brunei and its implications for the early structural evolution of large delta systems. *Marine and Petroleum Geology*, 17(8):861–872.
- [173] Van Rensbergen, P., MORLEY, C. K., ANG, D. W., HOAN, T. Q., and LAM, N. T. (1999). Structural evolution of shale diapirs from reactive rise to mud volcanism: 3D seismic data from the Baram delta, offshore Brunei Darussalam. *Journal of the Geological Society*, 156(3):633–650.
- [174] Vejbaek, O. V. (2008). Disequilibrium compaction as the cause for Cretaceous-Paleogene overpressures in the Danish North Sea. *AAPG Bulletin*, 92(2):165–180.
- [175] Vendeville, B. C. (2005). Salt tectonics driven by sediment progradation: Part I-Mechanics and kinematics. *AAPG Bulletin*, 89(8):1071–1079.
- [176] Vesga, L., Vallejo, L., and Lobo-Guerrero, S. (2008). Dem analysis of the crack propagation in brittle clays under uniaxial compression tests. *International Journal for Numerical and Analytical Methods in Geomechanics*, 32(11):1405–1415.
- [177] VonNeumann, J. and Richtmyer, R. D. (1950). A Method for the Numerical Calculation of Hydrodynamic Shocks. *Journal of Applied Physics*, 21(3):232–237.
- [178] Wangen, M. (2000). Generation of overpressure by cementation of pore space in sedimentary rocks. *Geophysical Journal International*, 143(3):608–620.
- [179] Wangen, M. (2001). A quantitative comparison of some mechanisms generating overpressure in sedimentary basins. *Tectonophysics*, 334(3-4):211–234.
- [180] Warren, C. J., Beaumont, C., and Jamieson, R. A. (2008). Deep subduction and rapid exhumation: Role of crustal strength and strain weakening in continental subduction and ultrahigh-pressure rock exhumation. *Tectonics*, 27(6).
- [181] Weber, K. and Daukoru, E. (1975). Petroleum geology of the Niger Delta: Proceedings of the ninth World Petroleum Congress. *Geology*, 2:210–221.

- [182] Wees, J. V., Bergen, F. V., David, P., Nepveu, M., Beekman, F., Cloetingh, S., and Bonte, D. (2009). Probabilistic tectonic heat flow modeling for basin maturation: Assessment method and applications. *Marine and Petroleum Geology*, 26(4):536–551.
- [183] Weimer, P. and Buffler, R. (1992). Structural geology and evolution of the Mississippi fan fold belt, deep Gulf of Mexico. *AAPG Bulletin* 76, pages 224–251.
- [184] Wong, L. N. Y. and Einstein, H. H. (2008). Crack coalescence in molded gypsum and carrara marble: Part 1. macroscopic observations and interpretation. *Rock Mechanics and Rock Engineering*, 42(3):475–511.
- [185] Wong, R. and Chau, K. (1998). Crack coalescence in a rock-like material containing two cracks. *International Journal of Rock Mechanics and Mining Sciences*, 35(2):147–164.
- [186] Wong, R., Chau, K., Tang, C., and Lin, P. (2001). Analysis of crack coalescence in rock-like materials containing three flaws. Part I- experimental approach. *International Journal of Rock Mechanics and Mining Sciences*, 38(7):909–924.
- [187] Wood, D. (1990). *Soil Behaviour and Critical State Soil Mechanics*. University Press.
- [188] Wu, S., Bally, A. W., and Cramez, C. (1990). Allochthonous salt, structure and stratigraphy of the north-eastern Gulf of Mexico. Part II: Structure. *Marine and Petroleum Geology*, 7(4):334–370.
- [189] Yamada, Y. and Ishihara, K. (1979). Anisotropic deformation characteristics of sand under three dimensional stress conditions. *Soils and Foundations*, 19:79–94.
- [190] Yang, S.-Q., Liu, X.-R., and Jing, H.-W. (2013). Experimental investigation on fracture coalescence behavior of red sandstone containing two unparallel fissures under uniaxial compression. *International Journal of Rock Mechanics and Mining Sciences*, 63:82–92.
- [191] Yasufuku, N., Murata, H., and Hyodo, M. (1991). Yield characteristics of anisotropically consolidated sand under low and high stress. *Soils and Foundations*, 31:95–109.

Appendix A

Modified Drucker-Prager Return-Mapping Algorithms

Algorithm 1 Modified Drucker-Prager Pseudocode

1: Compute

$$\begin{aligned}\boldsymbol{\sigma}^{trial,n+1} &= \boldsymbol{\sigma}^n + 2G \left(\Delta \boldsymbol{\varepsilon} - \frac{1}{3} \Delta \varepsilon_v^p \mathbf{I} \right) + K \Delta \varepsilon_v^p \mathbf{I} \\ p^{trial,n+1} &= \frac{1}{3} \text{tr} \left[\boldsymbol{\sigma}^{trial,n+1} \right] \\ q^{trial,n+1} &= \sqrt{\frac{3}{2}} \| \mathbf{s}^{trial,n+1} \| \end{aligned}$$

2: Compute $g \leftarrow g(\boldsymbol{\sigma}^{trial,n+1})$

3: Regularize $\bar{\varepsilon}^p$

4: Assume

$$\bar{\varepsilon}^{p,n+1} = \bar{\varepsilon}^{p,n}$$

$$\beta^{n+1} = \beta^n$$

$$d^{n+1} = d^n$$

5: Compute Drucker-Prager yield function

$$\Phi = gq^{trial,n+1} + (\tan \beta^{n+1}) p^{trial,n+1} - d^{n+1}$$

6: **if** $\Phi \leq 0$ **then**

$$\boldsymbol{\sigma}^{n+1} \leftarrow \boldsymbol{\sigma}^{trial,n+1}$$

7: **else**

8: YIELD=.TRUE.

9: GOTO Algorithm 2

▷ Stress correction algorithm

10: **end if**

Algorithm 2 Modified Drucker-Prager Smooth Return-Mapping Procedure

Initialise $\Delta\gamma = 0$

Set APEX=.FALSE., CONVERGE=.FALSE.

for $i = 1, i \leq \text{maxiter}, i++$,

 Compute hardening variables

$$\bar{\varepsilon}^{p,n+1} = \bar{\varepsilon}^{p,n} + \Delta\gamma^i$$

$$d^{n+1} = d(\bar{\varepsilon}^{p,n+1})$$

$$\beta^{n+1} = \beta(\bar{\varepsilon}^{p,n+1})$$

$$\psi^{n+1} = \psi(\bar{\varepsilon}^{p,n+1})$$

 Compute yield function

$$p^{n+1} = p^{trial,n+1} - K\Delta\gamma^i \tan \psi^{n+1}$$

$$q^{n+1} = q^{trial,n+1} - 3G\Delta\gamma^i$$

$$\Phi^{n+1} = gq^{n+1} + p^{n+1} \tan \beta^{n+1} - d^{n+1}$$

if $\text{abs}(\Phi^{n+1}) \leq \text{tol}$,

 CONVERGE = .TRUE.

$$\Delta\varepsilon_v^p = \Delta\gamma^i \tan \psi^{n+1}$$

$$\mathbf{N}_d^{n+1} = \frac{3}{2q^{trial,n+1}} \mathbf{s}^{trial,n+1}$$

$$\boldsymbol{\sigma}^{n+1} = \boldsymbol{\sigma}^{trial,n+1} - 2G\Delta\gamma^i \mathbf{N}_d - K\Delta\varepsilon_v^p \mathbf{I}$$

$$\bar{\varepsilon}^{p,n+1} = \bar{\varepsilon}^{p,n} + \Delta\gamma^i$$

 Exit loop

else

$$\Delta(\Delta\gamma) = - \left[\frac{\partial \Phi}{\partial (\Delta\gamma)} \right]_{\Delta\gamma=\Delta\gamma^i}^{-1} \Phi^{n+1}$$

$$\Delta\gamma^{i+1} = \Delta\gamma^i + \Delta(\Delta\gamma)$$

endif

endfor

GOTO Algorithm 3

Algorithm 3 Modified Drucker-Prager Apex Return-Mapping Procedure

if (.NOT. CONVERGE .OR. $q^{n+1} < 0$.OR. $p^{n+1} > d \cot \beta^{n+1}$)

APEX=.TRUE.

$\Delta \bar{\epsilon}^p = 0$

for $i = 1, i \leq \text{maxiter}, i++$,

 Compute hardening variables

$$\bar{\epsilon}^{p,n+1} = \bar{\epsilon}^{p,n} + \Delta \bar{\epsilon}^{p,i}$$

$$d^{n+1} = d(\bar{\epsilon}^{p,n+1})$$

$$\beta^{n+1} = \beta(\bar{\epsilon}^{p,n+1})$$

$$\psi^{n+1} = \psi(\bar{\epsilon}^{p,n+1})$$

 Compute increment volumetric plastic strain

$$\Delta \epsilon_v^p = \Delta \bar{\epsilon}^{p,i} \tan \psi^{n+1}$$

 Compute yield function

$$p^{n+1} = p^{trial,n+1} - K \Delta \epsilon_v^p$$

$$\Phi^{n+1} = p^{n+1} \tan \beta^{n+1} - d^{n+1}$$

if $\text{abs}(\Phi^{n+1}) \leq \text{tol}$,

 CONVERGE = .TRUE.

$$\bar{\epsilon}^{p,n+1} = \bar{\epsilon}^{p,n} + \Delta \bar{\epsilon}^{p,i}$$

$$\Delta \epsilon_v^p = \Delta \bar{\epsilon}^{p,i} \tan \psi^{n+1}$$

$$\sigma^{n+1} = \sigma^{trial,n+1} - K \Delta \epsilon_v^p \mathbf{I}$$

 Exit loop

elseif($d^{n+1} = 0$.OR. $\psi^{n+1} = 0$) **then**

▷ Critical state

CONVERGE = .TRUE.

$$d^{n+1} = 0$$

$$\psi^{n+1} = 0$$

$$\Delta \varepsilon_v^p = \frac{p^{trial,n+1}}{K}$$

$$\Delta \gamma = \frac{q^{trial,n+1}}{3G}$$

$$\bar{\varepsilon}^{p,n+1} = \bar{\varepsilon}^{p,n} + \Delta \gamma$$

$$\sigma^{n+1} = \sigma^{trial,n+1} - K \Delta \varepsilon_v^p \mathbf{I}$$

Exit loop

else

$$\text{Compute } \Delta(\Delta \bar{\varepsilon}^p) = - \left[\frac{\partial \Phi}{\partial (\Delta \bar{\varepsilon}^p)} \right]_{\Delta \bar{\varepsilon}^p = \Delta \bar{\varepsilon}^{p,i}}^{-1} \Phi^{n+1}$$

$$\Delta \bar{\varepsilon}^{p,i+1} = \Delta \bar{\varepsilon}^{p,i} + \Delta(\Delta \bar{\varepsilon}^p)$$

endif

endfor

endif

Appendix B

SR4 Return-Mapping Algorithms

Algorithm 4 SR4 Pseudocode

1: Compute

$$\begin{aligned}\boldsymbol{\sigma}^{trial,n+1} &= \boldsymbol{\sigma}^n + 2G \left(\Delta \boldsymbol{\varepsilon} - \frac{1}{3} \Delta \boldsymbol{\varepsilon}_v^p \mathbf{I} \right) + K \Delta \boldsymbol{\varepsilon}_v^p \mathbf{I} \\ p^{trial,n+1} &= \frac{1}{3} \text{tr} \left[\boldsymbol{\sigma}^{trial,n+1} \right] \\ q^{trial,n+1} &= \sqrt{\frac{3}{2}} \| \boldsymbol{s}^{trial,n+1} \| \end{aligned}$$

2: Compute $g \leftarrow g(\boldsymbol{\sigma}^{trial,n+1})$

3: Regularize $\boldsymbol{\varepsilon}_v^p$

4: Assume

$$\begin{aligned}\boldsymbol{\varepsilon}_v^{p,n+1} &= \boldsymbol{\varepsilon}_v^{p,n} \\ p_c^{n+1} &= p_c^n \\ p_t^{n+1} &= p_t^n \end{aligned}$$

5: Compute $p_{\Phi_{peak}}^{n+1}$, M_{Φ}^{n+1} , and $p_{\Psi_{crit}}^{n+1}$

$$\begin{aligned} p_{\Phi_{peak}}^{n+1} &= \frac{\mathfrak{m} p_c^{n+1} + p_t^{n+1}}{1 + \mathfrak{m}} \\ M_{\Phi}^{n+1} &= -(\mathfrak{m} + 1)^{-\frac{1}{\mathfrak{m}}} \left(1 - \frac{p_t^{n+1}}{p_{\Phi_{peak}}^{n+1}} \right) \tan \beta \\ p_{\Psi_{crit}}^{n+1} &= \frac{\mathfrak{m} p_c^{n+1} + p_t^{n+1}}{1 + \mathfrak{m}} \end{aligned}$$

6: Initialize flags:

CAP=.FALSE.
SHEAR=.FALSE.
SHRYD=.FALSE.

7: **if** $p^{trial,n+1} > p_{\Psi_{crit}}^{n+1}$ **then**

SHEAR=.TRUE.

Compute

$$\Phi_{shear}^{SR4,n+1} = gq^{trial,n+1} + (p^{trial,n+1} - p_t^{n+1}) \tan \beta \left(\frac{p^{trial,n+1} - p_c^{n+1}}{p_t^{n+1} - p_c^{n+1}} \right)^{1/n}$$

8: **else**

CAP=.TRUE.

if $p^{trial,n+1} > p_{\Phi_{peak}}^{n+1}$

SHRYD=.TRUE.

Compute

$$\Phi_{shear}^{SR4,n+1} = gq^{trial,n+1} + (p^{trial,n+1} - p_t^{n+1}) \tan \beta \left(\frac{p^{trial,n+1} - p_c^{n+1}}{p_t^{n+1} - p_c^{n+1}} \right)^{1/n}$$

else

SHRYD=.FALSE.

Compute

$$\Phi_{cap}^{SR4,n+1} = gq^{trial,n+1} - M_{\Phi}^{n+1} p_{\Phi_{peak}}^{n+1} \sqrt{1 - \left(\frac{p^{trial,n+1} - p_{\Phi_{peak}}^{n+1}}{p_{\Phi_{peak}}^{n+1} - p_c^{n+1}} \right)^2}$$

endif

9: **end if**

10: **if** $\Phi_{cap}^{SR4,n+1} > 0$.OR. $\Phi_{shear}^{SR4,n+1} > 0$ **then**

Check if apex condition

11: **if** $p^{trial,n+1} > p_t^{n+1}$ **then**

GOTO Algorithm 5

▷ Apex return

12: **else**

GOTO Algorithm 6

▷ Smooth return

13: **end if**

14: **else**

$$\sigma^{n+1} \leftarrow \sigma^{trial,n+1}$$

15: **end if**

Algorithm 5 SR4 Apex Return-Mapping Procedure

if (.NOT. CONVERGE .OR. $q^{n+1} \leq 0$.OR. $p^{n+1} > d \cot \beta^{n+1}$)

Initialise $\Delta \varepsilon_v^p = 0, \Delta \gamma = 0, N_v^{n+1} = 0$

Set APEX=.TRUE., CONVERGE=.FALSE.

for $i = 1, i \leq \text{maxiter}, i++$,

 Compute hardening variables

$$\varepsilon_v^{p,n+1} = \varepsilon_v^{p,n} + \Delta \varepsilon_v^{p,i}$$

$$p_c^{n+1} = p_c(\varepsilon_v^{p,n+1})$$

$$p_t^{n+1} = p_t(\varepsilon_v^{p,n+1})$$

 Compute stress terms

$$p^{n+1} = p^{trial,n+1} - K \Delta \varepsilon_v^{p,i}$$

$$p_{\Phi peak}^{n+1} = \frac{\eta p_c^{n+1} + p_t^{n+1}}{1 + \eta}$$

$$M_{\Phi}^{n+1} = -(\eta + 1)^{-\frac{1}{\eta}} \left(1 - \frac{p_t^{n+1}}{p_{\Phi peak}^{n+1}} \right) \tan \beta$$

 Compute functions

$$\Phi_{shear}^{SR4,n+1} = (p^{n+1} - p_t^{n+1}) \tan \beta \left(\frac{p^{n+1} - p_c^{n+1}}{p_t^{n+1} - p_c^{n+1}} \right)^{1/\eta}$$

$$f_{2,shear} = \Delta \varepsilon_v^{p,i} - 3 \Delta \gamma N_v^{n+1,i}$$

$$f_{3,shear} = N_v^{n+1,i} - \frac{\tan \psi}{3} \left(1 + \frac{1}{\eta} \left(\frac{p^{n+1} - p_t^{n+1}}{p^{n+1} - p_c^{n+1}} \right) \right) \left(\frac{p^{n+1} - p_c^{n+1}}{p_t^{n+1} - p_c^{n+1}} \right)^{1/\eta}$$

 Construct vector \mathbf{f}

$$\mathbf{f}^i = \begin{Bmatrix} \Phi_{shear}^{SR4,n+1} \\ f_{2,shear} \\ f_{3,shear} \end{Bmatrix}^i$$

if $\text{norm}(\mathbf{f}^i) \leq \text{tol}$,

CONVERGE = .TRUE.

$$\boldsymbol{\sigma}^{n+1} = \boldsymbol{\sigma}^{trial,n+1} - K\Delta\boldsymbol{\varepsilon}_v^{p,i}\mathbf{I}$$

else

$$\text{Update } \mathbf{x}^i = \begin{Bmatrix} \Delta\gamma^i \\ \Delta\boldsymbol{\varepsilon}_v^{p,i} \\ N_v^{n+1,i} \end{Bmatrix}$$
$$\mathbf{x}^{i+1} = \mathbf{x}^i - \left[\frac{\partial \mathbf{f}}{\partial \mathbf{x}} \right]_{\text{shear}}^{-1} \mathbf{f}^i$$

endif

endfor

endif

Algorithm 6 SR4 Smooth Return-Mapping Procedure

Initialise $\Delta \epsilon_v^p = 0, \Delta \gamma = 0, N_v^{n+1} = 0$

Set APEX=.FALSE., CONVERGE=.FALSE.

for $i = 1, i \leq \text{maxiter}, i++$,

 Compute hardening variables

$$\epsilon_v^{p,n+1} = \epsilon_v^{p,n} + \Delta \epsilon_v^{p,i}$$

$$p_c^{n+1} = p_c(\epsilon_v^{p,n+1})$$

$$p_t^{n+1} = p_t(\epsilon_v^{p,n+1})$$

 Compute stress terms

$$p^{n+1} = p^{trial,n+1} - K \Delta \epsilon_v^{p,i}$$

$$q^{n+1} = q^{trial,n+1} - 3G \Delta \gamma^i$$

$$p_{\Phi peak}^{n+1} = \frac{\eta p_c^{n+1} + p_t^{n+1}}{1 + \eta}$$

$$M_{\Phi}^{n+1} = -(\eta + 1)^{-\frac{1}{\eta}} \left(1 - \frac{p_t^{n+1}}{p_{\Phi peak}^{n+1}} \right) \tan \beta$$

if (.NOT.SHEAR) **then**

$$\text{SHRYLD} = p^{n+1} \geq p_{\Phi peak}^{n+1}$$

endif

if (SHEAR.OR.SHRYLD) **then**

 CAP=.FALSE.

$$\Phi_{shear}^{SR4,n+1} = g q^{n+1} + (p^{n+1} - p_t^{n+1}) \tan \beta \left(\frac{p^{n+1} - p_c^{n+1}}{p_t^{n+1} - p_c^{n+1}} \right)^{1/\eta}$$

$$f_{2,shear} = \Delta \epsilon_v^{p,i} - 3 \Delta \gamma N_v^{n+1,i}$$

$$f_{3,shear} = N_v^{n+1,i} - \frac{\tan \psi}{3} \left(1 + \frac{1}{\eta} \left(\frac{p^{n+1} - p_t^{n+1}}{p^{n+1} - p_c^{n+1}} \right) \right) \left(\frac{p^{n+1} - p_c^{n+1}}{p_t^{n+1} - p_c^{n+1}} \right)^{1/\eta}$$

else

CAP=.TRUE.

$$\Phi_{cap}^{SR4,n+1} = gq^{n+1} - M_{\Phi}^{n+1} p_{\Phi peak}^{n+1} \sqrt{1 - \left(\frac{p^{n+1} - p_{\Phi peak}^{n+1}}{p_{\Phi peak}^{n+1} - p_c^{n+1}} \right)^2}$$

$$f_{2,cap} = \Delta \varepsilon_v^{p,i} - 3\Delta \gamma^i N_v^{n+1,i}$$

$$f_{3,cap} = N_v^{n+1,i} - \frac{M_{\Psi}^{n+1} (p^{n+1} - p_{\Psi crit}^{n+1}) p_{\Psi crit}^{n+1}}{3(p_c^{n+1} - p_{\Psi crit}^{n+1})^2 \sqrt{1 - \left(\frac{p^{n+1} - p_{\Psi crit}^{n+1}}{p_c^{n+1} - p_{\Psi crit}^{n+1}} \right)^2}}$$

endif

Construct accordingly vector f

$$f^i = \begin{Bmatrix} \Phi^{SR4,n+1} \\ f_2 \\ f_3 \end{Bmatrix}^i$$

if $\text{norm}(f^i) \leq \text{tol}$,

CONVERGE =.TRUE.

$$N_d^{n+1} = \frac{3}{2q^{trial,n+1}} s^{trial,n+1}$$

$$\sigma^{n+1} = \sigma^{trial,n+1} - 2G\Delta \gamma^i N_d - K\Delta \varepsilon_v^{p,i} \mathbf{I}$$

else

$$\text{Update } \mathbf{x}^i = \begin{Bmatrix} \Delta \gamma^i \\ \Delta \varepsilon_v^{p,i} \\ N_v^{n+1,i} \end{Bmatrix}$$

$$\mathbf{x}^{i+1} = \mathbf{x}^i - \left[\frac{\partial \mathbf{f}}{\partial \mathbf{x}} \right]_{\text{cap/shear}}^{-1} \mathbf{f}^i$$

endif

endfor

GOTO Algorithm 5

Appendix C

Material Properties for Section 5.6 Simulation Tests

Material Properties	Values
Density (kg/m ³)	1600
Porosity	0.4
Young's modulus (Pa)	10 ⁶
Poisson's ratio	0.2
Biot constant	1.0

Table C.1 Poroelastic properties for Sand 1, 2, 3

Material Properties	Values
Density (kg/m ³)	1200
Porosity	0.1
Young's modulus (Pa)	10 ⁶
Poisson's ratio	0.2
Biot constant	1.0

Table C.2 Poroelastic properties for Wall

Material	Hydraulic Permeability (10 ⁻⁴ mm ²)
Sand 1	1.00
Sand 2	0.34
Sand 3	10 ⁻⁵

Table C.3 Hydraulic permeabilities

Effective Plastic Strain	0.00	0.05
Cohesion, d (Pa)	338.06	0.00
Friction angle, $\beta(^{\circ})$	43.55	43.55
Dilation angle, $\psi(^{\circ})$	43.55	0.00

Table C.4 Sand 1 hardening properties

Effective Plastic Strain	0.00	0.05
Cohesion, d (Pa)	176.89	0.00
Friction angle, $\beta(^{\circ})$	49.87	49.87
Dilation angle, $\psi(^{\circ})$	49.87	0.00

Table C.5 Sand 2 hardening properties

Effective Plastic Strain	0.00	0.05
Cohesion, d (Pa)	50	0.00
Friction angle, $\beta(^{\circ})$	49.87	49.87
Dilation angle, $\psi(^{\circ})$	49.87	0.00

Table C.6 Sand 3 hardening properties

Density (kg/m^3)	1.20410
Bulk modulus (Pa)	101000
Viscosity (Pa.s)	$2(10^{-5})$

Table C.7 Air properties